Development of High-Efficiency Cost-Effective, Zinc-Chlorine Batteries for Utility Peak-Shaving, 1976

EM-711
Research Projects 226-2 and 226-1-2

Interim Report, March 1978

Prepared by

ENERGY DEVELOPMENT ASSOCIATES
1100 W. Whitcomb Avenue
Madison Heights, Michigan 48071

Principal Investigator
Philip C. Symons

Prepared for

Electric Power Research Institute
3412 Hillview Avenue
Palo Alto, California 94304

EPRI Project Manager
James R. Birk
Fossil Fuel and Advanced Systems Division

ABSTRACT

The zinc-chlorine battery is presently under development for utility peak-shaving. The technical feasibility of the battery for this application was confirmed in an earlier program, RP226-1. The two principal thrusts of this follow-on program were battery scale-up by a factor of twenty and investigation of the economics of zinc-chlorine peak-shaving batteries located at utility substations. Development programs on cell performance, electrode research, and materials of construction were conducted in support of these objectives.

A battery was designed, built, and tested, which delivered 18 kWh dc at an electrochemical energy efficiency of 60%. This scale-up from a 1 kWh system was successful despite difficulties with excessive hydrogen evolution and zinc-dendrite formation during initial testing. Two smaller systems were built and tested in order to permit informed selection of the chlorine-electrode material. Porous graphite was chosen over ruthenia-catalyzed porous titanium because of considerations of ultimate cost, ease of system operability, and system safety. The cycle-testing of two battery systems was successfully automated -- one with hard-wired logic while the other was microprocessor-based. Experience with the automation activities indicated that the zinc-chlorine battery system can operate (charge and discharge) for extended periods without human intervention.

Two conceptual designs - Mark 2 and Mark 3 - of a 100MWh (20MW) zinc-chlorine battery plant were prepared. A detailed cost breakdown was provided for each design. In a mature market, the selling prices of the Mark 2 and Mark 3 plants would be $25/kWh and $21/kWh (1976$) respectively. These selling prices coupled with a 70% ac to ac storage efficiency would make the battery plants highly competitive with fossil fuel-consuming combustion turbines from an electricity-cost standpoint.

FOREWORD

Battery energy storage systems are being developed to improve the capacity factor of base-load generation plants and to reduce oil consumption by the electric utility industry. EPRI's battery subprogram involves assessment and development of several different battery energy storage systems. A major goal of the subprogram is to narrow down the number of battery technology options to two or three by 1979, before the important step of upscaling battery systems to the 5-10 MWh prototype level is taken. Presently the two largest battery development projects involve the zinc-chlorine system under RP-226, and the sodium-sulfur system under RP-128. This report presents a summary of the work performed by EDA during 1976 to further develop the zinc-chlorine system. Previous work on the zinc-chlorine battery is described in EPRI EM-249 which covers the testing of a 1 kWh zinc-chlorine battery in 1974-75, and EPRI EM-259 which covers an assessment by Bechtel Corp. of chlorine storage options for the zinc-chlorine battery. Future reports on the EDA project are scheduled for the summer of 1978, 1979 and 1980.

Project RP-226 began in 1974 and is being continued under a 39-month contract initiated in January, 1977; EPRI and EDA are sharing equally in the project costs of $7.6 million. The ultimate objective of this project is to commercialize the zinc-chlorine battery for electric utility energy storage application. An intermediate objective is to install a 5 MWh battery in the Battery Energy Storage Test (BEST) Facility (RP-255) by 1981. The specific objectives for 1976 were to: (1) scale-up battery size from full-scale cells (2 kWh) to multicell batteries (20 kWh); (2) continue work demonstrating potential for practical cycle life and identifying mechanisms that limit life; and, (3) conduct cost and design studies to ascertain the economic viability of the technology and to identify components and materials that have a major impact on total system cost, and thus are prime targets for cost reduction.

The zinc-chlorine development effort for 1976 was generally successful, although contrary to the year before the projected cycle life milestones were not achieved. However, the failure to achieve these milestones was caused by instrumentation and control difficulties rather than by inherent failure mechanisms which were not

expected during this early stage of testing. During the year, several of the major issues and concerns associated with developing an acceptable zinc-chlorine battery became better defined, including: (1) life of the positive electrode substrate; (2) electrolyte maintenance; (3) manufacturability of the cell stack; (4) cost of electrode substrates; (5) hydrogen evolution; (6) cost of plastic case materials; and, (7) ability to site the system in residential substations. Each of these issues is being addressed in the existing 39-month contract.

The risks in developing and commercializing the zinc-chlorine battery remains considerable. Nevertheless, the zinc-chlorine battery system continues to be one of the most promising for utility energy storage and is likely to be the first to be tested in the BEST Facility.

James R. Birk
EPRI Project Manager

February, 1978

MAJOR CONTRIBUTORS TO THIS REPORT

Energy Development Associates

P. C. Symons
C. J. Warde
H. A. Catherino
M. J. Hammond
A. F. Laethem
C. C. Whittlesey
H. K. Bjorkman

Wayne State University

J. Jorne
J. T. Kim

Purdue University

W. Leidenfrost
J. D. Loveley
B. Korenic
K. Lee

TABLE OF CONTENTS

Section		Page
	PART I--OVERALL STATUS OF ZINC-CHLORINE PEAK-SHAVING PROGRAM--1976	
1	Introduction and Summary	1-1
	PART II--DEVELOPMENT PROGRAMS	
1	Cell Development	1-1
	Introduction	1-1
	Modeling and Energy Efficiency	1-2
	Electrolyte pH Effects on the Voltaic Performance of Ruthenized-Titanium Electrodes	1-7
	NaCl/KCl Additions to Electrolyte	1-9
	Temperature	1-11
	Cell Gap	1-13
	Selection of Battery Operating Conditions	1-14
	References	1-15
2	Porous Graphite Chlorine Electrodes	2-1
	Introduction and Summary	2-1
	Experimental Detail	2-2
	Results and Discussion	2-9
	Conclusions	2-16
	Recommendations	2-17
	References	2-17
3	Materials Development	3-1
	Introduction	3-1
	Adhesives	3-2
	Graphite Studies	3-8
	Plastics and Ceramics	3-11
4	Single-Cell Life Testing	4-1
	Introduction, Program Overview, and Summary	4-1
	Experimental	4-2
	Results and Discussion	4-6
	Conclusions	4-8
	Recommendations	4-8

TABLE OF CONTENTS (Ctd.)

Section		Page
	PART III--ZINC CHLORINE BATTERY SYSTEMS BUILT AND TESTED IN 1976	
1	Basic Cell and Battery Concepts- - - - - - - - - - - - - - - - -	1-1
2	The 1.4 kWh Battery System and Controller- - - - - - - - - - - -	2-1
	Introduction	2-1
	1.4 kWh System Description	2-2
	Automation and Logic Controller	2-10
	Results and Discussion	2-22
3	1.7 kWh Battery System -	3-1
	Introduction	3-1
	System Description	3-2
	Experimental Results	3-8
	Cycling Results	3-12
	Discussion of Cycling Results	3-16
	Microprocessor Control	3-18
	Conclusions	3-31
	Recommendations	3-31
4	2 kWh Battery System -	4-1
	Introduction	4-1
	Experimental Results	4-2
	Discussion	4-5
5	20 kWh Battery System--Design, Assembly and Test - - - - - - - -	5-1
	Introduction	5-1
	General Engineering Specification	5-1
	Design, Specification and Assembly	5-7
	Battery Operation	5-25
	Conclusions	5-33
	PART IV--DESIGN AND COST ANALYSES OF 100 MWH ZINC-CHLORINE PEAK-SHAVING BATTERY PLANTS	
1	Introduction -	1-1
2	Mark 2 Design- -	2-1
	Introduction	2-1
	Basic Battery Modules	2-4
	Hydrate Store	2-8
	Assembling Basic Modules	2-9
	Summary	2-11
	References	2-14

TABLE OF CONTENTS (Ctd.)

Section		Page
3	Mark 3 Design	3-1
4	Design and Cost Analysis of 100 MWh (20MW) Peak-Shaving Battery Plant	4-1
	Introduction	4-1
	Titanium Versus Graphite as an Electrode Material	4-6
	Mark 2 Costing	4-12
	Mark 3 Costing	4-18
5	Summary and Discussion	5-1

APPENDICES

Appendix		Page
A	Fundamental Chemical and Electrochemical Processes at Zinc and Chlorine Electrodes in Zinc-Chlorine Batteries	A-1
	Introduction	A-1
	The Kinetics of Chlorine Graphite Electrodes in the Zinc-Chlorine Battery	A-2
	Mass Transfer of Dissolved Chlorine to a Rotating-Zinc Hemisphere in $ZnCl_2$ Solution	A-29
B	Analysis of Refrigeration Requirements of a 100 MWh Peak-Shaving Zinc-Chloride Battery and Estimation of Cost of System Components and Power Consumption	B-1
	Introduction and Summary	B-2
	Refrigeration Requirements	B-3
	Refrigeration-System Bill of Materials	B-30
	Thermal Design of Evaporative Condenser	B-36

PART I

OVERALL STATUS OF ZINC-CHLORINE PEAK-SHAVING PROGRAM--1976

Section 1
INTRODUCTION AND SUMMARY

Zinc-chlorine batteries have been under development for the past eight years by Energy Development Associates (EDA). Corporate funds in excess of ten million dollars have been expended through December 1976 on the research, development, and engineering of components for high-performance low-cost battery systems. From 1968 through early 1974, the sole emphasis was on the development of a battery suitable for electric-vehicle propulsion. The technical feasibility of the zinc-chlorine battery in this application was convincingly demonstrated in 1972 when a 60 kWh prototype was used to power a converted compact sedan through hundreds of miles of acceleration and endurance tests.

A simple illustration of how the zinc-chloride system stores and delivers dc electrical energy is provided in Figure 1-1 which shows the sequence of events occurring during charge and discharge. When fully discharged, the system consists of a cell and a separate container, termed a store, which is filled with water. As shown, the cell consists of a zinc electrode and a chlorine electrode and is filled with aqueous zinc chloride. In the charge mode, zinc is plated onto one of the inert graphite substrates while chlorine is evolved on the other. The chlorine thus formed passes into the store, and reacts with water chilled to less than 10°C to form solid chlorine hydrate. At full charge, the zinc-chloride concentration in the cell decreases to 0.5M (from an initial 2M), and the store is full of chlorine hydrate. During discharge, chlorine passes from the store into the electrolyte adjacent to the porous-graphite electrode, and electrochemical reaction of zinc and chlorine occurs, releasing electrical energy. (In a practical system, chlorine-saturated electrolyte is pumped through the electrode). Heat is generated in the cell because of the thermodynamic, electrochemical, and chemical inefficiencies of the zinc-chlorine cell reaction. Enough of this heat is transferred to the store to cause the desired amount of chlorine evolution by decomposition of the chlorine hydrate. A more detailed discussion of basic cell and battery concepts is provided in Part III-Section 1 of this report.

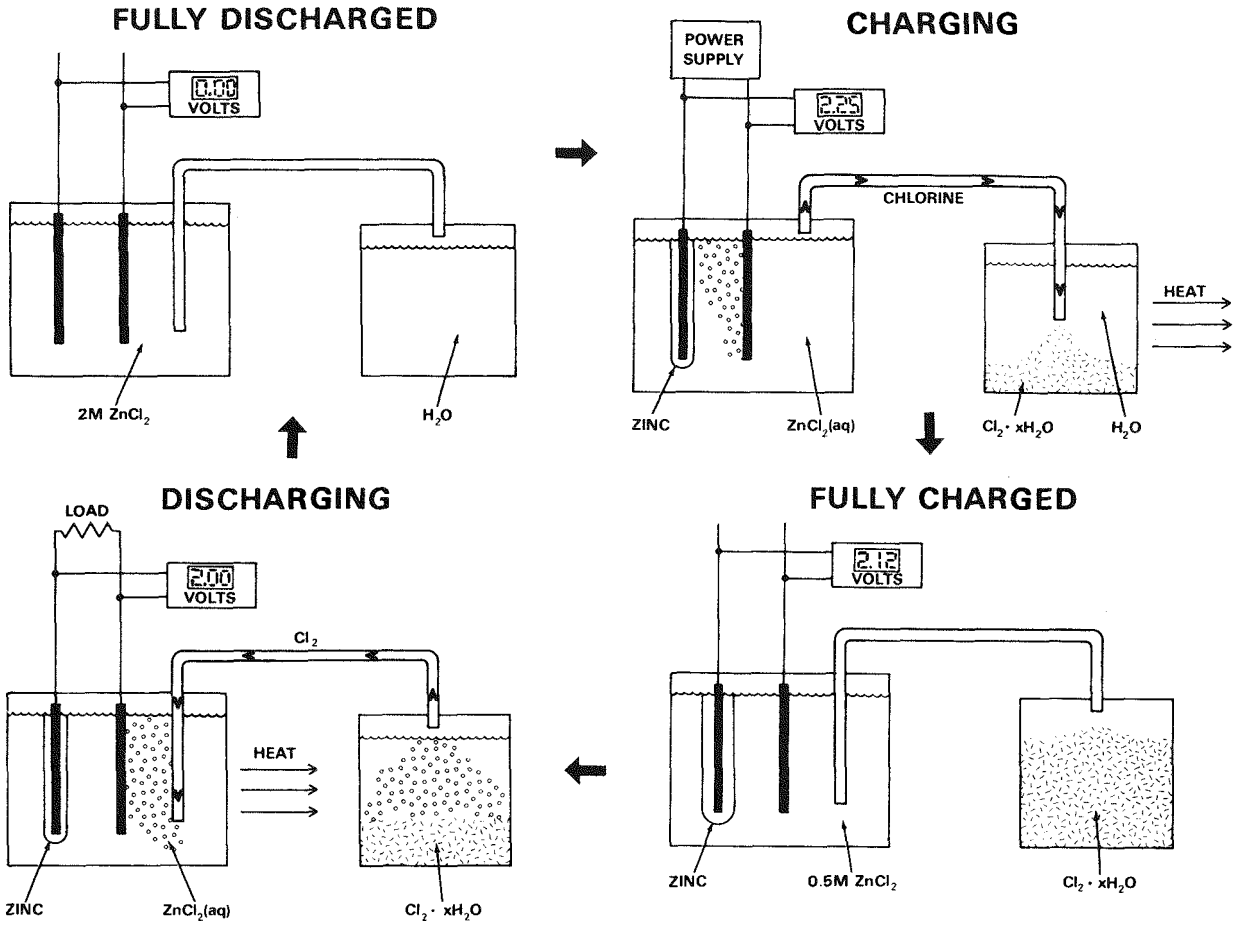

Figure 1-1. Schematic showing sequence of events in the charge and discharge of a zinc-chlorine cell. Note use of inert graphite substrates, water for hydrate formation, and stack heat for hydrate decomposition during discharge.

Many of the features of the zinc-chlorine battery, which make it so attractive as a power source for electric vehicles, carry over into a utility peak-shaving or load-leveling application. Among these advantages are:

- High electrochemical energy efficiencies — in excess of 75% — have been experimentally demonstrated.
- The system uses inexpensive and readily available materials.
- The electrochemistry of the system is well-behaved allowing the use of potentially inexpensive electrodes - uncatalyzed graphite substrates - which yield high voltage efficiency.
- At constant current, the voltage time profile for zinc-chlorine batteries is very flat during both charge and discharge. This allows the use of less-expensive and more-efficient converters than is possible without this characteristic.
- The system will operate close to ambient temperature suggesting that calendar life will be long relative to high-temperature systems. This also limits the degree of thermal cycling.

- Operating zinc-chlorine batteries with inactive substrates for zinc electrodes and with complete discharge each cycle leads to no loss of capacity with cycle number.
- The coulombic efficiency of the system can be made high by arrangements to control the dissolved chlorine concentration in charge and discharge, thus obviating the need for expensive and potentially life-limiting separators.
- Battery operating conditions can be chosen under which life expectancy of electrodes is acceptable and performance degradation is slow.
- Chlorine is stored safely as a stable solid-chlorine hydrate which forms at ambient pressure below 10°C.

With these considerations in mind, EPRI and EDA in mid-1974 co-funded a program, designated RP226-1, to explore the potential of the zinc-chloride battery for peak-shaving and load-leveling applications. The major accomplishment of this program was the demonstration of a 1 kWh cell system with an electrochemical energy efficiency of 75%. The performance of the system was stable over the 100 cycles required by contract. This work, concluded in December, 1975 has been described in detail in an earlier report (1-1). An independent evaluation by Stanford Research Institute, funded by EPRI under RP370, concluded that EDA's testing was objective and that the reported results were accurate.

In an amendment to RP226-1, EPRI funded a seven-month study in October 1975 directed towards the preparation of a design and a detailed cost analysis of a 100 MWh peak-shaving battery plant, based on the zinc-chlorine couple. This peak-shaving plant design, designated Mark 2 and shown in Figure 1-2, was based on a preliminary design (Mark 1) used for discussion with EPRI and electric-utility representatives.

A follow-on program—RP226-2, which was jointly funded by EPRI and EDA—was conducted in calendar 1976. The work statement for this program is outlined in Table 1-1.

This report describes all of the work performed under RP226-2 and the amendment to RP226-1. To maximize presentation effectiveness, the work accomplished at EDA is broken into three parts: Part II--Development Programs; Part III--Zinc-Chlorine Cell and Battery Systems; Part IV--Design and Cost Analysis of Zinc-Chlorine Peak-Shaving Battery Plants. The work performed in sub-contracts by Professor Jacob Jorne of Wayne State University and Professor Wolfgang Leidenfrost of Purdue University is reported in Appendices A and B, respectively. This introduction and summary constitutes Part I of this report.

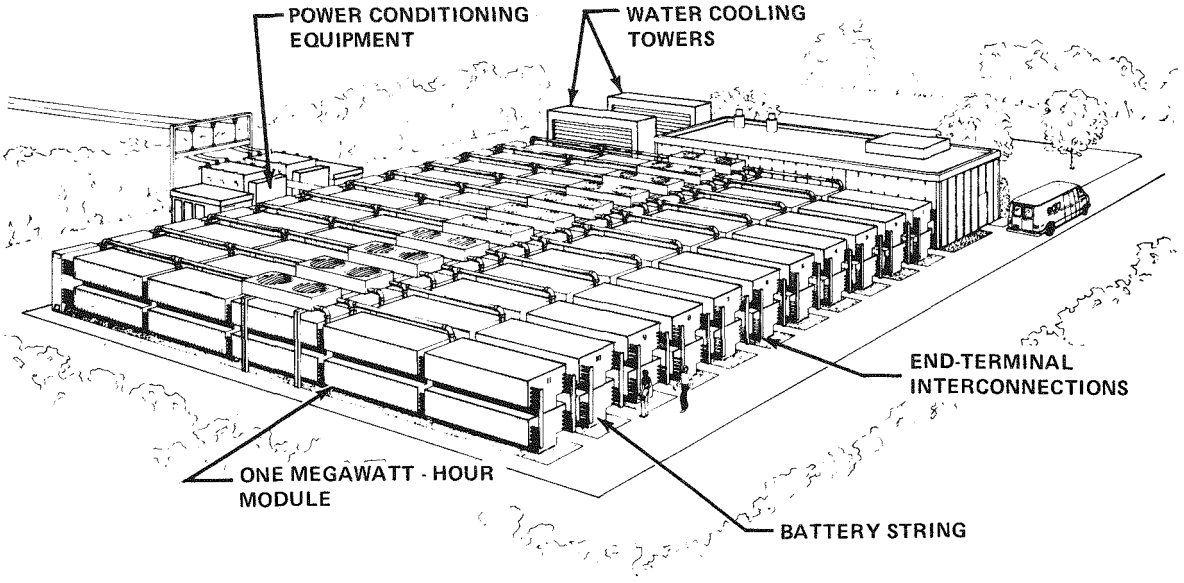

Figure 1-2. Artist's concept of Mark 2 design of a 100 MWh (20 MW) zinc-chlorine peak-shaving battery plant located near a utility substation.

The first task undertaken as part of RP226-2 was the automation, from the standpoints of control and data acquisition, of the 1975 1 kWh system. This system employed the desorber concept, i.e. creation of a partial vacuum over the flowing electrolyte in a separate compartment during charge. Thus, by forcing significant desorption of chlorine from the electrolyte, the charge coulombic efficiency was appreciably increased because of the reduction of chemical corrosion of electroformed zinc by dissolved chlorine. This concept underwent intense scrutiny in early 1976 as part of the design and costing task of RP226-1. It was concluded that because of cost, the concept could not be employed in commercial 100 MWh zinc-chlorine peak-shaving battery plants. In addition, serious questions were raised as to battery operability and the energy penalty associated with the desorber concept. Accordingly, the concept was abandoned. Among the consequences were (a) an immediate loss of 10-15% in electrochemical energy efficiency, and (b) a significant delay in the automation of the system. Cell development, described in Section 1 of Part II, was initiated immediately to define a new set of operating conditions so as to recover capacity and electrochemical energy efficiency. Section 2 of Part III describes the redesign and automation of the system. With the redesign and the new cycling routine, the capacity was raised to 1.4 kWh, while the loss in electrochemical energy efficiency was reduced to approximately 8%.

Table 1-1

OUTLINE OF TASK DESCRIPTIONS AND OBJECTIVES
IN RP226-2 WORK STATEMENT

TASK NO.	TASK DESCRIPTION	TASK OBJECTIVES
1	Cycle test 1975 1 kWh battery	• Determine life of ruthenized-titanium electrodes • Identify other life-limiting factors in battery • Establish extended system operability
2	Fabricate and test two 2 kWh cells - one with ruthenized-titanium the other with porous-graphite chlorine electrodes	• Permit making of an informed choice of chlorine-electrode material for 20 kWh battery
3	Design, build and test 20 kWh battery	• Demonstrate battery stack and store scale-up • Explore potential problems in integration of a large stack and store in charge and discharge
4	Design and cost analysis of 100 MWh zinc-chlorine peak-shaving battery plant	• Update 100 MWh plant design on basis of most recent technology • Refine costing of 100 MWh plants based on new design, materials, and proposed manufacturing processes • Identify limiting problems from design and cost standpoints for guidance of development programs
5	Fundamental Studies	• Address limiting problems in development programs • Develop information base for engineering design • Understand fundamental chemical/electrochemical processes in zinc-chlorine battery

Another major thrust of the program in the first half of 1976 (as is evident from the work-statement outline in Table 1-1) was to decide between ruthenium-catalyzed porous titanium and activated porous graphite as the chlorine-electrode material for the 20 kWh battery which was to be built in the second-half of the year. The problem was tackled simultaneously from three standpoints:

- Cost—The ultimate cost per square foot of both electrode materials was investigated as part of the design and cost study conducted under the amendment to RP226-1. The results of this study are described in Section 4 of Part IV.
- Development—Existing programs, directed towards the development of improved techniques for the ruthenizing of porous titanium and the activation of porous graphite, were accelerated. The work performed on porous-graphite activation is described in Section 2 of Part II.
- Demonstration—Two cell systems — a 1.7 kWh system with porous-graphite electrodes (Section 2 of Part III) and a 2 kWh system with ruthenized-titanium electrodes (Section 3 of Part III) — were designed, built, and tested.

Porous graphite was chosen in August 1976 as the chlorine-electrode material for the 20 kWh battery for the following four reasons: (a) the probability of meeting the desired cost target of $5-10/kWh for the chlorine electrodes in an ultimate 100 MWh battery system was much higher for porous graphite; (b) the voltaic-efficiency advantage offered by ruthenized-titanium electrodes at the beginning of 1976 was significantly reduced by the advances made in porous-graphite activation; (c) a comparison of the 1.4 kWh and 1.7 kWh systems showed clearly that a system with ruthenized-titanium chlorine electrodes is more difficult to control effectively because of the sensitivity of cell performance to changes in electrolyte pH; (d) because of the higher hydrogen overpotential of graphite, a battery with porous-graphite chlorine electrodes will be intrinsically safer under malfuncion.

The design, assembly, initial testing, and cycle-testing of the 20 kWh battery is described in Section 5 of Part III. Both stack and store performed to specification in December, 1976. However, excessive hydrogen evolution in the stack during discharge because of electrolyte contamination delayed coupling of the stack and store to form a complete battery system. After elimination of the contamination problem, the stack and store were coupled, and the battery ran smoothly as a system. Further delays were caused by a dendrite problem which reduced battery capacity. Finally, ten sequential cycles were taken in May. The average delivered energy was 15 kWh while the average electrochemical energy efficiency was 60%. An eleventh

cycle, for which the charge time was five hours at the rated charge current, yielded a delivered energy of 18 kWh at an electrochemical efficiency of 60%.

The design and cost analyses performed under RP226-1 and RP226-2 are presented in Section 1 through Section 5 of Part IV. The Mark 2 system, designed and costed for RP226-1, is described in Section 2. A description of the Mark 3 system shown in Figure 1-3, is provided in Section 3. A detailed costing for the Mark 2 system, given in Section 4, concluded that at a production rate of one hundred 100 MWh plants per year, the installed cost would be $25/kWh (1976 $). A similar analysis for the Mark 3 design yielded an installed cost of $21/kWh (1976 $). The lower cost for the Mark 3 relative to the Mark 2 system is due to a reduction in the required amount of electrode graphite -- the major cost item -- because of the higher design current density (40 mA/cm^2 versus 30 mA/cm^2).

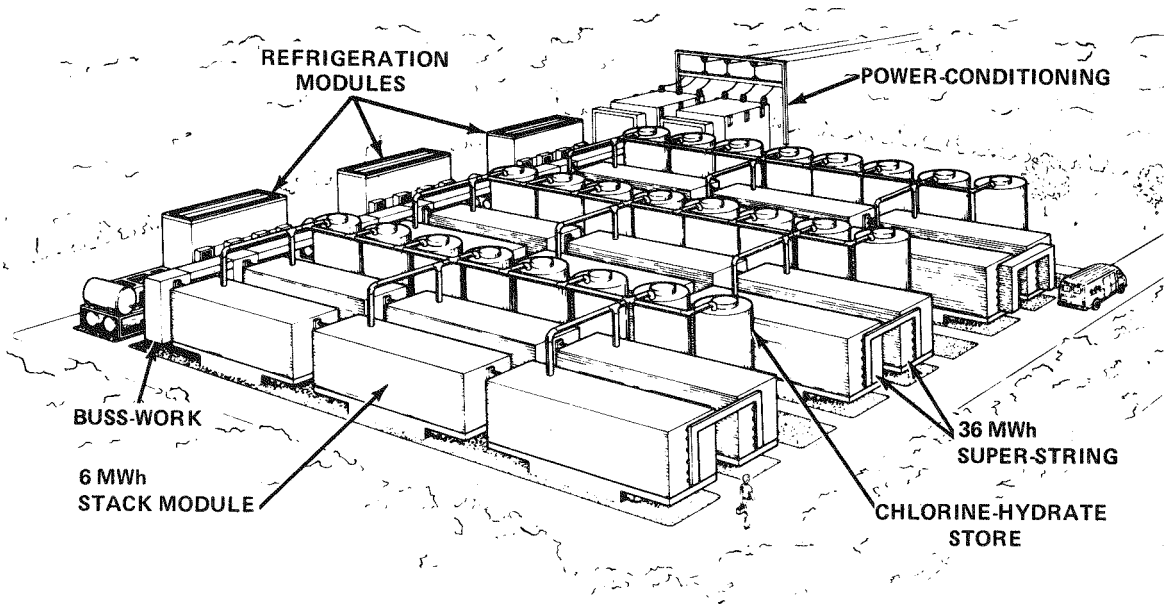

Figure 1-3. Mark 3 103 MWh zinc-chlorine peak-shaving battery plant.

The results of a materials program mainly directed towards the qualification of plastics and adhesives for long-term use in zinc-chlorine battery systems are described in Section 3 of Part II. The major accomplishment of this program has been the identification of a number of polyvinylchloride (PVC) formulations which are stable at 50°C in chlorine-saturated zinc chlorine solution. These PVC formulations offer the prospect of an order of magnitude reduction in cost relative to KYNAR, which is used presently for the battery case, piping, and manifolding.

Section 4 of Part II describes the life-testing of four single (∿ 20 Wh) cells. These cells were fabricated with porous-graphite chlorine electrodes, activated by a variety of techniques including thermal and electrolytic processing in nitric acid. The cell longest on cycle-test has demonstrated uniformity of voltaic performance through the equivalent of 365 full load-leveling cycles.

Two papers dealing with fundamental investigations of chlorine and zinc electrodes constitute Appendix A. This work was performed under the direction of Professor Jacob Jorne of Wayne State University. Appendix A1 describes an investigation of the kinetics of the cathodic and anodic reactions occuring at the chlorine electrode. The mass transfer of dissolved chlorine to a zinc electrode is discussed in Appendix A2. It was found that the chemical reaction of a rotating zinc hemisphere with dissolved chlorine is mass transfer-limited. This explains the experimental observation that the coulombic efficiency (or i_c, the corrosion current) is a strong function of the chlorine concentration in the electrolyte.

Appendix B describes an analysis of the refrigeration requirements of a 100 MWh peak-shaving zinc chlorine battery plant and an estimation of the costs and power consumption of system components. This work, performed under the direction of Professor W. Leidenfrost at Purdue University, costed a refrigeration system based on the use of air-cooled condensers. A brief report of a similar study with water-cooled or evaporative condensers is also included. This appendix reports work in progress and the results were not factored into the costing for the Mark 3 100 MWh battery plant. A final report will be issued in mid-1977.

As a result of work performed by EDA under RP226-2 and the amendment to RP226-1, a zinc-chlorine peak-shaving battery system has received significant research, development, and engineering efforts. In the work described in this report, EDA has:

- Designed, built, and successfully tested a 20 kWh, 20V battery with porous-graphite chlorine electrodes
- Designed, built, tested, and automated a 1.7 kWh cell system with porous-graphite chlorine electrodes
- Upgraded the performance of the 1975 1 kWh system to 1.4 kWh despite removal of a key auxiliary, the desorber, because of ultimate cost considerations

- Automated the cycle-testing of the 1.4 kWh system to permit unattended operation
- Designed, built, and tested a 2 kWh/4V battery with ruthenized-titanium chlorine electrodes
- Designed and costed a 100 MWh zinc-chlorine peak-shaving battery plant (Mark 2). This design and cost analysis was updated in late 1976 (Mark 3)
- Conducted productive development programs in porous-graphite activation, qualification of low-cost plastics, cell efficiency improvement, and ruthenization of porous titanium
- Selected activated porous graphite as the chlorine-electrode material in preference to ruthenium-catalyzed porous titanium
- Subcontracted fundamental research programs (a) to elucidate mechanisms and reaction kinetics in zinc-chlorine cells, and (b) to design the optimal refrigeration system for 100 MWh zinc-chlorine peak-shaving battery plants

As a consequence of these accomplishments, the zinc-chlorine energy-storage system is now firmly established as the leader among the candidate batteries for the peak-shaving application.

REFERENCE

1-1 "Evaluation of a 1 kWh Zinc-Chlorine Battery System," EPRI EM-249, Interim Report, September, 1976

PART II

DEVELOPMENT PROGRAMS

Section 1

CELL DEVELOPMENT

INTRODUCTION

Cell development in the 1976 peak-shaving program involved experimental work in a number of areas relating to the performance of the zinc-chlorine battery. The goals of this program were to:

- Define a new set of operating conditions for the 1975 1kWh battery
- Develop a mathematical model for the energy efficiency of the zinc-chlorine battery
- Evaluate the voltaic performance of the zinc-chlorine battery as a function of the electrolyte pH
- Evaluate leveling agents
- Evaluate supporting electrolytes
- Investigate battery performance over the temperature range of 30-50°C
- Investigate cell gap as a variable influence on voltaic performance, coulombic efficiency and cell capacity (mAh/cm^2)
- Select the operating conditions for a 4V-2kWh battery system (ruthenized-titanium chlorine electrodes) and for a 20kWh battery (porous-graphite chlorine electrodes)

The approach used in attaining these objectives was: firstly, to determine the new operating conditions for the 1975 1kWh battery; secondly, to apply that information to the electrolyte investigation; and finally, to use the experimental results as an aid in developing a simple theoretical model to explain the energy efficiency of the zinc-chlorine battery.

The reason for redefining the operating conditions for the 1975 battery came about as a result of a cost study based on that system. This study showed that the mechanical chlorine desorber used in the 1975 battery system would be too expensive to scale up for large battery installations. Based on other single-cell data, it was projected that the simple removal of the desorber, with no accompanying changes in the operating conditions, would result in a ten to fifteen percent decrease in the

electrochemical efficiency of the battery due to the use of chlorine saturated electrolyte during charge.

The following guidelines were used in determining a new set of operating conditions:

- Increase the battery operating temperature to 40°C so that heat exchangers could be used more effectively
- Increase the charge time from four to five hours and, if possible, increase the current density as well
- Attain a 70% electrochemical energy efficiency without the use of a mechanical chlorine desorber

The work, which details the selection of new operating conditions for the 1976 system, is described in the summary of this section. As a result of the work, the battery capacity increased to 1.4 kWh, the charge time was increased to five hours, the temperature was increased to 40°C and the loss in the electrochemical energy efficiency due to the removal of the chlorine desorber amounted to approximately 8%.

The evaluation of electrolyte components, operating temperature, additives and cell gap was performed in the cell design shown in Figure 1-1 which is the same cell design as the 1.4 kWh battery. For the cell-gap study, new chassis were machined with the appropriate interelectrode distance. The cell temperature was controlled by means of a hot water bath and heat exchanger. For a given set of conditions, the tests were repeated several times to verify the results.

For these energy efficiency studies and theoretical performance modeling, the removal of electrode overpotential as a limiting factor was of considerable importance.

Finally, the experimental information from the development program was used to select the operating conditions for the 20 kWh battery, which was the culmination of the 1976 effort. This battery contains a 0.150" interelectrode gap, uses porous graphite as the chlorine electrode, operates at 50°C and charges for five hours at 45 mA/cm^2.

MODELING AND ENERGY EFFICIENCY

The electrochemical energy efficiency, ε_e, of a zinc-chlorine battery is the product of the voltaic efficiency, ε_v, and the coulombic efficiency, ε_c. In this discussion it is assumed that the charge and discharge voltages are constant. Then, the

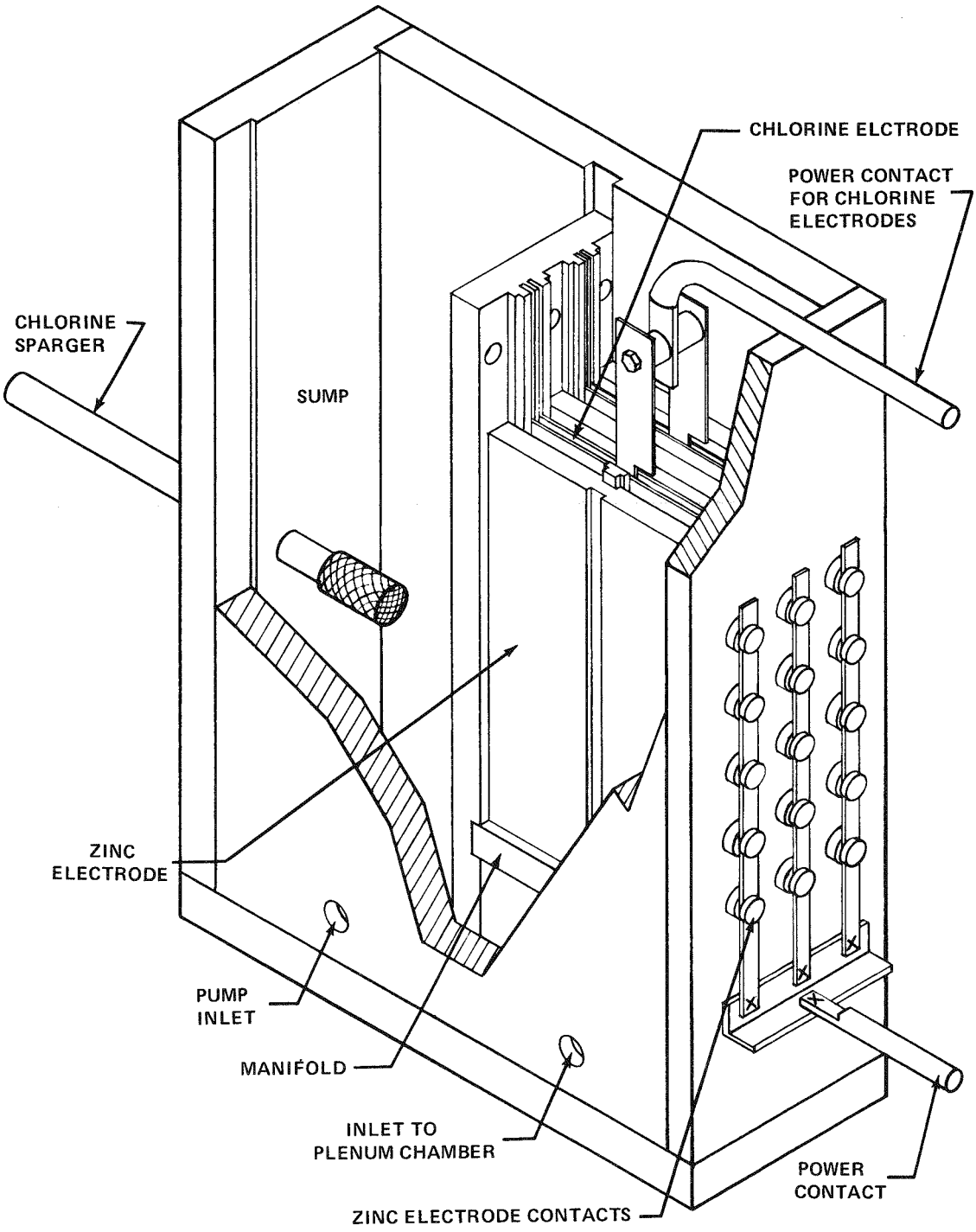

Figure 1-1. Test Cell used to Evaluate Battery Performance. The cell configuration is identical to that employed in the 1.4 kWh system.

voltaic efficiency, ε_v, is simply the discharge voltage divided by the charge voltage or Vd/Vc). The total coulombic efficiency is the number of ampere hours obtained from the battery during discharge divided by the ampere hours put into the battery during charge. In mathematical terms: $\varepsilon_e = \varepsilon_v \cdot \varepsilon_c$.

To develop a model for the energy efficiency of the zinc-chlorine battery requires some knowledge of the factors which contribute to the voltaic and coulombic efficiencies of the system. There are many factors which determine the voltaic efficiency. Important factors, which exhibit an intensive-like quality, are the chlorine electrode activity, conductivity of the electrolyte,and the current density. Other factors, which are more controllable are the cell gap, chlorine concentration, concentration polarization,and temperature. To determine the voltaic efficiency in a given cell, a polarization curve such as that in Figure 1-2 is obtained. From this curve, voltaic efficiency as a function of current density may be derived.

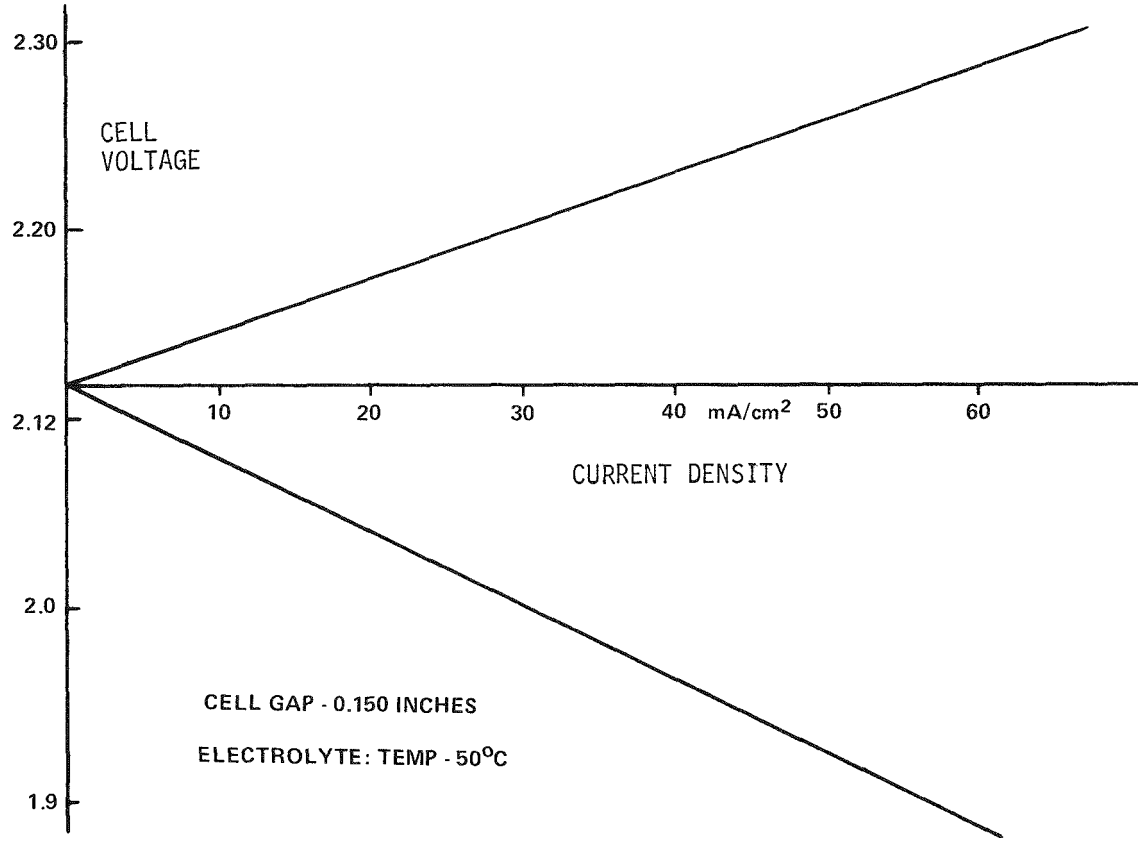

Figure 1-2. Charge and Discharge Polarization Curves for a Zinc-Chlorine Cell with Catalyzed Chlorine Electrodes.

The principal factors controlling the coulombic efficiency are electrolyte composition, current density, flatness of the zinc plate, and the flow rate on discharge. For modeling purposes, it is assumed that the coulombic efficiency on the discharge part of the cycle is high (greater than 95%) and is also constant over the current density interval being evaluated. It is also assumed that the zinc morphology does not change significantly with changes in the charging current density. With these assumptions a few tests at different current densities can be used to generate an effective corrosion current (i.e. which represents the coulombic inefficiency on the charge cycle). A coulombic efficiency curve as a function of current density is then obtained from $(i_a - i_c)/i_a$, where i_a = applied current density, and i_c = corrosion current on charge (Figure 1-3). Cross multiplication of the coulombic efficiency and the voltaic efficiency curves yields the desired energy efficiency curve, as shown in Figure 1-3.

The optimized energy efficiency may be obtained by setting the first differential of the energy efficiency curve equal to zero.

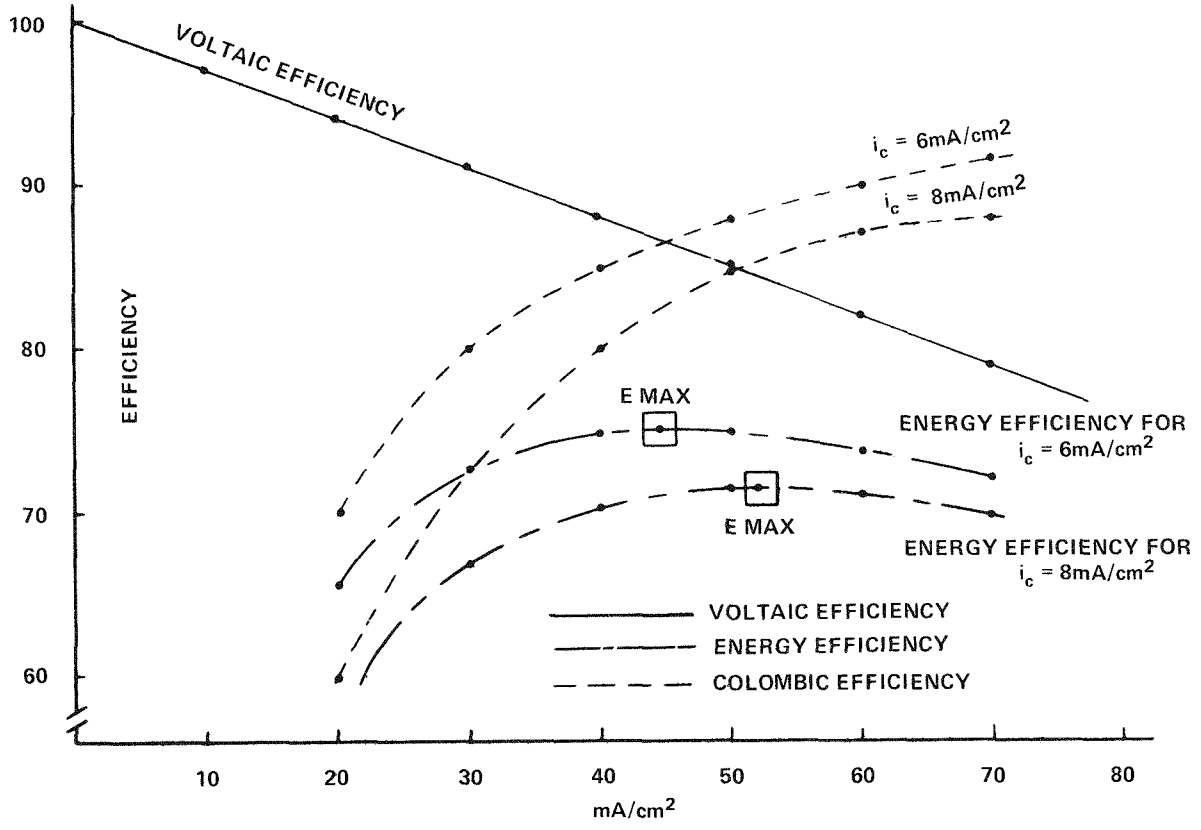

Figure 1-3. Energy Efficiency Model for a Zinc-Chlorine Battery. The voltaic efficiency depends only on the applied current density. The coulombic efficiency and energy efficiency are dependent on both the corrosion current and the applied current density.

From Figure 1-3:

1) $\varepsilon_v = 100 - 0.3\ i_a$
2) $\varepsilon_c = (i_a - i_c)/i_a$
3) $\varepsilon_e = (100 - 0.3\ i_a)\ \ (1 - i_c/i_a)$
4) $d\varepsilon_e/di_a = (100 - 0.3\ i_a)\ \ (i_c/i_a^2) - 0.3\ (1-i_c/i_a)$
5) $d\varepsilon_e/di_a = 0$
6) $0.3\ (1-i_c/i_a) = (100 - 0.3\ i_a)\ \ (i_c/i_a^2)$
7) $0.3 - 0.3\ i_c/i_a = 100\ i_c - 0.3 i_c/i_a$
8) $0.3\ i_a^2 = 100\ i_c$

From equations 8, 1 and 2 optimized energy efficiencies have been tabulated as a function of the corrosion current. The results are given in Table 1-1. From this table it is evident that as the corrosion current is decreased, the applied current density is also decreased to maximize the energy efficiency.

Table 1-1

MAXIMUM ENERGY EFFICIENCY - A FUNCTION OF CORROSION CURRENT

CURRENT DENSITY, mA/cm^2		EFFICIENCY		
Corrosion	Apparent at ε_g Max.	Voltaic	Coulombic	Maximum Energy
i_c	i_{opt}	ε_v	ε_c	ε_e MAX.
2	25.8	0.922	0.922	85.1%
4	36.5	0.89	0.89	79.2%
5	40.8	0.877	0.877	77%
6	44	0.868	0.86	74%
8	51.6	0.845	0.845	70.5%

As noted earlier, certain assumptions were made to simplify the derivation of a mathematical model for the energy efficiency. The assumption that the corrosion current is independent of the applied current density is greatly simplified. At high current densities, zinc plate roughness and hydrodynamic turbulence due to chlorine gas generation lead to an increase in the corrosion current. This would lower the calculated coulumbic efficiency by an undetermined amount and one might expect a negative deviation in the energy efficiency curves (Figure 1-3) at high current densities.

At lower current densities, decreasing the current density may improve the zinc plate flatness. This could result in a decrease in the corrosion current which would represent a positive deviation in the energy efficiency curve. Thus, the real optimized current density for maximum energy efficiency may be slightly lower than calculations indicate. Large deviations would not be expected.

Projected energy efficiency for 1976 was 70%. This efficiency relates to a corrosion current of about 8 mA/cm^2 using the voltaic efficiency of the model. The present activity of ruthenized-titanium electrodes is quite optimized and only marginal improvements in their voltaic performance can be expected in the future. For graphite chlorine electrodes, voltaic improvements are anticipated to make them equivalent to the ruthenized-titanium. This represents about a 4% voltaic improvement at 40-45 mA/cm^2. For either electrode material, the biggest energy improvements will be obtained through a decrease in the corrosion current.

Corrosion current may be decreased by at least three methods. The first involves modification of electrolyte composition by the addition of supporting electrolytes. The second method for reducing corrosion current involves additives to improve the zinc plate morphology and density. There are a number of elements to be evaluated in this area. The third method of reducing the corrosion current involves dechlorination of the electrolyte during the charge cycle. The effectiveness of this technique was demonstrated in the first EPRI project

ELECTROLYTE pH EFFECTS ON THE VOLTAIC PERFORMANCE OF RUTHENIZED-TITANIUM ELECTRODES

The 1975 load leveling battery system had a nominal electrolyte pH of 1.1 to 1.6. One of the first parameters studied in 1976 was the pH of the electrolyte. Both the charging and discharging of the battery were evaluated over a pH range of 0.5 to 3.0. In this study, it was found that the discharge voltage varies significantly with the electrolyte pH. Cell discharge voltage as a function of pH is shown in Figure 1-4. While the discharge voltage varies by over 200 millivolts in the pH interval, the charge voltage varies by only 10 to 20 millivolts.

The shape of the curves in Figure 1-4 indicate no gradual transition is occurring. The sharp inflection points are similar to those found in acid-base titrations. Using this analogy, it appears as though the conjugate base of a fairly strong acid is necessary for the efficient reduction of chlorine on ruthenized-titanium.

The equilibrium constant for the reaction is 4.5×10^{-4} according to:

$$Cl_2 + H_2O \rightleftharpoons HCl + HOCl$$

The concentration of HOCl as a function of pH results in a smooth curve which does not readily agree with the curve shape in Figure 1-4. The possibility exists that the pH sensitivity is located in the RuO_2 - TiO_2 film on the chlorine electrode. The surface of the film may have some acid characteristics and undergo

ionization via a number of mechanisms such as:

a) $\text{solid}\diagup\!\diagdown Ru{:}OH + OH^- \rightleftharpoons \underset{pH < 1.5}{\text{solid}\diagup\!\diagdown Ru\text{-}O^-} + H_2O$ $\quad > 1.5$

b) $\text{solid}\diagup\!\diagdown Ru{=}O + H_2O \rightleftharpoons \text{solid } Ru\langle^{OH}_{OH}\rangle Ru\ {}^{O^-}_{OH} + H^+$

One might then speculate that electron transfer from the film to the solution occurs more easily through the ionic bridge than through the aquo or hydroxide bridge.

Our findings show that this pH versus chlorine reduction phenomenon does not exist when graphite chlorine electrodes are substituted for the ruthenized-titanium electrodes.

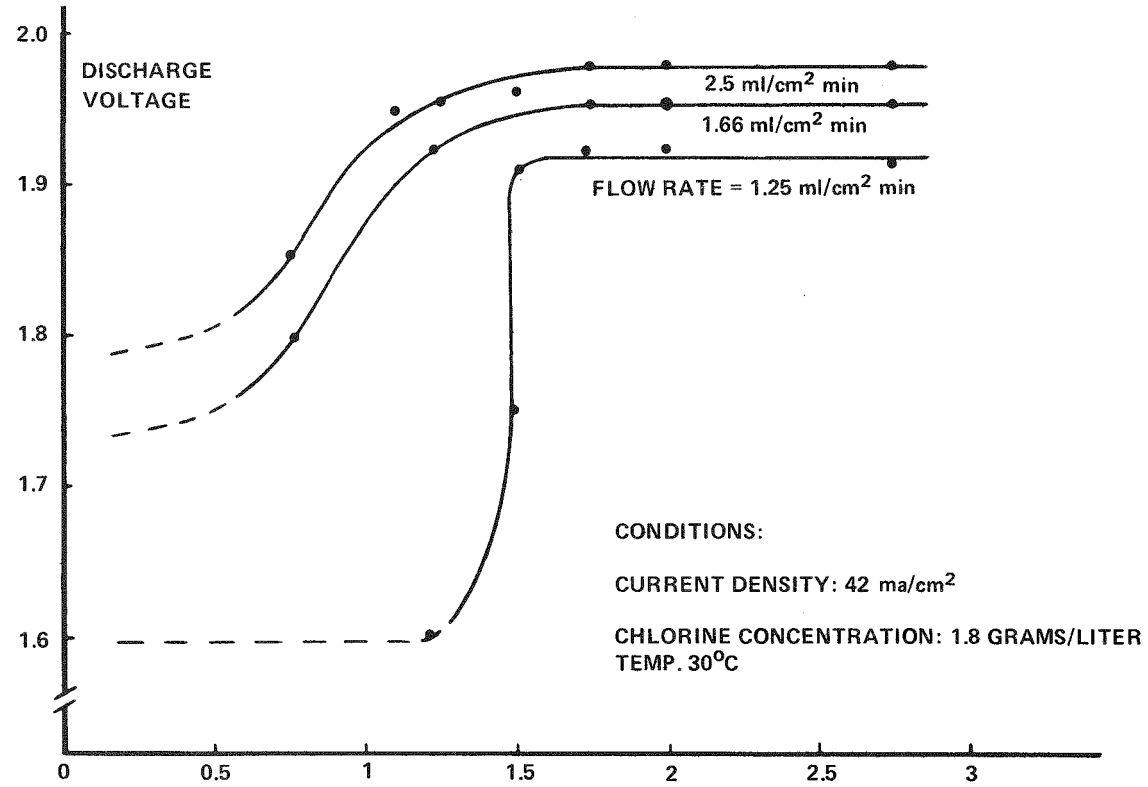

Figure 1-4. Discharge Voltage as a Function of Electrolyte pH for a Zinc-Chlorine Battery with Ruthenized-Titanium Electrodes.

Based upon this study, it is concluded that:

- Chlorine reduction on ruthenized-titanium electrodes is sensitive to the electrolyte pH.
- The oxidation of chloride ion to chlorine on ruthenized-titanium electrodes is only slightly dependent on pH.
- The chloride-chlorine couple on graphite is insensitive to pH.

NaCl/KCl ADDITIONS TO ELECTROLYTE

Effects on Cl_2 Solubility

Although potassium chloride was used in the 1975 EPRI project, very little experimental work was done on the use of supporting electrolytes. In late 1975, some tests conducted in the vehicle development program indicated that sodium chloride decreased the solubility of chlorine in the electrolyte. This chemical salting out effect was viewed as an alternative to a mechanical desorber. As a result, chlorine saturation levels were determined for a number of salt solutions. The experimental apparatus for determining chlorine saturation concentrations is shown in Figure 1-6. Samples of solutions were taken at regular intervals and the chlorine concentrations were determined by thiosulfate titration. The first erlenmeyer contained water and was used as a control for the other solutions. The solutions were considered to be saturated when consistent chlorine concentrations over a four-hour interval were obtained. The accuracy of the results is estimated to be ± 0.1 gram chlorine per liter. The chlorine saturation level as a function of electrolyte composition is shown in Table 1-2. A comparison of the chlorine saturation levels indicated that sodium chloride is very effective in depressing the solubility of chlorine.

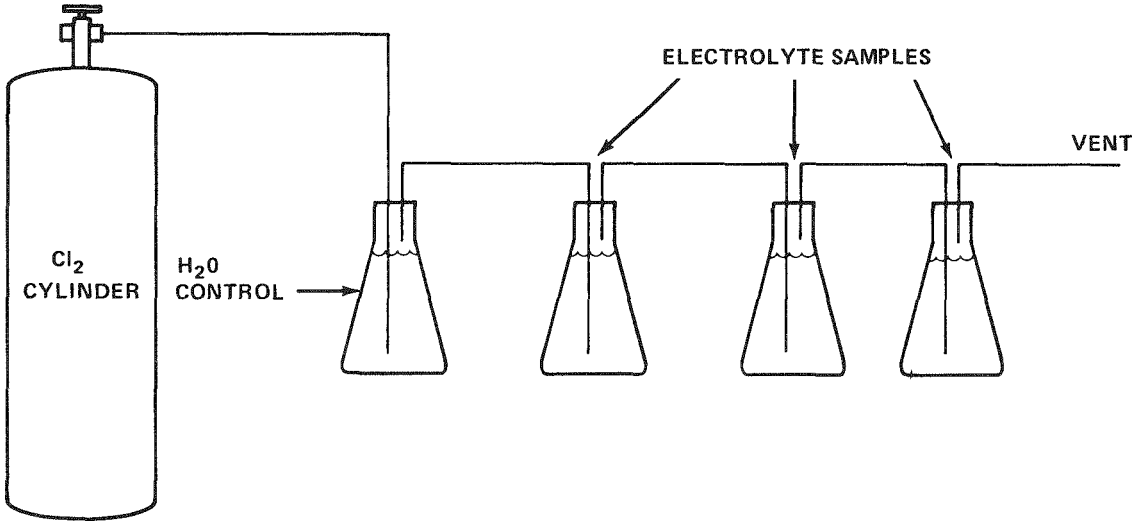

Figure 1-6. Experimental Equipment to Determine Chlorine Solubilities in Electrolytes. The Erlenmeyer flasks have sealed tops to prevent air from entering the system.

Table 1-2

CHLORINE SOLUBILITY IN BATTERY ELECTROLYTES AT 30°C

ELECTROLYTE COMPOSITION	CHLORINE SOLUBILITY g/ℓ
1 Molar $ZnCl_2$	3.1
2 Molar $ZnCl_2$	2.75
3 Molar $ZnCl_2$	2.5
4 Molar $ZnCl_2$	2.3
5.3 Molar $ZnCl_2$	2.15
2M $ZnCl_2$ + 3M NaCl	1.9
2M $ZnCl_2$ + 4M NaCl	1.7
2M $ZnCl_2$ + 3M KCl	2.4
2M $ZnCl_2$ + 1.5M $MgCl_2$	2.5
2M $ZnCl_2$ + 1.5M $CaCl_2$	2.3
2M $ZnCl_2$ + 2M $CaCl_2$	2.2
2M $ZnCl_2$ + 1M $AlCl_3$	2.6

Conductivity

To maximize the voltaic efficiency of the zinc-chlorine battery, the resistivities of a number of electrolyte solutions were measured to determine IR losses in the battery electrolyte and establish trends with respect to the valency of the cation. These measurements were made under thermostatic conditions using a "U" tube with platinum electrodes. The cell was standardized with 1.00 N potassium chloride. Resistance of the solutions was determined with a type 1650-B General Radio null-balancing impedance bridge. These results are listed in Table 1-3.

Conclusions

Chemical salting of electrolyte studies revealed that:

- Sodium chloride is more effective than potassium chloride in reducing the solubility of chlorine in the electrolyte.
- Potassium chloride electrolytes are slightly more conductive than electrolytes containing sodium chloride.
- Sodium chloride reduces battery capacity due to a morphological change in the zinc plate. Potassium chloride has no apparent effect on battery capacity.
- Sodium chloride causes some depression of the discharge voltage. This may be due to a decrease in the chlorine activity.
- The addition of sodium chloride to an electrolyte usually increases the coulombic efficiency.

Table 1-3

ELECTROLYTE RESISTIVITY AT 30°C

ELECTROLYTE COMPOSITION	RESISTIVITY (ohms-cm)
2M $ZnCl_2$ + 3M KCl	3.65
3M $ZnCl_2$ + 2M KCl	5.3
2M $ZnCl_2$ + 3M NaCl	5
2M $ZnCl_2$ + 2M $CaCl_2$	5.6
2M $ZnCl_2$ + 4M NaCl	4.7
3M $ZnCl_2$ (pH = 0.1)	7.6
3M $ZnCl_2$ + 3M NaCl	6.1
3M $ZnCl_2$ + 2M KCl (pH = 0.1)	4.5
2M $ZnCl_2$ (pH $\simeq$ 1.0)	8.6
2M $ZnCl_2$ + 2M KCl + 2M NaCl	4
2M $ZnCl_2$ + 1.5M $AlCl_3$	8.7
3M $ZnCl_2$ (pH = 1)	8.6

TEMPERATURE

The zinc-chlorine battery is an ambient temperature battery. It has been found to perform well in a temperature range from 20°C to 50°C. At present, little or no investigative work has been done at higher or lower temperatures. Singular thermal effects may be correctly anticipated but the overall performance of the battery at a given temperature can only be determined by experimentation.

Chlorine solubility shows a marked dependence on the electrolyte temperature. In general, the chlorine solubility is halved as the electrolyte temperature is increased from 30°C to 50°C. For most electrolyte compositions the chlorine saturation level at 50°C is 1 to 1.2 grams per liter. Surprisingly, this low chlorine level causes no apparent concentration polarization on the chlorine electrode.

The coulombic efficiency is also related to the chlorine concentration and should increase with increasing temperature for a fixed electrolyte compositon. However, no significant data has been obtained to demonstrate this effect. It may be that

the flatness of the zinc plate and the diffusion rate of chlorine from the bulk solution to the zinc electrode are more controlling than is the chlorine concentration per se.

Increasing the temperature increases the electrolyte conductivity and hence the voltaic efficiency of the battery. Figure 1-7 shows the charging voltage as a function of temperature for a typical electrolyte. The voltage is taken at the terminals and includes IR drops. The important parameter is the displacement of the curves as the temperature is increased. The straightness of the current-voltage curves indicates that any overpotentials associated with the electrodes are also ohmic in nature. Due to the increased conductivity associated with elevated temperatures, the battery may be operated at higher current densities with a favorable voltaic efficiency. The net effect is that both battery capacity and energy efficiency are increased.

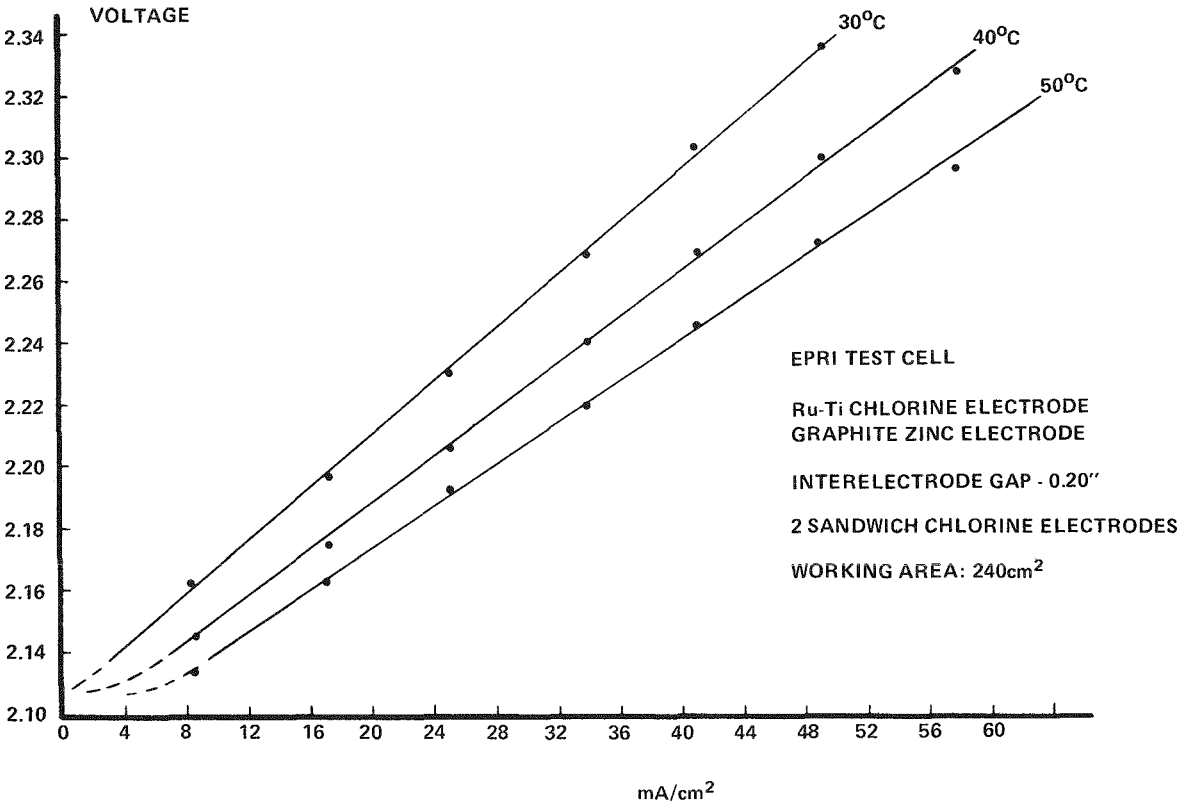

Figure 1-7. Temperature Dependence of the Charge Voltage for a Zinc-Chlorine Battery.

No systematic testing was done to evaluate thermal effects on the zinc plate morphology. The use of plate modifiers effectively masks most such effects. In electrolyte solutions containing potassium chloride and a plate modifier, increasing the temperature leads to a more uniform and smooth zinc deposit. Again, higher current densities may be used at elevated temperatures to increase the capacity of the battery.

Hydrogen evolution from the zinc plate should increase with increasing temperature. This has not been observed. However, significant hydrogen evolution on zinc metal usually is found to occur only when a catalyst, such as copper, is present. Measurements on hydrogen evolution made by EDA indicate that temperature plays only an insignificant part in hydrogen evolution.

Thus, investigations to determine the effect of temperature on battery performance indicated that:

- The solubility of chlorine in electrolytes is very temperature-dependent. The reduced chlorine solubility has little or no effect on the voltaic performance.
- The voltaic performance of the battery improves with increasing temperature due to increased conductivity.
- Elevated temperatures permit the use of high current densities.
- Hydrogen evolution has not been observed to increase due to increasing the temperature.

CELL GAP

Inter-electrode gap, the distance from the chlorine electrode surface to the zinc electrode surface, may influence several aspects of battery performance. Voltaic efficiency is in part, determined by the IR drop in the electrolyte and is inversely proportional to the inter-electrode gap. The battery capacity may also be influenced by the cell gap. A large inter-electrode distance may improve the current spreading and therefore, hinder dendrite formation. Thus, battery capacity may be increased. Also, the coulombic efficiency may change as changes in the intracell hydraulics affect chlorine diffusion to the zinc electrode. To evaluate the effects of the cell gap, cells of a design identical to Figure 1-1 were constructed. The cell gaps evaluated were 0.125", 0.150", and 0.200".

The first parameter tested was voltaic performance. No unusual data was generated in this testing. The experimental data closely agreed with calculated values of the IR drops. Increasing the cell gap from 0.150" to 0.200" increased the

charging voltage by about 20 mV at 50 mA/cm^2. A similar effect was noted on the discharge cycle. The loss in voltaic efficiency by increasing the cell gap from 0.150" to 0.200" amounted to about 2%. Due to the negligible change in voltaic efficiency between the 0.125" cell and the 0.150" cell, it was decided to discontinue testing on the 0.125" cell.

Capacity and coulombic tests were performed on a comparative basis between the 0.150" and 0.200" cell. Both cells demonstrated 250 mAh/cm^2 capacity when charged at 50 mA/cm^2 for five hours.

The 0.150" gap was selected for battery design because it afforded a slightly better voltaic efficiency. In addition, it physically presented a more compact battery than did the cell with a 0.200" gap. Once the cell gap was chosen, the preliminary design of a 2 kWh-4V ruthenized-titanium system began.

It was therefore concluded that:

- A 250 mAh/cm^2 capacity can be repeatedly demonstrated in a 0.150" gap cell.
- There are no significant changes in the coulombic efficiency as a function of the cell gap.

SELECTION OF BATTERY OPERATING CONDITIONS

The selection of the operating conditions for the 1.4 kWh ruthenized-titanium system was the result of two interactions. The battery temperature, cell gap and charge time were selected before the experimental work began. The battery's capacity and energy efficiency were selected as a compromise as they may not be optimized independently of one another. Coulombic efficiency was maximized by the use of large amounts of sodium chloride, while battery capacity was maximized by the elimination of sodium chloride in the electrolyte. The compromise led to an electrolyte formulation which included sodium chloride and a charging current density of 37 mA/cm^2. Increasing either the current density or the sodium chloride concentration resulted in a high frequency of internal shorting (dendrites).

For the 2kWh-4V ruthenized-titanium system none of the operating conditions were fixed although it was desirable to operate at 50°C for favorable heat exchanger design in the ultimate 100 MWh system. Experimental work was conducted using different mole ratios of potassium chloride and sodium chloride. The total amount of supporting electrolyte was found to be important. In this way, a battery

capacity of 250 mAh/cm^2 was achieved with the optimum electrolyte formulation. Again, the use of higher current densities or more sodium chloride led to a high frequency of internal shorting. Using the ruthenized-titanium electrodes, laboratory experiments indicated a voltaic efficiency of approximately 90% and a coulombic efficiency of about 80%. The 4V-2kWh ruthenized-titanium system was designed to use the optimal electrolyte, charge at 50 mA/cm^2 for five hours, and discharge at 45 mA/cm^2 for approximately five hours. Again, a zinc leveling agent was employed.

For the 20 kWh graphite system design, it was necessary to decrease the charge current density from 50 mA/cm2 because of voltaic efficiency considerations. The discharge current density was similarly decreased from 45 mA/cm^2 to 40 mA/cm^2.

REFERENCES

1-1 Cotton, F.A., Wilkinson, G., "Advanced Inorganic Chemistry," Interscience Publishers, 1962, page 446.

Section 2
POROUS GRAPHITE CHLORINE ELECTRODES

INTRODUCTION AND SUMMARY

Porous graphite electrodes were used nearly six years ago in the first large (60 kWh) $ZnCl_2$ demonstration battery system. Used as the energy source to propel a Vega passenger car, the zinc-chlorine battery successfully demonstrated the feasibility of the battery concept; however, relatively poor voltaic performance was achieved at this time (2-1). Subsequently, excellent voltaic performance was achieved in batteries operating with ruthenium-catalyzed, porous-titanium (DSA) electrodes (2-2).

Our return to porous graphite became feasible when in the third quarter of 1975, improved voltaic performance was demonstrated for nitric acid treated graphites. It resulted from a deliberate attempt to thermochemically modify surface area and pore size distribution characteristics of machined graphite plates. Oxidizing properties made nitric acid a natural choice.

At approximately the same time, similar voltaic improvement was demonstrated for graphite anodically worked in 50% HNO_3. Improved performance had also been observed for some cells after cycling for extended periods at higher ("natural") pH. Repeatability with this process was never demonstrated, however. A decision was made to discontinue investigation of this latter approach and concentrate instead on the two HNO_3 techniques.

The first quarter of 1976 was devoted to a more thorough evaluation of the thermal HNO_3 activation process. Fabrication of a 20 kWh demonstration battery system requires the production of a significant number of chlorine plates. Therefore, the study was directed toward evaluating activation parameters (primarily time and temperature), and formulating a repeatable procedure for producing activated Cl_2 electrode plates.

The second quarter and part of the third quarter of 1976 were devoted to cycle testing the 1.7 kWh all graphite system. This unit represented EDA's first attempt

to extend the thermal activation technique from small single cells to a reasonably sized demonstration battery. Although only partial activation was demonstrated, the scale-up was considered a definite success. Life testing of the 1.7 kWh system is now in progress. Performance characteristics of the 1.7 kWh battery system are documented in Section 2 of Part III of this report.

The remainder of the third quarter was used to investigate the electrolytic process in the hope it could be employed for in situ activation of an assembled battery. Obviously, activation of an assembled unit would be advantageous for both material handling and economic considerations, as activated chlorine plates are demonstrably weaker than their machined precursors.

Electrolytic activation had repeatedly been shown to yield voltaic improvement equivalent to the best thermal plates in much less time (hours vs. in excess of a week). Concurrent with activation and during the electrolysis, however, dimensional changes in the chlorine plates resulted in deformation and bowing; in extreme cases electrodes would even break apart. Efforts to demonstrate an electrochemical "window" to activate chlorine plates without this dimensional change were unsuccessful.

In the fourth quarter, the thermal HNO_3 process was scaled-up to a small pilot-plant level. Approximately 1400 electrodes were produced for use in the 20 kWh system. Qualification tests on each of seven separate batches demonstrated two significant aspects of the process:

- Excellent voltaic repeatability
- Dimensional growth was observed, but uniform to the degree that "flatness" was still acceptable

EXPERIMENTAL DETAIL

Thermal Processing

Heavy walled Pyrex resin reaction flasks were employed whose size was dictated by electrode dimensions. A porous teflon gasket cut from Gortex sheet was utilized in sealing the ground glass flanged top to its mating surface on the vessel. The ground joints in the cap were utilized to mount a condenser and a ground joint mercury thermometer suitably bushed to fit. The remaining ports were sealed with ground stoppers. Teflon cuffs were employed on all ground joints to effect the necessary seal.

The "L" shape of the original test electrodes (Figure 2-1)in the first test cell provided natural spacing for the plates. Circulation of HNO_3 during the thermal treatment was thereby insured. Subsequent flat plate electrodes (used in "comb" type assemblies), not surprisingly, were shown to require similar spacing to allow some acid circulation. To accomplish this, 5 mm glass rods cut to a suitable length were employed. Spacing plates singly and in pairs was evaluated.

Heating was achieved with Glas-Col heating mantles run off of a Powerstat. Acid replenishment was periodically necessary to keep the electrode plates submerged. Leakage past the porous teflon gasket was primarily responsible.

Electrode plates at various stages of activation were then removed from the reaction vessel and rinsed with deionized water prior to test. Simple overflow rinsing of separated electrodes in a beaker - typically overnight - was satisfactory for voltaic evaluation. Flow-through rinsing of a completed cell was obviously more efficient and preferred. Deionized water was only used in rinsing, primarily for convenience.

Air drying when desired was accomplished in a simple lab convection oven at 110°C. Experimentation with vacuum ovens or furnaces was not attempted during this period of investigation.

The HNO_3 (common to both the thermal and electrolytic activation processes) employed was ACS reagent grade "concentrated" (15.9M) acid. This azeotropic solution has a boiling point of 120.5°C.

HNO_3 assay was accomplished titrimetrically. Standard NaOH of appropriate normality was employed as the titrant; phenolphthalein was the indicator.

Electrochemical Activation

Processing in this manner through the end of 1976 was exclusively in completed cells. Bath composition was varied as desired by dilution of the stock nitric acid with distilled water. Constant current conditions were maintained through the use of controllers supplied by the electrical group.

No attempt was made to control temperature. It was monitored, however, with standard mercury laboratory thermometers located in the system electrolyte loop. Ohmic losses typically resulted in a rise from room temperature to 35-37°C. Electrolyte flow rate was monitored with appropriately sized rotometers, again the device being an integral part of any cell test system.

Electrode Testing

From an experimental viewpoint, this topic is sub-divided as follows:

- Electrolyte
- Description of test cells employed
- Test system
- Voltage measurement
- Measurement of electrode dimensional changes

Only voltaic considerations are emphasized. Topics of interest coulombically, such as electrolyte analysis, are generally excluded since they are adequately covered elsewhere in the report.

Electrolyte. The zinc chloride employed was the high-purity material produced here at EDA. Supporting electrolyte formulations were made up using ACS reagent grade sodium and potassium chlorides weighed on a beam balance. To adjust pH (to 0.1 - 0.3) reagent grade concentrated HCl was employed. Dilutions and water loss make-up when necessary were made using distilled water exclusively.

Electrolyte pH measurements were made only after carefully calibrating the meter. If expanded scale was available on the meter it was normally employed. Specific gravity determinations, correct to $\pm$ 0.005 units, was made routinely with laboratory hydrometers.

Test Cells. Only a cursory overview of the three cells employed is given. A more thorough description is not considered necessary since voltaic performance after compensating for differences in gap proved comparable.

Initial data was generated with the "PCS" type (Figure 2-1) cell utilized extensively in 1975. This is a true "single cell", having but a single anode and cathode face. Contact to both graphite plates is made via titanium bolts pressing against the electrode edge. A contact bolt on each side is reserved for current free ("reference") voltage measurement.

With the advent of the "comb" configuration in late 1975 - early 1976, EDA's test cell (shown in Figure 2-2) became a single chlorine pair between two zinc "end electrode" faces. This cell - along with the PCS cell - was utilized extensively in the first quarter of 1976.

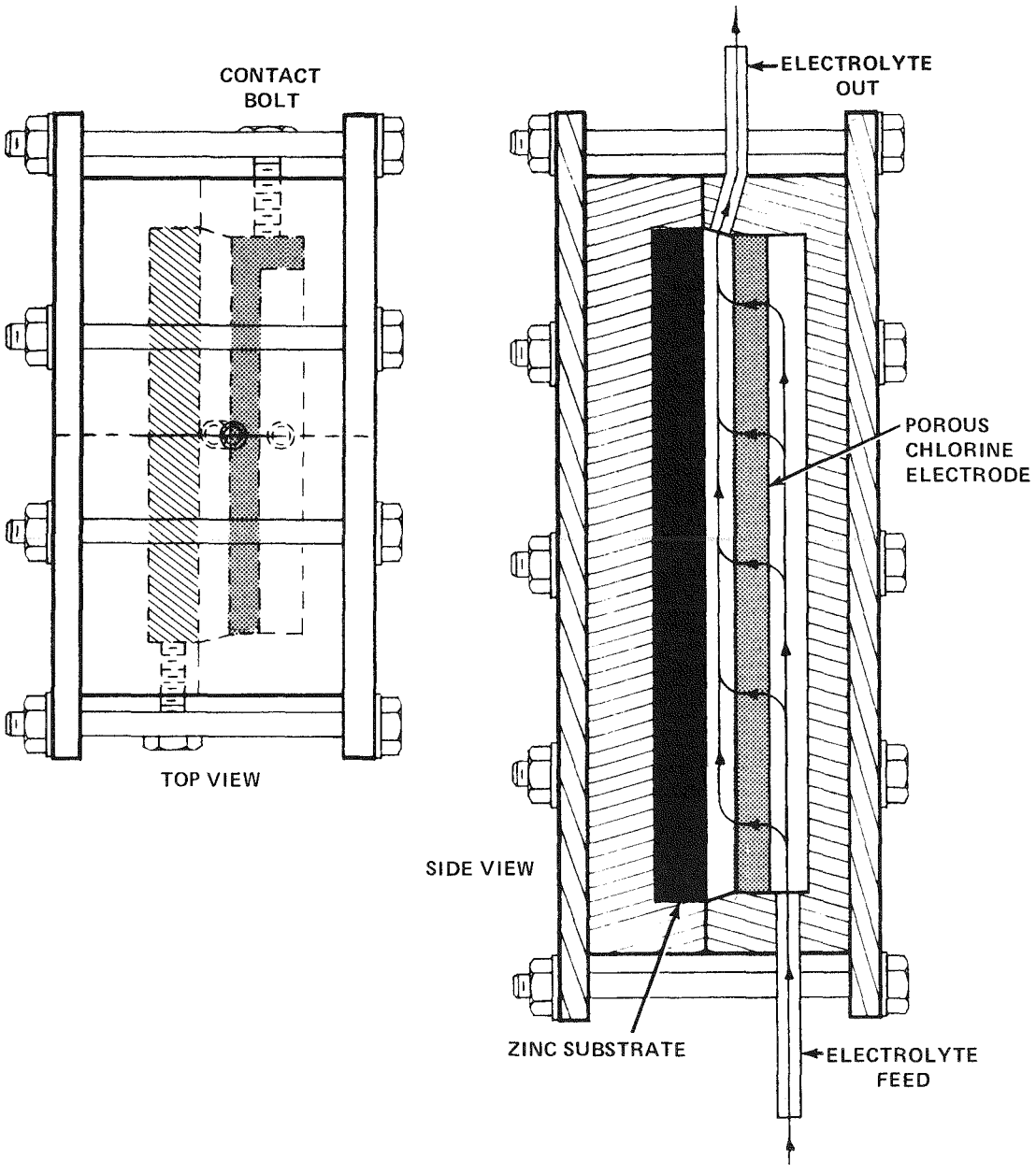

Figure 2-1. "PCS"-Type Test Cell. Note "L" shape of chlorine electrode, and use of titanium bolt contacts. Inter-electrode gap is 0.080 inch.

In the third quarter of 1976, for reasons of relevancy to the 20 kWh unit to be assembled, an expanded version of the above cell was used. This cell (see Figure 2-3) utilized two chlorine pairs in conjunction with four zinc faces, thus allowing test of one central "double-sided" zinc.

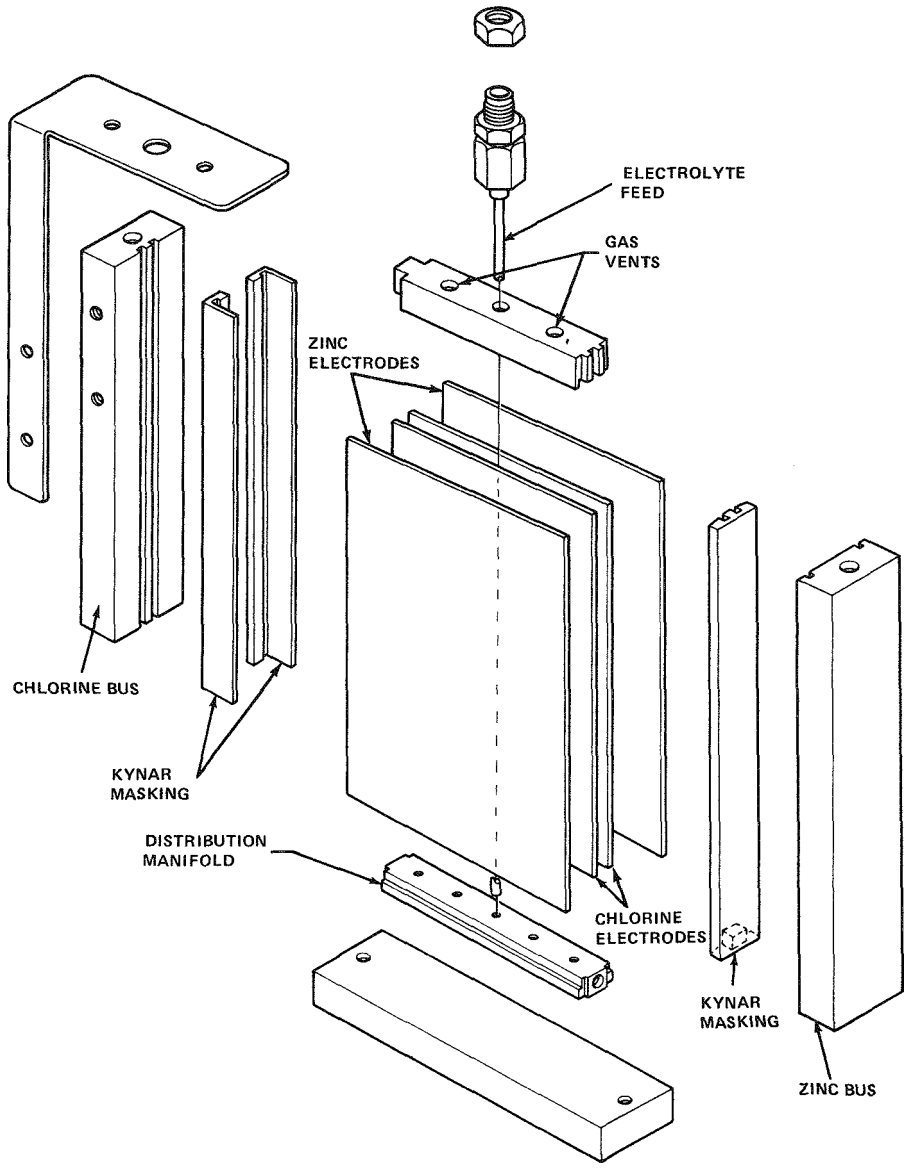

Figure 2-2. Early Comb-Type Cell. Note use of flat-plate chlorine electrodes. Cells with various inter-electrode gaps were employed.

Test Systems. Materials of construction were limited to graphite, Kynar, glass and Teflon. Titanium, usually in the form of bolts and/or nuts, also was employed, but only under circumstances where electrolyte contact was held to a minimum. This was not necessary from the point of view of voltaic considerations, but instead because of coulombic efficiencies which were also being monitored routinely.

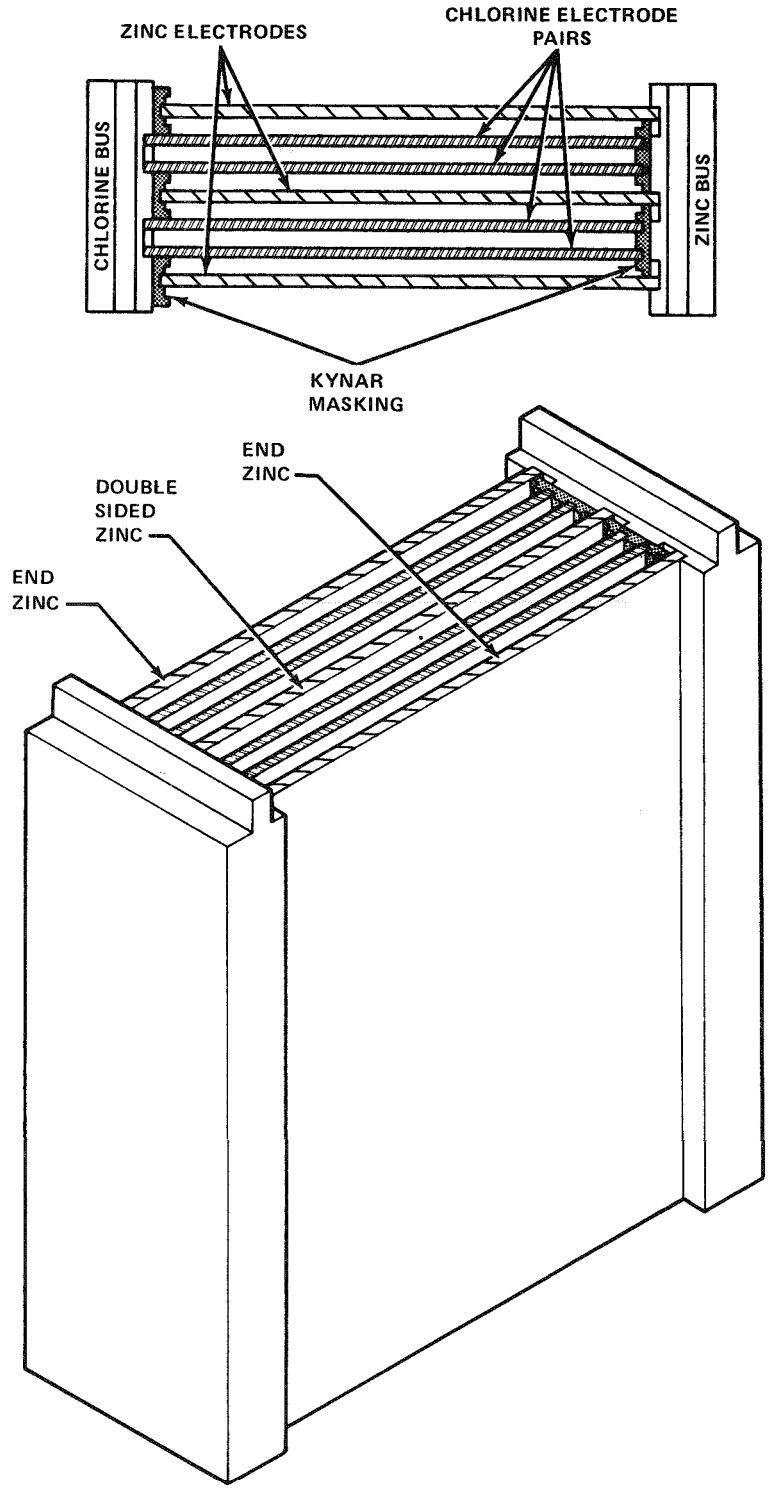

Figure 2-3. Expanded Comb-Type Cell. Note incorporation of central double-sided zinc electrode. Chlorine electrode-pair "caps", made of Kynar and having two gas vent holes, have been removed for clarity. Electrolyte feed manifolding has been incorporated into base of cell.

A schematic of a typical test system is shown in Figure 2-4. Flow to the cell was provided by a small gear pump. A Brooks rotameter of appropriate size monitored the flow rate. Flow was controlled by pump speed and/or a teflon/glass needle valve. A mercury thermometer was included in the loop to monitor temperature.

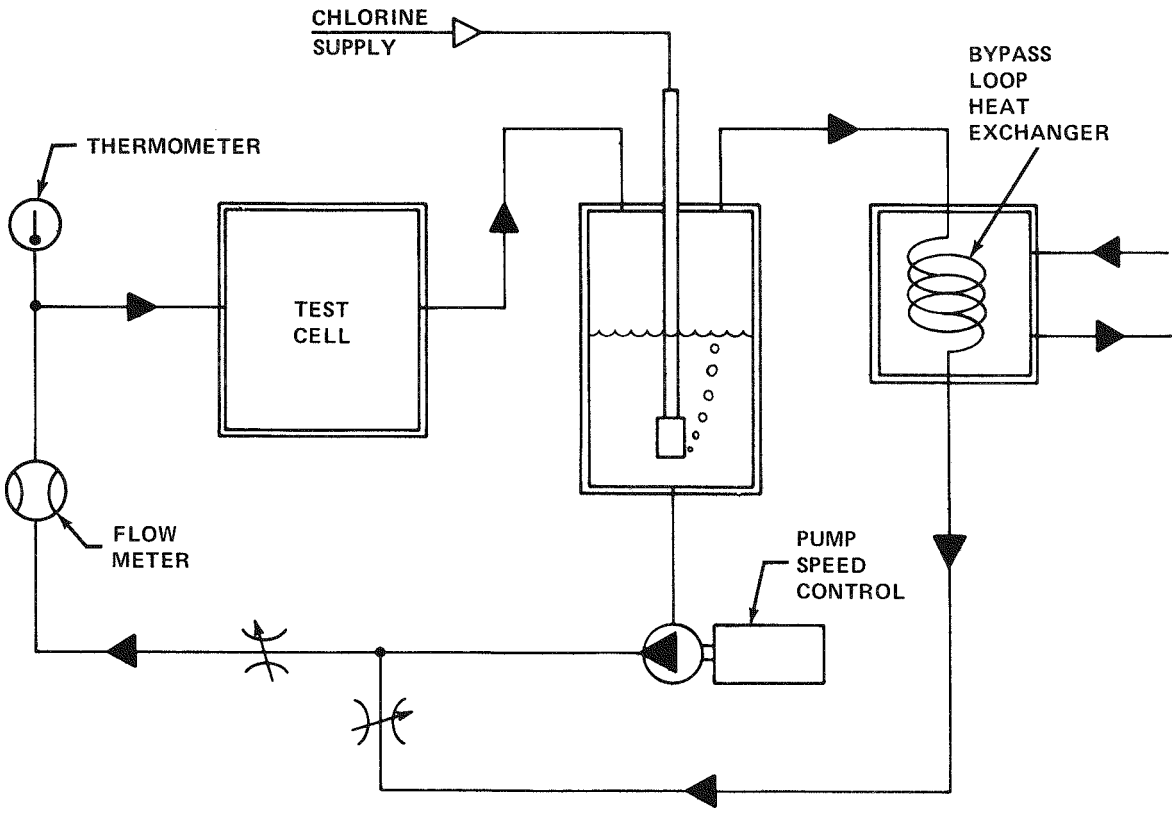

Figure 2-4. Typical Test System Employed for Chlorine Electrode Evaluation.

System temperature was controlled by a heat source operating where necessary in a bypass loop. A Haake constant temperature circulator was used to pump heated water through a condenser - used for heat exchange - in the bypass line.

Chlorine dissolution on discharge was achieved by feeding Cl_2 to a sintered glass gas dispersion tube located in the electrolyte sump. As long as sufficient gas/electrolyte contact was maintained, primarily by insuring sufficient electrolyte height above the sparger in the sump, dissolved chlorine levels up to saturation could be maintained. With mixed electrolytes operating at elevated temperature this approach was satisfactory. In order to operate at 2 g/ℓ (with straight 25% $ZnCl_2$ at 30°C) it was necessary to meter the Cl_2 feed using a precision needle valve in conjunction with a rotameter.

Voltage Measurements. Current free or reference voltages are reported except where otherwise noted. With the PCS cell this simply represents use of the voltage probe bolts supplied. With the comb cells physical probing of the electrode - usually the top edge near the buss - was accomplished, typically by using .050 inch graphite rods. The bus to electrode contact resistance was therefore documented, shown to be reproducible, and later used as a correction factor when desired. Bus voltages were thenceforth routinely recorded. Thereafter probing was employed less frequently, primarily when bus voltages were suspect.

A calibrated digital voltmeter was used for the measurement; accuracy of the measurement is 0.5%.

Electrode Dimensional Changes. Vernier calipers were employed whenever practicable to measure "before activation"and "after activation" dimensions of electrode plates. This procedure was limited to those plates which remained flat and hence would give meaningful results. This limited the measurement to thermally activated plates before cell assembly. Caliper measurements were demonstrated to give an accuracy (conservatively) of ±0.00025 inch.

Plates electrolyzed "in place" in a cell obviously could not be measured. Dimensional increases were instead estimated arithmetically utilizing visual estimates of the decrease in gap after the electrode had "bowed" during activation.

RESULTS AND DISCUSSION

The first two topics describe the performance of thermally processed and electrolyzed plates, and allows a comparison of the two types of plates under identical test conditions - which differ from final use conditions. Cell test results are then presented for operation under approximate 20 kWh operating conditions.

Electrode dimensional growth with activation is detailed. A possible explanation for this phenomena is proposed, and a potential relationship with activity briefly discussed.

Thermally Activated Electrodes

Periodic analysis of the nitric acid in the reactor vessels showed a minimal change in composition. No set frequency was employed. Typically, the stock reagent concentration is 15.8 - 15.9 moles/liter (by titrimetric analysis). A reactor sample

after 7 to 10 days was found to be between 15.1 and 15.3 molar. It is assumed the decrease is attributable to oxidative attack on the graphite and decomposition - possibly catalyzed - of the HNO_3. Graphite weight change was not determined during this study, so a materials balance has not been attempted. The significance of the 5% loss (0.5M - 0.8M) to the thermal process also was not investigated.

As would be expected, thermal treatment of unseparated flat plate electrodes was unsuccessful. Although outer plates activated, effectiveness on the inner plates dropped off. Separation - either singly or in pairs - proved acceptable.

A series of electrode plates were activated in concentrated HNO_3 at 112-115° for varying time periods (seven hours up to 13 days). The temperature employed (115° - 117°C) is slightly below the 120.5°C boiling point for the commercially available azeotrope. Small scale early runs in 1975 under boiling conditions did not yield significantly different results. Therefore, the more moderate temperature has routinely been employed this past year. Electrodes were removed from the reactor vessel at the desired intervals, briefly rinsed with D.I. water to allow handling and then assembled while wet into the test cell. Thorough flow-through rinsing on a D.I. line overnight was then performed.

These electrodes, along with electrode plates as received from the machine shop (debris had been removed by plunging into boiling water) were then tested and compared. Test conditions employed were as follows:

Table 2-1

TEST CONDITIONS EMPLOYED IN
EVALUATION OF CHLORINE ELECTRODE ACTIVITY

$ZnCl_2$:	Typically 30% by weight		
pH:	0.1 - 0.3	Resistivity:	7.6 Ωcm
Flow:	2ml/min/cm^2	Temperature:	28-30°C
[Cl_2]:	2.0-2.2 g/ℓ	Gap:	0.080 inch

The designated flow rate was chosen after first determining a voltage-flow profile at 40 mA/cm^2 (discharge) as presented in Figure 2-5. Coulombic considerations dictated operation just beyond the knee. At the same time voltaic performance limitations due to chlorine starvation were also avoided, but only with certainty up to and including this current density. A flow of 2 ml/min/cm^2 was shown to be satisfactory. At increased discharge currents higher flow rates are obviously necessary; no attempt was made to thoroughly investigate this situation.

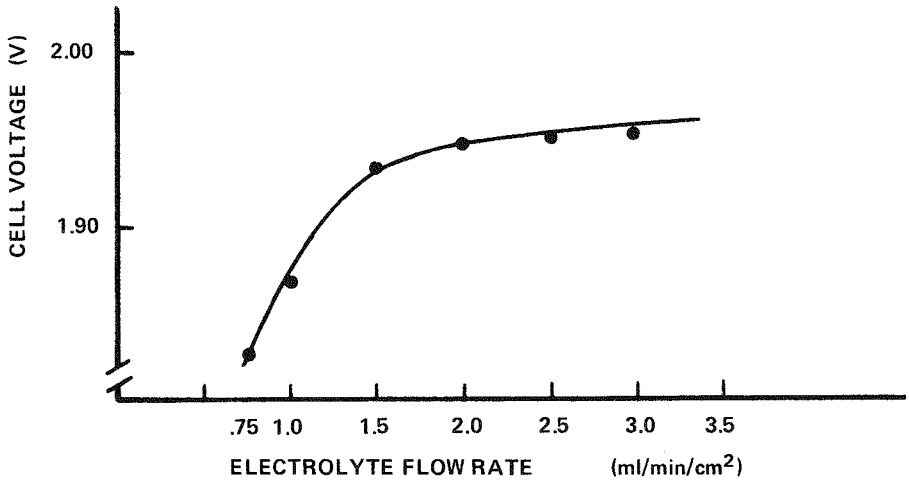

Figure 2-5. Typical Discharge Voltage/Flow Rate Profile. Position of "knee" depends upon discharge conditions. For a given current density, flow rate is chosen to be beyond the knee, thereby avoiding chlorine starvation.

The results for this series of tests are shown in Figure 2-6 presented as working cell polarization curves. Complete charge data for all of the test pieces were not available; hence the presentation in some cases of only a single value.

This simple and straightforward data graphically details the lowering of chlorine charge and discharge overvoltages for electrode plates of increasing activity. Cell performance is considered a measure of chlorine electrode activity. Zinc electrode overpotentials and voltaic losses in the electrolyte are taken to be invariant.

Repeatability of the process appears to be quite good, though somewhat dependent on either a) the parent graphite, or b) some unknown (or poorly controlled) factor associated with the thermal process. For example, the polarization curves labeled F in Figure 2-6 are for a "ten-day" electrode produced under the same conditions

but processed subsequent to the above test series. The variance, although slight, does appear to be real. Excellent repeatability - though with somewhat lower activity than expected from the above test series - was realized with the large number of electrodes activated for the 20 kWh demonstration battery. This is more fully discussed later in the report.

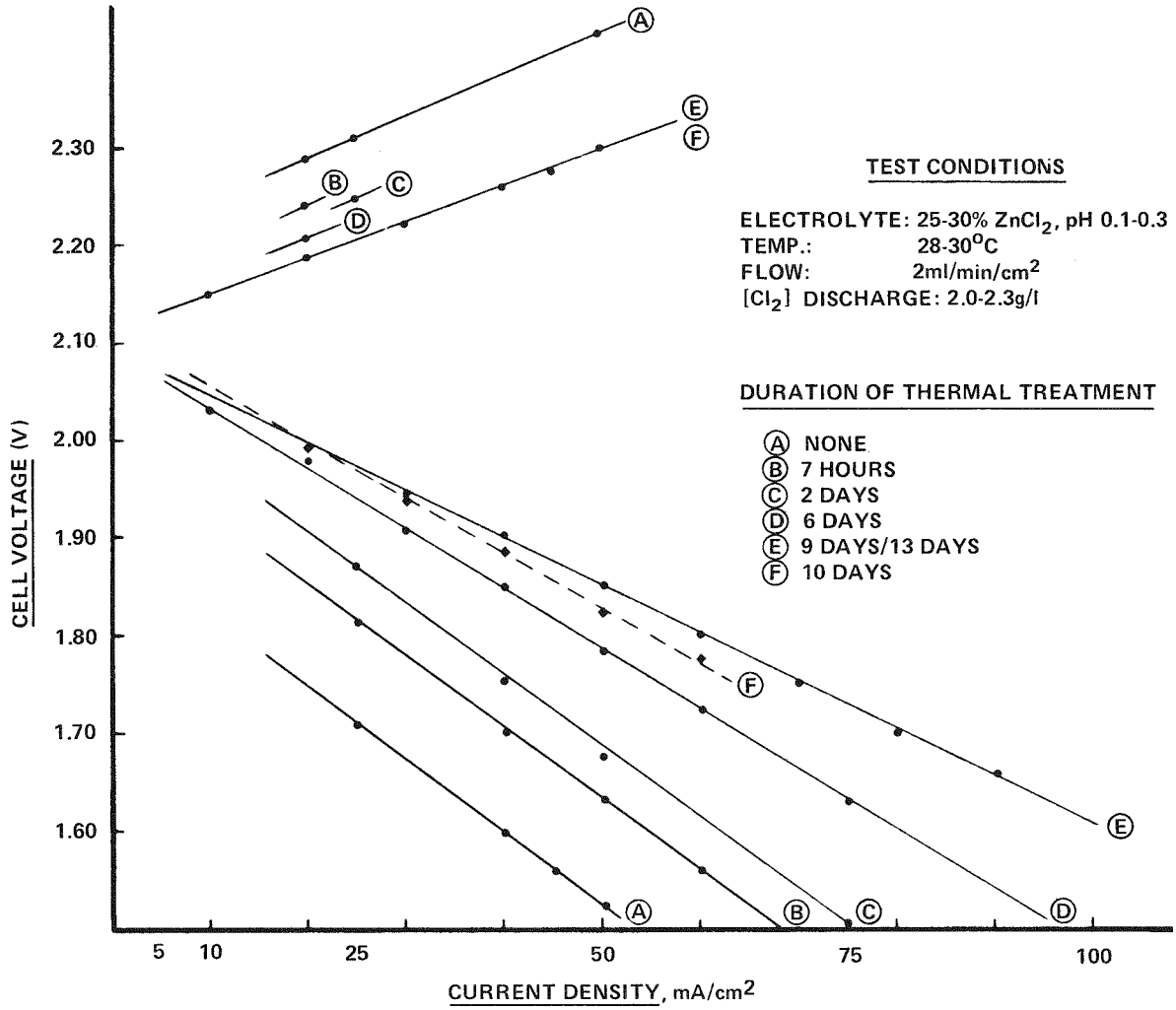

Figure 2-6. Performance of Selected Thermochemically Activated Electrodes. Cell performance, with test parameters held constant, is a measure of chlorine electrode activity.

In Figure 2-7 charge and discharge overvoltages at selected current densities are graphed as a function of the length of the activation period. The rate of activation is shown to definitely be leveling off. These data would indicate that whatever further improvement is achievable is at an ever increasing time penalty period.

Electrochemically Activated Plates

The procedure yields impressive results in a most surprising manner. To be specific, when successful, the voltaic performance demonstrated is equivalent to curve E of Figure 2-6. Unsuccessful anodizations have always yielded essentially "as machined" performance.

Activation has been most repeatable with 50% HNO_3 as the electrolytic medium. This has been accomplished over the following wide range of current densities and time shown in Table 2-2.

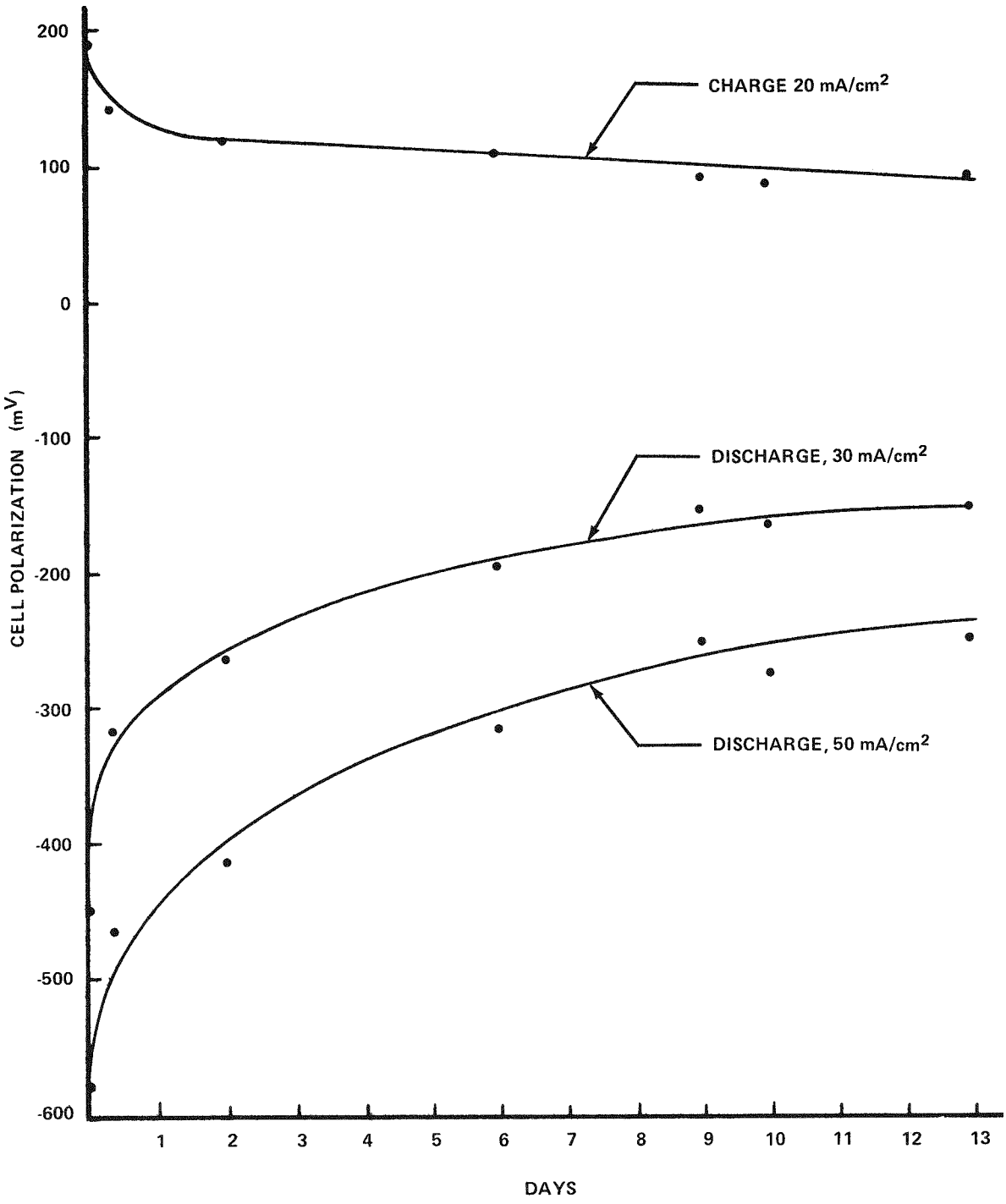

Figure 2-7. Relationship of Cell Polarization to Thermal Activation Period. Effect of thermochemical treatment with nitric acid shows a diminishing rate with time.

Table 2-2

TYPICAL ELECTROLYTIC ACTIVATION CONDITIONS

Run Designation	Current Density mA/cm^2	Time (hours)	Comments
A	100	1	Flow through electrode
B	50	2	Flow through electrode
C	10	15	Flow by or flow through many times
D	10	4	Flow by electrode
E	10	1-1/2	Flow through electrode
F	5	2	Flow by or flow through

The desired effect was achieved in either the normal flow through mode, or flow by accomplished with the top frame member removed from the electrode pair. Indeed, electrochemical activation most likely does not require flow. During processing, however, flow offered a mechanism thereby heat generated could be rejected.

All attempts using 50% HNO_3 have eventually been successful. Some 10 mA/cm^2 tests yielded no voltaic improvement after the first anodization. After rinsing, a second treatment was always successful.

Electrode Processes Occurring During Electrochemical Activation

Indeed, the very electrodic reactions occurring during anodization in HNO_3 are not understood. Gas evolution on both electrodes is minimal, leaving only some form of valence state "shuffle" involving various nitrogen-containing species. It seems unlikely that a simple nitrate-nitrite redox couple is the only mechanism involved.

During electrolysis copious quantities of particulate graphitic debris are generated. In addition, solution discoloration to a deep brownish-orange is also observed. After standing for some period of time particulate graphite does settle out. The solution phase retains its discoloration, however. Although graphitic decomposition products cannot be ruled out as at least contributing to the coloration, its appearance is quite similar to that of partially decomposed nitric acid containing N_2O_4.

Dimensional Growth of Activated Plates

Significant dimensional increases have been observed and documented for electrode plates activated by both processes. It was first - and repeatedly - noticed for anodically worked plates; subsequent measurement of those thermally treated showed a similar effect.

Electrolyzed Plates. With the advent of open-top comb-type cells, continuous visual inspection between the electrodes was possible. In the course of electrochemical activation with these cells an immediate explanation for previous catastrophic failures with the closed PCS cells become evident. On virtually every successful activation, extreme bowing of the chlorine plates outward toward the zinc substrate occurred. Since it was not possible to successfully disassemble one of the cells to allow actual measurement of dimensions, an estimation was made arithmetically.

In the "bowed" or "dished" state, the center of the electrode has moved the greatest distance. If a perpendicular plane disects the electrode at this central point, a parabola is generated. After visually estimating the resulting gap at the narrowest point, which could be done with reasonable accuracy since the initial gap was a built-in reference, calculating the length of the arc of the parabola was a simple matter. For the four-inch high electrodes in the .160 inch gap cell employed, a gap increase to .080 inch translates into a growth of 4.3 mil (0.1%). Extreme deformation to the extent that the chlorine plate touched and shorted to the cathode would require a 17.0 mil increase (0.4%). These calculations do not allow for whatever expansion the cell design would permit.

Thorough rinsing - flow through with D.I. water - quickly (in 1-2 hours) resulted in the chlorine plates relaxing back and again becoming essentially flat.

With the above disconcerting occurrence repeating itself unremittingly, the measurement of thermally treated plates was naturally implemented. The data were gathered from a significant large number of plates (the 20 kWh production electrodes) to convincingly demonstrate an 8 mil (0.2%) growth. Determination of thickness changes was not possible due to machining tolerances.

Intercalation/Lamellar Compounds of Graphite

Swelling of the graphite lattice as measured by x-ray diffraction is well documented (2-3, 2-4 and 2-5) . Inclusion of cations, anions or compounds between the graphite

layers results in a spacing increase (compared to 3.7 Å with pure graphite) of varying degrees dependent upon the nature and amount of intruding species. Removal of some but not all of the intruding species - most likely HNO_3 in this case - is accomplished by rinsing. The resultant specimen containing some residual "intruder species" in the host graphite lattice, termed a "residual compound", has an intermediate c axis spacing between that of pure graphite and the fully swelled lamellar compound. Hence the partial but almost complete relaxation after rinsing with anodized plates would occur.

It remains to be determined if the enhanced activity produced is in any manner attributable to an intercalation effect. With the electrochemical process, dimensional growth is much more pronounced than for the thermal treatment, and is definitely indicative of a significant degree of intercalation.

The original purpose of the thermal HNO_3 treatment was to chemically modify surface area and pore size distribution so as to yield improved performance, and indeed this must be occurring. With the electrochemical method, however, processing conditions may be quite mild, utilizing extremely low current density along with ambient temperature. Moreover the processing time required even under these conditions is quite small, requiring but a few hours. Modification of surface area and pore size distribution as extensively as with the slow thermal process is difficult to justify.

Intercalation definitely plays a more major role in the electrochemical process than it does in the thermal. If in fact the enhanced activity is not of itself due to intercalation, then at least in the electrochemical case it is responsible for enhancing the rate at which those parameters responsible for the increased activity are being modified.

CONCLUSIONS

General Observations

Electrodes activated by both processes have a number of features in common.

- Equivalent activity is attainable with both processes, possibly indicating a common or very similar cause.
- Activated PG-60 plates are definitely weaker than their machined precursors, although in operating cells and batteries breakage has not been a significant problem.
- Newly activated plates show impressive performance on the first cycle, and tend to improve after a number of cycles. At 45/40 mA/cm^2, this varies but usually levels off after approximately

1% voltaic is gained. Cause of this effect is not yet understood; it could be related to a gradual wetting of the graphite pores, leading to greater electrode activity.

- Possibly the most significant effect is specimen swelling, a possible indication of intercalation between the hexagonal graphite layers. The magnitude is significantly greater for electrolyzed specimens, but after rinsing relaxation is observed. Intercalation and lamellar compound formation - and modification during rinsing - is indicated.
- Neither method is amenable to in-situ activation of an assembled battery. It is difficult to visualize a battery design compatible with electrolysis in nitric acid solutions.

Thermally Activated Plates

Reasonable repeatability was demonstrated, with every good reason to predict easily achievable improvement. Leveling off in the over-voltage improvement with time appears to be asymptotic; little increase in improvement was noted after 9 or 10 days.

Electrochemically Activated Plates

Varying levels of activity are not produced. Instead, performance after the electrolysis has always been equivalent to our better thermally produced specimens. In a matter of at most hours, performance equivalent to that realized after 10-13 days thermal treatment is achievable, and has been demonstrated repeatedly.

RECOMMENDATIONS

- Physical changes to the specimens associated with enhanced performance should be determined. An in-depth program should be implemented to monitor physical parameters thoroughly.
- Anodization of electrode plates external to the battery has economic implications that warrant further, more intensive effort.
- A better understanding of graphic intercalation chemistry could lead to improved methods capable of electrode activation.

REFERENCES

2-1 Symons, P.C., and Carr, P., "Chlorine Electrodes in the Zinc-Chlorine Battery System," Proceedings of the 8th Intersociety Energy Conversion Engineering Conference, Philadelphia, Pa., August 13-17, 1973

2-2 Symons, P. C., and Hammond, M. J., "Evaluation of a 1 kWh Zinc Chloride Battery System," Electric Power Research Institute Report No. EPRI EM-249, September, 1976

2-3 Cotton, F. A., and Wilkinson, G., "Advanced Inorganic Chemistry," Interscience, Third Edition, 1972, pp. 286-290

2-4 Barnett, E. B., and Wilson, C. L., "Inorganic Chemistry," Longmans, Second Edition, 1957, pp. 308-313

2-5 Emeleus, H. J., and Anderson, J. S., "Modern Aspects of Inorganic Chemistry," Van Nostrand, Third Edition, 1960, pp. 525-540

Section 3

MATERIALS DEVELOPMENT

INTRODUCTION

Throughout the development of zinc-chloride ($ZnCl_2$) battery systems, a continuing effort has been expended to locate materials that not only resist the corrosive effects of zinc-chloride saturated with dissolved chlorine gas, but also do not release contaminants into the battery electrolyte which could adversely affect the battery system's efficient operation. Therefore, there is an obvious on-going need to develop materials specifications simultaneously with the $ZnCl_2$ battery system's development to support anticipated system fabrication and production on a large scale.

In this search for materials for use in battery fabrication, three factors are examined:

- the chemical properties of the material (i.e. additives, elemental analyses, etc.)
- the physical properties of the material (i.e. flexural and tensile strengths, resistivity, etc.)
- the economics (i.e. the material and fabrication costs to produce end-item components for the battery system)

Manufacturer's technical literature is collected and samples are obtained, tested and evaluated to determine each sample material's reactivity under various conditions. Then the test results and any supporting information are catalogued and identified by groups for easy retrieval and reference. From these tests, final material specifications are being formulated. The physical and chemical test methods for use in materials quality control are also being compiled.

Numerous materials have shown promise as suitable candidates for the zinc-chlorine battery system. Polyvinylidene fluoride (KYNAR) is presently used as casing and frame material; TEFLON type compounds (TFE and FEP) as tubing; graphite for electrodes; titanium for tubing, fasteners, etc. Specifications have been compiled for the KYNAR and TEFLON plastics, as well as for the titanium components used in the battery. PVC and CPVC plastics, polysulfone, epoxies, polycarbonate, perfluoroelastomers, polypropylene, polyethylene, polyesters, silicon, acrylics, and ceramics are among the materials tested and evaluated. Studies have been made of various adhesives for use in bonding the electrodes to the buss. Of equal importance is the evaluation of selected grades and cuts of graphites. The major thrust of the materials development studies has been to qualify a low-cost plastic for use as the battery construction material. In this report, a brief account is given of the studies on adhesives and graphites. A more detailed report on plastics has been prepared and follows these first two accounts.

ADHESIVES

Presently, an interference-fitted electrode-buss assembly is being used to join the electrodes to the buss. Low electrical resistances were observed at these interference-fit joints. However, due to the close tolerances, great care must be taken during the cutting of these electrodes. Also, graphite waste is much higher. This form of buss-to-electrode contact is considered to be a very expensive way to make this joint. A more cost effective method was sought.

Previously, a KYNAR-dimethylacetamide-graphite mixture was used as an adhesive to join the various joints within the battery. Large surface areas were involved. As battery design was modified and small joint areas became prevalent, adhesives were considered as a means to bond the electrodes to the busses.

Numerous conductive adhesives have been evaluated and several more are to be investigated to determine the one most suitable for this application. Initial testing consisted of a manual bond strength test and measurement of joint resistance with

a Kelvin Bridge. Then, if the adhesive joint resistance is comparable to the resistance of interference-fit joints and adequate bonding strength observed, further testing of the adhesive joints in a cell environment will follow.

Considerable work was done on the formulation of a conductive adhesive. Viscosity, percentage of graphite, graphite particle size, and type of binder were the main variables of interest. Some commercially available conductive adhesives were also evaluated. A list of the developed conductive or commercially available adhesives studied follows:

- PVC/tetrahydrofuran/graphite (two molecular weights of PVC resin were evaluated)
- KYNAR/dimethylacetamide/graphite
- LUCITE/dichloromethane/graphite
- LUCITE/dichloromethane/titanium
- Conductive Epoxy cements
- Ceramic Cement
- Proprietary adhesive from Airco Speer (bonding titanium contacts to 37G graphite)

The developed adhesives were prepared initially by varying only the percentage of graphite (20 to 80 gr. graphite - 40 gr. binder - 200 ml. solvent). Resistance measurements were made according to ASTM Method C611; bond strength was determined by manually applying pressure to the joints and observing whether the joint or the graphite failed. PVC, KYNAR, LUCITE, Epoxy cement, and ceramic adhesives were evaluated in one-half inch tongue-in-groove joints of 0.08" $\pm$ 0.003" gap (Figure 3-1) and in the form of adhesive strips. In all cases the resistance of the adhesive strip was much higher than the observed joint resistance. Epoxy and ceramic adhesives showed poor bond strength and high joint resistances. Good bonding, but high joint resistances were obtained with PVC adhesives. Only the LUCITE adhesive provided both good bonding and satisfactory low joint resistances. Generally, the adhesive strips showed decreased resistance with increased percentages of graphite. However, the joints seemed to have a relatively constant resistance over all

percentages of graphite. This seems to indicate that graphite-buss-to-graphite-electrode resistance is independent of the percent graphite in the adhesive. Contact resistance between an electrode and buss without any adhesive was measured for comparison. Table 3-1 lists the resistance of various adhesives. This forcefully confirms that the adhesive serves only to hold graphite to graphite.

Table 3-1

RESISTANCE OF ADHESIVES - VARIOUS COMPOSITIONS

Binder	% Graphite	Resistivity* (Ω-cm)	Resistance of Joint**(Ω)	Joint Failed
PVC #342	20	∞	0.025±0.010	No
	40	∞	0.028±0.003	Yes
	60	77 ±16	0.024±0.007	Maybe
	80	2.5± 0.6	0.021±0.002	Yes
KYNAR	20	∞	0.008±0.001	Yes
	40	13 ±5	0.010±0.003	Yes
	60	0.22±0.06	0.006±0.002	Yes
	80	0.24±0.05	0.019	Yes
LUCITE	0	---	0.039	No
	20	∞	0.009±0.005	No
	40	∞	0.006±0.002	No
	60	1.58±0.23	0.009±0.001	No
	80	0.44±0.12	---	Yes
COMMERCIAL ADHESIVES:				
Graphpoxy	?	16.0±4.9	1.20 ± .26	No
Graphite Cement	?	3.0±0.5	0.012±0.002	Yes
Ceramic Conductive Adhesive	?	10.9±3.7	0.028±0.009	Yes
NO ADHESIVES:				
Resistance of Graphite Buss to Electrode	0	---	0.01	No pressure applied to joint
	0	---	0.004	Pressure applied to joint

* Resistivity of adhesive itself - no joint used.

** Extrapolated Values for tongue-in-groove joints.

From these initial studies a LUCITE adhesive appeared to be the most feasible candidate for use in the battery. Further testing with filled LUCITE adhesives at 70%, 80% and 90% graphite was done. Resistance measurements indicate a LUCITE adhesive with 80% graphite forms a bond of suitable strength and sufficient conductivity for use in the battery system. In addition, studies were conducted to determine the relationship of graphite particle size to joint resistance.

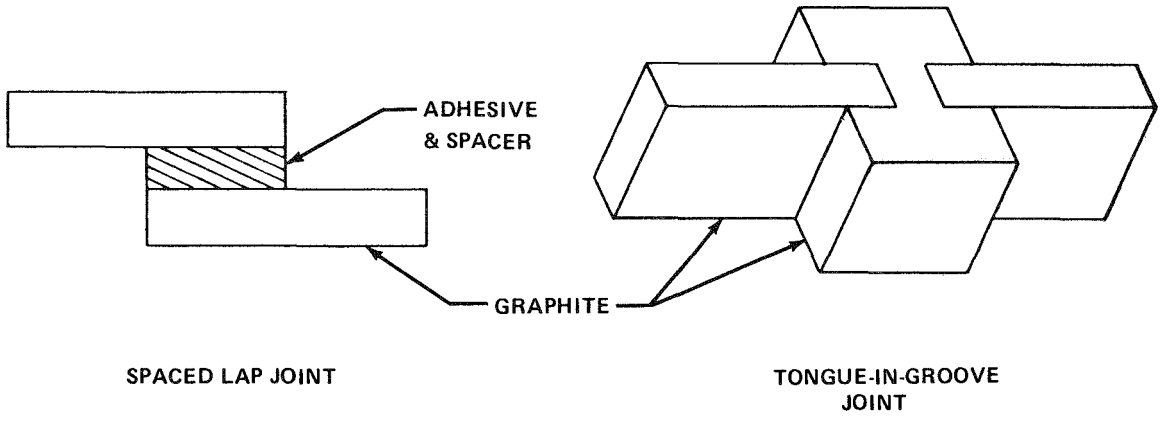

Figure 3-1. Typical electrode-to-buss jointing methods

Though lower resistances are observed in a spaced lap joint (Figure 3-1) for the larger graphite particle size (sieve size +10, -30), the most suitable graphite particle size for the tongue-in-groove joint (Figure 3-1) is a powdered graphite (sieve size +150) of 20-30 micron size. A powdered graphite makes more uniform contact along the entire groove than the inconsistant contact made by larger graphite particles in a small groove.

Another factor to be considered is the viscosity of the adhesive. A ratio of 8/2/15 was determined to be the most satisfactory balance for the grams graphite powder/grams LUCITE/milliliters methylene chloride. With this adhesive, a joint resistance of 0.0007 of an ohm appears possible for a 3.5" joint.

Table 3-2

JOINT RESISTANCE VS. PARTICLE SIZE

Graphite Particle Size	Tongue-in-Groove Joint Resistance* (extrapolated)
+150	.0007 Ω
	.0002
+60 -150	.0054
	.0074
+30 -60	.0109
	.0119
+10 -30	.0059
	.0054

*Joints were 3.5" long

Further tests were performed using a buss and 5.75" electrodes of EPRI design with a 0.100 of an inch gap and 0.0855 of an inch depth (Figure 3-2). Electrodes were glued into place with the 8/2/15 LUCITE adhesive, cured, and the resistances measured across the joint with a Kelvin Bridge.

These test results are listed in Table 3-3.

Table 3-3

AVERAGE ELECTRICAL RESISTANCE

Location of Probes*	Average Resistance
$A_0 - A_1$	0.0075 $\pm$ 0.0006
$A_0 - A_2$	0.0060 $\pm$ 0.0004
$A_0 - A_3$	0.0084 $\pm$ 0.0006
$A_0 - A_4$	0.0057 $\pm$ 0.0005
$A_0 - A_5$	0.0048 $\pm$ 0.0005

*See Figure 3-2

An extrapolated value for the joint resistance was calculated to be approximately 0.0025 $\pm$ 0.0002 ohm for a 5.75" joint length. Voltage drop across the joints was 0.0426 $\pm$ 0.0034 volts when 8 amps was applied. This figure compares with actual voltage drops measured across press-fit joints under the came conditions (8 amps current applied, 153 cm^2 electrode surface area and a 4.0" joint). From tests performed, the voltage drop across a buss and electrode with a LUCITE joint appears very reproducible and as good as the joints presently being used.

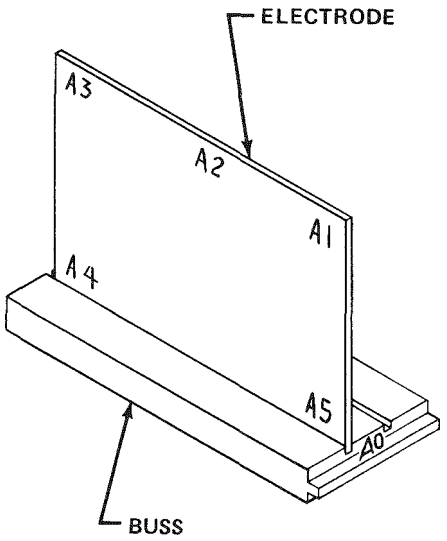

Figure 3-2. Interference-fitted electrode used in joint resistance measurements

Test samples of graphite electrodes with bonded titanium wire contacts were supplied by Airco Speer. An average resistance of 0.0419 $\pm$ 0.0059 ohm (corresponding to resistivity of 0.3508 $\pm$ 0.0492Ω -cm) was measured. Numerous attempts were made to duplicate the method and low resistances observed with Airco Speer's contacts, but no success was achieved. Poor bonding and extremely high resistances were encountered. Another alternative to adhesives is a metal-to-graphite clip joint. The average joint resistance for a 1/2" joint of clip type $\int\!\!\lambda\!\!\lfloor$ was 0.0082 $\pm$ 0.0020 ohm.

Durability of the bond in a $ZnCl_2$ cell system is another area of concern. Problems had been encountered where the KYNAR glued joints were suspected to increase in resistance following exposure as chlorine electrodes in $ZnCl_2$. Tests were conducted on the KYNAR adhesive. No increase in resistance was measured (actually a slight decrease was noted). A 60/40 graphite-LUCITE adhesive also was used to glue small electrodes into a buss. Resistance across these joints was measured before and after a 3-day exposure as chlorine electrodes in a 1:1 HCl dilution. No significant change in resistance was observed.

To further qualify an adhesive for final use in $ZnCl_2$, a cell with a bonded electrode design must be cycled to determine both the durability of the bond and the electrochemical effects of possible leachants from the adhesives. A program to implement this type of study is planned for the coming year.

A point of importance is that in order to use this adhesive concept, a design is required that would be consistent with adhesive bonding and high production rates. To date, this design has not been generated.

GRAPHITE STUDIES

Because of economic considerations, graphite electrodes must inevitably replace ruthenized titanium electrodes. Graphite, however, will still be a major cost item. Various grades and cuts of graphite were investigated to determine the effect of surfaces upon zinc plating and chlorine evolution. These studies were carried out in a simple cell system. More detailed experiments will need to be performed before a selection of the most suitable electrode material can be made.

Graphite Samples

Graphite samples, listed below, are standard, low-cost grades provided for testing by Airco Speer and Union Carbide:

Ground Cut - extruded grade graphite

Type #873G Very coarse with prominent crevices.

Crevice width = 0.18 mm ± 0.07
Crevice length = 0.49 mm ± 0.27
Crevice depth = 0.30 mm ± 0.14

Comments: During zinc plating small dendrites formed (approximately 0.63mm) and some crevices were not plated, though the zinc deposit adhered well.

Type #873S Coarse though crevices are closer and smaller.

Crevice width = 0.18 mm ± 0.03
Crevice length = 0.43 mm ± 0.13
Crevice depth = 0.16 mm ± 0.07

Comments: A few crevices still unplated but good overall plating. Dendrites of approximately 0.11 mm formed.

Type #890S Crevices smaller and more directional (perpendicular to length).

Crevice width = 0.13 mm ± 0.05
Crevice length = 0.54 mm ± 0.22
Crevice depth = 0.12 mm ± 0.04

Comments: Some unplated areas noted in plating and dendrites formed (approximately 0.26 mm in height).

Type #580 No crevices visible to the naked eye, but microscopic measurements possible.

Crevice width = 0.09 mm ± 0.03
Crevice length = 0.21 mm ± 0.08
Crevice depth = 0.08 mm ± 0.04

Comments: A very fine plating with a great decrease in open spots in the zinc deposit. Average dendrite height is 0.36 mm.

Type #37G (Porous graphite for use as chlorine electrodes) - no crevices visible to naked eye and very few viewed microscopically.

Crevice width = 0.07 mm ± 0.02
Crevice length = 0.13 mm ± 0.02
Crevice depth = 0.06 mm ± 0.01

Saw Cut Graphite

Type #873S Saw cut ridges were quite visible to the naked eye. Ridge height = 0.15 mm $\pm$ 0.028.

Comments: Preferential dendrite growth observed along saw cut ridges. Dendrites ranged from 0.41 to 0.95 mm in height.

Type #580 Saw cut ridges are more visible than on 873S, but are fewer crevices observed here. Ridge height = 0.15 mm $\pm$ 0.044.

Comments: Preferential dendrite growth along ridges (average dendrite height approximately 0.33 mm).

Type #37G (Porous graphite for use as chlorine electrodes) - ridges visible - ridge height = 0.17 mm $\pm$ 0.036.

Cut-Off-Wheel Cut Graphite

Type #873G Looks coarse and grainy to the naked eye; cut off wheel occasionally showed ridges like band-saw cut marks (were visible microscopically).

Crevice width = 0.20 mm $\pm$ 0.07
Crevice length = 0.46 mm $\pm$ 0.15
Crevice depth = 0.11 mm $\pm$ 0.03

Comments: Satisfactory as zinc electrodes.

Type #37G (Porous graphite used as chlorine electrodes)- no crevices noted, a fine finish.

Grafoil Electrodes - pressed graphite grade GHM

Knife Cut and Saw Cut edges - quite shiny; and fragile. During the zinc plating process, some exfoliation occurred when the grafoil was used as the chlorine electrode. Uneven zinc plating and numerous dendrites suggests that grafoil is unsuitable as zinc or chlorine electrode material.

Laminated Grafoil Electrodes

This type electrode was evaluated as both a chlorine and zinc electrode. As the chlorine electrode, the laminate rapidly blistered up. When the blisters were cut open, exfoliation was observed beneath the laminate. Zinc plating was even and no blistering occurred on this type electrode, however.

General Observations

Despite increased dendritic growth over the entire plate, the most even plating occurred on the #873S and #580 saw cut samples. Whereas, ground cut samples #873S and #580 showed the least dendrite growth.

A definite preferential dendritic growth was noted along saw cut ridges. Zinc deposition on the graphite electrodes was crystalline in nature, while the plating on grafoil was notably different.

Grafoil seems unsuited as an electrode material. Although zinc plates rather well on the surface, laminated grafoil blisters excessively when used as chlorine electrodes.

Future materials evaluation studies, using actual cell environments, will be initiated to examine further the various graphite cuts and grades.

PLASTICS AND CERAMICS

Introduction

Machinable ceramic materials and/or a moldable and extrudable plastic compatible with the zinc chloride is needed for battery casing, electrode frames, and piping. Presently, these components are fabricated from KYNAR (polyvinylidene fluoride) and TEFLON (polytetrafluoroethylene).

Alternate materials must be found, however, to make the zinc chloride battery economically feasible. Current price of polyvinylidene fluoride resin is nearly $5.00 per pound; however, available, potentially usable plastics only cost 30 to 40 cents per pound. Although their cost is somewhat higher, machinable ceramics are also being considered.

The cheaper plastics, however, must be screened with regard to their resistance to chlorinated zinc chloride and contamination of the electrolyte. Actually, a wide variation in each generic plastic exists by virtue of different combinations of additives.

Variations of many generic types of plastics have been screened in chlorinated zinc chloride. Special emphasis was placed on the specification of polyvinylchloride due to the close relation in chemical structure to polyvinylidene fluoride and the substantially cheaper price of PVC.

A plastic consists of a chemical combination of a relatively simple compound (the monomer) forming a polymer (repeating units of the monomer). For example, the monomer vinylchloride ($CH_2 = CHCl$) polymerizes to form long chains

$$(-CH_2-\underset{Cl}{CH}-)_n$$

The length of these chains (polymer molecular weight) can be controlled by the temperature and mode of polymerization. Most polymers require additives to facilitate processing and chemical resistance. Heat stabilizers are necessary in many plastics to prevent degradation during processing. Stabilizers often react with the unstable end groups of a polymer chain to prevent decomposition initiating at these sites. Some plastics require UV stabilizers and antioxidants be added as well as heat stabilizers. Metal soaps, organotins (i.e. dibutyltin laurate and maleate), lead stearates and phthalates, and organophosphites are common heat stabilizers. Lubricants can influence the processing and chemical characteristics of resins and physical properties of the finished products. The most important chemical property influenced by a lubricant is chemical stability. Lubricants are classified into two categories, internal or external. Internal lubricants attack the cohesive forces between molecules and form a mixture with the resin which has a lower coefficient of friction. External lubricants promote release from metal processing equipment since they migrate to the surface of the molded form. Polyethylene often is added to polymers as an external lubricant. Fillers are used as functional additives to obtain improved properties in the composite (i.e. shrinkage and strength) and as extenders to reduce costs. Glass, carbon, cellulose fibers, metallic oxides and powders are common fillers.

The flexibility required for many applications can be achieved by mixing a polymer with a compatible plasticizer. Plasticizers are usually high boiling, organic liquids. It is theorized that a plasticizer reduces the van der Waals and dipole-dipole forces between the polymer chains or acts as a lubricant between the chains, thus increasing flexibility of the polymer. Phthalate esters are the most commonly used plasticizers. Colorants, processing aids, antistatic agents, and flame retardants are other components often added to plastics.

Various processing methods are available to formulate plastics. Bulk processing is used to polymerize monomers with an oil-soluble free-radical initiator in the absence of water and surfactant additives. In Suspension processing, monomer droplets are dispersed in water in the presence of suspending agents (methyl cellulose, gelatin, or partially hydrolyzed PVA). Particle size of the suspension grade resin ranges from 90 to 130 microns. Smaller particle sizes of approximately 0.5 microns can be achieved with an Emulsion processing. In this method, an aqueous colloidal dispersion of the monomer is polymerized with water soluble free-radical initiators. Each processing method involves different catalysts and varying levels and combinations of additives, thus affecting the chemical composition of the final product.

Review of Commercial Plastics

A list of commercial plastics reviewed for feasibility and resulting comments relative to their properties and suitability as a usable battery system material follows:

- METHYL METHACRYLATE POLYMERS (LUCITE)
  - A thermoplastic homopolymer
  - Soluble in dichloromethane
  - Relatively inexpensive
  - UV and heat stabilizers usually added, but could be left out
  - Methyl abietate and disoctyladipate, although not necessary, may be used as plasticizer

- CROSSLINKED METHYL METHACRYLATE WITH MINOR COPOLYMERS (POLY '76)
  - A thermoset which cannot be injection molded
  - Is similar to compound used in lead-acid storage batteries (grafted, crosslinked acrylic acid - polyethylene copolymer)
  - Insoluble with cyano-acrylate
  - More expensive than LUCITE, but a feasible laminant material
  - Additives and lubricants are proprietary
  - No fillers
  - Only a UV stabilizer necessary
- POLYESTERS

  Aromatic Polyesters:
  - Compression and injection moldable
  - Can be solvent cemented
  - Composed of p-oxybenzoyl units
  - Can be copolymerized with moieties of aromatic dicarboxylic acid and aromatic bisphenols

  Thermoplastic Polyesters:
  - Compression and injection moldable
  - Can be solvent cemented
  - Composed of polyethylene-teraphthalate or polybutylene teraphthalate

  Vinyl Polyester Resins (DERAKANE):
  - Peroxide initiators
  - Amine promoters
  - Clay and glass fillers may be added
- POLYETHYLENE
  - Can be injection, extrusion or blow molded
  - Inexpensive
  - Soluble in carbon tetrachloride at elevated temperature

- A high pressure, free radical polymerization process is used to manufacture low density polyethylene (branched). Low density polyethylene is used in films and has a density of 0.918 - 0.930 gr/cm^3

- A high density polyethylene (linear) is manufactured by a low pressure process using catalysts such as chromium oxide, vanadium, and molybdenum oxide. High density polyethylene (0.955 - 0.960 gr/cm^3) is used in bottles and pipe extrusions

- Comonomers include vinyl acetate, acrylate esters, carboxylic acids, and metallic ion-neutralized carboxylic acids

Additives:

- Antioxidants are needed; phenols, alkylamines, and phosphites are common antioxidants

- Lubricants: not normally used (is self-lubricating); sometimes a silicone mold release is necessary

- Stabilizers: only a UV stabilizer is needed (carbon black)

- May add antistatic agents (1% fatty acids-amides)

- Fillers are not necessary, but may be added to improve rigidity and tensile strength (clays, glass)

- POLYIMIDES

Thermoplastic Polyimide (ENVEX):

- Compression moldable, but not injection or transfer moldable

- Can be bonded using dimethyl formamide or dimethyl pyridene

- Approximately $100/10" x 10" x 1/4"

Additives:

- Lubricants: none necessary except a fluorocarbon mold release agent

- Stabilizers: none necessary

- Fillers: none necessary though carbon and TFE may be used.

Graphite Filled Thermoset Polyimide (FEURLON):

- Compression moldable, but not injection or transfer moldable
- Can be bonded using dimethyl formamide or dimethyl pyridene
- Approximately $400/10" x 10" x 1/4"
- Has a higher service temperature range than ENVEX

Additives:

- Lubricants: none necessary except a fluorocarbon mold release agent
- Stabilizers: none necessary
- Fillers: none necessary though carbon and TFE may be used

NOTE: PTFE filled polyimide: A film produced by polycondensation reaction of aromatic tetrabasic acid and an aromatic amide

- POLYPROPYLENE
  - A thermoplastic which can be molded, extruded or made into a film or fiber
  - Solvent cementing is not possible, but polypropylene can be welded
  - An inexpensive plastic
  - Catalyst residues, unreacted propylene, amorphous polymer, and reaction diluents are removed from polymer slurries by centrifugation, filtration, or distillation
  - A high density polypropylene has an average number molecular weight of 250,000 - 300,000

  Additives:

  - Uses a transition metal compound with certain organometallic compounds as catalysts
  - Often blended with polyisobutylene to remedy low temperature brittleness
  - UV and heat stabilizers needed
  - Common copolymer: polypropylene-ethylene
  - Amorphous polymer is vulnerable to oxidative degradation through free radical chain reaction accelerated by heat and UV radiation; therefore, an antioxidant is necessary

- POLYSULFONE
  - Can be molded, extruded, or thermoformed
  - Characterized by diphenylene repeating unit
  - Produced by reaction between the sodium salt of 2, 2-bispropane and 4, 4-dichlorodiphenyl sulfone. The sodium phenoxide end-group reacts with methyl chloride to terminate polymerization
  - 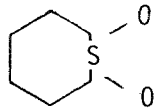

the highly resonating structure of sulfone group ties up oxygen electrons resulting in oxidative stabilization
  - Good resistance to detergents, oils, alcohols at elevated temperatures and under moderate stress
  - Highly resistant to mineral acids, alkali, and salt solution
  - Blisters badly and becomes opaque when exposed to chlorinated zinc chloride

- COPOLYMER OF VINYLIDENE FLUORIDE AND HEXAFLUOROPROPYLENE (VITON)
  - A fluoroelastomer
  - No plasticizers
  - No lubricants
  - May be pigmented (with carbon black)
  - Elastomers are often attacked by chlorine
  - May be amine cured or lead oxide cured (litharged)
  - Surface was visibly pitted and expanded from exposure to chlorinated $ZnCl_2$

- ACETALS (DELRIN)
  - Homopolymer of formaldehyde
  - Can be injection molded or extruded
  - Not solvent bondable
  - Relatively inexpensive
  - Complete dissolution in $ZnCl_2$

- POLYPHENYLENE SULFIDE (RYTON - 40% GLASS FILLED)
  - Injection or compression molded
  - Not solvent bondable
  - Natural pigmentation is black or dark brown; this color fades out upon exposure to chlorinated $ZnCl_2$
  - Has a rigid backbone of 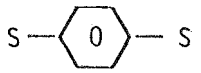

- PHENYLENE OXIDE BASED RESIN (NORYL)
  - A thermoplastic which can be injection molded or extruded
  - Soluble in tetrahydrofuran
  - Inexpensive

  Additives:

  - is often glass reinforced
  - formulated from oxidative coupling of phenolic monomers
  - Appears unsuitable for use in $ZnCl_2$

- POLYCARBONATE
  - Can be injection, extrusion, foam, and blow molded
  - Inexpensive
  - UV stabilizers needed
  - Unsuitable for use in $ZnCl_2$

- POLYVINYL CHLORIDE COMPOUNDS
  - Are thermoplastics derived from vinyl chloride (CH_2=CHCl)
  - PVC resins and copolymers with vinyl acetate, ethylene, propylene, and acrylic esters are produced by free radical initiated polymerization in bulk, suspension, emulsion, or solution systems. Temperature is the primary control to vary molecular weight
  - Chlorinated polyvinyl chloride extends utility of PVC type compound to higher service temperatures, but is more difficult to process

Additives:

- Stabilizers: requires thermal stabilization to prevent heat degradation during processing (i.e. metallic soaps of Pb, Cd, Ba, Ca, Zn, Sn, or fatty acid salts). The possibility of zinc soap stabilizers in PVC was discussed with RUCO. PVC compounds stabilized in the manner are hard to make and are provided only with UV stabilization from the zinc compounds. Also, different degrees of zinc tolerance are exhibited by different resins. Tin stabilized PVC's from RUCO contain a butyl tin mercaptide stabilizer. Tin maleates are also effective stabilizers. Considerations were also made of an organo-phosphite stabilized PVC.

- Lubricants: calcium stearates and/or polyethylene are used as common lubricants. Lubricants facilitate melt flow during processing by (a) internal reduction of intermolecular forces between polymer chains and/or (b) external reduction of adhesion to metal surfaces of processing equipment

  Other lubricants consist of paraffin base waxes, fatty esters, metallic soaps of fatty acids

- Processing Aides: methyl methacrylate esters; copolymer of styrene/acrylonitrile copolymers (added at levels of 8-12%) could be used, but are not necessary

- Plasticizers: a major additive in flexible PVC (20-100%); phthalate esters are used as plasticizers, but are readily degraded by $ZnCl_2$; it appeared that plasticization may be accomplished by laterally decreasing the van der Waals forces between polymer chains (solvating polar groups of polymer) or by a copolymerization mechanism of plasticizer with vinyl chloride monomer

- Impact modifiers: used with unplasticized rigid PVC; methyl methacrylate/butadiene/styrene, and chlorinated polyethylene are common impact modifiers added at levels of 15%

- Fillers: asbestos, glass, carbon, TiO_2, $CaCo_3$

- Mold Releasing Agents: may be used and consist of silicon metallic stearates

- POLYVINYLIDENE FLUORIDE - (KYNAR #460 is the primary grade ordered by EDA)

  - A high molecular weight homopolymer:

    $$-CH_2-CF_2-$$

  - Solvent bondable with dimethylacetamide

  - Can be made heat shrinkable and has good molding characteristics

- Emulsion method prepared
- KYNAR is stable to UV and gamma radiation

Additives:

- Initiators - are necessary, but contain no heavy metals
- Lubricants - paraffin waxes to prevent coagulation on walls of vessel
- Stabilizer - none in #460, but ZnO_2 used in #320
- Filler - glass beads and furnace black used in #315 and #320 respectively; none used in #460
- Plasticizer - #320 uses a dioctylphthalate
- Pigments - available in many colors, but are unnecessary additives

  ZnO_2 - white
  Cadmium, mercury - red, maroon
  Chrome, tin - pink
  Cobalt - violet
  Cadmium sulfide - yellow

Method of Screening Materials

A screening program for plastics and ceramics was prepared according to ASTM D543 (Test for Resistance of Plastics to Chemical Reagents). A set of standard test parameters was selected and maintained throughout this physical degradation testing in order to produce comparable data. Screening tests were performed using the system shown in Figure 3-3.

Standard parameters were selected with regard to the various conditions in use for battery operations. All plastics and ceramics were viewed microscopically and photographed prior to any degradation studies. Initially, all test specimens were exposed to chlorinated zinc chloride (30% solution, pH 1.0) for 29 days at ambient temperature. Whenever the specimens and their test solutions appeared unaffected by this initial exposure, the temperature was increased to 50°C and the tests continued for an extended period of time. Further testing also was conducted in wet chlorine gas and chlorinated water.

Selected measurements were made on each plastic or ceramic sample and the test solution to determine whether any degradation had occurred. These physical

measurements included weight and dimensional changes, durometer (hardness), blisters/mm^2, surface area, and blister diameter for each test specimen. Changes in the specific gravity and pH of the zinc chloride also were recorded. An atomic absorption analysis of the test solutions was made to check for any leached out components. At present, a program to electrochemically qualify materials passing this screening test is being planned.

Screening Test Results

Table 3-4 summarizes the test data obtained from material screening tests conducted during the 1976 program.

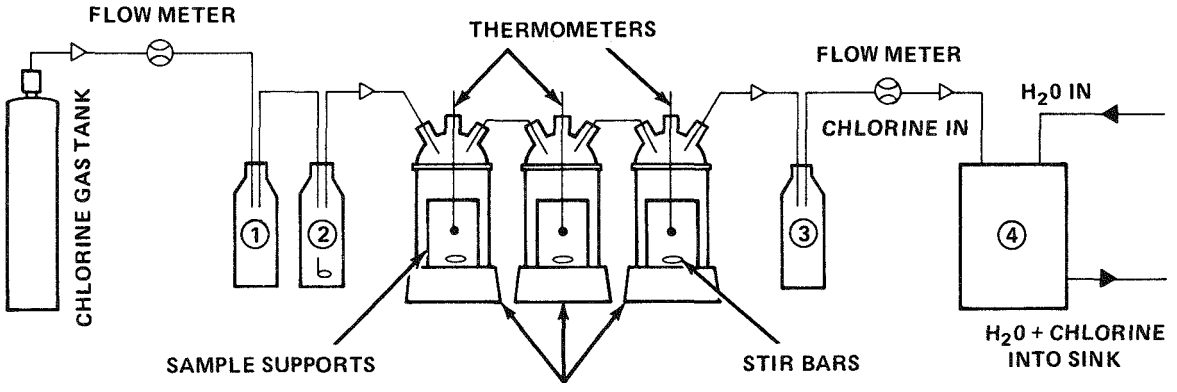

LEGEND

1. WET CHLORINE TRAP: PREVENTS WETTED CHLORINE FROM FLOWING BACK INTO CHLORINE GAS STORE IN CASE OF VACUUM.
2. GAS WASHING BOTTLE: WET CHLORINE SUCH THAT DRY CHLORINE FROM STORE DOES NOT EVAPORATE WATER FROM CELL $ZnCl_2$ SOLUTION.
3. THIS TRAP PREVENTS SCRUBBER SOLUTION FROM ENTERING CELL SYSTEM IN CASE OF PRESSURE DROP IN SYSTEM.
4. CHLORINE SCRUBBER CONSISTING OF WATER RUNNING OVER BERL SADDLES WITH CHLORINE ENTERING FROM SIDE.

NOTE: ENTIRE SYSTEM IS WITHIN A HOOD.

Figure 3-3. Plastics and Ceramics Screening System. Physical degradation testing conducted in accord with ASTM standards discloses the effect of temperature and operational environment on sample materials.

Table 3-4

PLASTICS AND CERAMICS SCREENED

Generic Name	Trade Name	Test Results
Acetals	DELRIN	Complete dissolution in four days exposure to chlorinated zinc chloride.
Machinable Ceramics	MACOR, LAVA, CERAMESE	Four ceramics evaluated. One sample showed definite weight loss. High levels of Fe, Mg, Pb, (in excess), and Si leached out. Extended individual tests in progress.
Polyvinylidene fluoride	KYNAR	Unpigmented KYNAR appears inert in chlorinated zinc chloride. The pigment of colored KYNAR is leached out. Presently a KYNAR encapsulated stainless steel rod is being tested.
Methyl Methacrylate (MMA)	LUCITE	Annealed and unannealed MMA compound were compared. (An annealed compound blisters less). A high density MMA compound blisters less than annealed MMA. A modified acrylic (cross linked MMA with minor copolymers) appeared stable in chlorinated zinc chloride after 30 days; extended tests in progress.
Phenylene oxide based resin	NORYL	Grossly faded out and blistered.
Polycarbonate	-----	Excessive blistering; degraded to such a degree as to become completely opaque; iron leached out.
Polyesters	DERAKANE, GLASTIC	DERAKANE vinyl resin tested (#470 and #411); 470 appeared more stable though did show some blistering. No cobalt catalyst leached out, but Fe, Mg, and Ca were found in solution. Glass fiber reinforced sheet (red color) appeared unblistered after one month in chlorinated zinc chloride; but Cr, Co (both possible pigment or catalyst components). Fe, Mg, Pb, Si, and Ca were leached out

Table 3-4

PLASTICS AND CERAMICS SCREENED

Generic Name	Trade Name	Test Results
		at relatively high levels. Tests are being continued.
Polyethylene	-----	A black low molecular weight sample blistered and faded after 1 month exposure to chlorinated zinc chloride. A high density unpigmented polyethylene copolymer showed only slight blistering after two months in chlorinated zinc chloride at 50°C (further specification and testing being pursued).
Chlorosulfonated Polyethylene	HYPALON	A flexible plastic which greatly expanded and curled upon exposure to chlorinated zinc chloride.
Polyimides	KAPTON, FEURLON, ENVEX	Graphite filled polyimides do not leach out any carbon, but the zinc chloride test solution showed numerous other elemental components of concern present (further testing in progress).
Polyphenylene Sulfide	RYTON	Excess fading of natural RYTON observed as well as leaching of numerous elemental components.
Polypropylene	-----	Filter screen showed cracking at points of weave stress when exposed 30 days to chlorinated zinc chloride. Stock samples showed blistering in 30 days also. A high density polypropylene is presently being evaluated.
Polysulfone	-----	Badly blistered within 30 days exposure to chlorinated zinc chloride.
Polyvinyl Chloride	-----	Numerous samples were tested with varying results

Table 3-4

PLASTICS AND CERAMICS SCREENED

Generic Name	Trade Name	Test Results
Polyvinylidene Chloride	SARAN	Four different types of SARANS were exposed to chlorinated zinc chloride. 25°C tests showed three samples stable, but at 50°C tests, samples flowed (became gummy and distorted). Cu, Mg, Ca, and Fe were leached out.
Polytetrafluorinated Ethylene	TEFLON type compounds (TFE)	A sample of cured and uncured TFE (ARMALON) appears to show uncured TFE to be reactive with chlorinated zinc chloride. Carbon filled TFE does not leach out carbon. CeO_2 and ZrO_2 filled TFE's appeared stable (no means was available to analyze for leached out Ce or Zr). Ethylene-chlorotrifluoro-ethylene (HALAR film) appears stable in chlorinated zinc chloride.
Copolymer of Vinylidene Fluoride and Hexafluoro-propylene and TFE	VITON	Appears to be degraded by chlorine gas somewhat.

Future Testing Program - Electrochemical Evaluation

If a test material appears to be physically and chemically stable in a chlorinated zinc chloride solution at 50°C, the electrochemical compatibility of the sample in a cell system will then be evaluated. The objective of the electrochemical test will be to determine the compatibility of a plastic or ceramic material in $ZnCl_2$ battery environment. A cell system will be designed and constructed from KYNAR, glass, and TEFLON (Figure 3-4). These test cells will follow an EPRI design with activated graphite electrodes. By exposing a test material to the electrolyte in an operating cell, any leachable components from the test material should show their effects on electrochemical properties. The sump will be separated from the

cell and will expose the test materials to the electrolyte. An operating cell temperature of 50°C has been selected and a current density of 45 mA/cm^2 on charge and 40 mA/cm^2 on discharge maintained. Each sample will be exposed to the electrolyte for 10 cycles initially.

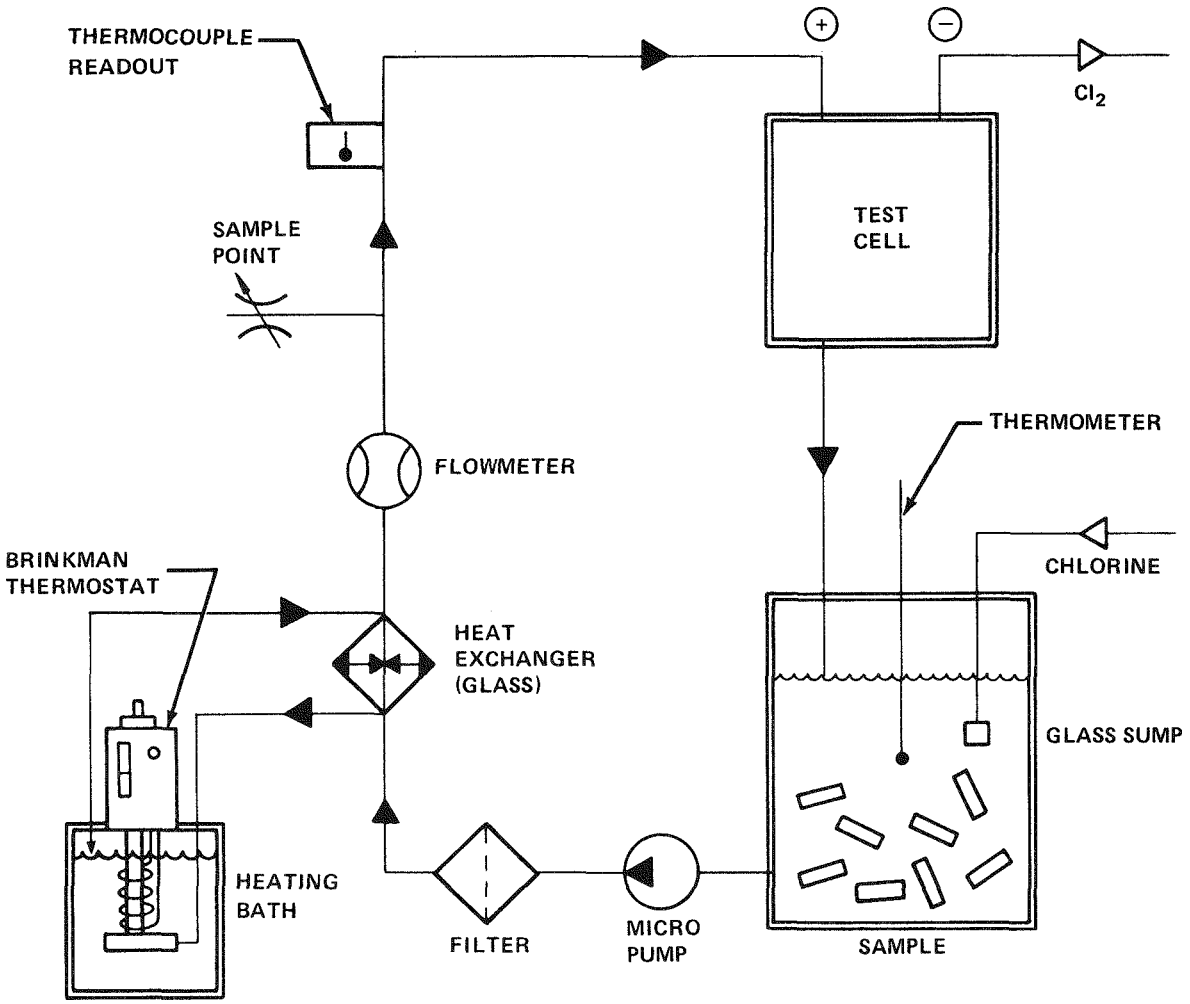

Figure 3-4. Diagram of test setup to be used for electrochemical evaluation of materials within battery environment

During testing, voltaic and coulombic efficiencies will be determined and atomic absorption analysis of the electrolyte made. If test cells show a voltaic and total coulombic efficiency comparable to the control, cycling will be extended for

100 cycles. If efficiency and atomic absorption analysis remain relatively stable, a cell will be fabricated from the test plastic and cycled for an extended period.

Polyvinyl Chloride (PVC)

Polyvinyl chloride samples with specified levels of additives and/or specified components were supplied for evaluation from the RUCO Division of the Hooker Chemical and Plastics Corporation. Initial screening consisted of twelve PVC samples which were tested with two controls - KYNAR sheet stock and a commercially - available PVC formulation. The KYNAR and commercially-available PVC appeared quite stable in the chlorinated zinc chloride, though lead was observed to be leaching into the test solution from the commercial PVC formulation.

RUCO prepared a second group of samples for our evaluation based upon the initial test results. The testing of these PVC materials identified the optimum resin and stabilizer. Further testing also indicated that insufficient mastication of components in the PVC formulation can lead to degradation. Testing beyond the initial screening of selected PVC formulations is now being pursued.

Plastic Status

Materials which pass the preliminary screening, will be electrochemically evaluated. At present, a polyvinyl-chloride formulation is ready for such testing in a cell environment. Polyethylenes and polyesters require further specification through the screening test before electrochemical testing of these compounds begins. Thus far, studies of a glass filled polyester indicate that the type of glass filler used may be a problem. Ashland Chemicals is assisting in the specification of a suitable polyester.

After demonstrating satisfactory performance during a large number of cycles in an operating test cell constructed with the desired plastic(s), larger batteries will be evaluated using these same materials. These original test cells will continue cycling in order to assess the long term suitability of the plastic(s) in the battery. The use of a specified PVC instead of KYNAR for the battery casing and store would drastically reduce the battery cost . The further specification of a stable polyethylene compound is desirable in that this compound is injection-moldable and could thus be used for the present frame design. A glass-reinforced

polyester tank may be useable as the hydrate store provided an inert polyester compound could be qualified. Studies will continue to develop new formulations as well as to more completely specify the most desired compounds for each battery application.

A grand summary of the plastics studied has been compiled and presented in Table 3-7 for easy reference.

Table 3-7

PLASTICS RESISTIVE TO CORROSIVE BATTERY ENVIRONMENT

PLASTICS EVALUATED	SPECIFIC GRAVITY (D792) (ASTM TEST)	TENSILE STRENGTH (PSI) (D638) (ASTM TEST)	HARDNESS (ROCKWELL) (D785) (ASTM TEST)	% WATER ABSORPTION (D750) (ASTM TEST)	EFFECT OF SUNLIGHT	EFFECT OF WEAK ACID (D543) (ASTM TEST)	EFFECT OF STRONG ACID (D543) (ASTM TEST)	EFFECT OF AQUEOUS CHLORINE SOLN.
CURED TFE FIBER IMPREGNATED WITH UNCURED TFE (ARMALON)	2.14 - 2.20	2000 - 5000	D50 - D55 (SHORE)	----	NONE	NONE	NONE	DISCOLORED (UNCURED TFE REACTS)
CHLORO-SULFONATED POLYETHLYLENE (HYPALON)	1.12-1.28	OVER 3000 (BLACK-LOADED STOCK)	40-95 SHORE DURO A	----	NONE	NONE	NONE	LOSS OF ELASTICITY AND EXPANSION
COPOLYMER OF VINYLIDENE FLUORIDE AND HEXAFLUOROPROPYLENE (VITON FLUOROELASTOMER)	1.85	OVER 2000 (BLACK-LOADED STOCK)	60-95 SHORE DURO A	----	NONE	NONE	NONE TO SLIGHT	ATTACKED (PITTED)
POLYSULFONE	1.24	10,000	M69, R120	0.22%	STRENGTH LOSS WITH SLIGHT YELLOWING	NONE	NONE	DROP OF TENSILE STRENGTH BY 9-14% *
POLYETHYLENE (LOW DENSITY)	0.910 - 0.940	600 - 2300	D44-D50 (SHORE) R10	<0.01%	**	ATTACKED BY OXIDIZING ACIDS	RESISTANT	BLISTERED
POLYETHYLENE (MEDIUM DENSITY)	0.926 - 0.940	1200 - 3500	D50-D60 (SHORE) R15	<0.01%	**	ATTACKED BY OXIDIZING ACIDS	VERY RESISTANT	----
POLYETHYLENE (HIGH DENSITY)	0.941 - 0.965	3100 - 5500	D60-D70 (SHORE)	<0.01%	**	----	VERY RESISTANT	UNBLISTERED
CHLORINATED POLYVINYL CHLORIDE COMPOUND (CPVC)	1.49 - 1.58	7500 - 9000	R117 - 122	0.02 - 0.15%	SLIGHT	NONE	NONE	METAL CHLORIDE COMPOUNDS ATTACKED
VINYLIDENE CHLORIDE MOLDING COMPOUND (SARANS)	1.65 - 1.72	3000 - 5000	M50 - M65	0.1%	SLIGHT	NONE	RESISTANT	FADED, BUT NOT BLISTERED AFTER 1 MONTH OF TESTS AT 25°C
PROPYLENE VINYL CHLORIDE COPOLYMERS	1.28 - 1.40	5000 - 8000	M18 - M55	0.07 0.4%	SLIGHT	NONE	NONE	----
VINYL CHLORIDE POLYMERS AND COPOLYMERS*** (RIGID)	1.30 - 1.58	6000 - 7500	65 - 85D (SHORE)	0.04 - 0.4%	VARIES WITH FORMULATION	NONE	NONE TO SLIGHT	NONE
VINYL CHLORIDE POLYMERS AND COPOLYMERS*** (FLEXIBLE & FILLED)	1.30 - 1.70	1000 - 3500	50 - 100A (SHORE)	0.5 - 1.0%	SLIGHT	NONE	NONE TO SLIGHT	PLASTICIZED PVC ATTACKED
VINYL CHLORIDE POLYMERS AND COPOLYMERS*** (FLEXIBLE & UNFILLED)	1.16 - 1.35	1500 - 3500	50 - 100A (SHORE)	0.15 - 0.75%	VARIES WITH STABILIZER	NONE	NONE TO SLIGHT	PLASTICIZED PVC ATTACKED
POLYVINYLIDENE FLUORIDE (KYNAR)	1.75 - 1.78	5500 - 7400	D80 (SHORE)	0.04%	NONE	NONE	ATTACKED BY FUMING H_2SO_4	NONE (PIGMENT OF RED KYNAR LEACHED)

NOTES: * 9% DROP @ 180°F, 3 DAYS UNDER STRESS
14% DROP @ 70°F, 7 DAYS

** UNPROTECTED MATERIALS CRAZE RAPIDLY: MUST USE BLACK OR COLORS FOR COMPLETE PROTECTION

*** HIGHER MOLECULAR WEIGHT, DEVOLATILIZED TOTAL COMPOUND PVC'S APPEAR MORE RESISTANT

**** FIBER SHOWED DEGRADATION AT POINTS OF STRESS WITHIN ONE MONTH

PLASTICS EVALUATED	SPECIFIC GRAVITY (D792) (ASTM TEST)	TENSILE STRENGTH (PSI) (D638) (ASTM TEST)	HARDNESS (ROCKWELL) (D785) (ASTM TEST)	% WATER ABSORPTION (D750) (ASTM TEST)	EFFECT OF SUNLIGHT	EFFECT OF WEAK ACID (D543) (ASTM TEST)	EFFECT OF STRONG ACID (D543) (ASTM TEST)	EFFECT OF AQUEOUS CHLORINE SOLN.
MOLDING METHYL METHACRYLATE (MMA) (LUCITE-PLEXIGLASS)	1.17 - 1.20	7000 - 11,000	M85 - M105	0.1 - 0.4%	NONE	NONE	ATTACKED BY HIGH CONCENTRATION OF OXIDIZING ACIDS	UNANNEALED BLISTERS MORE THAN ANNEALED
MMA STYRENE COPOLYMER	1.09	10,000	M75	0.15%	NONE	NONE	NONE	SOLUABLE IN CHLORINATED HYDROCARBONS
POLYPROPYLENES (UNMODIFIED)	0.902 - 0.910	4300 - 5500	R80 - 110	<0.01 - 0.03%	**	NONE	ATTACKED SLOWLY BY OXIDIZING ACIDS	NONE TO SLIGHT ATTACK IN HCl ACID IN 2 WEEKS ****
POLYPROPYLENES (COPOLYMER)	0.890 - 0.905	2900 - 4500	R50 - 96	<0.01 - 0.03%	**	NONE	ATTACKED SLOWLY BY OXIDIZING ACIDS	NONE TO SLIGHT ATTACK IN HCl ACID IN 2 WEEKS ****
POLYPROPYLENES (INERT - FILLED)	1.0 - 1.3	4500 - 8200	R94 - 100	.02 - 0.1%	**	NONE	ATTACKED SLOWLY BY OXIDIZING ACIDS	NONE TO SLIGHT ATTACK IN HCl ACID IN 2 WEEKS ****
POLYPROPYLENES (GLASS REINFORCED)	1.05 - 1.24	6000 - 14,500	R110	0.01 - 0.05%	**	NONE	ATTACKED SLOWLY BY OXIDIZING ACIDS	NONE TO SLIGHT ATTACK IN HCl ACID IN 2 WEEKS ****
POLYTETRA-FLUORINATED ETHYLENE - PTFE (TEFLON)	2.14 2.20	2000 - 5000	D50 - D55 (SHORE)	.00%	NONE	NONE	NONE	NONE (CURED TFE IS STABLE)
FLUORINATED ETHYLENE PROPYLENE (COPOLYMER TFE & HEXAFLUORO-PROPYLENE)	2.12 2.17	2700 - 3100	D60 - D65	<0.01%	NONE	NONE	NONE	NONE
ETHYLENE TRIFLUORO-ETHYLENE-ETFE (TEFLON TYPE)	1.7	6500	R50, D75	0.029%	NONE	NONE	NONE	NONE
ACETAL HOMO-POLYMER OF FORMALDEHYDE (DELRIN)	1.42	10,000	M94, R120	0.25%	CHALKS SLIGHTLY	RESISTS SOME	ATTACKED	COMPLETE DISSOLUTION IN 4 DAYS
POLYPHENYLENE SULFIDE - 40% GLASS FILLED (RYTON)	1.64	21,000	R123	0.01%	- - - -	NONE	ATTACKED SLOWLY BY OXIDIZING ACIDS	ORIGINAL DARK BROWN FADED TO YELLOW
PHENYLENE OXIDE BASED RESIN (NORYL - CARBON-FILLED-GLASS REINFORCED)	1.21 - 1.36	14,500 - 17,000	L106 - 108	0.06%	COLORS MAY FADE	NONE	NONE	BLISTERED (GROSSLY FADED - CARBON LEACHED OUT)

NOTES: * 9% DROP @ 180°F, 3 DAYS UNDER STRESS
14% DROP @ 70°F, 7 DAYS

** UNPROTECTED MATERIALS CRAZE RAPIDLY: MUST USE BLACK OR COLORS FOR COMPLETE PROTECTION

*** HIGHER MOLECULAR WEIGHT, DEVOLATILIZED TOTAL COMPOUND PVC'S APPEAR MORE RESISTANT

**** FIBER SHOWED DEGRADATION AT POINTS OF STRESS WITHIN ONE MONTH

PLASTICS EVALUATED	SPECIFIC GRAVITY (D792) (ASTM TEST)	TENSILE STRENGTH (PSI) (D638) (ASTM TEST)	HARDNESS (ROCKWELL) (D785) (ASTM TEST)	% WATER ABSORPTION (D750) (ASTM TEST)	EFFECT OF SUNLIGHT	EFFECT OF WEAK ACID (D543) (ASTM TEST)	EFFECT OF STRONG ACID (D543) (ASTM TEST)	EFFECT OF AQUEOUS CHLORINE SOLN.
POLYCARBONATE	1.2	8000 - 9500	M70-78 R115-125	0.15 - 0.18%	SLIGHT COLOR CHANGE AND EMBRITTLE-MENT	NONE	ATTACKED SLOWLY	BADLY BLISTERED AND DEGRADED (APPEARS UNSUIT-ABLE FOR USE IN $ZnCl_2$)
THERMOPLASTIC POLYESTER RESIN (NOT REINFORCED)	1.31 - 1.38	8200	M68, 78 85, 98	0.08 - 0.09%	DISCOLORS VERY SLIGHTLY	RESISTANT	ATTACKED BY OXIDIZING ACIDS	- - - -
THERMOPLASTIC POLYESTER RESIN (30% GLASS REINF)	1.52	17,000 - 19,000	M90	0.07 - 0.08%	COLORS MAY FADE	NONE	NONE	- - - -
THERMOSETTING CAST VINYL POLYESTER RESIN (RIGID)	1.10 - 1.46	6000 - 13,000	M70, M115 50-70 (BARCOL)	0.15 - 0.60%	YELLOWS SLIGHTLY	NONE	ATTACKED	MED. MOL. WT. COMPOUND ATTACKED. HIGH-ER WT. COMP. MORE STABLE
METHYL METHA-CRYLATE - CAST (HIGH IMPACT HACKENSACK)	- - - -	6500	M61	- - - -	SLIGHT	NONE	ATTACKED BY HIGH CONC. OF OXIDIZING ACIDS	BLISTERED
CeO_2 FILLED POLYTETRA-FLUORINATED ETHYLENE	———	———	———	———	———	———	———	NONE OBSERVED (AA ABSORPTION NOT POSSIBLE)
ZrO_2 FILLED POLYTETRA-FLUORINATED ETHYLENE	———	———	———	———	———	———	———	NONE OBSERVED (AA ABSORPTION NOT POSSIBLE)
CARBON-FILLED POLYTETRAFLUOR-INATED ETHYLENE (DIXON COMP.)	2.0 MIN.	ASTM D1457-69 1200 PSI	D65 (SHORE)	- - - -	- - - -	- - - -	- - - -	NONE
ETHYLENE CHLOROTRI-FLUOROETHYLENE (HALAR FILM)	1.68 - 1.69	7000	R95	0.01%	NONE	- - - -	- - - -	APPEARS STABLE
POLYIMIDE THERMOPLASTIC (ENVEX)	1.43	17,100	E99	0.3%	- - - -	RESISTANT	RESISTANT	- - - -
POLYIMIDE PTFE-FILLED (KAPTON)	1.42	5000	M115	0.6%	- - - -	RESISTANT	RESISTANT	EMBRITTLED
GRAPHITE-FILLED POLYIMIDE (FEURLON C)	1.45	5700	M110	0.2%	- - - -	RESISTANT	RESISTANT	NONE (NO GRAPHITE LEACHED OUT)

NOTES: * 9% DROP @ 180°F, 3 DAYS UNDER STRESS
14% DROP @ 70°F, 7 DAYS

** UNPROTECTED MATERIALS CRAZE RAPIDLY: MUST USE BLACK OR COLORS FOR COMPLETE PROTECTION

*** HIGHER MOLECULAR WEIGHT, DEVOLATILIZED TOTAL COMPOUND PVC'S APPEAR MORE RESISTANT

**** FIBER SHOWED DEGRADATION AT POINTS OF STRESS WITHIN ONE MONTH

Section 4

SINGLE CELL LIFE TESTING

INTRODUCTION AND SUMMARY

The major objective of single cell life testing is the determination of the usable life of zinc-chlorine cells operated under both peak shaving and mobile conditions. The information generated is expected to be applicable as much as possible to both applications.

The porous graphite chlorine electrode is the cell component whose life expectancy inherently is open to question. Permanency of the activation process is also suspect. Life data with porous graphite electrodes at elevated temperature is being accumulated with the 1.7 kWh battery which is now operating continuously with microprocessor control as described in Section 3 of Part II. Automated single cell cycling is a relatively simple exercise whereby operating time can be expeditiously accumulated on this and other system components. Although major emphasis is placed upon monitoring the chlorine electrode's voltaic performance with time, attention is also focused upon other system components (electrolyte, materials).

The current series of tests pertinent to the peak-shaving application were initiated in late 1975. Obviously, the cells utilized and test conditions employed reflect state of the art at that time. Operation at ambient temperature was therefore employed. This represents the most significant variance with present peak shaving methodology which involves operation at 50°C. Test cell design inherently precludes use at elevated temperature.

Voltaic performance is monitored routinely on a weekly basis. Cell polarization data generated on complete discharge cycles are of major significance to both the peak shaving and the mobile programs. The remainder of the time cells are cycled in the zinc on zinc mode (i.e. partial discharge). In this manner, operational life data relevant to both programs are obtained while allowing the simultaneous generation of additional information pertinent to the recharge capacity problem which exists for the mobile application. In addition, available electrical cycle control units are not amenable to dependable complete discharge operation, and indeed had

been fabricated for this cycling mode.

Current densities employed are lower than those presently employed. They are again a compromise dictated firstly by the paralleling of two programs, and secondly by characteristics of the test cell employed in that recharge capacity is reduced if higher charging currents were to be employed.

Of the four cells put onto test in 1975, two remain operational at the close of 1976. Their voltaic performance - as was that of the two discarded cells upon termination - remains at or slightly above their initial capability.

The two discontinued cells in no way represent chlorine electrode failure, but instead were caused by human error in attempting to rectify loss of electrical contact with the porous plate. New titanium contact bolts were unfortunately screwed in too far, cracking the electrode and making continued operation impossible.

EXPERIMENTAL

Description of Test Cell

The test cell employed was designed, fabricated and first tested in mid-1975 and reflects technology at that time. Although not of the more recent comb-design with its press-fit busing, it at that time represented our most dependable unit. For that reason it was selected for use in our initial phase of life testing cells with porous graphite electrodes.

A drawing of the "PCS"-type cell employed here is shown in Figure 3-1. Kynar is employed as the framework holding the electrodes. Massive titanium plates and tie-bolts bind the cell halves together. Sealing difficulties when encountered were overcome by using Teflon tape on the lands of the mating surfaces. Effect on the 80 mil gap by this requirement was negligible.

Titanium bolts threaded through the Kynar body halves are employed in making electrical contact with the two electrodes. On the porous chlorine side, four such bolts are harnessed together and carry current; the fifth is employed as a voltage probe. Although fewer bolt contacts are employed on the zinc side due to its massive nature and less demanding requirements, the configuration employed is equivalent. Current free voltage measurements without contact losses are thereby insured.

Various flow configurations of this type cell are available. In this study only the rear-feed flow-through version is employed.

Pre-Treatment (Activity Level) of Porous Test Electrodes

The four cells tested all employ PG-60 porous graphite chlorine electodes, but having widely different levels of activity due to distinctly different pre-treatment history and/or origin as detailed in Table 4-1. All the electrodes date back to late-1975, however.

Table 4-1

ORIGIN OF CHLORINE TEST ELECTRODES

Cell Designation	Source and/or Pretreatment of Chlorine Electrode	Testing Initiated
PCS-PC	Control; employed "as machined". Operated at low pH (0.1 - 0.4) exclusively.	August, 1975
PCS-HB	Activated electrode resulted from extended operation at high pH (1.5 - 2.5)	January, 1976
PCS-AFL	Activated electrochemically in nitric acid.	November, 1975
PCS-MH-2	Activated thermochemically in nitric acid (7 days).	December, 1975

The origin of the test electrode in cell PCS-PC is satisfactorily detailed in the table.

Cell PCS-HB was generated during an in-depth "Parametric Study" in mid-1975. Enhanced voltaic performance was observed for this cell - and others - after extended cycle testing at higher ("natural") pH. This effect indeed was the immediate precursor to and provided a "lead in" to our graphite activation program.

Cell PCS-AFL employed an electrode activated by the electrolytic nitric acid treatment described in Section 2 of this part. It was processed anodically at 93 mA/cm^2 for 2 - 5 hours in 50% by volume nitric acid. An electrolyte flow rate of 2 $ml/min/cm^2$ through the electrode was maintained during processing. Temperature was allowed to rise from ambient up to 40°C during the electrolysis period. Thorough, overnight flowing D.I. water rinsing of the assembled cell was employed prior to operation.

Cell PCS-MH-2 contains an electrode activated thermally in concentrated nitric acid for approximately seven days. It was rinsed as described above prior to cycle testing.

The Test System

The test system utilized in this study is similar to that shown in Figure 2-4 (see Section 2 of this part). Certain differences, however, are present. The heat-exchange bypass loop is not required since this study was done at ambient temperature. A second major variance is that a sintered glass filter (medium porosity; Corning No. 39580) is employed between the pump and flow meter. To avoid contamination, system materials are limited to Kynar, glass and Teflon. A gear pump (of Kynar) is fed from a glass/Kynar sump. Flow is monitored with a Brooks R-6-15-A flow meter, and is controlled by varying pump speed and/or by the glass-Teflon needle valve.

With single cells it is extremely difficult, if not impossible, to assemble a test system whose electrolyte volume is small enough to allow a realistic "swing" in $ZnCl_2$ concentration. For ease and dependability of operation 500 to 600 ml of electrolyte is required. The large volume desensitizes testing to moisture loss. Sump volume is also then sufficient to allow control of dissolved chlorine levels. On charge N_2 fed to a glass sparger is employed to remove chlorine from the electrolyte to the control point chosen; on discharge, cylinder chlorine is employed. Pneumatic valving (not shown in the figure) in conjunction with the cycle control unit automates the required switching of gas feed between charge and discharge.

Electrolyte

High purity zinc chloride electrolyte manufactured here at E.D.A. is employed exclusively. Adjustments in pH are made with A.C.S. Reagent Grade hydrochloric acid. Dilutions and water make-up are accomplished with triple-distilled water. Where noted, A.C.S. Reagent Grade potassium chloride is employed as supporting electrolyte.

Test Parameters

Control of certain test conditions while under continuous operation, primarily due to the "open loop" system configuration, is the source of some difficulty. Variances in electrolyte composition due to loss of H_2 and water vapor are unavoidable.

Control within the following limits is, however, practical (and sufficient):

- Electrolyte pH: 0.1 - 0.4; either manual on a daily basis, or HCl additions with a peristaltic pump/timer assembly.
- Electrolyte Specific Gravity: ±0.02 g/cc (depends upon electrolyte formulation). Control is either manual or automatic as described above.

As previously mentioned, no attempt is made to control temperature. Due to the relatively large electrolyte volume, cell heating can be ignored. Operational temperature is therefore that of the ambient environment (25-30°C).

During routine cycling charge and discharge current densities are respectively 20 and 30 mA/cm^2. Chlorine concentration dissolved in the electrolyte is maintained at 1 g/ℓ on charge, and 2 g/ℓ on discharge. An electrolyte flow rate of 2 $ml/min/cm^2$ is employed for both test modes.

An initial eight-hour charge under above conditions stores approximately 145 mAh/cm^2 of zinc. Partial discharge (30-75% of this amount) and zinc on zinc cycling is then initiated. Recharge capacity as a function of depth of discharge was being evaluated for the mobile application. Recharge capacity tends to steadily decrease due to the dendritic zinc morphology, eventually necessitating termination of the series with a complete discharge.

The cell polarization data employed in evaluating performance is taken on the next cycle. In this manner, conditions equivalent to a peak-shaving regime are insured.

The initial eight-hour charge and the final complete discharge require operator attention and are performed manually. Cycling, however, is controlled automatically by a MK-IV unit designed and assembled here at EDA. Besides controlling current, the unit switches the cell from charge to discharge - and vice versa. This switching occurs as follows:

- Charge to discharge
  - -- When a preselected charge (mAh/cm^2) is reached, or
  - -- When an undervoltage excursion occurs, indicating cell shorting due to dendrite formation.
- Discharge to charge
  - -- When a preselected discharge (mAh/cm^2) is reached, or
  - -- When a pre-set, abnormally low discharge voltage indicating shrinkage of the zinc plate area is seen.

The MK-IV control unit also automatically operates the system's pneumatic valving,

thereby switching between N_2 and Cl_2 feed to the sump and controlling the dissolved chlorine level in the electrolyte loop.

RESULTS AND DISCUSSION

Operational Time Accumulated Through 1976

Of the four test cells put into operation late in 1975, two are still in operation as 1976 closes. Operational ampere-hours/cm^2 accumulated (charge and discharge) are listed in Table 4-2. Variance in coulombic efficiency is

Table 4-2

ELECTROCHEMICAL OPERATIONAL TIME ACCUMULATED THROUGH 1976 ON TEST CELLS

CELL DESIGNATION	AMPERE HRS/cm^2 CHARGE	DISCHARGE	PRESENT STATUS
PCS-HB	73.3	53.6	On test
PCS-MH-2	51.5	38.3	On test
PCS-AFL	35.3	24.2	Retired
PCS-PC	46.5	33.5	Retired

primarily the result of zinc lost due to the dendritic nature of the recharge deposit during zinc on zinc cycling, and is of no significance to the peak-shaving application. Electrochemical working hours on the chlorine electrode are obviously not affected.

Since operational current densities are significantly lower than presently targeted for a peak shaving installation, correlation of these values with cycle life is difficult. Chlorine electrode life is indeed expected to be dependent upon operational voltage range, and hence these values are being generated under admittedly mild conditions.

If, however, the operational voltage range is ignored, an approximation of peak shaving cycles accumulated to date can be made. Using 0.2 ampere hrs/cm^2 as a full charge, PCS-HB can be considered to have accumulated 365 cycles to date.

The two cells retired during 1976 are not in any way indicative of electrode or cell failure, in that termination of operation was due to human error. When operated over long periods of time these PCS type cells developed contact problems.

The current carrying titanium bolts (usually on the chlorine side) were found to have corroded away, necessitating periodic clean-out of the threaded feed-throughs and replacement with new bolts. We now fully understand the condition, and have learned how to successfully accomplish the required repair. With the two retired cells, however, the chlorine electrodes were physically damaged - cracked - in attempting the repair, and as a result are no longer operational.

Debris is generated during operation, collecting on the filter. Although the filter is definitely darkened, the quantity of material is small. It has never necessitated replacement due to an increased pressure drop, or any significant increase in pumping pressure or throttle valve setting. Particles filtered are typically extremely small in size. The debris is considered to primarily be graphitic in nature, and the result of chlorine electrode corrosion.

Stability of Voltaic Performance

Zinc on zinc cycling as detailed above obviously does not provide the voltaic performance data necessary for a peak-shaving life evaluation. Polarization data was therefore taken weekly for each cell on its initial cycle after a complete discharge. In this manner its true performance on a complete-discharge peak-shaving regime was conveniently monitored.

Over the test period, voltaic performance either remained constant (PCS-PC, PCS-MH-2 and PCS-AFL) or improved (PCS-HB). Since performance does fluctuate with test temperature, data cited in the following discussion have been selected for 28-30° operation.

Cell PCS-PC provides a baseline in that the unactivated PG-60 electrode was cycled exclusively at low pH until accidentally cracked. Its voltaic performance remained essentially invariant, charging at 2.27-2.29V (45mA/cm^2) and discharging at 1.75-1.80V (40mA/cm^2). Sensitivity to temperature was more pronounced than with the other cells containing activated electrodes. On discharge especially, 5-8°C drop in temperature gave a 60-80mV penalty.

Cell PCS-AFL, also terminated due to accidental breakage, performed voltaically in the same stable manner but due to the pre-treatment activation, at a significantly higher level. At a current density of 40 mA/cm^2, a discharge voltage lying in the range of 1.87-1.89V was routinely recorded. Charge voltage at 30mA/cm^2 was typically 2.25V.

Cell PCS-MH-2 has performed similarly and is still operating. Initially 3 M $ZnCl_2$ was utilized as electrolyte; voltages were somewhat poorer than with the preceding cell. In the first quarter of 1976 operation with 2 M $ZnCl_2$ + KCl was substituted to allow generation of preliminary life data for the 20 kWh program. The resulting enhanced performance exhibited again similar repeatability. Voltages of 2.22-2.24 on charge at 45 mA/cm^2 and 1.93-1.96 on discharge at 40 mA/cm^2 were obtained for the remainder of the year.

The remaining cell, PCS-HB has for some as yet undetermined reason behaved differently. Over the test period its performance has increased significantly:

Charge, 45mA/cm^2: 2.27 V initial, decreased to 2.24-2.25 V

Discharge, 40mA/cm^2: 1.83-1.85 V initial, increased to 1.93-1.95 V

As detailed in the experimental section, this PG-60 electrode was received in a partially activated state and is the result of higher, natural pH cycle testing.

Performance of Kynar over Extended Periods

No deterioration of the Kynar cell body or spacer has been observed to date by visual inspection. With time, sealing of the assemblies has become more difficult, but this appears to be due to cold-flow and warpage of the plastic. The cell design leads to just such a problem.

CONCLUSIONS

- Extended life of the PG-60 graphite chlorine electrode material has been demonstrated. Test conditions are less severe than presently envisioned, representing previous cell technology, conditions and capabilities.
- Activated electrodes have shown stable, invariant voltaic performance over the testing period. No losses whatsoever have been observed.
- In a like manner the performance of an untreated electrode also remained constant. Electrode stability in the pH range employed has therefore been demonstrated through approximately 365 cycles.

RECOMMENDATIONS

- Cycle testing must be updated to reflect current peak-shaving conditions which are more severe and may have an adverse effect on the life of porous graphite electrodes.
- The potential for a meaningful accelerated life test should be explored. This should be done in parallel with a detailed evaluation of potential failure mechanisms.

- Presently ongoing tests should continue uninterrupted. The addition of temperature control should be considered to allow more straightforward interpretation of data.

PART III

ZINC CHLORINE BATTERY SYSTEMS

BUILT AND TESTED IN 1976

Section 1

BASIC CELL AND BATTERY CONCEPTS

The zinc-chloride battery concept as it is being applied by EDA for peak-shaving applications is based upon the electrochemical reaction between zinc, chlorine, and aqueous zinc chloride solution, and the simultaneous chemical reaction between chlorine and water. The reactions are illustrated in Fig. 1-1, and both reactions are highly reversible. The emf of a zinc-chlorine cell under standard conditions is 2.12 V corresponding to a free energy of reaction of 97.9 kcal/mole. It must be emphasized that the active materials come from and are returned to the electrolyte during cycling. This is opposite to the general concept prevailing in alkaline battery systems wherein the active materials are localized at the electrode surface as insoluble materials.

$$ZnCl_2(aq) = Zn(s) + Cl_2(g)$$

$$Cl_2(g) + xH_2O = Cl_2 \cdot xH_2O(s)$$

Figure 1-1. Cell and store reactions during battery charging. The value of x, which is dependent on experimental conditions, can be as low as 5.9.

The sequences of reactions occurring in the system during charge and discharge are illustrated in Figure 1-1. The cells are buildt in a completely uncharged state with both the positive and negative electrodes being simply current collectors and there are no separators in the cells. In essence, during the charging step, the zinc-chloride electrolyte is electrolyzed yielding a uniform deposit of zinc on an inert graphite electrode. Inefficiencies in charge arise from voltaic losses and from coulombic losses due to recombination of zinc with small requirement for heat exchange during charge. The chlorine gas is removed from the cell and is passed to another chamber where it is mixed with water at approximately 10°C and chlorine hydrate is formed. The heat of formation of chlorine hydrate (18 kcal/mole) must be removed from the hydrate as it forms in charge. At ambient pressure (at which it is intended to operate the chlorine hydrate chamber) this heat must be removed by means of a refrigerator. The energy

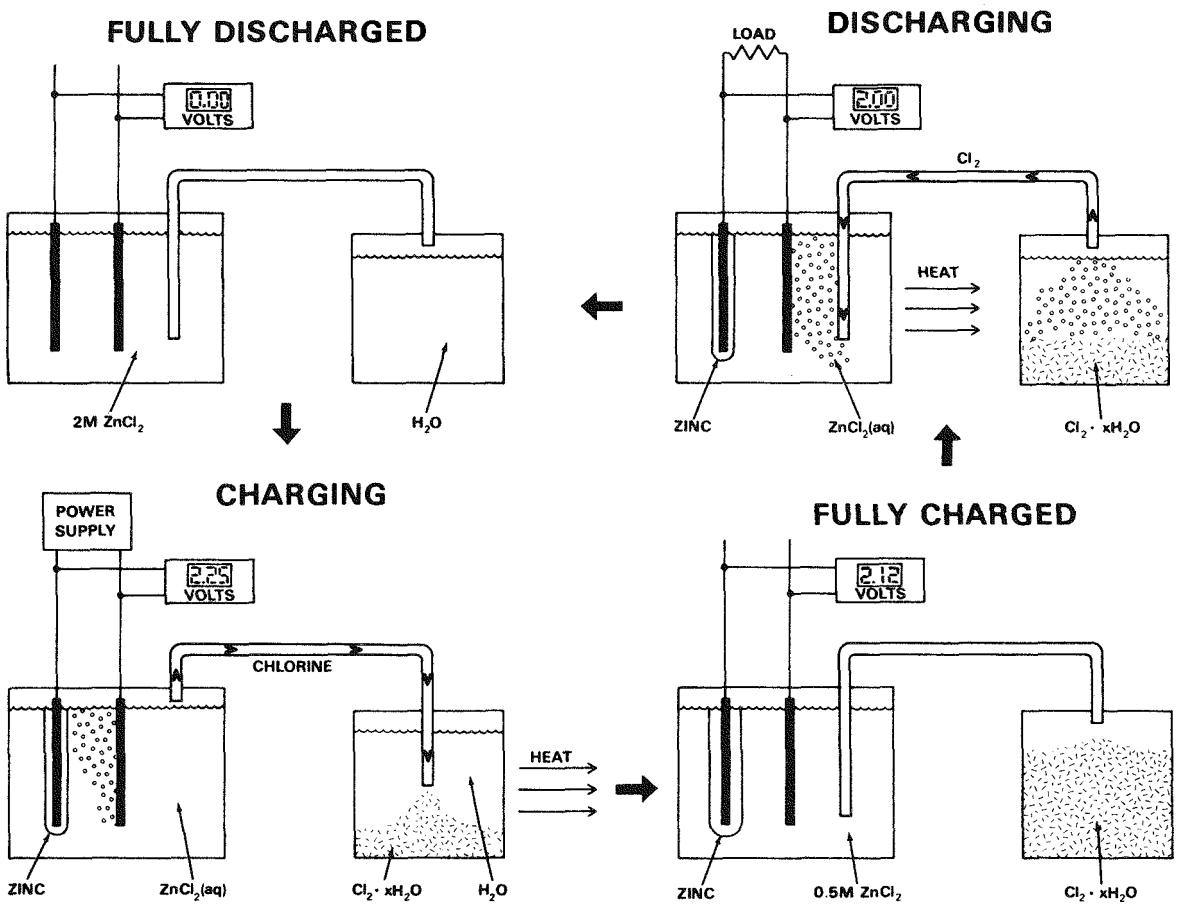

Figure 1-2. Schematic showing sequence of events in the charge and discharge of a zinc-chlorine cell. Note use of inert graphite substrates, water for hydrate formation, and stack heat for hydrate decomposition during discharge.

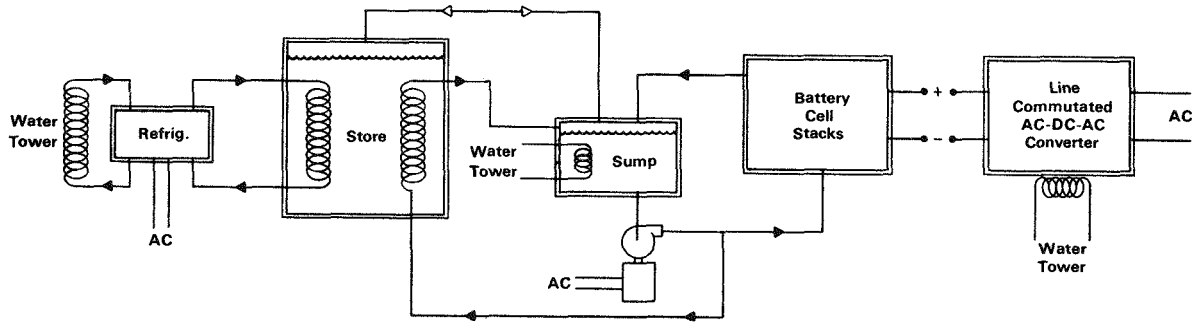

Figure 1-3. Flow schematic for a zinc-chlorine load-leveling battery plant.

consumption of the refrigerator represents a charging inefficiency for the battery. The charge is terminated when the concentration of zinc chloride in the cell reaches about 0.5 M.

During charged-stand, chlorine forms very slowly from chlorine hydrate contained in a well-insulated chamber, and no refrigeration is required. Chlorine dissolved in the electrolyte at the end of charge migrates to the zinc electrode and is consumed. After approximately an hour, the voltage of a cell drops from 2.12 V to almost zero. Charged-stand losses are thus minimized.

To initiate discharge, the store is heated by the exchange of heat between the warm stack electrolyte (40-50°C) and the chlorine hydrate-water mixture in the store (see Fig. 1-2). Chlorine is, therby, evolved at the desired rate by decomposition of the hydrate. The chlorine is mixed with electrolyte and chlorine-saturated electrolyte is passed through the porous positive electrode and is consumed electrochemically as zinc dissolves at the negative electrode. During discharge, the coulombic inefficiency is less than during charge since chlorine is removed from the electrolyte by electrochemical reaction before it reaches the zinc. The heat due to discharge inefficiencies plus that due to ΔQ (see above) are counteracted by the heat of decomposition of the chlorine hydrate. This greatly reduces the heat exchanger requirement in discharge. The battery is fully discharged when all the zinc is dissolved. In peak-shaving applications, it is intended to completely discharge zinc-chlorine batteries before they are recharged.

The overall battery system efficiency is determined by inefficiencies in the battery stack and by the energy consumed by auxiliaries. In addition to the refrigerator, pumps are required in the system to transfer chlorine between the cell stacks and the chlorine hydrate stores and to carry chlorine-saturated electrolyte to the positive electrodes during discharge. The overall system schematic is shown in Fig. 1-3. It has been found beneficial to operate the electrolyte pump at about the same rate in charge and discharge.

Section 2

THE 1.4 kWh BATTERY SYSTEM AND CONTROLLER

INTRODUCTION

The 1.4 kWh system in many ways represents a continuation of the 1975 EDA-EPRI program. The ruthenized titanium chlorine electrodes contained in the 1975 1.0 kWh battery are presently undergoing life testing in the 1.4 kWh system. Because it is generally believed that the chlorine electrode is the life limiting factor in the zinc-chlorine battery, the acquisition of data demonstrating adequate electrode life for peak shaving applications is of considerable importance.

The design and cost study on the 1975 system indicated the mechanical chlorine desorber was too costly for commercial systems. The removal of this desorber resulted in a potentially large loss in the battery's electrochemical energy efficiency. Much of this energy loss was never realized due to changes in the operating conditions of the battery. These changes may be summarized as follows:

- Sodium chloride is added to the electrolyte to reduce chlorine solubility. This is to improve the coulombic efficiency of the zinc electrode during charge. Sodium chloride was not used in the 1975 battery.
- The electrolyte temperature is 40°C in the 1976 battery as compared to 30°C in the 1975 battery. This increases the electrolyte conductivity and somewhat reduces the chlorine solubility.
- The charging current density in the 1975 program was 33 mA/cm^2. The current density on charge for the 1976 battery is 37 mA/cm^2. This helps to increase the coulombic efficiency.
- The charge time is increased from 4 hours in 1975 to 5 hours in 1976. This increases the battery capacity with no increase in electrode area.

The net result of these changes is that the 1976 battery delivers 1.4 kWh of energy at 67% electrochemical energy efficiency while the 1975 battery delivered 1.1 kWh of energy at 74% electrochemical energy efficiency.

The battery system has also undergone many changes when contrasted to the 1975 system. As already mentioned, the mechanical desorber has been eliminated. Other

changes include the installation of a H_2-Cl_2 recombination loop, the use of chlorine injection into the electrolyte during discharge, and more control devices so that the system could be automated. This system represents EDA's first attempt to fully automate a system with a hard wired logic controller. As a test system for automation, further changes in the system may be expected as improvements become available.

The following sections begin with a physical description of the 1.4 kWh battery system followed by a description of the system operation through a complete cycle. After that, the logic controller is discussed in some detail. Finally, the results of the testing program are presented. These results are compared to the program objectives which consist of: electrode life evaluation; automation of the zinc-chlorine battery system; and the evaluation of battery performance for peak shaving applications.

1.4 kWh SYSTEM DESCRIPTION

The electrode array contained in the 1.4 kWh system is shown in Figure 2-1. The Lucite framing at the bottom of the electrodes also contains holes which serve as the electrolyte manifold system. This manifold arrangement is very similar to that contained in the 1975 system. The electrolyte is fed into a plenum chamber which lies directly below the manifold plate.

The chlorine electrodes consist of two rectangular plates of ruthenized porous titanium which are spot welded to the center titanium post. Four of these electrodes are then connected together by means of titanium spacers, threaded rod and nuts as shown in the figure. These four electrodes are then connected to the titanium clad copper bus with a compression clamp. The bus extends the length of the electrode array and finally through the chassis wall for the main power connection.

The zinc electrodes are dimensionally identical to those in the 1975 system. Power connections to the electrodes are made by screwing titanium bolts into the 6-32 tap holes provided in the electrodes. These screws extend through the wall of the chassis for the external power connections. Externally, the four screws are electrically tied together with a piece of copper strip. A four inch length of #14 stranded copper wire is soldered to this strip and provides the electrical connection to the main zinc bus. This length of wire serves as a shunt and by measuring the IR drop through it, the approximate current passing through the zinc electrode may be obtained. From these shunt measurements, then, current sharing among the electrodes in the battery may be evaluated.

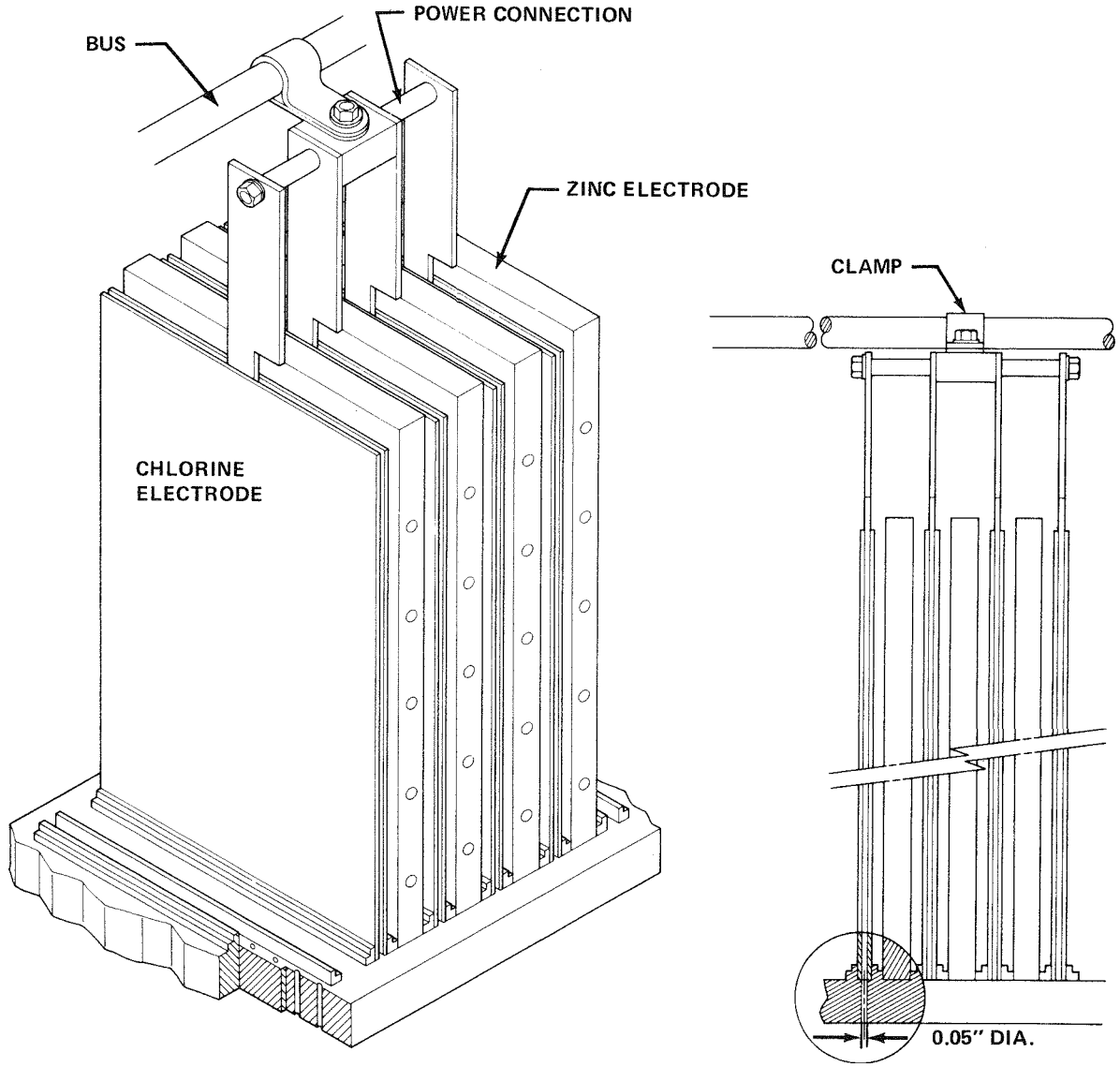

Figure 2-1. Electrode Arrangement in the 1.4 kWh Battery. The ruthenized-titanium electrodes are electrically connected in groups of four and clamped to the bus.

The electrolyte loop is shown in Figure 2-2. The electrolyte enters the pump, passes through a 10 micron filter, through a heat exchanger which maintains isothermal operation and then to the plenum chamber. The plenum chamber maintains a constant pressure head so that the electrolyte is uniformly distributed to the chlorine electrodes through the manifold. After the electrolyte passes through the chlorine electrodes into the cell gap, it flows in an upward direction and is returned to the sump through exit holes in the battery compartment wall.

The valve which admits chlorine into the inlet of the main electrolyte pump is preset so that very little chlorine is admitted when the pump is operating at low speed on charge. The pump is operated at a higher speed on discharge and the pressure drop at the pump inlet is then large enough so that adequate chlorine is drawn into the pump for the discharge cycle.

The hydrogen-chlorine reactor loop is shown in Figure 2-3. A liquid sealed gear pump is used to continuously circulate the gas space in the battery. From the pump outlet, the gas enters a chamber which contains two ultra-violet lights. The action of ultra-violet light on chlorine gas generates monatomic chlorine which reacts with hydrogen to form hydrogen chloride. After passing through the reaction

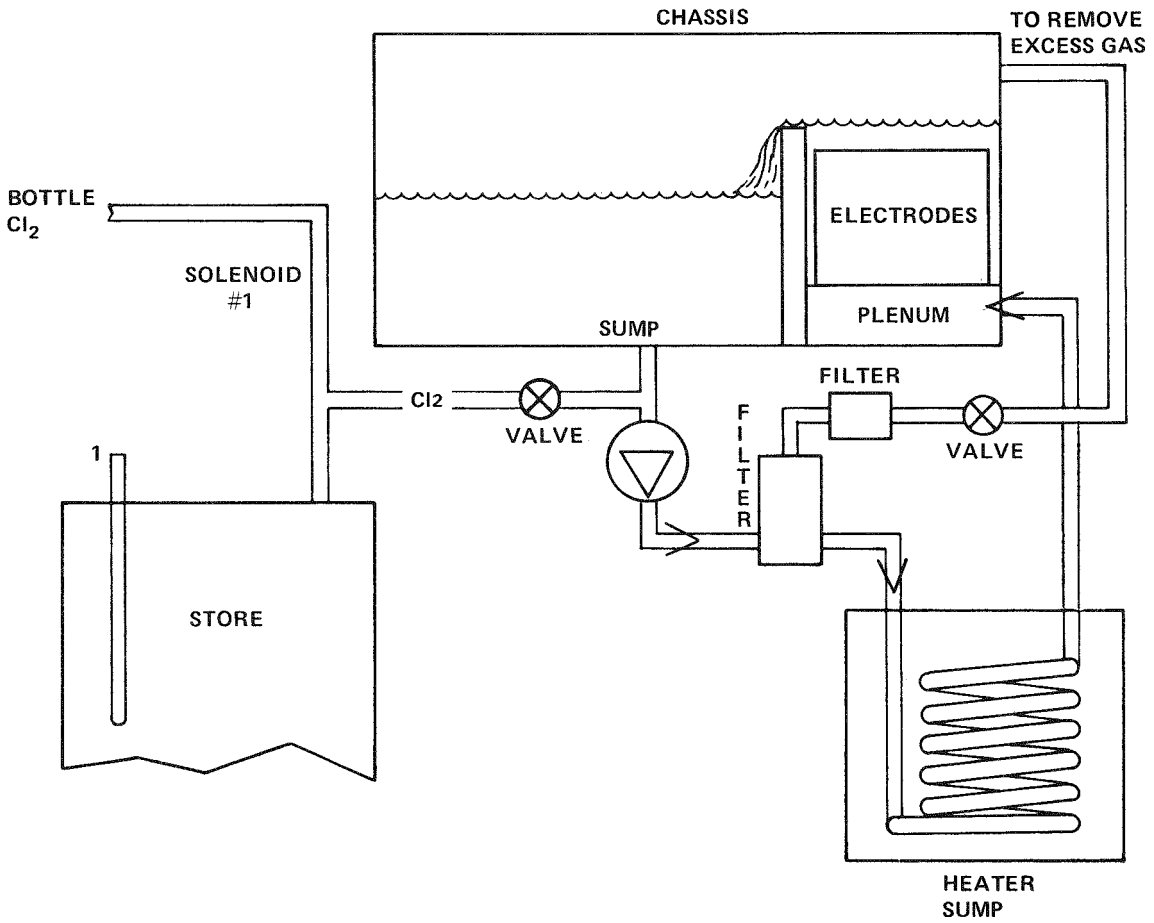

Figure 2-2. Electrolyte Flow Diagram for the 1.4 kWh System.

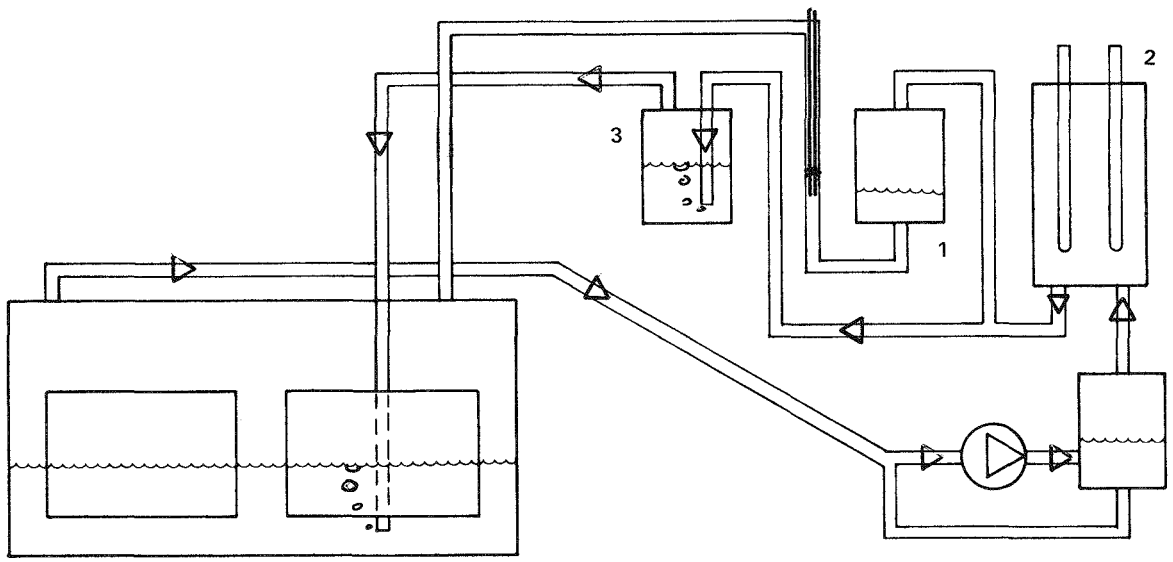

1 GAS PUMP SENSOR FOR FAILURE

2 U.V. LIGHTS

3 SCRUBBER

Figure 2-3. Hydrogen-Chlorine Recombination System. The system uses ultra violet light to initiate the reaction between hydrogen and chlorine to form hydrogen chloride.

chamber, the gas is returned to the battery through the scrubber. This system maintains the hydrogen at a very low level and therefore prevents a buildup of hydrogen in the system.

The failure sensor consists of a differential manometer with two electrical contact wires placed in the high pressure side of the manometer. The height of these wires is adjusted so that electrical contact is maintained through the conducting liquid in the manometer. If the recirculation loop fails, the liquid level drops and electrical contact between the two wires is broken which transmits a signal indicating the failure of the loop.

The store, which consists of a cold water reservoir and a mechanism to intimately mix the chlorine gas with the water, is shown in Figure 2-4. The heat of formation of chlorine hydrate is removed from the store by use of a heat exchanger, thermally controlled pump and the refrigeration unit. The pump is turned on and off by a thermal sensor located in the store. The refrigeration loop is operated during the charge cycle only.

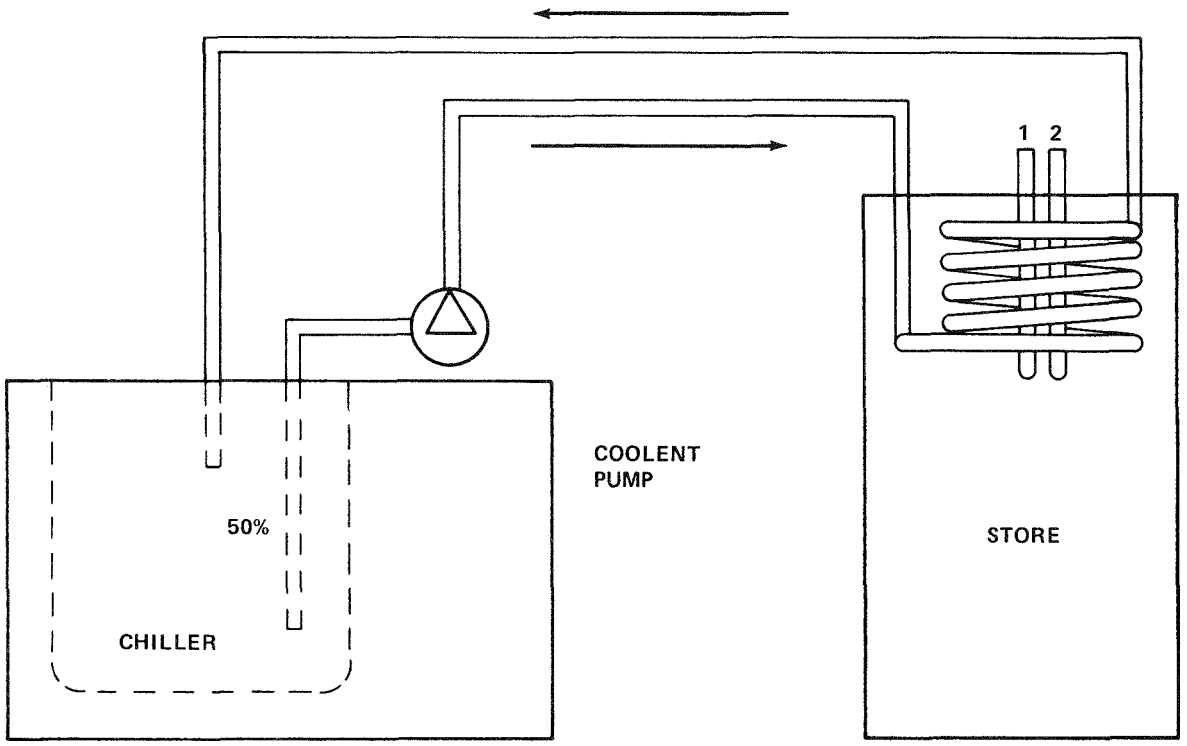

1 THERMOCOUPLE TO CONTROL COOLENT PUMP MOTOR

2 THERMOCOUPLE TO CONTROL SOLENOID #1 TO SUPPLY AUX. Cl_2

Figure 2-4. Chlorine Storage System used in the 1.4 kWh Battery System.

The gas space in the zinc chlorine battery acts as the connecting medium for all the components. This interconnecting loop is shown in Figure 2-5. On charge the chlorine generated in the battery is drawn into the store through the inlet tube. The agitator is located near the inlet tube and disperses the chlorine in the water to hasten the formation of chlorine hydrate. The heating element, labeled 3 in the figure, prevents the inlet tube from becoming blocked during the charge cycle. Pressure sensor number one serves to control the vent pump. If the store should become pressurized, the liquid sealed gear pump turns on and pumps the chlorine gas

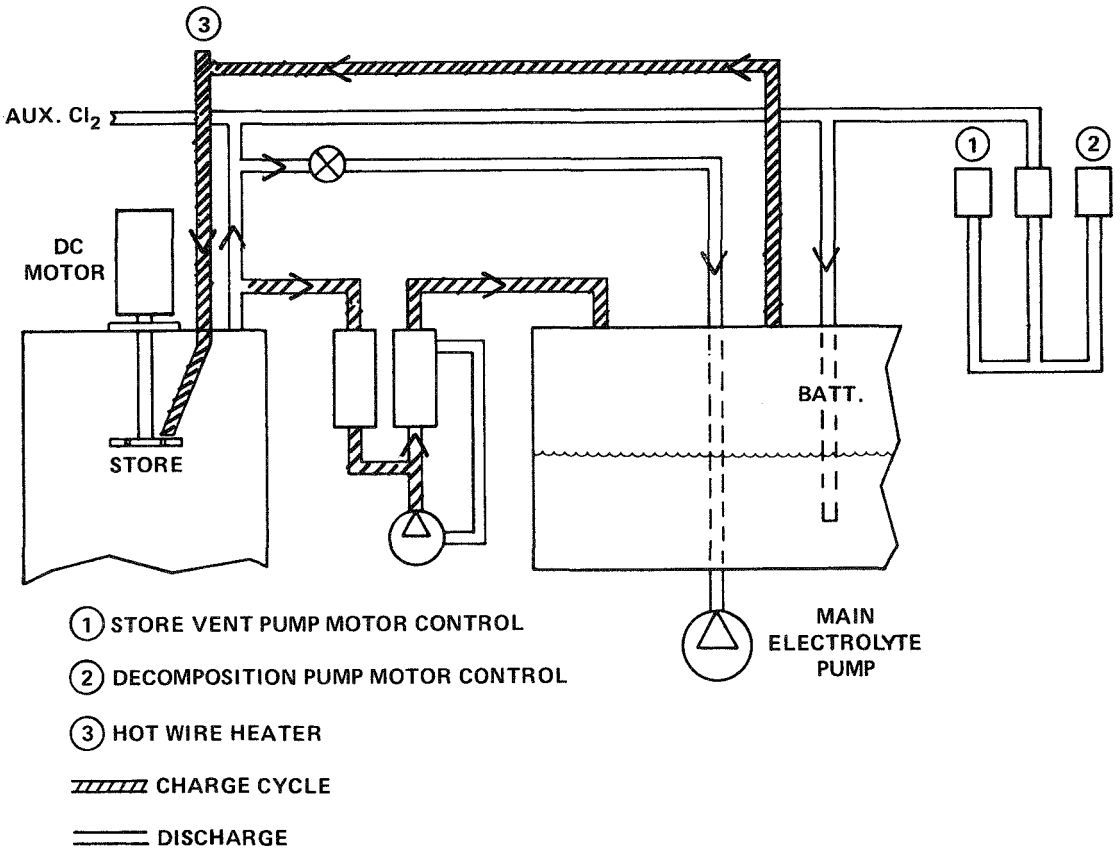

Figure 2-5. Gas Space Interfacing of Store and Battery. The phase of the battery cycle determines the flow path of the chlorine gas.

from the store to the battery. This eliminates venting from the store and increases the reliability of the system by permitting some recirculation of the chlorine on the charge cycle. The vent pump is inoperative during the discharge cycle.

On discharge, heat is added to the store in a manner so that the rate of chlorine release from the store is closely matched to the chlorine consumption rate in the battery. This is achieved by using a pressure switch located in the store. This control is labeled number 1 in Figure 2-6. Heat is added to the store by the decomposition loop shown in Figure 2-6. When the store pressure drops below a preset value, the pump is turned on to decompose more hydrate. The pump is turned off when the pressure in the store reaches preset upper limit.

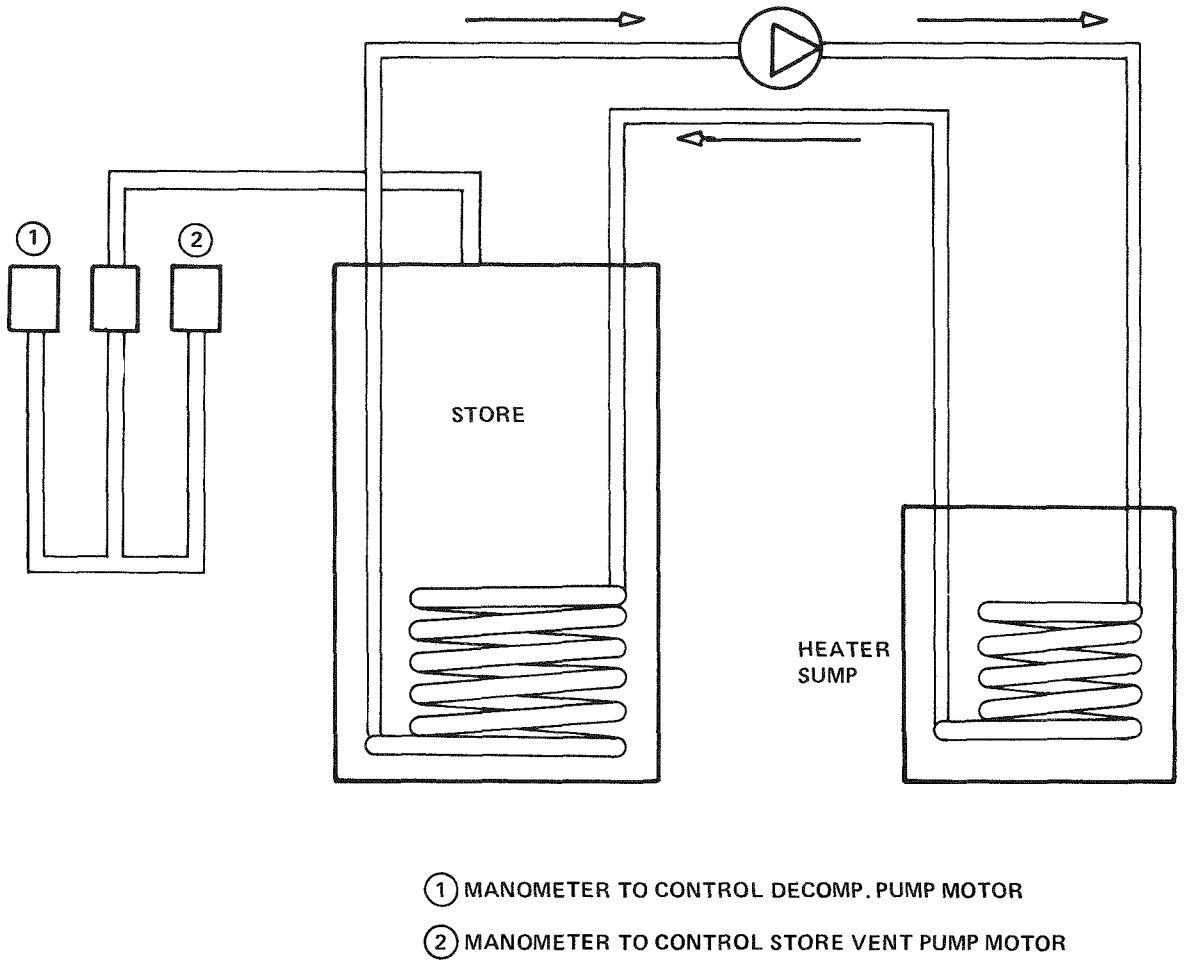

Figure 2-6. Heat Exchanger Used to Release Chlorine From the Store During Discharge. The pump is controlled by the sensor contained in manometer number one.

The interfacing of the components to form a complete battery system is shown in Figure 2-7. Included in this figure but not shown in the component drawings is the carbonate addition loop. This loop adds a fixed volume of alkali carbonate contained between the two solonoids prior to the discharge of the battery. This predetermined volume adjusts the pH of the electrolyte to about pH=2. This loop is necessary due to the pH sensitivity of the ruthenized titanium electrodes (see Part II, Section 1) in the discharge cycle.

The battery charges at 180 amps ($37mA/cm^2$) for five hours. The 900 ampere hour charge requires about sixteen mols of zinc chloride, or twelve liters of electrolyte. The constant current portion of the discharge is at 160 amps ($33mA/cm^2$). The battery nominally delivers 1.4 kWh of energy.

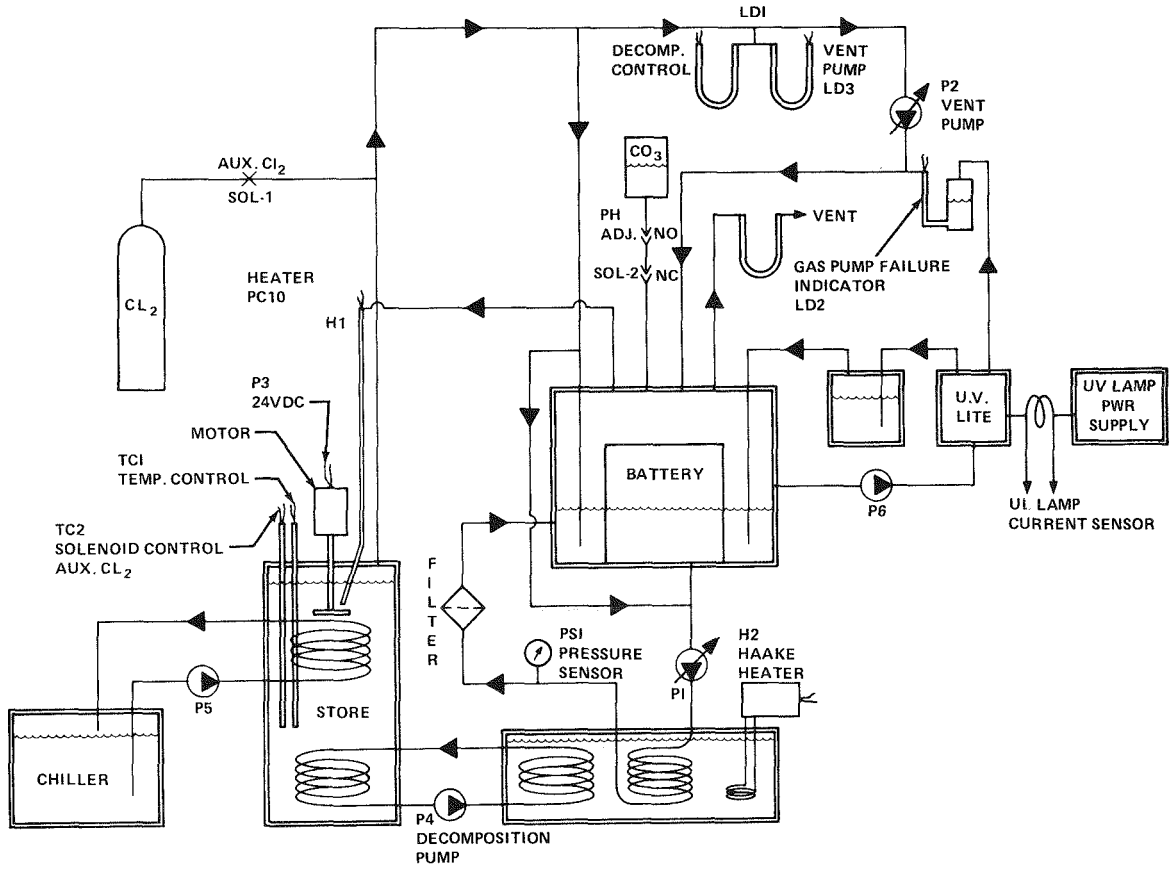

1.4 KWh TITANIUM BATTERY SCHEMATIC

P1	–	ELECTROLYTE PUMP	H1	–	INLET HEATER
P2	–	VENT PUMP	H2	–	SUMP HEATER
P3	–	AGITATOR MOTOR	LD1, LD2	–	GAS PRESSURE DETECTOR
P4	–	DECOMPOSITION PUMP	LD3	–	UV LOOP GAS PRESSURE DET.
P5	–	COOLANT PUMP	TC1	–	STORE TEMP .
P6	–	UV GAS LOOP	LD3	–	UV LOOP GAS PRESSURE DET.
PSI	–	ELECTROLYTE PRESSURE SENSOR	TC1	–	STORE TEMP.
SOL-1	–	AUXILIARY CHLORINE SOLENOID	TC2	–	STORE TEMP. (SOL-1 CONTROL)
SOL-2	–	PH ADJUST SOLENOID	TC3	–	STACK TEMP.

Figure 2-7. Detailed Schematic of the 1.4 kWh System.

AUTOMATION AND LOGIC CONTROLLER

Introduction

This section describes the automatic control and data acquisition system which has been applied to the 1.4 kWh titanium battery. The primary task was to provide the necessary circuitry to step the battery through a predetermined test profile. This included control of the test cycle and the various battery auxiliaries. The second, but equally important, requirement was to provide the monitoring and logic necessary to protect the battery from damage due to the failure of either a battery component or an auxiliary function. A third task was to provide for the logging of various battery data in a form that would allow immediate access and long term data analysis.

The battery control consists of a hardwired logic circuit. The circuit input consists of information input from voltage comparaters, timers and analog to digital converters. Control of the various auxiliaries is organized by a series of "phase" signals used by interface circuitry to identify ON and OFF conditions for battery pumps, solenoid, timing signals and other peripheral circuitry.

The phase signals identify portions of the test profile. Cooldown, charge, and discharge are examples of some of the test profile phases. Accordingly certain auxiliaries are on during charge, off during discharge. The auxiliary functions themselves are controlled by an appropriate drive circuit. A pump is controlled by a phase control, a solenoid by a switch, etc. The hardware for these functions is divided into two parts; a logic panel and a control panel. These panels are mounted in a single enclosure with information readout display and manual controls and switches available on the front panel. Details of these panels are contained in the body of this report.

Battery failure monitoring and safety control is provided by another series of control and monitor circuitry. Control to this function is a logic circuit which uses the output from various monitor circuits to determine that a failure is imminent.

If a component has failed or a parameter such as voltage indicates that there is faulty battery operation, a signal is sent to the main control circuit to terminate the test cycle. At the same time a visual indicator on the front panel identifies the parameter which is out of a safe operating range.

Recording of data during a battery test is accomplished by a data acquisition and logging system which was previously built for use in battery testing. The system is comprised of a voltmeter, control circuit, data point selector switches, a BCD to ASCII converter and a teletypewriter. A maximum of 48 separate data points may be monitored and recorded. The teletypewriter includes a paper tape punch for use in off-line data analysis.

Automation Sequence and Controller Description

The battery test profile describes the orderly sequence of events that occur during the charge and discharge cycle of the battery. The flow chart in figure 2-8 graphically indicates the sequence of events, the decision points and the auxiliary operations which take place during a cycle.

The sequence is divided into eight parts or phases. Each phase determines a set of conditions under which the battery and auxiliaries operate. A front panel pushbutton starts the cycle by forcing the controller into the cooldown phase in this mode. The battery store is cooled to the proper temperature range at which hydrate will form. Upon cooling down to this preset temperature, the controller then switches into the charge phase. Here a constant charge current is maintained for a specified period of time. The charge current is preset by means of a control potentiometer on the front panel. Elapsed time and ampere minutes of charge are displayed by LED readouts on the front panel.

At the end of the charge the test goes to a timed turnaround phase where the bat- is prepared for discharge. The controller then proceeds to the polarize phase. The main electrolyte pump is turned off and the rectifier is turned on to approximately one half normal. The battery voltage drops toward a low limit voltage due to lack of chlorine. At the limit, the main electrolyte pump is turned on to a predetermined speed. After a short delay, the controller switches to constant current discharge and the rectifier current is increased to its normal discharge current.

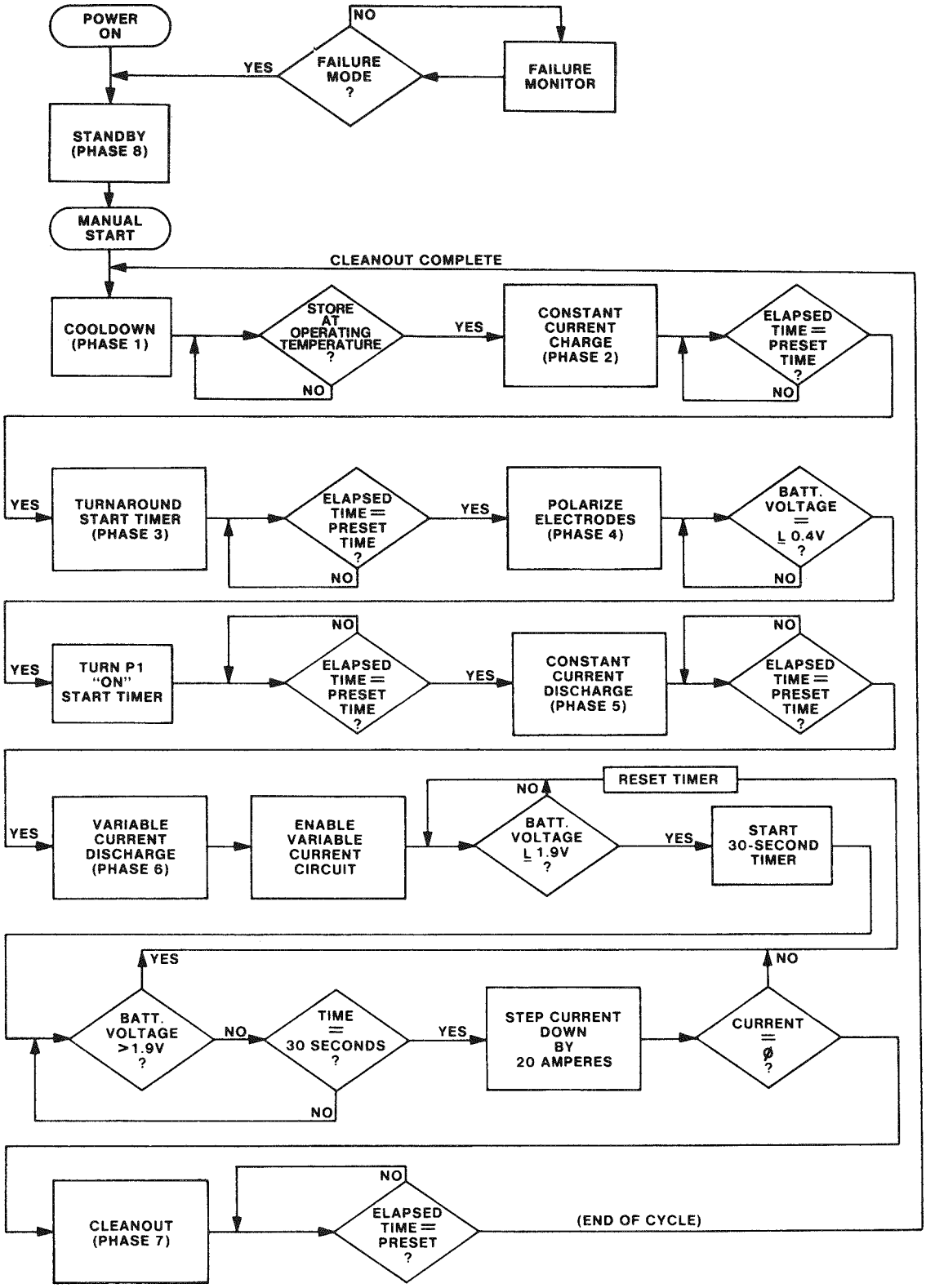

Figure 2-8. Flow Chart of Logic Sequence Used to Cycle 1.4 kWh System. Cycle phases and decision points are shown in the diagram.

The constant discharge is a timed phase which normally discharges half the capacity. At that time the controller shifts to a "variable voltage" phase. The battery continues to discharge at a constant current until it approaches the end of useful capacity where its voltage begins to drop off. A part of the control circuitry senses the change and begins a programmed decrease in discharge currents. This current is decreased in 20 ampere steps to maintain the battery voltage above a preset limit. End of discharge is assumed when the current makes the last step to zero.

The final phase of the cycle is "cleanout". Most auxiliaries are turned off with exception of the main electrolyte pump. A resistor is switched across the battery terminals and remaining zinc stripped from the electrodes. At the end of this timed phase, test returns to cooldown to begin a new cycle.

The logic controller makes its decisions based on various inputs from the battery and from peripheral control circuits associated with the control logic. Voltage and current signals are received by way of amplifiers and level detecting comparators. Timing of cycle phases such as Constant Current Charge is accomplished by a series of presettable counters.

Time of the Charge, Turnaround, Discharge and Cleanout phases is set and controlled by a counter in conjunction with a series of preset switches. The counter is a three stage binary coded decimal circuit. The BCD output is decoded to a decimal output representing hours and minutes. A clock circuit synchronized from the 60Hz line frequency produces a pulse signal to increment the counter by minutes. Four pair of decimal switches, one pair for each timed phase, are connected to the counter such that by closing the proper switches the counter output sets a latch at the desired preset time. The latch outputs then signal the control logic that the current phase should be terminated. The time counter and latches receive reset signals from the control logic which also determines which time signal to recognize. The counter also serves the anciliary function of displaying the driven seven segment light emitting diodedisplays which indicate elapsedtime in hours and minutes.

A battery current signal is used by the controller to prevent switching the rectifier from the charge to the discharge mode before the current has dropped to zero. The current signal is also used by failure detection logic and the ampere time counter. A current signal supplied by a 50 millivolt shunt is amplified and converted to a pulse frequency.

The frequency is directly proportional to current. The current amplifier circuit which is common with the rectifier and battery ground is electrically isolated from the logic circuit by an opto-isolator. Pulses from the amplifier are transmitted thru the opto-isolator and converter back to electrical signals by the opto-isolator. The pulses are then scaled and accumulated in a counter which displays the count as ampere minutes on the front panel light emitting diode display. The current pulse signal is also input to a missing pulse detector. If the pulse rate drops low, indicating a low current, the detector presents a low signal to the Control and Failure logic circuits.

Battery voltage is monitored for control of the Variable Discharge phase and for overvoltage and undervoltage failure detection. The circuit consists of an input filter and buffer amplifier and three voltage comparators. The filtered battery voltage is continuously compared against a voltage reference which is set by seperate adjustment potentiometers on the circuit board. The potentiometers and test points are accessed thru the hinged front panel. Detection of a low (or high) voltage results in a level change at the comparators output. The level change is transmitted thru opto-isolators to the control and failure logic.

Temperatures are monitored by means of thermocouples at the battery. Thermocouple amplifiers provide a voltage which is proportional to the temperature to comparators which can sense a preset limit. The limit signals are sent to the control logic, failure logic or, in the case of a pump or solenoid, a power driver.

A store temperature limit signal is sent to the control logic to signal the end of the cooldown phase. A second store temperature limit signal is sent to a solenoid (sol-1) to control auxiliary tank chlorine. Store high and low limits and sump temperature limit signals are sent to the failure detect logic. Each of these limits are separately adjustable by means of a potentiometer adjustment on the front panel of the temperature control panel. An analogue panel meter gives a continous indication of store and sump temperature.

Certain battery pressure indicators are needed to operate various auxiliaries and the failure logic. The pressures are in the range of plus and minus 10 to 20 inches of water. These pressures are measured by means of level detectors situated in water manometers. The level detectors are one or two point (2 or 3 wire) contacting type. The wires are immersed in the leg of a manometer. One of the wires is a source for a 1000 Hz low voltage signal. The second and/or third wire acts as a pickup for the signal.

The wires are positioned in the open leg of a manometer such that pressure on the manometer raises the liquid level to the wires and completes the circuit between source and pickup. The level detector circuitry sees the closed circuit and closes a relay or sets a latch. As the pressure on the manometer decreases, the liquid level falls below the wires, causing the relay to open or the latch to reset. In the case where hysteresis is desired, the three wire detector is used. The common and low level wires are positioned at the low pressure point in the manometer. The high level contact is positioned some distance above at the high pressure points. As the level rises above the high wires, the signaling relay is caused to close. As the manometer pressure and liquid level fall, the relay remains closed until the level falls below the lower contacts. The relay then opens. When the pressure again rises, the relay remains closed until the high contact is reached. This action prevents the rapid on/off cycling which might occur if the single point detector were used to control a pump or solenoid.

Three level detectors are used in the system. Two units, LD1 and LP3, detect store pressure. These are three wire (two point) types and control the decomposition pump and the store vent pump. The third unit, LD2, is a single point detector. This unit detects pressure across the U.V. gas loop pump to indicate a failure in the gas burning loop.

The U.V. lamp detector is a safety monitor input to the failure detector circuit. If the U.V. lamps in the gas burning system should burn out or otherwise fail, the battery test should be terminated. Failure of the lamps is detected by monitoring the loop supply current by means of a current transformer and amplifier. If the lamps burn out the supply current is reduced: if the lamps or supply should short circuit, a fuse will blow out and open the supply circuit. In either case the current transformer and amplifier detect the change and send a signal to the failure monitor logic.

The control logic can be broken down into two parts. The first part controls the cycle and the second part consists of logic designed to implement on-off action of the various auxiliaries.

The responsibility of the control logic is to step the battery thru the test cycle in response to timing and limit signals, and give commands to peripherals and output interfaces. It steps thru the cycle by making logical decisions based on inputs and sequentially sets and resets a series of latches representing the phase of the cycle.

Lamps on the control panel are driven on by the latches and indicate the current state of the cycle.

The latch output are used by the auxiliary control logic to determine whether or not a battery auxiliary should be activated. The output circuitry, the second part of the control, logically combines state of cycle outputs of the latches with temperature and pressure inputs to provide on-off signals to auxiliaries. There is a control path for each auxiliary. For instance, the decomposition pump is activated in all phases of the cycle except cooldown and charge. It is ON in these phases only if store pressure is low. Therefore a logic circuit combines the proper signals. If they are all true, the circuit output signals the pump driver and the pump is turned on. Similarly, logic signals are combined to operate the remaining controlled functions.

Battery - Controller Interfacing

The battery auxiliaries that require control or modulation during the test cycle are interfaced to the control logic by means of an appropriate driver circuit. These may be static switches, relays, adjustable controls or analogue circuits. The following is a list of the auxiliaries, their control inputs and description of the on-off requirements. All auxiliaries are equipped with a manual over ride switch on the front panel and a speed adjust control where applicable.

- Electrolyte Pump (P1)
  - Dayton 3/4 HP motor and controller. Controller modified for remotely switchable two speed operation and remote ON-OFF control.
  - High or low speed switched by phase of cycle.
- Vent Pump (P2)
  - 115 Volt Micropump, adjustable speed via triac thyristor control.
  - Controlled ON-OFF by phase in response to store pressure level detector, LD3.
- Agitator Motor (P3)
  - 24 Volt, 1/7 HP Rae Motor, adjustable speed via thyristor control.
  - Controlled ON-OFF by phase of cycle
- Decomposition Pump (P4)
  - 115 Volt Micropump, adjustable speed via triac thyristor control.
  - Controlled ON-OFF by phase of cycle in response to store pressure level detector, LD1.

- Coolant Pump (P5)
  - 115 Volt Micropump, controlled by triac switch
  - Controlled ON-OFF by phase in response to store temperature thermocouple, TC-1.
- UV Gas Pump (P6)
  - 12 Volt DC Rae Motor, adjustable speed via triac thyristor control.
  - On Always
- Auxiliary Chlorine Supply Solenoid Valve (SoL-1)
  - 115 Volt, 6 Watt Solenoid Valve, controlled thru triac switch.
  - Active always in response to store temperature uppper limit.
- PH Adjust Solenoids (SoL-2)
  - Two 115 Volt, 6 Watt Solenoid valves (normally open, normally closed) controlled by triac switch.
  - Controlled ON-OFF by phase of cycle.
- Store Inlet Heater Supply (H1)
  - 10 Volt, 10 Ampere adjustable power supply controlled by relay.
  - Controlled ON-OFF by phase cycle.
- Cleanout Relay (CR-1)
  - 100 Ampere Contactor
  - Controlled ON-OFF by phase of cycle.
- Rectifier Reversing Relay (CR-2)
  - 24 Volt reversing contactor
  - Controlled ON-OFF by phase of cycle.
- Rectifier Reference (REF)
  - 0-5 Volts, D.C. Remote control to charging rectifier
  - Controlled ON-OFF by phase of cycle; level controlled by pre-set potentiometer adjustment and logic controlled digital to analog converter.

The auxiliary controls are supplemented by front panel voltage and current meters. Each Selector switch on the panel permits viewing the voltage and current of adjustable speed motors.

Failure Monitors

The purpose of the Battery Automation System was to enable the battery to be operated continously on a 24-hour basis withour human interaction. The control logic and associated interfaces have accomplished this. However, the control cannot guarantee the performance of the battery or auxiliaries.

Therefore, the need exists for a safety or failure monitor capable of determining if a component failure has occured or if the battery is operative in an abnormal manner requiring termination of the test cycle.

The known failure modes were identified from previous battery experience. Additional possible failure modes were also identified. These determined the battery parameters that needed to be monitored. The failure monitor was designed to insure that if a critical parameter exceeds a preset limit, then a signal is sent to the control logic circuit. When the control receives the failure signal, it causes the battery test to abort into a standby mode.

The various parameter limits are logically combined with phase signals from the control logic. Thus a parameter that exceeds its set limit will only be recognized as a failure if it occurs during the particular phase or phases of the cycle to which it applies. For instance, an agitator failure in the store will only be recognized during cooldown and constant current charge. At other times the agitator is off.

The parameter limits, after being combined with phase signals, is delayed for a period of approximately 45 seconds before actually causing an abort. This prevents a transient condition from being confused with an actual failure. If a parameter fault indication persists beyond the delay period, then a failure latch is set and the control logic puts the battery in the standby phase. All auxiliaries are turned off except the electrolyte pump. At the same time, a front panel lamp is lit to indicate which failure mode has occurred. The battery and controller remain in standby until the failure monitor is manually reset.

The following is a list of the parameters which are monitored and what their failure signifies:

- Store Temperature
  - High and low preset limits signals that the store is too cold or that the coolant system has failed.
  - This mode is enabled only during charge.
- Sump Temperature
  - If a high limit is exceeded the heater latch has lost control.
  - Enabled always.

- Agitator Motor Current
  - If current drops below a limt, power has been lost or there is a failure in the agitator mechanism.
  - Enabled only during cooldown and charge.
- UV Loop Gas Pump Pressure
  - Reduction in pressure across the pump is detected by a manometer level detector indicates that the loop on the pump has failed.
  - Always enabled regardless of phase.
- UV Lamp Supply Current
  - Loss or reduction of current to the U.V. lamp power supply indicates that the U.V. lamps are not on.
  - Always enabled.
- Battery Undervoltage - Charge
  - Drop in battery voltage below 2.20 volts indicates a system malfunction
  - Enabled only during charge
- Battery Undervoltage - Discharge
  - A drop in battery voltage below 1.50 volts curing discharge indicates a system malfunction.
  - Enabled during constant current discharge and variable discharge.
- Battery Overvoltage
  - An increase in battery terminal voltage above 2.50 volts indicates system malfunction.
  - This mode is enabled at all time regardless of the phase of the cycle.
- Rectifier Current
  - A decrease in rectifier current below a preset minimum indicates a charge supply failure.
  - Enabled during charge, constant current discharge and variable discharge.

A photograph of the controller unit is shown in Figure 2-9. The lower panel contains three D'Arsonval-type panel meters to monitor the currents and voltages of the motors contained in the 1.4 kWh battery. At the bottom of the panel, the manual overide switches can be seen and the adjustment controls are shown in the middle of the panel.

The left side of the middle panel contains the LED's which indicate the present phase of the cycle and also indicate if a failure has been detected. The current adjust controls are contained on the right side of the panel. The cycle clock and ampere-minute counter are displayed in the LED meters contained in the center of the panel.

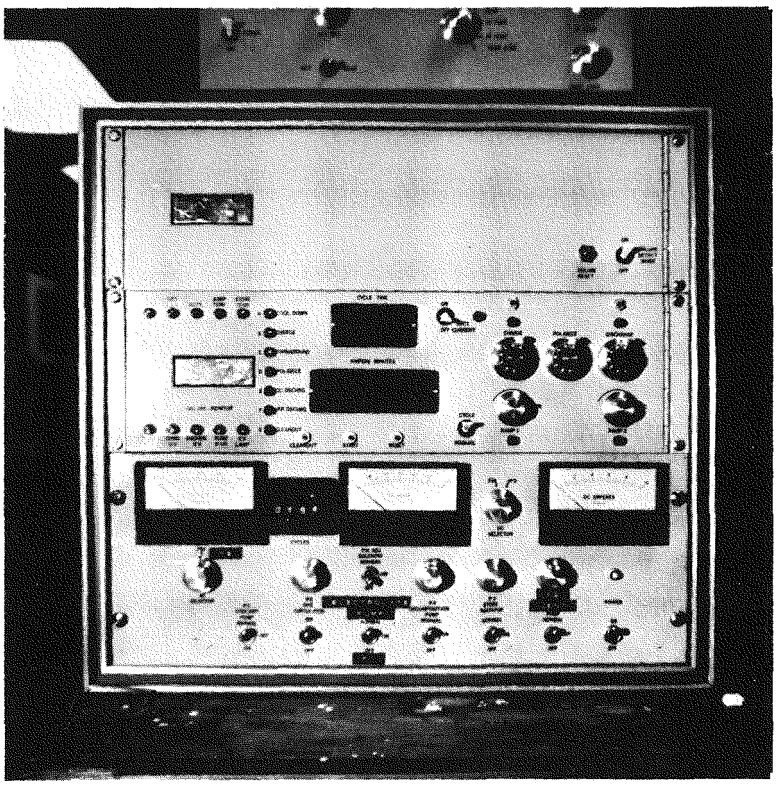

Figure 2-9. Hard-Wired Logic Controller for the 1.4 kWh System.

Data Acquisition

The continuous unattended cycling of the battery requires a means of recording test data for evaluation. In 1974-1975 a data logging system was designed and built in-house for the purpose of continuous data logging of battery cell tests. It was decided that this system would be used for data logging.

The data logger includes provision for up to 48 separate analog inputs. Of these, three inputs may be converted to six digits of binary coded decimal (BCD) inputs by proper programming of the front panel matrix boards.

The system is made up of six major functions plus a time of day clock. The functions are: (1) control circuit, (2) analog multiplexer, (3) digital voltmeter with BCD output, (4) BCD multplexer, (5) parallel BED to serial ASCII converter and (5) a power supply.

Connection of data points to the system is made thru screw terminals to the analog multiplexer. The analog multiplexer consists of two-twenty five position, five deck stepping switches. The switches are ganged with extra decks being used by the control circuit for position sensing and voltmeter range switching. The wipers of the switch are inputs to the digital voltmeter which performs the analog to digital conversion function. The resulting digital binary coded decimal (BCD) outputs are mixed with other digital inputs, such as the time of day clock and ampere minute counter, in a four channel to one channel multiplexer. The control circuit determines which digital channel should be gated on. The selected channel is routed to the BDC-to-ASCII converter where, upon a command from the control circuit, the teletype compatible output is enabled to drive a Model 33 ASR Teletypewriter.

The data logger operates automatically or manually thru controls on the front panel of the system. For automatic operation a thumb wheel switch permits setting the cycle time from one to 99 minutes. For manual operation, start, a single step, read, and log pushbuttons are provided.

The system is programmed by inserting diode pins into selected locations of matrix boards on the panel. Voltmeter range selection, BCD channels, and last position functions are all programmable. By indications the number of data points desired, the system will cycle thru only that number of data points. The time of day clock is permanently wired into a BCD input. Therefore, it only need be selected on the matrix board in order to give a time printout on each data logging cycle.

The data logger is being used to record data on the 1.4 kWh battery. Battery test parameters are read out recorded on the teletypewriter. At 5 minute intervals the time of day, battery terminal voltage, battery current, ampere minutes of charge and store temperature are recorded.

RESULTS AND DISCUSSION

Automation

The removal of the mechanical chlorine desorber and subsequent experimental program undertaken to develop a new operational mode for the ruthenized-titanium battery system caused a considerable delay in developing the logic controller for the system. The logic sequence could not be fully developed until a cycling regimen was established for the battery. After the experimental cycle had been developed in test cells the battery cycling regimen had to be developed in the battery system. The logic sequence was determined from the cycling regimen established through manual operation of the system. Manual cycling of the battery was begun in mid-May and the controller was interfaced to the battery in late August.

Many probems were encountered when the controller was interfaced to the battery. Electrical noise in the controller, generated by relays, solonoids and motors, caused events to occur out of sequence and activated failure detectors which responded appropriately. In the battery, response to controller commands was poor due to location of sensors, response time lags and overall system imbalance.

The difficulties in the controller were gradually resolved by the use of line filters, electrical isolation loops and installation of shielded wiring where necessary. Also, the physical separation of signal sensing wires from current carrying wires was beneficial in eliminating false signal pickup. Improvement of the battery's response to the controller commands required many adjustments on the sensors, relocation of some sensors and some minor changes in the battery to store interfacing. In early November, continuous automated cycling was begun and minor manual adjustments were made to smooth out the battery response to automation. After several successful automated cycles were obtained with supervision, there was enough confidence in the automated system to permit unattended cycling.

While the interfacing of the controller to the battery has been successful, it has also demonstrated the need for greater component reliability in the battery system. The use of failure detectors to prevent battery damage from occurring has been very successful. These detectors have also shown that most system failures are associated with moving parts such as the store agitator or the various pumps. The automation of this system is an on-going program and, as more is learned about automating battery systems, improvements in battery operation and control are expected.

Battery Cycling Results

Manual operation was used for cycles one through fifty-four on the system. In this interval, the cycling regimen for the cycle controller was established. The average energy efficiency for this cycling interval was 71% using the standard electrolyte formulation. The electrolyte was changed a total of six times in this interval, the last change occurring on cycle number 30. The high energy efficiencies obtained in this interval are largely due to the presence of sodium chloride in the electrolyte, which reduces the chlorine solubility.

On cycle fifty, the IR drops across the short lengths of wire that represent current shunts for the zinc electrodes were measured. For the charge cycle, the battery current was temporarily reduced to 160 amperes to match the discharge current. A graph of the measured IR drops (nominally 3.5 mv) provides a pictorial presentation of the current sharing is the system. Figure 2-10 shows the current sharing on both the charge and discharge cycle. The current sharing on discharge is not as good as the current sharing on the charge cycle. If the system demonstrated perfect current sharing, the end zinc electrodes, numbers 1 and 41, would

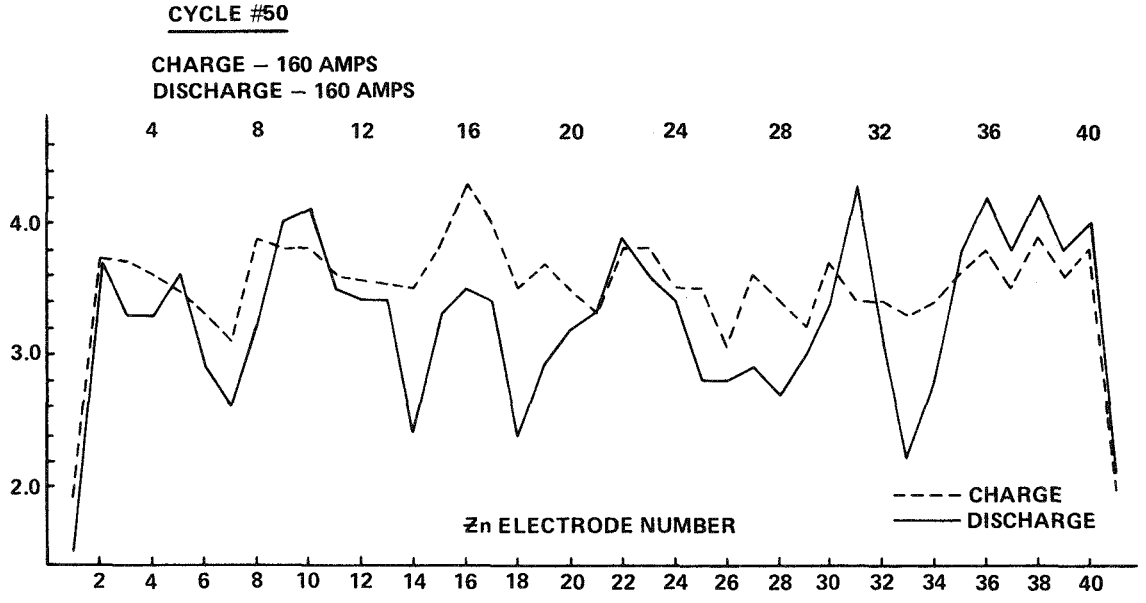

Figure 2-10. Graphical Presentation of the Electrode Current Sharing in the 1.4 kWh Battery. The ordinate is the millivolt reading obtained from the individual zinc electrode shunts.

each carry 2 amps and all other zinc electrodes would carry 4 amps, to total 160 amps. A comparison of these profiles at suitable cycle intervals will help to identify changes in the electrode performance over extended periods of time.

A charge-discharge polarization curve was obtained on cycle 44. These results are shown in Figure 2-11. Note the apparent concentration polarization on discharge for a current density exceeding 35 mA/cm^2. This is most likely due to the use of excessive sodium chloride in the electrolyte. For this reason and because of recurring dendrite problems in the final hour of the charge cycle, the electrolyte composition was modified and the new formulation is still being used as of this writing.

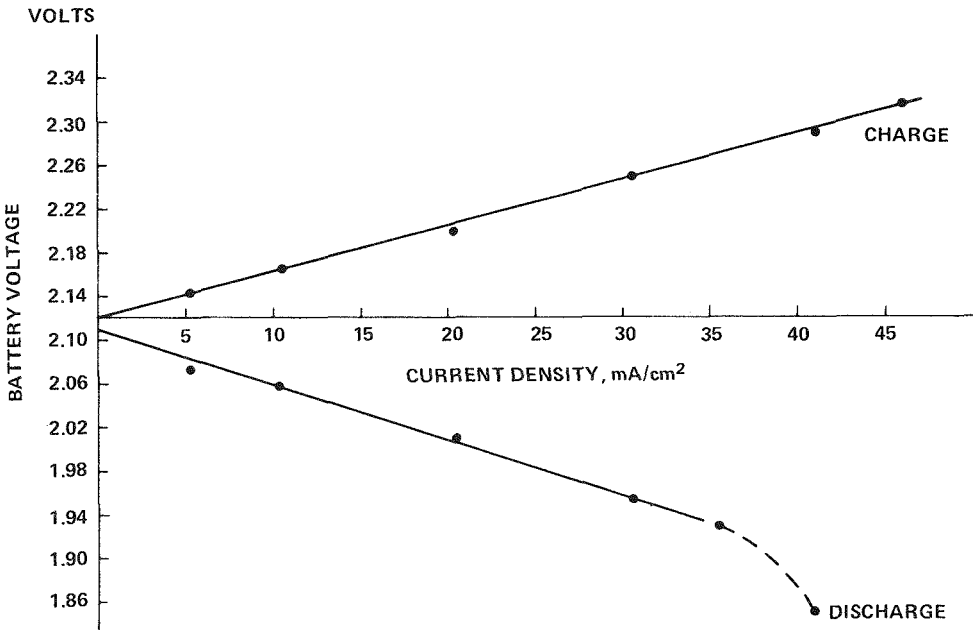

Figure 2-11. Charge and Discharge Polarization Curve for the 1.4 kWh Battery. The onset of chlorine concentration polarization is observed in the discharge mode direct the high sodium chloride concentration in the eletrolyte.

For the cycle interval 55-88, the electrolyte was changed four times. The average energy efficiency in this interval is 67%. The controller was interfaced on cycle 53, and debugging was in progress throughout this cycling interval. Both automated and manual control of the system was used to maintain a daily cycling schedule. Beginning with cycle 86, the system was operated continuously to establish full, unattended automation. The first attempt for fully automated unattended cycle was on cycle 91. This first attempt was not successful and the system went into a

failure mode. The second attempt, cycle 92, resulted in a cycle fully controlled by the control equipment.

Cycles 89-135 were run without an electrolyte charge. The average energy efficiency for these cycles was 67%. Some continuous cycling was obtained in this interval, and the battery was allowed to operate unattended. The energy efficiencies obtained from controller operation do not differ significantly from those obtained in manual operation. Table 2-1 contains the cycling data for the 135 cycles obtained to date.

The high energy efficiencies on the first ten cycles are most likely due to the addition of excess alkali in the turn-around phase. In this cycling interval the electrolyte pH was usually about 2.5 on discharge. Although this high pH helps increase the energy efficiency, the carbon dioxide released in the battery system is undesirable for controller cycling. The pH is normally adjusted to 2 for discharge. For the remainder of the cycles, energy efficiencies are consistent. The cycling data indicate no change in battery capacity or electrode performance has occurred.

Table 2-1

CYCLE PERFORMANCE OF 1.4 kWh BATTERY

CYCLE #	CHARGE CAPACITY (Ah)	DELIVERED ENERGY (kWh)	ENERGY EFFICIENCY (%)	CUMULATIVE AVERAGE ENERGY EFF. (%)
1	900	1.51	74.1	74.1
2	900	1.52	74.6	74.4
3	900	1.46	71.9	73.5
4	900	1.38	67.6	72.1
5	720	1.15	70.8	71.8
6	900	1.51	74.2	72.2
7	900	1.49	73.0	72.3
8	900	1.49	73.0	72.4
9	837	1.35	71.0	72.2
10	900	1.44	70.6	72.1
11	900	1.37	67.0	71.6
12	900	1.42	69.8	71.5
13	900	1.43	70.0	71.4
14	900	1.41	69.0	71.2
15	900	1.47	71.9	71.2

Table 2-1

CYCLE PERFORMANCE OF 1.4 kWh BATTERY

CYCLE #	CHARGE CAPACITY (Ah)	DELIVERED ENERGY (kWh)	ENERGY EFFICIENCY (%)	CUMULATIVE AVERAGE ENERGY EFF. (%)
16	900	1.41	68.9	71.1
17	900	1.41	69.3	71.0
18	900	1.41	70.4	71.0
19	900	1.46	71.7	71.0
20	900	1.45	71.2	71.0
21	900	1.44	71.0	71.0
22	720	1.15	70.6	71.0
23	900	1.43	70.3	71.0
24	900	1.41	69.3	70.9
25	900	1.38	67.6	70.8
26	900	1.43	70.6	70.7
27	900	1.45	71.3	70.8
28	900	1.42	69.8	70.7
29	900	1.45	71.1	70.7
30	900	1.38	67.5	70.6
31	900	1.38	67.9	70.5
32	900	1.36	66.8	70.4
33	800	1.38	67.9	70.4
34	900	1.39	68.3	70.3
35	900	1.43	70.1	70.3
36	900	1.44	70.3	70.3
37	900	1.41	69.2	70.3
38	900	1.41	69.2	70.2
39	900	1.38	68.0	70.2
40	900	1.39	68.5	70.1
41	900	1.40	68.6	70.1
42	900	1.40	68.7	70.1
43	900	1.39	68.1	70.0
44	900	1.42	70.3	70.0
45	900	1.40	68.8	70.0
46	900	1.43	70.1	70.0
47	900	1.37	67.2	69.9
48	900	1.39	68.0	69.9
49	900	1.39	68.1	69.9

Table 2-1

CYCLE PERFORMANCE OF 1.4 kWh BATTERY

CYCLE #	CHARGE CAPACITY (Ah)	DELIVERED ENERGY (kWh)	ENERGY EFFICIENCY (%)	CUMULATIVE AVERAGE ENERGY EFF. (%)
50	800	1.26	69.9	69.9
51	722	1.13	68.9	69.8
52	844	1.32	69.0	69.8
53	892	1.38	68.8	69.8
54	896	1.39	68.4	69.8
55	900	1.41	68.9	69.8
56	900	1.41	69.1	69.8
57	897	1.40	68.8	69.7
58	900	1.39	68.0	69.7
59	889	1.40	69.1	69.7
60	890	1.34	66.1	69.6
61	719	1.13	69.4	69.6
62	844	1.31	68.9	69.6
63	789	1.21	68.5	69.6
64	794	1.20	67.2	69.6
65	892	1.30	64.2	69.5
66	895	1.33	65.7	69.4
67	900	1.41	69.4	69.4
68	718	1.13	69.1	69.4
69	896	1.40	68.9	69.4
70	854	1.27	65.7	69.4
71	900	1.38	67.5	69.3
72	901	1.38	67.4	69.3
73	710	1.09	67.7	69.3
74	892	1.35	66.7	69.3
75	897	1.35	66.3	69.2
76	900	1.35	66.2	69.2
77	902	1.36	66.5	69.1
78	916	1.39	67.0	69.1
79	882	1.34	67.0	69.1
80	900	1.36	66.8	69.1
81	900	1.34	65.8	69.0

Table 2-1

CYCLE PERFORMANCE OF 1.4 kWh BATTERY

CYCLE #	CHARGE CAPACITY (Ah)	DELIVERED ENERGY (kWh)	ENERGY EFFICIENCY (%)	CUMULATIVE AVERAGE ENERGY EFF. (%)
82	898	1.35	66.3	69.0
83	897	1.37	67.4	69.0
84	863	1.35	68.6	69.0
85	897	1.32	64.6	68.9
86	904	1.36	66.3	68.9
87	814	1.26	68.4	68.9
88	903	1.30	63.5	68.8
89	900	1.41	69.0	68.8
90	894	1.37	67.3	68.8
91	892	1.35	66.8	68.8
92	875	1.36	68.3	68.8
93	910	1.28	62.0	68.7
94	890	1.38	68.1	68.7
95	889	1.36	67.4	68.7
96	889	1.37	68.1	68.7
97	884	1.37	68.5	68.7
98	887	1.39	69.0	68.7
99	890	1.39	69.1	68.7
100	886	1.38	68.6	68.7
101	884	1.37	68.4	68.7
102	887	1.37	68.4	68.7
103	890	1.37	68.2	68.7
104	890	1.38	68.5	68.7
105	890	1.39	69.0	68.7
106	887	1.39	69.3	68.7
107	870	1.36	69.3	68.7
108	880	1.39	69.9	68.7
109	873	1.38	69.9	68.7
110	882	1.37	68.5	68.7
111	869	1.38	69.8	68.7
112	876	1.33	67.1	68.7
113	901	1.27	62	68.6

Table 2-1

CYCLE PERFORMANCE OF 1.4 kWh BATTERY

CYCLE #	CHARGE CAPACITY (Ah)	DELIVERED ENERGY (kWh)	ENERGY EFFICIENCY (%)	CUMULATIVE AVERAGE ENERGY EFF. (%)
114	888	1.36	67.6	68.6
115	888	1.38	68.9	68.6
116	878	1.35	68.3	68.6
117	888	1.38	68.9	68.6
118	878	1.38	69.3	68.6
119	883	1.36	67.9	68.6
120	884	1.36	68.0	68.6
121	886	1.35	67.3	68.6
122	883	1.37	68.6	68.6
123	887	1.31	65.2	68.6
124	876	1.37	69.3	68.6
125	887	1.35	67.1	68.6
126	885	1.37	68.0	68.6
127	888	1.35	66.8	68.6
128	887	1.35	67.1	68.5
129	815	1.20	65.1	68.5
130	887	1.31	65.2	68.5
131	888	1.37	68.1	68.5
132	884	1.25	62.3	68.4
133	901	1.29	62.8	68.4
134	888	1.24	61.3	68.3
135	858	1.27	65.3	68.3

Summary

The 1.4 kWh system and logic controller represents the first attempt to fully automate a zinc-chlorine battery system. Although long term continuous cycling has not been demonstrated, the progress to date indicates a large measure of success. Further progress towards continuous cycling will require changes in some components and the hydrate store, which is a frequent cause of cycling failure.

The use of failure detectors in the system has been very successful. Whenever a component has registered a failure, the controller has successfully terminated the cycle in a prescribed manner. Due to the success of the failure detectors, unattended operation of the system is considered normal, rather than the exception.

Battery capacity has not diminished with time. The voltaic efficiency, coulombic efficiency and energy efficiency have also remained constant throughout the 135 cycles.

Section 3

THE 1.7 kWh BATTERY SYSTEM AND MICROPROCESSOR CONTROLLER

INTRODUCTION

The 1.7 kWh battery unit represents the entry of graphite chlorine electrodes into the EDA-EPRI peak-shaving program. Use of graphite in mobile applications had always been considered feasible. The more demanding performance requirements for a peak-shaving unit, however, could not be achieved prior to the introduction of thermo-chemical graphite pretreatment in 1975. Voltaic performance enhancement resulting from the treatment demonstrated new potential for the material, and led to the consideration of graphite for peak-shaving also.

Additionally, cost and availability factors for the ruthenized electrodes being employed in the peak-shaving program were coming under increasing scrutiny. Potential significant cost savings and unquestioned availability, therefore, mandated construction and testing of a peak-shaving graphite battery.

The unit constructed is one of our earliest graphite comb designs, and as such, represented a state of the art requiring further development. Initial operation, therefore, was devoted to the testing of numerous design concepts. Manifolding technology, static head above the electrodes and internal cell masking all required development and optimization. Outlet power busing design options and concepts were to be studied. Uniformity of current density distribution was to be determined, and modifications made where practical to improve the discharge voltage profile.

System development was also in progress, resulting from the deletion of the previously employed desorber unit for economic considerations. As a result of this major change, the battery was also utilized in testing system concepts in conjunction

with and complimenting developments from the ongoing 1.4 kWh battery program. For example, developments in electrolyte formulation and operational temperature resulting from desorber removal were demonstrated first on the 1.4 kWh system, and then verified with the 1.7 kWh unit.

This initial phase of battery modification and system's development complicates the early data generated for the unit. By the close of 1976, however, the battery was operating as an integral battery system and delivering 1.7 kWh with an electrochemical energy efficiency of approximately 64%. This performance is admittedly lower than that predicted from graphite single cell studies, and results from incomplete activation of the electrodes. These electrodes represented, however, our first attempt at scaling-up the thermochemical activation process, and the resultant partial activation is not surprising when viewed in this context.

Manual operation of the 1.7 kWh system continued through the close of 1976. Continuous automated operation under microprocessor control was scheduled, but awaited completion of the control unit. Battery system performance under peak-shaving conditions was considered sufficient at this stage of development to warrant life-testing of battery unit. Interfacing with the microprocessor controller is scheduled for early 1977.

The following sections begin with a physical description of the 1.7 kWh graphite battery system. Details in system operation differing from the 1.4 kWh unit are then described. Results of the initial test and development program follow. Cycling data generated to date are then detailed, followed by a discussion of battery performance. The microprocessor controller, now awaiting interfacing with the battery, is then described.

SYSTEM DESCRIPTION

The battery stack is the monopolar "comb" design shown in Figure 3-1. Electrode

are press fit into slots machined in graphite buses; contact resistance for this interference fit is quite low. Chlorine electrodes are arranged in pairs; and hence, share a single electrolyte feed tube. To accomplish this, the mating surfaces of two contoured porous plates are first bonded together with KYNAR cement. Three holes are then drilled through the top edge; two are for gas vents and the third is used for the electrolyte feed tube.

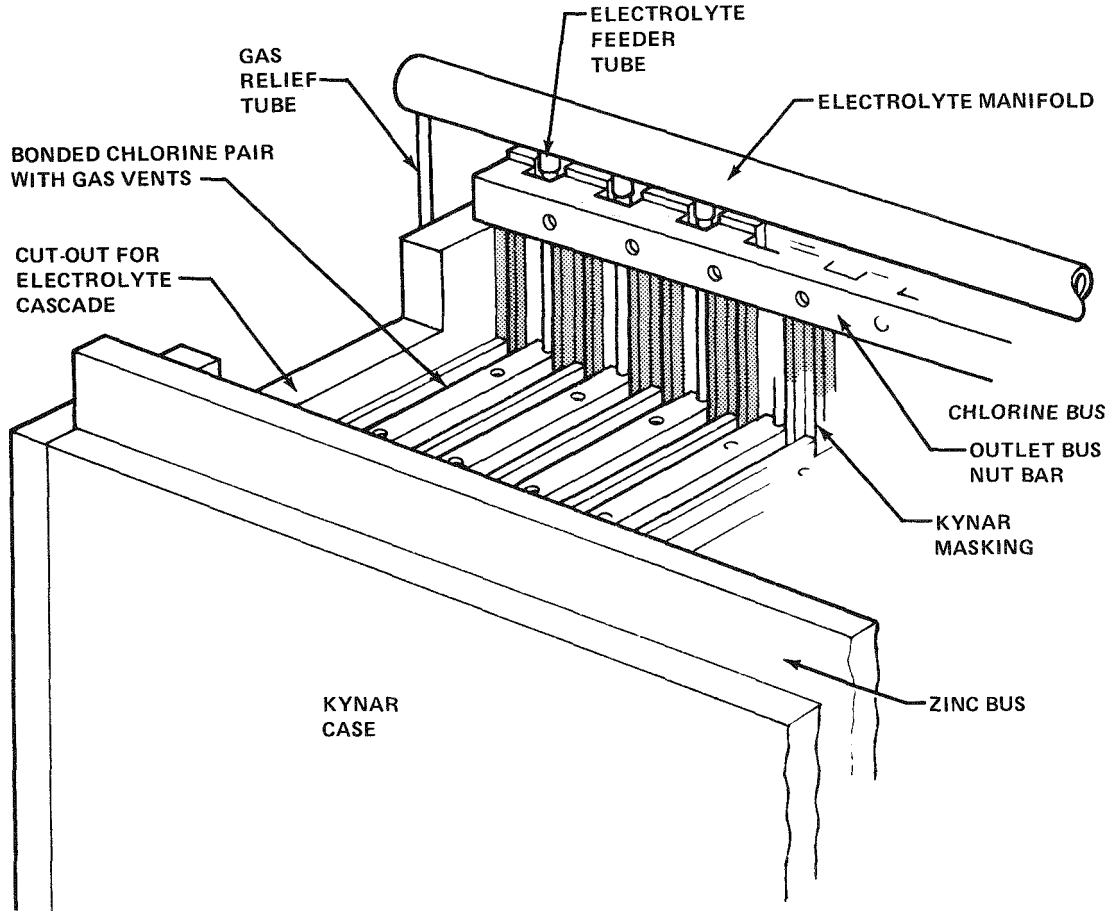

Figure 3-1. Section of 1.7 kWh Battery Showing Construction Details. Chlorine outlet-bus nut-bar with provision for electrolyte feed tubes as shown; remainder of secondary outlet busing removed for clarity.

When the zinc comb is meshed with the "paired" chlorine bus assembly, "double sided" zincs (excluding those at the end) result. During operation a continuous zinc plate is generated, covering top and bottom edges in addition to both faces.

Necessary masking of the zinc and chlorine electrodes, and their associated buses, is accomplished by using machined KYNAR inserts. The active chlorine faces are 2.5 inches wide by 4 inches high. Area of each chlorine plate, therefore, is 64.52 cm^2. As is our practice, this value (instead of the somewhat larger zinc plate area) is used in the calculation of current density. These masking inserts also assist in maintaining the 0.120 inch gap.

A tubular manifold distributes electrolyte to feeder tubes. To minimize gas being fed to the battery, suitably positioned manifold vents are employed. These gas vents are simply additional tubes (identical to the feeder tubes) which empty into the battery sump. Two are employed for each battery half, one at each end. Therefore, the four "extra" tubes must be taken into account when calculating electrolyte flow. For this purpose, the battery may be considered to contain 100 equal cells of 64.52 cm^2, giving a total flow through "area" of 6452 cm^2 for electrolyte flow calculation.

Electrolyte feed from the manifold is by means of small diameter TEFLON feeder tubes that are located near the chlorine buss and extend down into the chlorine pair. Clearances are such that a tight fit results, insuring a reasonable seal. Feeder tube I.D. and length were sized to provide a flow controlling pressure drop. This was preferred over the chlorine plates being controlled since variability in porosity from plate to plate cannot be avoided. With this battery unit, no attempt was made to match plates in a given pair. This practice has been instituted with subsequent batteries.

The battery is made up of two equivalent units paralleled through common secondary buses as shown in Figure 3-2. Practical considerations dictated this design. Each unit is made up of a monopolar array of 48 chlorine and 25 zinc electrodes. Of the zincs, 23 are "double sided" substrates, the remaining two being single-sided end electrodes. The 96 paralleled cells so generated have a total electrode area of 6194 cm^2.

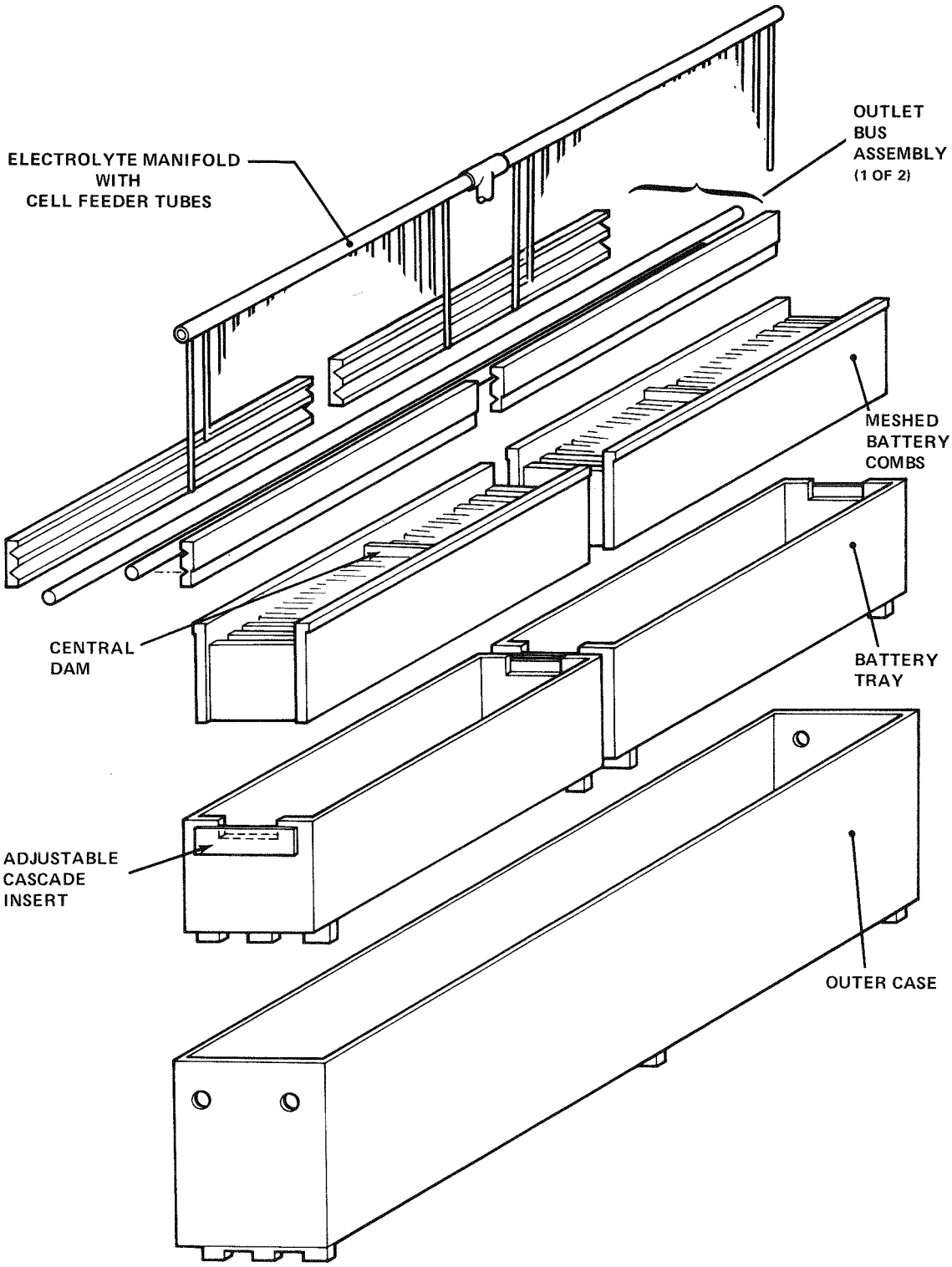

Figure 3-2. 1.7 kWh Stack Unit. Outer case serves as electrolyte sump, and defines major gas space in system. Note that electrolyte head over cells is adjustable by adjustment of inner case cascade inserts. Outer case cover not shown.

The major differences between the two systems include the following:

- A separate pump is employed to inject gas into the outlet (high pressure) side of the main electrolyte pump for discharge. This is the major difference between the two systems.
- System electrolyte is employed in the hydrate decomposition loop, resulting in more realistic operation.
- Because the operational pH range is materially different, periodic addition of HCl is required instead of carbonate as with the 1.4 kWh unit.

As presently operated, 15 liters of electrolyte are required to complete a five-hour charge. The resultant gas volume as defined by the outer battery case is approximately 18 liters. The gas recirculation/hydrogen reactor loop operates at about 10 liters/min.

Although still not optimized, test conditions were eventually chosen to allow life testing of the graphite battery. Performance during the initial test period was first evaluated, leading to the use of the following conditions:

- Charge current: 220 amperes
- Discharge current: 190 amperes
- Electrolyte flow: 12 liters/min
- Dissolved chlorine levels: 1.4 g/l during charge
  1.0 g/l during discharge

Charge and discharge current densities are, therefore, 35.5 and 30.8 mA/cm^2 respectively. The electrolyte flow rate of 1.86 $ml/min/cm^2$ with a 1.0 g/l dissolved chlorine level is sufficient to insure an adequate chlorine supply on discharge.

Each of the above discussed battery halves sit inside of an open-top KYNAR tray. These trays are tight fitting, and hence, provide necessary bus masking. Electrolyte overflows at each end; at the midpoint, a dam segregates the flow and insures equal flow out each end. Electrolyte level in the tray and hence, over the electrodes is controlled by tray height at each end. This is adjustable through the use of appropriately sized inserts.

The 1.7 kWh battery is essentially identical to the basic system previously detailed for the 1.4 kWh unit. The integrated battery system is shown in Figure 3-3.

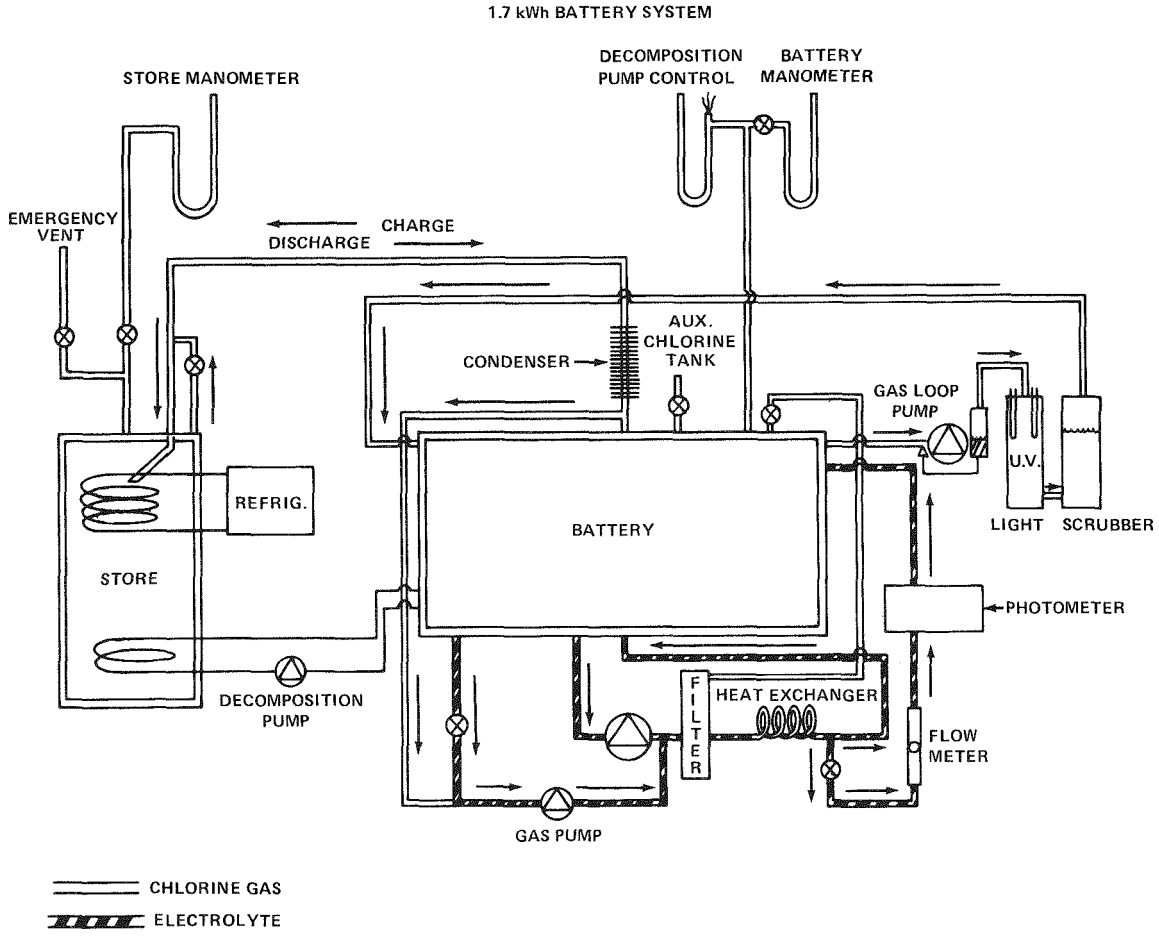

Figure 3-3. The 1.7 kWh Battery System

The 1.7 kWh system was operated manually throughout the year. Basically, operation is equivalent to that of the automated 1.4 kWh battery, consisting of five major phases:

- Cooldown - phase to bring the store into the temperature range of hydrate formation.
- Constant Current Charge - phase during which zinc is deposited on the graphite electrode and chlorine is evolved on a porous graphite electrode. This phase is five hours in length at 220 amps with a current density of 35.5 mA/cm^2.
- Turnaround - phase which allows chlorination of electrolyte in preparation for discharge.
- Discharge - discussed below.
- Cleanout - phase during which the remaining zinc is stripped from the electrodes via a resistor switched across the battery terminals. At the end of this timed phase, the system returns to the cooldown phase to begin a new cycle.

Two discharge modes, constant current and constant voltage, were evaluated. In the constant voltage mode, discharge current was varied to maintain a specified battery voltage range just as with the 1.4 kWh operation. The discharge profile, however, of the graphite battery is superior to that with ruthenized titanium electrodes. Therefore, while operating manually the less time consuming constant current discharge was primarily employed. System performance is not materially affected by discharge mode employed. This evaluation is detailed later in the discussion of cycle results.

EXPERIMENTAL RESULTS

In this section the more significant experimental aspects of the initial development period for the battery system are detailed. Modifications to the cell design are

first discussed, followed then by the more system's related developments.

Early testing revealed that electrical contact between the titanium clad copper and the graphite bus was found to be quite resistive resulting in a nominal 100 millivolt drop. Subsequent testing on power contacts demonstrated that if the graphite bus was first flame sprayed with titanium, the voltage drop was a nominal 20-25 millivolts. This same technique was later incorporated in the bus connections on the 20 kWh battery.

Testing of comb-type single cells had demonstrated that some maldistribution of current existed for cells of this design. Visual inspection revealed a zinc plate which was thickest near the chlorine bus, and tapering down to its thinnest adjacent to the zinc bus. As the discharge progresses the zinc plate is observed to be shrinking in size. This begins to occur at the top and bottom corners near the zinc bus early in the discharge. The rate of shrinkage is quite slow at first, but later in the discharge it materially increases. The discharge voltage profile remains quite steep, however, in that only a 25-40mV decay is seen with single cells operated at constant current. Concern existed, however, that with scale-up to larger sized batteries the problem would be magnified.

The problem partially results from resistive deficiencies in the chlorine comb design. An attempt was made to overcome this nonuniformity in current density in the initial battery unit through the use of unsymmetrical zinc electrodes. This electrode shape is shown in Figure 3-4. Its purpose was to equalize the current

density over the electrode surface by providing a somewhat larger plating area near the chlorine bus.

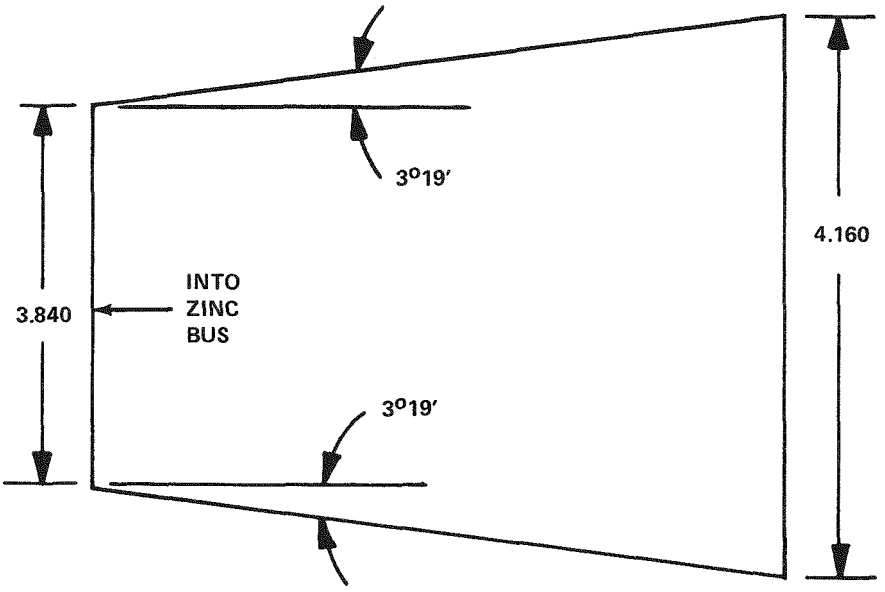

Figure 3-4. Unsymmetrical Zinc Electrode Employed to Overcome Current Maldistribution in an Earlier Version of the 1.7 kWh Battery. Although successful to a significant degree, cost factors mandated discontinuance of their use.

Performance of the battery with these tapered electrodes was impressive from the point of view of its discharge voltage profile. Cost considerations were shown, however, to be overwhelming and to negate what turns out to be only a slight performance increase. After a reasonable test period, therefore, these shaped electrodes were replaced with standard rectangular plates.

Use of rectangular plates in the battery did slightly steepen the discharge profile, as expected. The plating problem at the corners was magnified in that during discharge a tendency developed for the zinc plate to peel away from the substrate and short to the chlorine electrode. Undercutting of the zinc was obviously due to corrosion. The corrosion rate was being enhanced by the couple formed due to zinc being in contact with bare graphite.

Insufficient zinc bus masking was shown to be a contributing factor in addition to the current density maldistribution described previously. Although the zinc bus face was both KYNAR coated and masked, the unused portion of the slots into which the zinc electrodes are forced were not protected. Zinc undercutting and shorting was overcome by press fitting KYNAR bars into the unused portions of the slot above and below the zinc plate.

Early in the operation of the 1.7 kWh unit difficulty was experienced with the zinc plate refusing to cover the top edge of the electrodes. In extreme cases, during discharge the plate again would "peel off" and short to the adjacent chlorine. This was successfully rectified by raising the electrolyte level over the electrodes by adjustment of the cascade inserts on each end (see Figure 3-2). A more laminar flow, and hence less turbulence, significantly lessened corrosion losses in the region of the top edges.

The zinc plate problem near the zinc bus was, therefore, overcome sufficiently to allow extended cycling of the battery. It was not, however, completely solved during these exercises. Improved masking and/or modifications to improve uniformity of current density across the zinc plate are in order.

In another set of experiments, methods of introducing chlorine into the electrolyte during discharge were evaluated. Initially, chlorine was admitted at the inlet of the main electrolyte pump. This technique offers as a disadvantage little or no independent control of the gas and liquid flow rates. Independent control of both the liquid and gas flow rates was achieved by installing a gas pump on the outlet (high pressure) side of the main electrolyte pump.

A major system modification was made after the outer battery case ruptured on cycle 14-A. Although a definitive judgment could not be made concerning the cause, a hydrogen-chlorine explosion could not be ruled out. Shattering of stressed KYNAR components could just as easily be the cause. System operation was not affected

CYCLING RESULTS

Cycling of the 1.7 kWh system was not a routine operation due to the ongoing developmental program detailed in the previous section. The scatter in the results presented here is to a great extent caused by this situation.

Discharge mode employed, however, did not materially influence cycle performance. The excellent discharge voltage profile as detailed in Figure 3-5 is primarily due to the flow uniformity of the porous graphite chlorine electrodes resulting from pressure drop characteristics of the material. In contrast, the low pressure drop of the ruthenized tititanium electrodes in the 1.4 kWh unit results in flow non-uniformity which materially affects its discharge voltage profile, essentially precluding the use of constant current discharge.

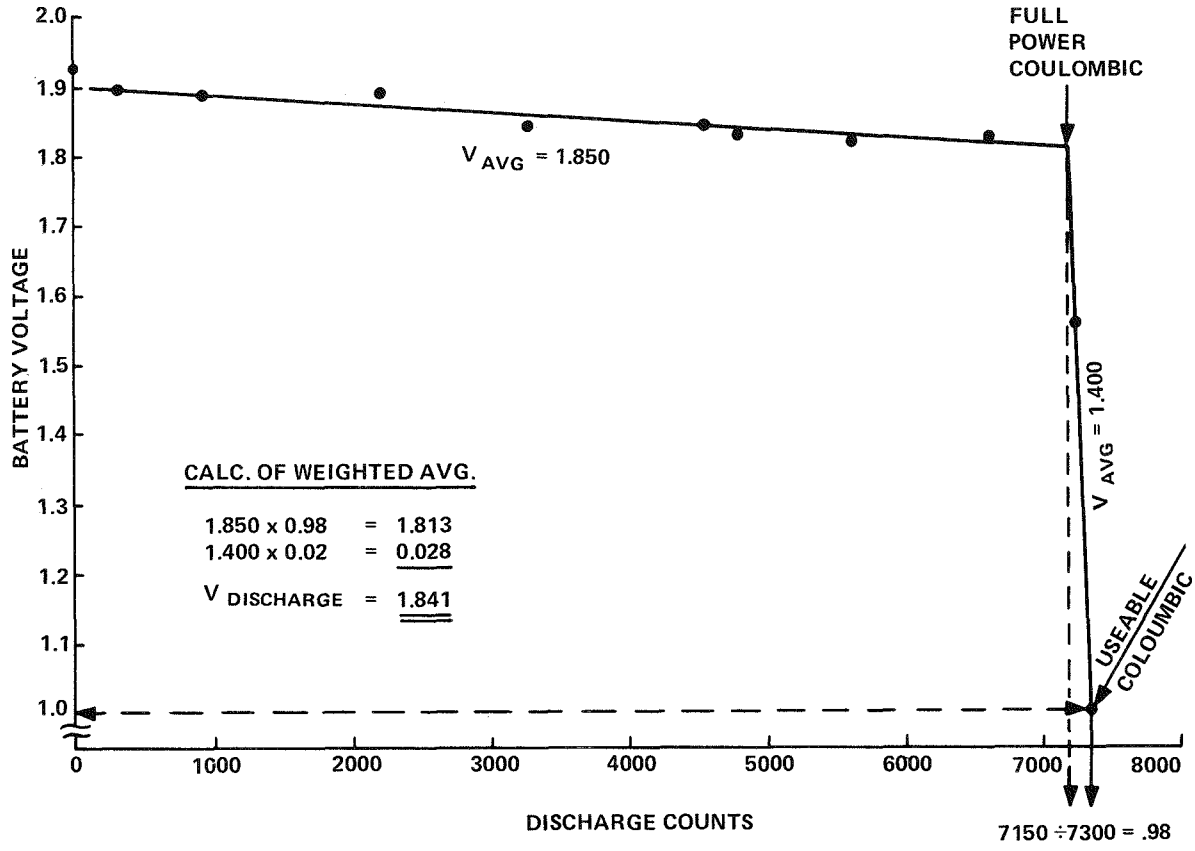

Figure 3-5. Method of Evaluation Employed for Constant Current Discharge Operation. Shape of the discharge profile minimizes effect of the approximations made.

Constant current discharge is evaluated as detailed in Figure 3-5. The discharge profile is flat enough, and the fall in voltage at the knee sharp enough, to warrant the approximations employed.

A compilation of the results for the years fifty four cycles is given in Table 3-1. The average energy efficiency is 64.5% with a standard deviation of 2.0%.

Discharge mode is detailed in the table for each cycle. Comparison of performance for the two discharge modes for consecutive cycles reveals less than a 0.5% difference.

Shown in Figure 3-6 are the useable and total coulombic efficiencies as a function of cycle. Full power coulombics are not graphed. Difficulties encountered on constant voltage cycles was the reason for this not being done. Ramping down of the current very often was required early in the discharge. This situation in retrospect was the result of poor judgement. In attempting to demonstrate voltaic performance, the operational state of the system could not satisfy the voltage restrictions dictated.

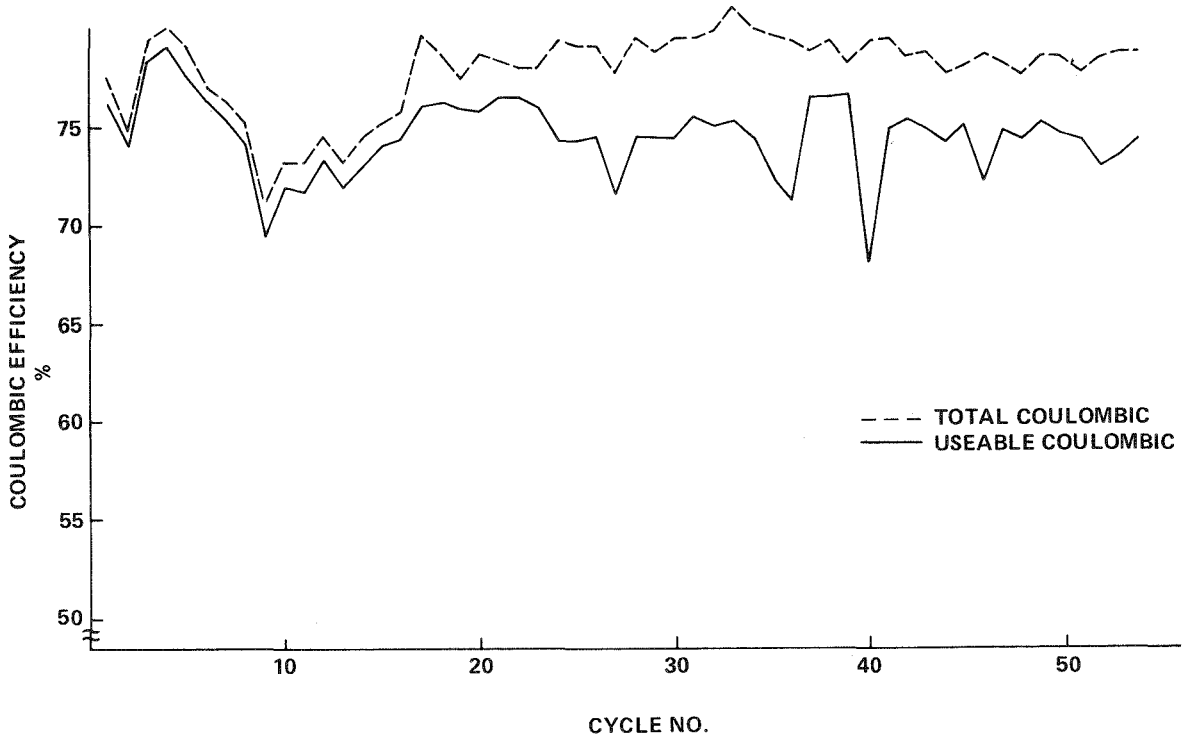

Figure 3-6. Coulombic Efficiencies for Qualified Cycles Completed During Test Program.

Table 3-1
1.7 kWh System Performance

Cycle No.	Disch. Mode	Chg. (Amp.-Hrs.)	Voltaic Eff. %	Coulombic Eff. Usable %	Energy Eff. %
1	CC	875	82.0	81.2	66.6
2	CV	934	83.2	79.0	65.7
3	CV	1087	81.0	83.3	67.7
4	CV	1074	81.9	84.1	68.9
5	CV	1074	82.2	82.6	67.9
6	CV	887	82.3	81.3	66.9
7	CV	1058	82.5	80.4	66.3
8	CV	1052	82.5	79.2	65.3
9	CV	1052	82.5	74.4	61.4
10	CV	1100	82.5	77.0	63.5
11	CV	899	82.5	76.7	63.3
12	CV	880	82.5	78.4	64.8
13	CV	1100	82.8	76.9	63.7
14	CV	1099	82.0	77.9	64.0
15	CV	1099	82.0	79.0	64.8
16	CV	879	82.4	79.3	65.4
17	CC	880	79.7	81.0	64.6
18	CC	1076	80.3	81.1	65.1
19	CV	990	81.5	80.9	65.9
20	CC	974	81.3	80.8	65.7
21	CV	991	81.5	81.5	66.6
22	CV	993	81.5	81.5	66.4
23	CC	1081	80.1	81.0	65.9
24	CC	1100	79.0	79.3	62.6
25	CC	880	80.3	79.2	63.6
26	CC	880	79.4	79.5	63.1
27	CC	894	79.7	76.5	61.0
28	CC	880	78.5	79.4	62.3
29	CC	880	79.7	79.5	63.4
30	CC	880	79.9	79.3	63.4
31	CC	1100	79.9	80.5	64.3
32	CC	1100	79.6	80.0	63.7
33	CC	880	81.0	80.3	65.0

Table 3-1 (cont.)
1.7 kWh System Performance

Cycle No.	Disch. Mode	Chg. (Amp.-Hrs.)	Voltaic Eff. %	Columbic Eff. Usable %	Energy Eff. %
34	CC	882	81.4	79.4	64.6
35	CC	1100	80.5	77.3	61.3
36	CC	880	80.9	76.2	61.6
37	CV	1100	81.3	81.4	66.2
38	CV	1100	81.3	81.5	66.3
39	CV	1100	81.3	81.6	66.3
40	CC	1100	79.5	73.1	58.1
41	CC	1100	80.6	79.8	64.3
42	CC	880	82.3	80.4	66.2
43	CC	880	80.3	79.8	64.1
44	CC	887	80.9	79.2	64.1
45	CC	880	81.3	80.1	65.1
46	CC	911	80.7	77.0	62.1
47	CC	1100	80.9	79.7	64.5
48	CC	1100	80.9	79.3	64.2
49	CC	1100	80.7	80.1	64.6
50	CC	889	79.6	79.5	66.3
51	CC	1100	80.1	79.2	63.4
52	CC	942	79.6	77.8	61.9
53	CC	896	80.4	78.4	63
54	CC	880	80.3	79.2	63.6

Full power coulombic with constant current cycles as defined in Figure 3-5 does not depend upon such dictates which are subject to errors in judgement. Sharpness in the discharge voltage profile results in full power coulombic being typically 1-3% lower than that considered useable.

Finally energy efficiencies are graphically presented in Figure 3-7.

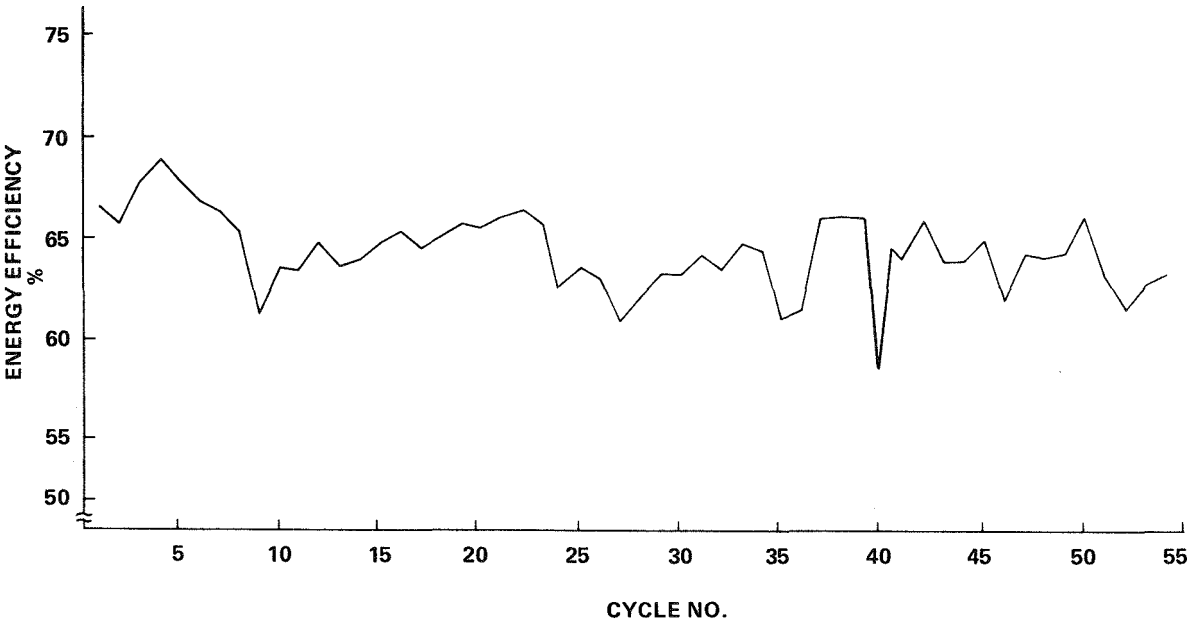

Figure 3-7. Energy Efficiency for Qualified Cycles Completed During Test Program.

DISCUSSION OF CYCLING RESULTS

Because of the large number of modifications made to the system, their timing, and the incident on cycle 14-A, it is not practical to categorize cycles into chronological groups to show performance trends. Instead, operational aspects are discussed in a more general manner.

Variability in Performance Due to System Modifications

The scatter in these performance data over the first 25 cycles, as mentioned,

is to a large extent due to the development program going on in parallel with battery testing. This experimentation has already been detailed under EXPERIMENTAL RESULTS. During this period testing was not on a daily basis. In addition, cycle length varied extensively. Very often short 2 or 3 hour charge cycles were performed to evaluate modifications. To qualify for presentation here, however, a minimum charge of 4 hours was required. Obviously, then, days or even weeks may have elapsed between a given pair of "qualified" cycles.

The scatter after cycle 25 reflects instead difficulties encountered with the operation of the system as finalized. This is discussed in more detail later under gas injection mode.

The Cycle 14-A Incident

Detailing of the incident, and corrective measures taken, have been covered previously under EXPERIMENTAL RESULTS.

The battery combs and manifolding were inspected thoroughly before rebuilding the system. No significant damage was found. Visual inspection of the more fragile chlorine comb revealed nothing suspicious at this time. With the battery unit reassembled, and electrolyte flowing, again nothing wrong was found.

Cycling of the rebuilt system was therefore undertaken. No significant effect on performance is discernable over the next ten cycles.

Gas Injection Mode on Discharge

The first 23 cycles were generated with discharge chlorine admitted at the inlet of the main electrolyte pump. The remainder of the year's cycles employed instead a separate gas pump to inject chlorine on the outlet (high pressure) side of the main electrolyte pump. Rationale for the modification is found in the EXPERIMENTAL DETAILS.

The differential between usable and total coulombic before this modification does appear to be less. The abruptness of the change would appear to indicate correlation. Automation of system operation, however, necessitated the modification. Manual operation of the system in the original gas injection mode required was feasible. Constant attention to the gas/electrolyte ratio was, however, required. Automation of the adjustment required was not feasible. Practicality, therefore,

necessitated the change.

Most importantly, usable coulombic was not materially affected. Excursion in this respect before and after this modification can be taken to reflect lack of control over other parameters.

MICROPROCESSOR CONTROL

Introduction

The development of a microprocessor control package for automatic zinc-chlorine system cycling was a contractual requirement of the 1976 program. System changes necessitated modification of the units requirements, and this along with vendor problems delayed completion of the unit.

As the contractual year closes, the microprocessor control unit has been delivered and is undergoing final programming. Interfacing with a working system will occur early in 1977. Automated operation will begin shortly thereafter.

The following is a detailed presentation of the microprocessor development program.

Objectively, the task of cycle testing the 1.7 kWh battery required a completely hands off, automatic control system. It had to repeatedly step the battery system through each charge/discharge cycle while controlling auxiliary subsystems and monitoring various battery operating parameters. Also, it must contain a provision for detecting the failure of a battery component or subsystem; then it must safely terminate the test upon occurrance of a failure. In addition, data acquisition and visual display of battery parameters was a necessary part of the system's hardware and software.

Solution to Task

A design task similar to this was described previously in developing the automatic control for the 1.4 kWh battery system. Utilizing in-house designed, hardwired logic circuits, the 1.4 kWh battery controller, although functional, was quite inflexible to change and modification.

Reliability, cost, time, complexity and size are all factors to be considered when choosing an automatic control. Future requirements for peak-shaving batteries in

the megawatt size likely will necessitate computer control for process management, data acquisition and monitoring, and remote control. Recent growth in microprocessor technology has brought computer control costs down to an affordable range. In consideration of these facts, the use of a microprocessor was investigated for application to the battery cycle testing program.

Investigation revealed that microprocessors were cost competitive with a hard-wired design and superior in reliability, capacity, and time to implement. In addition, microprocessors were extremely flexible. Simply by reprogramming the process portion of the system software (instructions), microprocessors can be changed to accomodate new test requirements. The hardware need not be obsolete when the test is complete; it may be reused with a new software program for other testing functions.

After reviewing several vendors' quotations, Omicron, Inc. of Madison Heights, Michigan was chosen to provide the computer hardware. During system development Omicron proved to be competent, very cooperative and supplied useful suggestions to improve design of the system.

The entire automation control evolved into a central computer controller interfaced to the battery system through power drivers to pump motors, solenoid valves, current signal amplifiers, and the like. Battery system operating parameters are displayed on a cathode ray tube (CRT). Communication with the microprocessor control system to modify control instructions or parameters is by way of a panel-mounted keyboard. A teletypewriter provides hard copy printout of operational data; it includes a paper tape punch to acquire this data in a form easily communicated to a larger data processing computer (such as a time-sharing service). EDA designed and constructed the interface (battery system-to-controller) hardware. It was mounted, along with the CRT display, keyboard and computer logic hardware, in a NEMA-12 cabinet supplied by the vendor. The whole system presents a clean appearance with easy access to all controls.

Control Requirements

Various pumps, solenoids and motors involved with battery operation need to be switched on or off according to the state of the cycle or value of some battery control parameter. Control is exercised by the computer through ON/OFF signals to interface circuits. These ON/OFF signals cause small reed relays to close or open which, in turn, activates the drive circuit of the auxiliary unit. A description of some of the auxiliary subsystem components, the control scheme applicable to that particular

unit and schematic (Figure 3-8) of the 1.7 kWh battery system follows:

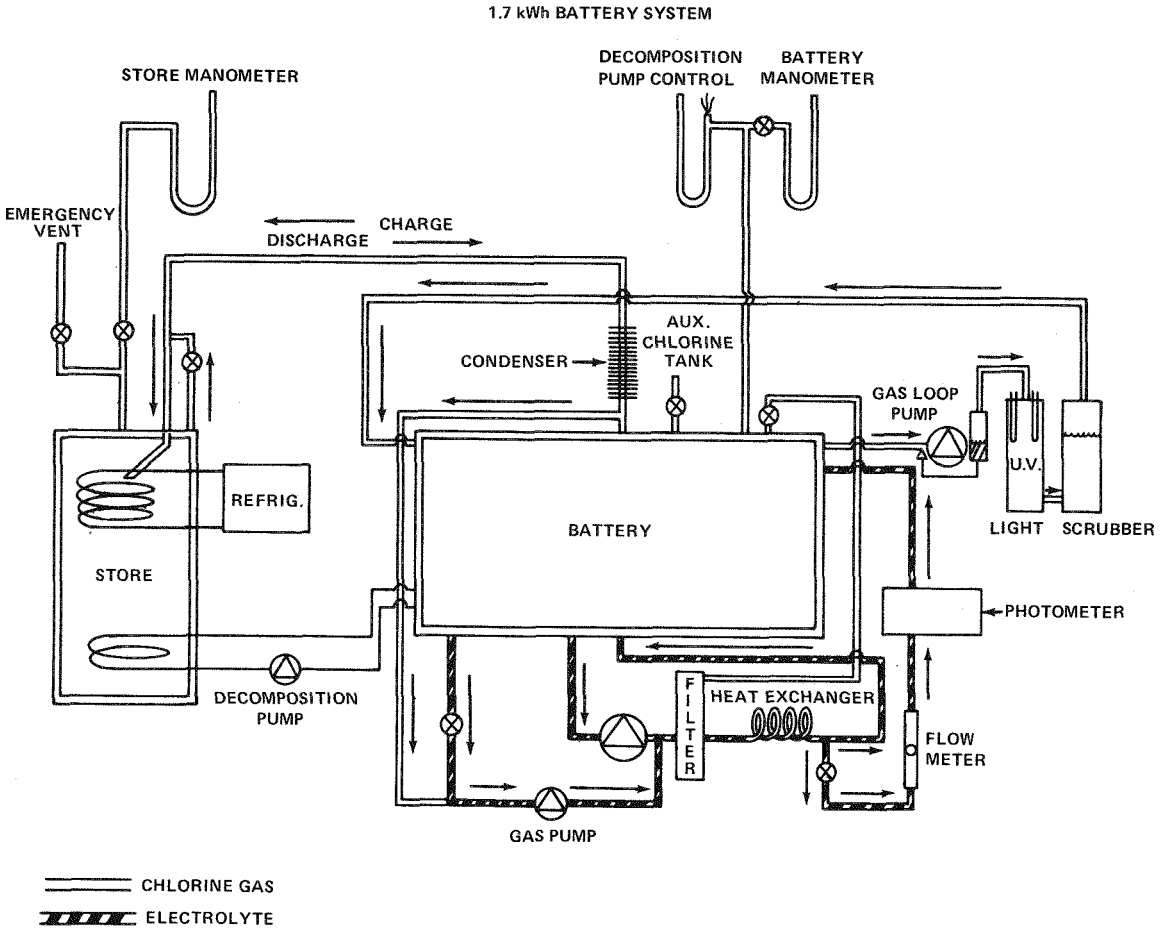

Figure 3-8. Diagram of the 1.7 kWh System Monitored and Controlled by Microprocessor.

- Main Electrolyte Pump (P1)
  - Dayton Model 27846 motor and controller.
  - 3/4 HP, 2500 RPM, variable speed.
  - Control: ON always.
- Store Agitator Motor (P2)
  - RAE Motor
  - 1/7 HP, 24V, variable speed by thyristor control
  - Control: ON during cooldown and constant current charge. OFF all other times.

- Decomposition Pump (P3)
  - Micropump
  - 115 volt, variable speed via triac control
  - Control: Activated by store pressure.
    (1) OFF during cooldown and constant current charge.
    (2) Active all other times unless store temperature exceeds a preset limit.

- Coolant Pump (P4)
  - Dayton Model 2Z846 Motor and controller.
  - 3/4 HP, 2500 RPM, variable speed.
  - Control: Activated by store temperature. Active during cooldown and constant current charge.

- Gas Injection Pump (P5)
  - Micropump
  - 115 volt, variable speed via triac control.
  - Control: ON during turnaround, constant current discharge and variable current discharge.

- Gas Vent Pump (P6)
  - Micropump
  - 115 volt, variable speed via triac controller.
  - Control: Activated by store pressure only during constant current charge.

- Ultra Violet Gas Loop Pump (P7)
  - Delta Motor
  - 1 HP, 100 V DC, variable speed via thyristor controller.
  - Control: ON always.

- Rectifier Charge/Discharge Relay (SW1)
  - General purpose relay, Potter & Brunfield KRP11DG
  - 24 volt DC, 0.1 ampere.
  - Control: Switches power supply between charge discharge. In charge mode during cooldown, constant current charge, cleanout and standby. All other times in discharge mode.

- Auxiliary Chlorine Supply Valve (SOL-1)
  - Solenoid activated pneumatic valve
  - 115 Volt, AC
  - Controlled: Active always according to store temperature or if store pressure is low during cooldown.

- Sump Heater (HI)
  - Haake Model E52 temperature controlled heater
  - 115 Volt AC, 1050 volt-amperes, self regulated.
  - Control: ON always unless sump reservoir exceeds a preset limit.
- Cleanout Resistor Relay (CRI)
  - 100 ampere contactor
  - 28 volt DC, 0.6 ampere coil
  - Control: On only during cleanout.
- Store Inlet Heater (H2)
  - Heating element
  - 5 volt, 10 ampere supply, transistor regulated
  - Control: ON only during turnaround and constant current charge.
- Current Supply
  - Udylite Rectifier Model 2CSC-3C003-251
  - 230 volt, 3 phase input; 3 volt, 300 ampere DC output.
  - Control: 0 to +5 volt DC Reference signal from controller scaled to 300 amperes.
    (1) On during constant current charge to preset current.
    (2) On during constant current discharge to preset current.
    (3) On during variable current discharge to preset current. Controlled decrease in current at end of useful discharge to zero current.
- STANDBY

  Upon initial power up, the control system enters the STANDBY mode. In an idle state, battery cycling is not initiated until manually switched to another phase in the cycle.
- COOLDOWN

  During COOLDOWN, the first step in cycle testing, the store is cooled to operating temperature.
- CONSTANT CURRENT CHARGE

  A timed phase, the CONSTANT CURRENT CHARGE mode, entered when the store reaches operating temperature, controls power rectifier current flow at a preset level.
- TURNAROUND

  A short timed mode, TURNAROUND set the period between CHARGE AND DISCHARGE modes to allow chlorination of the electrolyte.

- CONSTANT CURRENT DISCHARGE

  This mode is a timed phase during which current is held at a preset level.

- VARIABLE DISCHARGE

  This phase removes all useful charge from the battery. Constant current flow is maintained until the battery can no longer support the normal output voltage level. As voltage drops, the current is incremental toward zero current flow, the test cycle automatically proceeds to the CLEANOUT phase.

- CLEANOUT

  Any zinc remaining on the electrodes is stripped from the battery stack by circulating electrolyte and a 'short' (load resistors) connected across the battery terminals during this timed phase. Then, control returns to COOLDOWN and the test cycle is repeated.

Phase Control of Battery Test Cycle

Each battery test cycle includes seven test phases and the various actions taken by the auxiliary devices. Repetitive cycling of the system from charge to discharge and back to charge is the normal test operation. Figure 3-9 is a flow chart representation of the microprocessor system. A brief description of each cycle testing phase follows.

Failure Detection

Along with controlling the battery cycle, the microprocessor control system recognized symptoms of battery or auxiliary unit malfunctions. Data read by the computer is compared against preset system limits. If the battery cycle is in a phase where an auxiliary or battery parameter is not active the limits do not apply. If a limit is exceeded, an audible alarm sounds, a warning lamp is illuminated and an error message is displayed on the CRT screen.

To prevent unnecessary shutdown due to a transient condition, no further action is taken by the controller for a short period of time. Subsequently if data indicates that the faulty condition no longer exists, then the controller terminates the test cycle by reverting to STANDBY, or by taking some other predesignated course of action to prevent damage to the battery system.

Error messages are printed out on the teletypewriter; conditions existing at time of the malfunction and what failure occurred are identified. The error lamp remains lit to call attention to the fault and battery cycle testing shutdown. Recognized faults and a list of the action automatically taken by the controller is shown in Table 3-2.

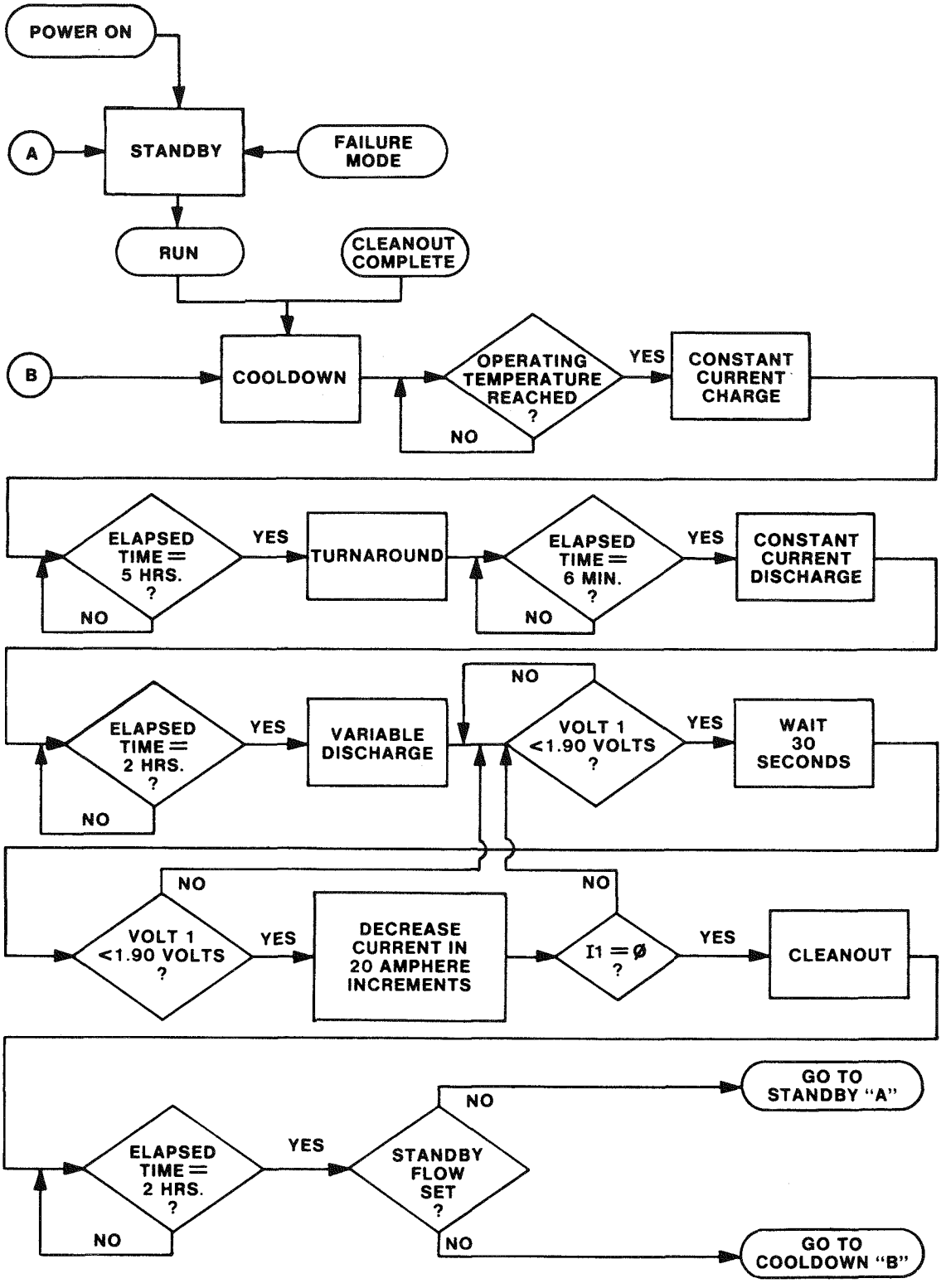

Figure 3-9. Logic Flowchart of Microprocessor System Operation.

Table 3-2

RECOGNIZED FAULTS AND CONTROL ACTION TAKEN

RECOGNIZED FAULTS MALFUNCTIONING CONDITION	CONTROL ACTION
BATTERY OVERVOLTAGE	Abort cycle testing; switch to STANDBY mode
BATTERY UNDERVOLTAGE	Abort cycle testing; switch to STANDBY mode
RECTIFIER CURRENT LOW (possible current supply and feeder circuit failure)	Abort cycle testing; switch to STANDBY mode
AGITATOR FAILURE (overload fuse blown; agitator unloaded)	Abort cycle testing, switch to STANDBY mode
LOW AUXILIARY POWER	Abort cycle testing; switch to STANDBY mode
CONTROLLER POWER INTERRUPTED	Switch to STANDBY mode (when power returns)
SUMP TEMPERATURE HIGH	Abort cycle testing; switch to STANDBY mode
GAS LOOP PRESSURE LOW	Abort cycle testing; switch to STANDBY mode
LOSS OF U.V. GAS BURNING LOOPS	(one lamp out) Alarm indicated; (both lamps out) Abort to STANDBY
HIGH SUMP HEATER BATH TEMPERATURE	Turn heater OFF
STORE TEMPERATURE (Out of operating range)	Switch to VARIABLE DISCHARGE mode-continuing test cycle to that point.

Commands are available to the operator which will override the failure mode abort command. Such operator commands, entered by way of the panel-mounted keyboard, are in effect until a counter-command is issued.

Data Display

Data for display, printout and control is read and stored in memory by the central processing unit of the computer. Status of battery parameters and calculated performance data are displayed on the cathode ray tube screen. Hardcopy printout of this information also is available on the teletypewriter. Merely by keyboarding the appropriate parameter description a printout of displayed data can be obtained (Figure 3-10). Table 3-3 lists the battery data displayed directly in the proper engineering units along with their printer descriptors.

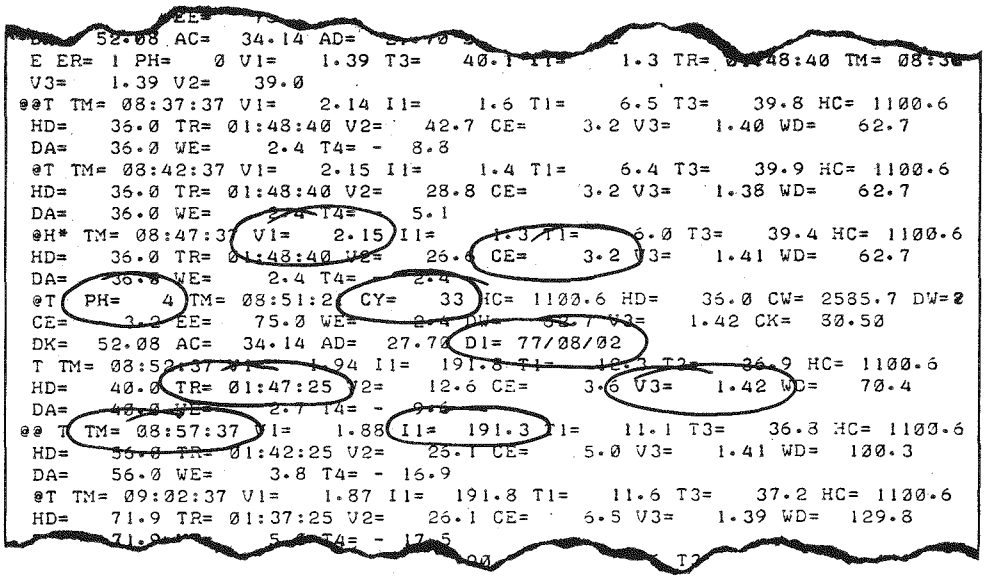

Figure 3-10. Typical Printout Obtained from the Microprocessor's Control and Data Acquisition Functions Monitoring the 1.7 kWh Battery System Operation.

Certain computer calculated data is displayed: Ampere-Hours, Watt-Hours, Coulombic and Voltaic efficiencies, etc. This data is calculated from instrumented devices reading battery current, voltage, time, and the like. Voltage and current readings are taken at the rate of ten-per-second. Each reading and the time increment between readings are used to calculate ampere-hours and watt-hours. Totals are

Table 3-3

DISPLAY FORMATS AND DESCRIPTORS

DATA SYMBOL	PRINTER DESCRIPTOR
V1	Battery terminal voltage
V2	Spectrophotometer (% transmittance)
V3	U.V. lamp detector voltage
T1	Store temperature
T2	Sump heater bath temperature
T3	Sump temperature
T4	U.V. burning system temperature
I1	Battery current
I2	Agitator motor current

the accumulation of summed individual calculations. These values are then displayed and available for printing. Cycle efficiencies are calculated at the end of each test cycle. Data descriptors reflecting status of the battery system under test and displayed on the CRT screen or printed by the teletypewriter at periodic intervals are shown in Table 3-4

Hardware

The microprocessor with its associated memory and input-output control is standard hardware manufactured by PCS, Inc. of Ann Arbor, Michigan. The control component (CPU), an 8080 microprocessor based board, controls the battery processes, test cycle, data acquisition and data logging functions.

Programmed instructions are contained in the processor's semi-permanent (PROM) memory; while test data is stored in the read/write (RAM) memory. Located on a second module, the memory may be reprogrammed by removing the PROM memory chips, and replacing them with chips containing new instructions.

Table 3-4

DATA DESCRIPTORS AND DISPLAYED BATTERY OPERATING STATUS

Symbol	Description of Symbology
HC	Current Cycle Charge Ampere hours ($\Sigma I \Delta t$)
HD	Current Cycle Discharge Ampere hours
CW	Current Cycle Charge Watt hours ($\Sigma VI \Delta t$)
DW	Current Cycle Discharge Watt hours
CE	Current Cycle Coulombic Efficiency ($\frac{HD}{HC} \times 100\%$)
WE	Current Cycle Energy Efficiency ($\frac{PW}{CW} \times 100\%$)
EE	Current Cycle Voltaic Efficiency ($\frac{WE}{CE} \times 100\%$)
AC	Accumulated Charge Kiloampere hours
AD	Accumulated Discharge Kiloampere hours
CK	Accumulated Charge kilowatt hours
DK	Accumulated Discharge Kilowatt hours
AA	Accumulated Coulombic Efficiency ($\frac{AD}{AC} \times 100\%$)
AW	Accumulated Energy Efficiency ($\frac{DK}{CK} \times 100\%$)
AE	Accumulated Voltaic Efficiency ($\frac{AW}{AA} \times 100\%$)
PH	Phase of the Cycle
CY	Cycle Count

Incoming analog signals from test probes (i.e. thermocouples, sensors, etc.) are fed into two analog-to-digital converter (ADC) modules that digitize the data for further processing. The CPU instructs the ADC's when and what to read, and then transfers the digitized data into memory. One ADC reads high level voltage signals; the second ADC reads low level signals in the millivolt range (such as current shunt signals and thermocouples). Thermocouple signals are linearized and converted to degrees Celcius by the computer.

Analog output signals, such as the voltage reference level (0 to 5 Volts) for the battery charge/discharge rectifier, are converted from digital signals by a digital-to-analog converter (DAC).

Battery auxiliary subsystems are connected to the computer through digital circuits which produce either ON/OFF states or recognize ON/OFF states. Circuit boards are packaged in a 20-slot card rack mounted in a NEMA-12 cabinet with front and rear doors. A panel mounted keyboard and CRT (Cathode Ray Tube) are visible through a window in the front door. The computer power supply is mounted in the rear of the cabinet near I/O connection terminal boards for interconnecting the microprocessor control unit with the battery and its auxiliaries.

Man-machine interface is accomplished through the panel-mounted keyboard and CRT. An operator can enter commands, change limits and tailor the print-out data. Also, the operator controls the changes through visual readout of entries, data and limits displayed on the CRT. Data logging is accomplished through printing on a teletypewriter. Optionally, data can be saved in machine usable form (paper tape) by operating the TTY punch.

Software

Computer software is divided into three catagories: process control, data display and logging. Process control comprises the major portion of the software instructions. It controls battery auxiliary subsystems, cycling and failure monitoring. These instructions direct the computer to compare battery operating parameters against predetermined limits, check conditions and turn an auxiliary unit on or off, or take no action. These instructions are not changeable from the controller keyboard since they are stored in the read-only memory.

Process parameter limits can be changed by entering the new limit in the appropriate location as it appears on the CRT display. For example, if Battery Overvoltage is set at 2.50 volts, and a change to 2.40 volts is desired, the operator "calls" the limit page on the CRT, positions the cursor (CRT pointor) at Battery Overvoltage, and then enters the new value via the keyboard. The new value digits appear at the top of CRT screen for confirmation. If entry is correct, the operator depresses the LOAD key and the new voltage limit replaces the old figures in

the location indicated by the cursor. Similarly, any other failure limit process set point or process time may be modified in a like manner. Overall supervision of the data logging and display also is a function of Process Control. It determines when data should be read and when it should be printed. It also transfers data to the CRT manager for display and instructs the manager to update the display.

Data collection and printout is the second function of the software. As previously described, analog-to-digital converters read data and store it in preassigned memory locations. Once in memory, it is available for operational and data logling purposes. Process instructions convert the binary data to decimal numbers (scaled in the appropriate engineering units). Upon command, either from process control or operator control, the information is converted to a teletype compatible form and sent over a two-wire current loop to the teletypewriter. The printer copy is formatted to print whatever data the operator desires. Also, at operator's option, a paper tape copy can be punched for later machine readable use.

Three separate print formats are available. Each may be ordered according to data descriptors listed previously in Table 3-4. "Print Format" output is a time cycle printout (shown in Figure 3-10) which periodically prints data at intervals preselected by the operator. This format may also be printed on command from the operator by entering the designator (:PR) via the keyboard. The command does not interfere with the normal print interval.

The "Phase Change Format" is printed whenever the cycle changes from one phase to another (either from process control or when forced to change by the operator). This format identifies the phase entered, time of entry, and any other data desired by the operator.

The third printout, is printed out whenever a battery system failure is detected which causes an interruption of the normal cycle. A descriptor coded to the type of failure plus any other data is printed on the teletypewriter at this time. This is when data descriptors are entered for the separate printout formats.

The third software function is information display. Data taken by the system is entered into the CRT manager's memory. The data is then continously displayed on the CRT page selected and continously updated as new data is taken. The inform-

ation is divided into blocks called "pages". There are seven pages of display. Pages are changed by pressing a key which causes the pages to alternately appear on the screen. Upon releasing the button, the last page displayed remains on the screen.

CONCLUSIONS

- The battery system developed as a result of the 1.7 kWh program represents a significantly improved state of the art. Automation operation on a continous basis is easily achievable, requiring only interfacing with the microprocessor control unit.
- Modifications made to the battery unit successfully minimized zinc plate nonuniformities, thereby allowing extended testing to be implimented.
- Nonuniformities in current density distribution resulting from resistance considerations associated with the chlorine comb design, and bus masking deficiencies (primarily on the zinc side) remain.
- From the standpoint of the porous-graphite chlorine electrodes, the 1.7 kWh battery represents a partially activated unit. Electrode processing for the unit represented a preliminary state of the art, and as such incomplete activation is understandable.

RECOMMENDATIONS

- Cycle-testing of the 1.7 kWh system should continue to failure. Although it now represents an earlier state of the art, valuable information concerning the permanency of electrode activity with time, and the stability of graphite in the battery environment will result.
- Attention should be given to correcting the current density nonuniformity resulting from the chlorine comb design. An improved discharge profile will result.
- Bus masking, primarily on the zinc side, should be further refined. Corrosion couples generated by bare graphite areas, although minized in this battery, are still present.
- If operation of the more fully activated 20 kWh system cannot be expedited and automated consideration should be given to the fabrication of another smaller, fully-activated battery. Life testing of this size unit could possible be more easily expedited.

Section 4

2 kWh BATTERY SYSTEM

INTRODUCTION

The 4v-2kWh battery system was built as a continuation of the technological development. This zinc-chlorine battery also uses ruthenized titanium electrodes. However, in comparison with the existing 1.4 kWh ruthenized-titanium battery, the new system contains more active chlorine electrodes. Electrode-to-electrode uniformity has been improved. The chlorine electrode framing and electrolyte manifolding are considerably more sophisticated in the new system. The battery represents state-of-the-art developments in several areas including electrode packaging, electrode-to-buss connections, voltaic performance and energy density for load-leveling applications.

Except for the chlorine electrode substrate, the battery design closely follows the 20 kWh battery design discussed in Part III, Section 5 of this report. The 2 kWh package contains two - 1 kWh monopolar cells. Each cell contains sixteen chlorine electrode pairs and seventeen zinc electrodes. The active area of the chlorine electrodes is 80 cm^2/face. The two cells are internally connected by a common buss which also functions to isolate the electrolyte from one cell to another.

The power connections to the end busses are constructed of titanium clad copper. To achieve good electrical contact between the titanium and the graphite, the graphite was first flame sprayed with titanium hydride to provide a thin, intimately contacted layer of titanium. A top view of the battery is shown in Figure 4-1.

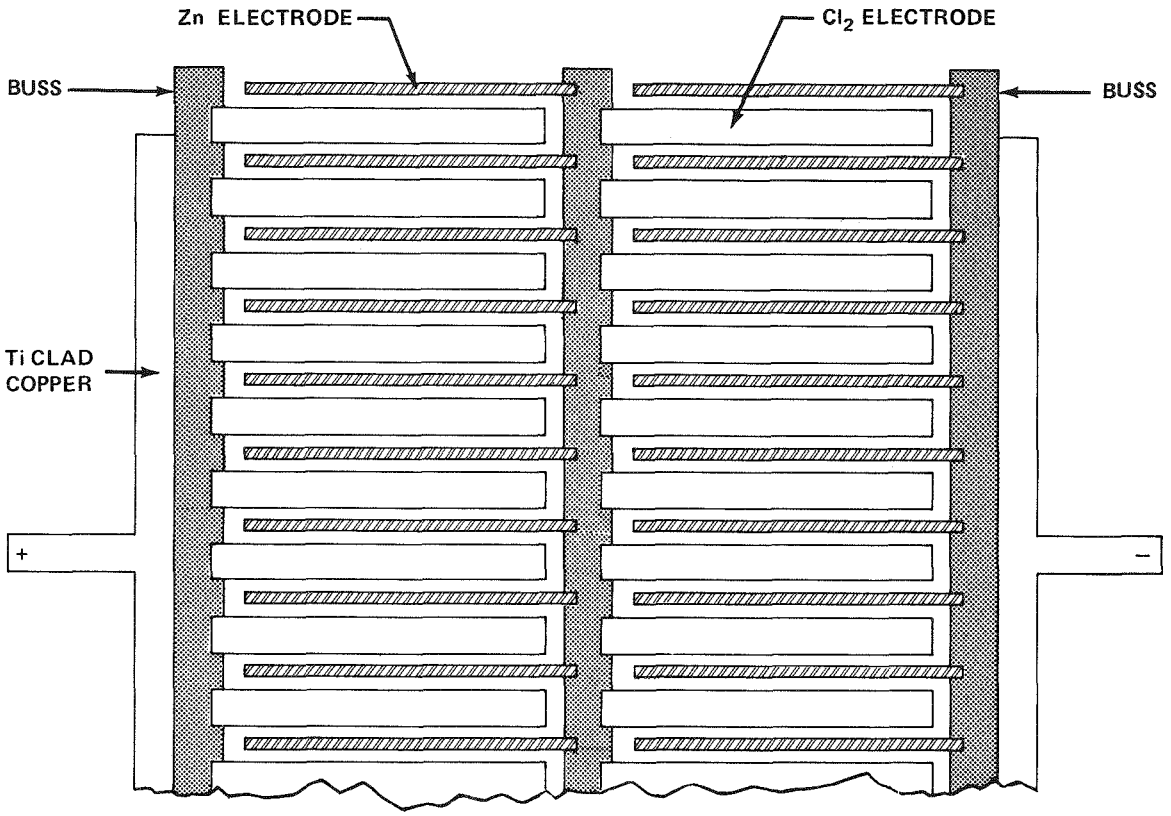

Figure 4-1. Top View of Electrode Array in the 4V-2kWh System
The busses and zinc electrodes are machined graphite.
The chlorine electrodes are ruthenized-titanium.

The battery was designed to charge at 50 mA/cm^2 for five hours followed by discharge at 45 mA/cm^2. From experimental data, the expected charging voltage was 2.25 volts per cell, or 4.5 volts total and the average discharge voltage was expected to be 1.95 volts per cell or 3.9 volts. A coulombic efficiency of 80% was anticipated to give an overall energy efficiency of about 70%.

EXPERIMENTAL RESULTS

As of this writing, modifications and changes are still being made on the battery. Although various problems associated with electrical contacts and electrolyte

hydraulics have been encountered, several have been solved. Some problems, however, still exist. Presently, the battery is being operated as a vented system and is using cylinder chlorine during discharge.

A polarization curve for the battery is shown in Figure 4-2. The voltaic measurements were made on the terminal graphite busses and do not include a 0.1 volt drop associated with titanium clad copper power connections. The discharge curve was obtained after the battery was well into its discharge cycle

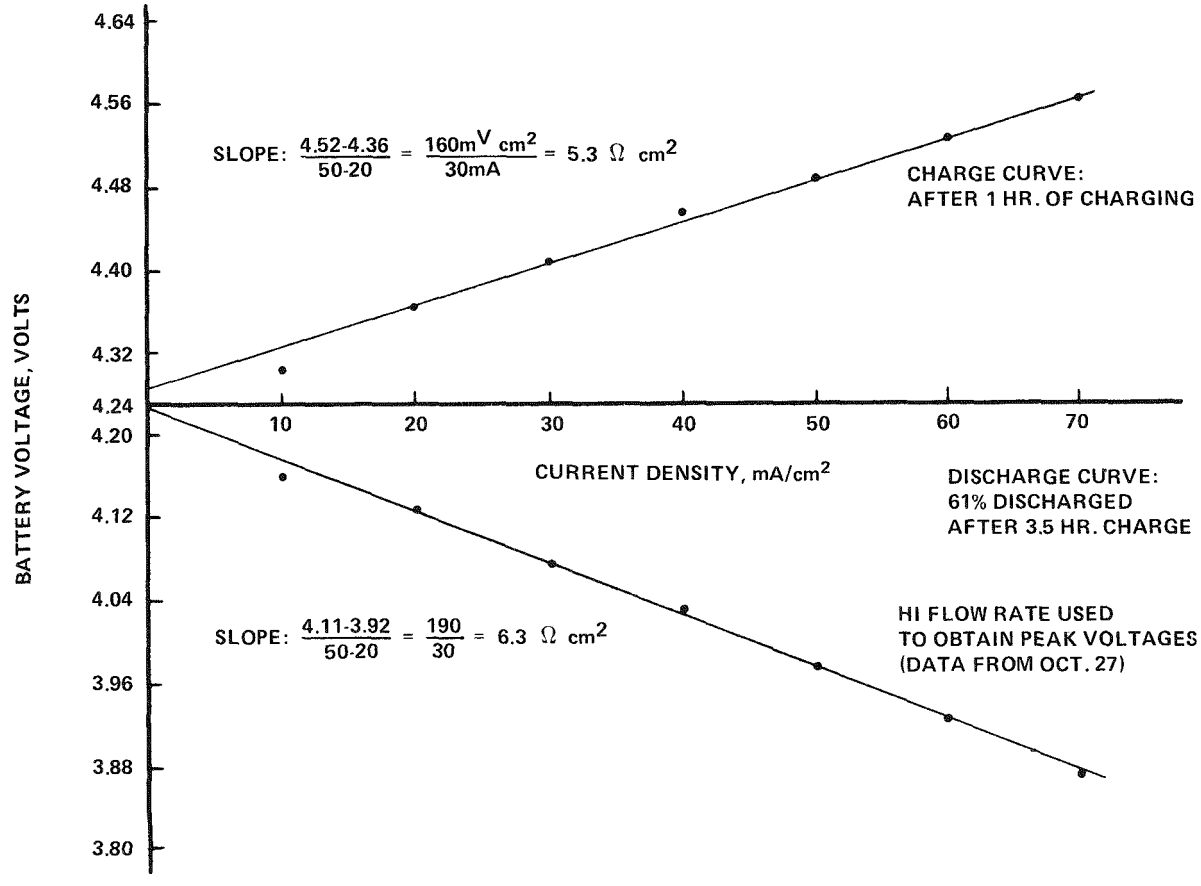

Figure 4-2. Charge-Discharge Polarization Curves for the 4V-2kWh Battery. Note the exceptional voltaic performance of the system.

In Figure 4-3, the charge-discharge profile is shown as a function of ampere-hours put into or taken out of the battery. The use of ampere-hours in the abscissa, rather than time, allows a more graphical presentation of the energy output of the battery in its final stages of discharge.

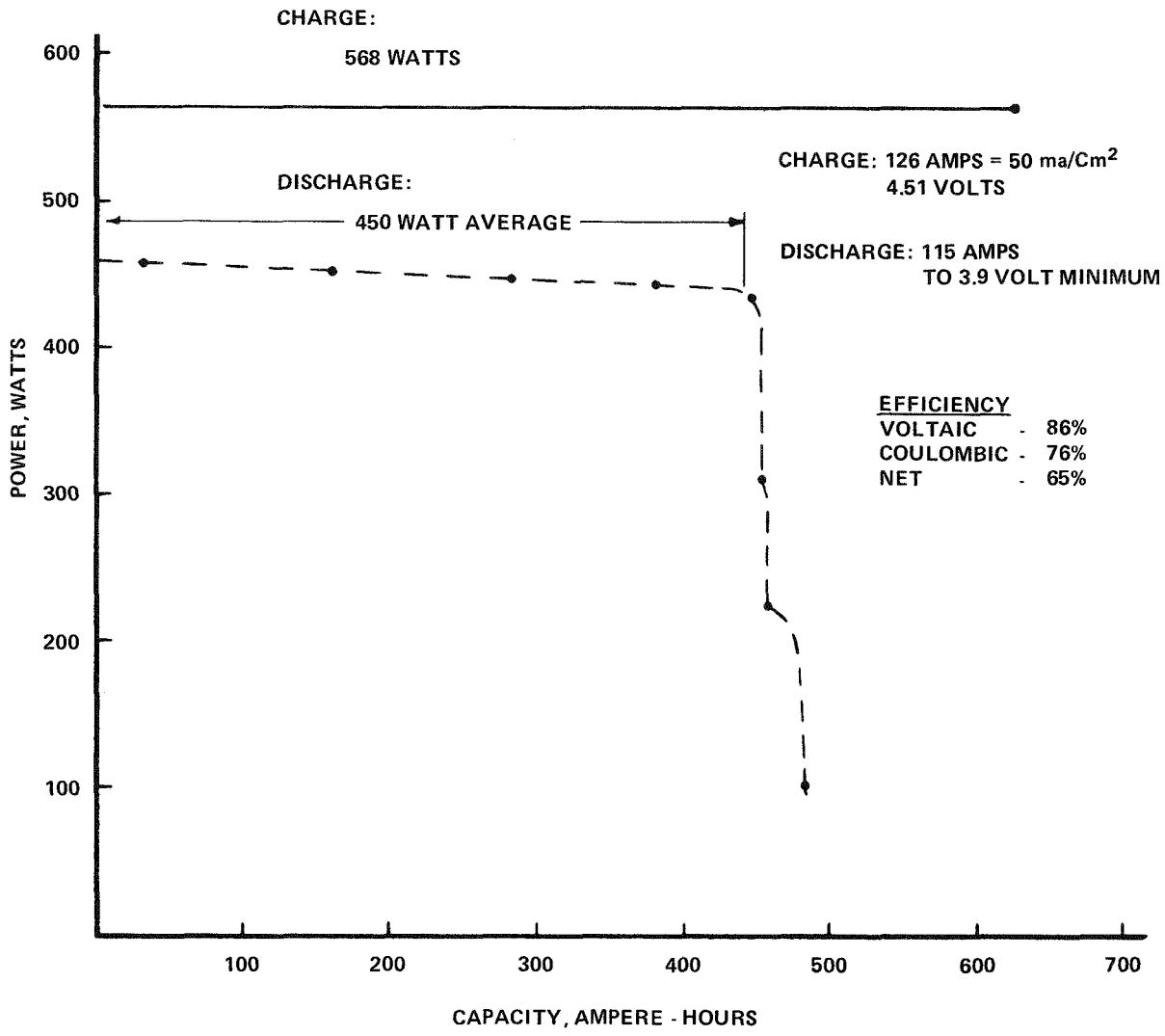

Figure 4-3. Charge-Discharge Characteristics of a 4V-2kWh Zinc-Chlorine Battery with Ruthenized-Titanium Chlorine Electrodes. Charge time is 5 hours. The slope of the power curve at the end of the discharge cycle is due to improvements in chlorine-electrode activation and cell hydraulics.

DISCUSSION

The high activity of the ruthenized-titanium chlorine electrodes is confirmed by the voltaic performance of this system. However, the low hydraulic throughout the system has caused problems in maintaining a consistent electrolyte flow from one electrode to another. This inconsistency of flow leads to voltaic stability problems on discharge. A solution to this problem would be to rebuild the manifold system and incorporate a flow controlling high pressure drop in the feeder tube. Coulombic performance of the system has been observed to be variable and generally poor. Intercell leakage, bad flow distribution, and poor zinc morphology would contribute to this lackluster performance. Proper identification of the associated problems would be helpful in improving the performance of this system and future systems. Because graphite is now the accepted chlorine electrode material, the importance of this ruthenized titanium electrode system has diminished considerably.

Section 5

20 kWh BATTERY SYSTEM - DESIGN, ASSEMBLY AND TEST

INTRODUCTION

Assembly of a 20 kWh battery was a primary goal of the hardware development program of the 1976 EPRI contract. This effort was to build an operational unit and simulate, on a small scale, the $ZnCl_2$ battery system considered for installation at the BEST facility.

The 20 kWh battery, currently under test, reflects modifications dictated by EDA's most recent state-of-the-art knowledge. Essentially, it is based upon a scale-up of $ZnCl_2$ batteries built and tested last year. Progressive battery scale-up revealed problems associated with battery capacity and physical size. Another important by-product of this rationale is creation of a data base from which materials, assembly and labor costs and facilities requirements can be projected for building larger battery systems.

Each of the significant facets of battery construction are presented in the following subsections. Order of presentation is chronological and, in that way, emphasizes significant concepts as they occurred during each step of the construction effort.

GENERAL ENGINEERING SPECIFICATION

Present design configuration of the 20 kWh battery (Figure 5-1) consists of a system operating on a five-hour charge-discharge cycle, a discharge power of approximately 4 kilowatts, and an expected overall energy efficiency of 66%. Nominal charging current is 260 amperes at 23 volts; whereas, nominal discharge current is 230 amperes at 19 volts.

Principal subsystems consist of the battery stack and the hydrate store. Six secondary subsystems interconnect with either the stack or store.

They have the following functions:

- heating and filtration of the electrolyte
- measurement of the chlorine concentration in the electrolyte
- recombination of hydrogen gas
- supplying coolant for the hydrate store
- chlorine gas makeup

During charge, zinc is deposited and chlorine gas generated. The electrolyte is circulated through each battery cell and returned to the sump by the electrolyte pump. Removed from the stack subassembly during charge by a slight vacuum, created by the hydrate formation process, chlorine gas accumulates in the store subassembly as chlorine hydrate.

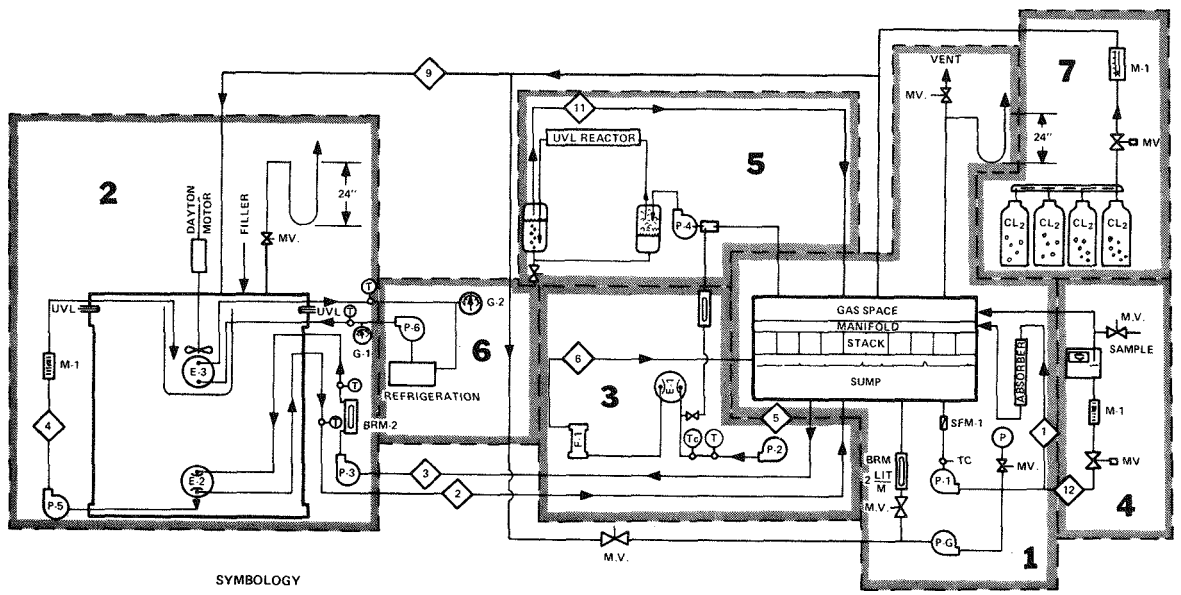

SYMBOLOGY

SFM – SONIC FLOW METER	TC – THERMOCOUPLE				
SP-1 – SPARGER	PC – PHOTO CONDUCTIVE CELL				
G-1&2 – GAUGE	UVL – ULTRA VIOLET LIGHT SOURCE				
MV – MANUAL VALVE	C – CONDENSOR				
SV – SAMPLE VALVE	VC – VELOCITY CHAMBER				
BRM – BROOKS ROTOMETER	Ⓣ – THERMOMETER				
E-1, 2, 3 & 4 – HEAT EXCHANGER	Ⓟ – PRESSURE GAUGE				
P-1, 2, 3, 4, 5 & 6 – PUMP	P-G – GAS PUMP				
F-1&2 – FILTER	M.V. – MANUAL VALVE				
M-1 – BALL TYPE FLOW METER					

FLOW LINES

1 – MAIN ELECTROLYTE SUCTION		8 – Cl_2 TO STACK	
2 – FROM DECOMPOSITION LOOP		9 – STACK TO STORE (ON CHARGE)	
3 – TO DECOMPOSITION LOOP		10 – Cl_2 TO STORE	
4 – WATER RECIRCULATION		11 – GAS FLOW IN REACTOR LOOP	
5 – $ZnCl_2$ ELECTROLYTE FILTER LOOP FLOW		12 – MONITOR $ZnCl_2$	
6 – FILTERED $ZnCl_2$ LINE		13 – GAS LOOP	
7 – Cl_2 GAS FROM FILTER			

Figure 5-1. 20 kWh Battery System Flow Diagram Identifying Seven Discrete Subsystems. Battery Stack 1, Hydrate Store 2, Heating and Filtration 3, Chlorine Concentration 4, Hydrogen Reactor 5, Coolant Supply 6, and Chlorine Supply 7.

Hydrogen gas, produced during the charge cycle, combines with chlorine in the hydrogen reactor subsystem to produce hydrogen chloride. Product of this recombination is reintroduced into the electrolyte.

During discharge, chlorine hydrate is decomposed by circulating warm electrolyte through heater coils located within the store subassembly. Chlorine (Cl_2), thus produced, is returned to the battery stack subassembly by a gas pump. The Cl_2 is introduced into the electrolyte recirculation line on the high pressure side of the electrolyte pump where it rapidly dissolves into the electrolyte. This dissolved chlorine reacts electrochemically with the deposited zinc to produce an electric current.

Components directly supporting operation of the battery are defined as subsystems. This includes the battery stack with its manifold and container; the main electrolyte pump; the electrolyte header between the pump and battery manifold containing the chlorine absorber; and a gas pump for injecting the chlorine gas into the chlorine absorber.

Battery Stack

Thirty-six cells, each with an active area of 80 cm^2, were connected in parallel to a common bus. Then buses were connected in series to form a 10 kWh/20V bank. Two of these banks were connected in parallel to give 20 kWh/20V. Hydraulically, all cells were in parallel. Electrolyte was supplied to the cells through capillary tubing from a sub-manifold running the length of the buses. The sub-manifolds, in turn, were supplied from the main battery manifold perpendicular to the bus and run the length of the stack. After passing upward through the cells, the electrolyte was separated at the bus level for electrical isolation and was allowed to overflow the stack into a common sump. From the sump, the electrolyte entered the suction side of the main pump. The main pump delivered the electrolyte through the header back into the battery manifold.

Main Pump

A Mission 1 x 1-1/2 PA centrifugal pump with a 3/4 HP variable speed D.C. motor (Dart Industries) circulates the electrolyte through the battery system. Operation at 1300/1400 RPM gave the desired 28 to 30 gpm flow rate (2cc/min/cm^2) at 3 to 4 psig The battery subsystem is shown schematically in block 1 of Figure 5-1

Store Subsystems

The store subsystem was defined to include those components directly supporting the storage of chlorine, as chlorine hydrate during charge, and the regeneration, for battery consumption, during discharge.

The "hydrate store" was a cylinder 23 inches in diameter and 36 inches high. It contained the means for formation and served as a storage container for the hydrate. Also included as part of the store subsystem were the store liquid pump, whose purpose was to recirculate hydrate forming water within the store, and a decomposition pump for circulation of the warm battery electrolyte during discharge.

Hydrate was formed during charge by contacting the chlorine gas with cooled water under turbulent conditions in a formation zone at the top of the cylinder. The cylinder contained approximately 80% water by volume. The formation apparatus consisted of a shrouded impeller driven by a 3/4 HP Dayton motor serving to create a turbulent contacting condition a few inches below the gas-liquid interface. Cooling was provided by a coil heat exchanger 7 inches in diameter located around and below the formation zone. A second impeller on the shaft, 8 inches below the first, served to agitate the solution below the formation zone for the purpose of improving the heat exchange and keeping the cooling coils free of hydrate. Cooling was accomplished by circulating 25% ethylene glycol solution in the coils. The power requirements for the impeller are shown in Figure 5-2.

The formation temperature was maintained at 7-8^{o}C. In this temperature regime the equilibrium pressure for formation was low enough to draw chlorine into the store from the battery. Hydrate formed in the formation zone settled to the bottom of the store against a bottom filter. This was continued until the available volume was approximately 2/3 filled. Water was circulated continuously from below the filter located at the bottom of the store to the formation zone in the top to provide cooling for the bearings in the impeller drive shaft assembly.

Hydrate was decomposed during discharge by circulation of warm electrolyte through heating coils located in the bottom of the store above the filter. Rising gas bubbles from the decomposition served to promote mixing and temperature uniformity. Water was continously circulated during the discharge from bottom to top. Coolant was not circulated. This subsystem is shown schematically in block 2 of Figure 5-1.

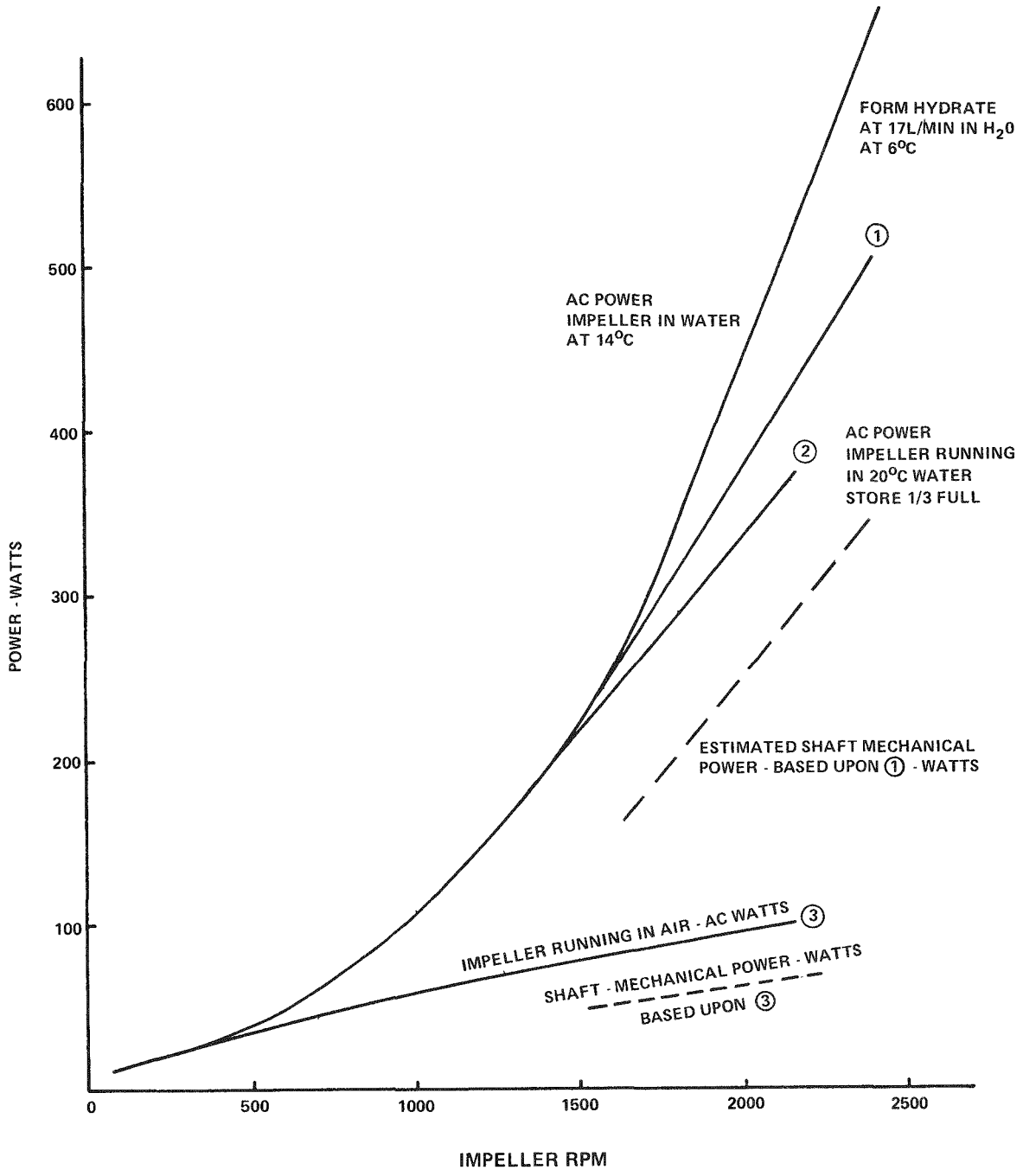

Figure 5-2. Hydrate Store Impeller Power Requirements

Heating and Filtration Subsystem

The heating and filtration subsystem served to maintain the battery at operating temperature and to filter suspended particulate matter from the electrolyte. It consisted of six primary components. A small magnetically-coupled centrifugal pump circulated a stream of electrolyte from the battery through a coiled titanium tube heat exchanger and a sintered glass filter back to the battery. Heat was supplied through the shell side of the exchangerfrom an electrically heated

water bath located external to the system and equipped with a pump for hot water circulation. Temperature regulation was maintained by operating hot water pump in an on-off control mode with a thermocouple temperature controller sensing battery temperature. This subsystem is shown schematically in block 3 of Figure 5-1.

Chlorine Concentration Subsystem

The chlorine concentration subsystem consisted of three components, a U.V. absorption spectrophotometer, a flowmeter and a valve for flow regulation. Electrolyte from the high pressure side of the main pump was passed through a control valve, through a flow meter and through the spectrophotometer. Chlorine concentration in the electrolyte was measured as proportional to absorbance at 3800 Angstroms. This subsystem is shown schematically in block 4 of Figure 5-1.

Hydrogen Reactor

Function of the hydrogen reactor subsystems was to photochemically recombine hydrogen gas formed in the battery with chlorine under controlled conditions. In this way, any hazard due to excessive hydrogen accumulation was eliminated. The hydrogen chloride thus formed was returned to the battery system. This system consisted of three major components, a G-10 titanium gear pump to move the gas through the reactor followed by the reactor chamber with fluorescent U.V. lamps for the photochemical energy source. A liquid trap at reactor outlet served to thermally isolate the gas in the reator chamber from the battery gas space, for the purpose of flashback prevention.

The pump operated continously throughout charge and discharge at a rate of 15 to 30 liters/minute of gas. Hydrogen present in the gas was 98% removed when hydrogen concentrations in the gas were 3.5% or greater. Removals were somewhat less efficient at lower concentrations.

Battery electrolyte circulated continously through the gear pump to provide the liquid seal. It also circulated through the gas trap at the reactor outlet and back to the battery through the gas return. This served to return HCl collected in the trap to the battery system.

The liquid seal in the pump thermally isolated the inlet of the reactor from the battery gas space. This subsystem is shown schematically in block 5 of Figure 5-1.

Coolant Supply

The coolant supply subsystem, operated only during the charge cycle, consisted of an ethylene glycol bath cooled by a Dunham-Bush-CB5DO chiller. Glycol was circulated to the hydrate store by a March (TE5-MD) pump. This pump was operated in an on-off mode with a temperature controller operating from a thermocouple located in the formation zone of the chlorine hydrate store. (Block 6 of Figure 5-1).

Chlorine Supply

Chlorine supply consisted of four chlorine cyclinders connected in parallel with an inline flow meter. It was used on an intermittant basis for make up chlorine or for operation of the battery independent of the store. (Block 7 of Figure 5-1).

DESIGN, SPECIFICATION AND ASSEMBLY

For success within the overall framework of this program, the battery, or more particularly, the stack had to meet certain design objectives. These can be stated as follows:

- Battery was patterned as much as practical after concepts envisioned for the Mark 2 peak-shaving battery design.
- Design details provide experience with features suited to high volume production.
- To meet program time schedules, the stack had to be constructed of available materials and by relatively conventional methods.
- Battery was used to investigate operating variables and useful as a laboratory tool.

Stack Specifications

The following is a list of specifications developed for the 20 kWh battery stack. This list evolved from meetings with project team members wherein existing test battery performance was reviewed and consideration given to the existing studies of proposed large scale systems. The desired characteristics for the 20 kWh battery stack are:

- All electrodes flat, graphite plates not requiring close manufacturing tolerances
- Activated chlorine electrodes produced from porous graphite (2 mm thick with active area of 80 cm^2) - discussion of the activation process will be found below.
- Zinc electrodes produced from ATJ graphite plates (2 mm thick) with an active all around surface larger than the chlorine electrodes by 0.050 of an inch
- Spacing between electrodes measures 0.150" of an inch

- Circulating liquid fed to chlorine electrolyte chamber at a designed rate of 2 ml/min/cm^2 of electrode face
- Electrolyte circulated to the electrode chamber from a manifold through a control tube that provides ½ psi pressure drop and 4" of flow path for electrical resistance to parasitic currents
- Electrode chamber vented in the top with 0.055" diameter holes to allow accumulated gases to escape
- A unit cell will be established containing 18 chlorine electrode packs and 19 zinc electrode plates and will be rated at 1 kWh capacity
- Battery contains 20 unit cells, arranged two in parallel and ten in series, and operates at a nominal 20 volts dc.
- Circulating electrolyte will be distributed evenly to all chlorine electrode packs through a constant velocity manifold system in order to maintain a homogeneous mixture of dissolved and entrapped gases in the liquid
- Inlet to this manifold system will be at a point of approximate mid-voltage for the stack to minimize parasitic currents within the manifold
- Stack construction materials will be limited to those which are presently qualified for use in the battery environment. Other than graphite, these are KYNAR and TEFLON plastics and titanium metal.

Activation of Porous-Graphite Chlorine Electrodes

The thermochemical activation in nitric acid of electrode plates for the 20 kWh battery stack necessitated scaling-up of existing procedures. Over 1500 plates were successfully processed. Of these, 720 (for 360 pairs of chlorine electrodes) were employed in the battery, the remainder serving as a back-up in case spares were required. Electrode plates remaining after completion of the stack were employed in other testing programs.

Processing was done in seven batches of approximately 220 pieces each. This represented a scale-up by a factor of ten to twenty based upon previous small-scale testing. The processing time of ten hours employed was chosen firstly because acceptable voltaic performance was ensured based on previous test results.

Figure 5-3 is a drawing of the reactor unit employed. The outer PVC shell was employed as a safety measure. Power to the immersion heaters was regulated by a temperature-control unit which operated off of the thermocouple indicated. In this manner temperature was maintained at $112^{o} \pm 2^{o}C$. Although the condensing unit employed minimized acid losses, the periodic addition of stock concentrated nitric acid was still required.

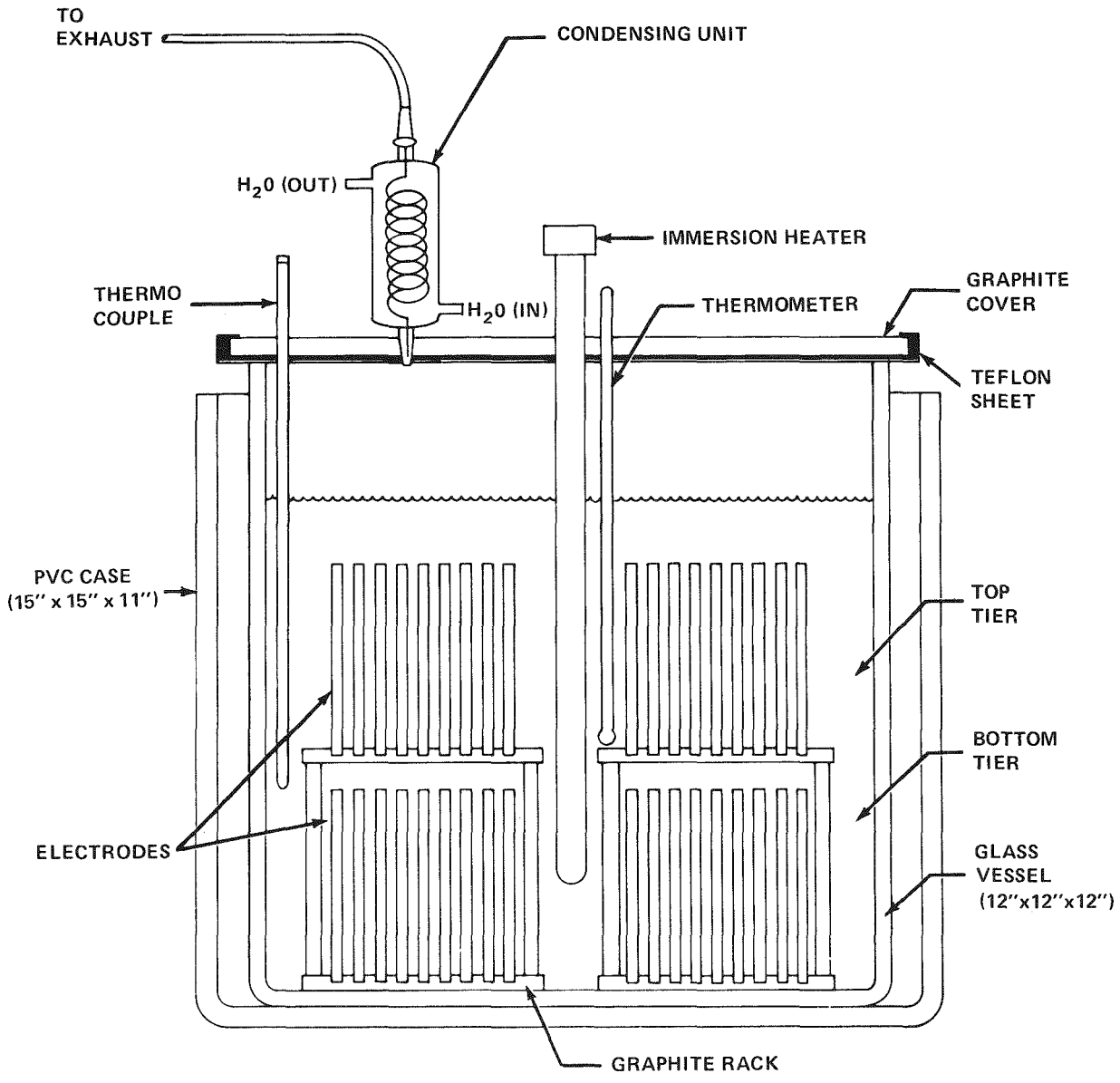

Figure 5-3. Vessel Designed for Electrode Activation Showing the Method of Arrangement of the Porous-Graphite Electrodes

After activation, the electrodes were washed thoroughly with water and air-dried in an oven at 110°C. The processed electrodes were then stored until needed for stack assembly. The seven batches were sampled for qualification purposes, and tested in a zinc-chlorine cell. The test conditions approximated those used later in 20kWh battery operation. The results of these qualification tests are shown in Table 5-1.

Table 5-1

EPRI 20 kWh CHLORINE ELECTRODE QUALIFICATION RESULTS

BATCH IDENTIFICATION		No. of Days in HNO_3	Max^m Voltage Discharge	Max^m Voltage Charge	Max^m Voltaic Efficiency	Mean Voltage Discharge	Mean Voltage Charge	*Calculated, Mean Voltaic Efficiency
A	Top Tier	7	1.945	2.257	86.3	1.920	2.257	85.1
	Bottom Tier	10	1.928	2.252	85.6	1.905	2.253	85.6
B	Top Tier	9	1.973	2.235	88.3	1.950	2.235	87.2
	Bottom Tier	10	1.954	2.233	87.5	1.920	2.233	86.0
C	Top Tier	8	1.960	2.255	86.9	1.945	2.255	86.3
	Bottom Tier	10	1.929	2.227	86.6	1.923	2.227	86.3
D	Top Tier	9	1.978	2.235	88.5	1.947	2.235	87.1
	Bottom Tier	10	1.970	2.237	88.1	1.940	2.235	86.8
E	Top Tier	10½	1.980	2.235	88.6	1.966	2.235	88.0
	Bottom Tier	10½	1.950	2.250	86.7	1.920	2.250	85.1
F	Top Tier	10½	1.950	2.242	87.0	1.935	2.242	86.3
	Bottom Tier	10½	1.950	2.264	86.1	1.910	2.265	84.3
G	Top Tier	10½	1.957	2.252	86.9	1.935	2.252	85.9
	Bottom Tier	10½	1.970	2.274	86.6	1.915	2.257	84.8

* Based on average of a 4 chlorine electrode cell.

GRAND AVERAGE 85.99 ± 1.09

Based on the results in Table 5-1, it was concluded that the activation procedure had been scaled-up satisfactorily. It was observed that the voltaic efficiency was consistently better for electrodes in the top tier as compared to the bottom tier. The reason for the above variation was assigned to the fact that cold HNO_3^- was added periodically in order to bring up the level in the pot, which caused a lowering of temperature by about 25^oC in the bottom zone of the pot. Pre-heating of acid added would have eliminated this problem.

Stack Design

The 20 kWh battery stack design created for the purpose of meeting the objectives and specifications outlined in the preceding section is illustrated in Figure 5-4. A general description of the overall design will be presented first. Certain details will be described more explicitly further on in this report.

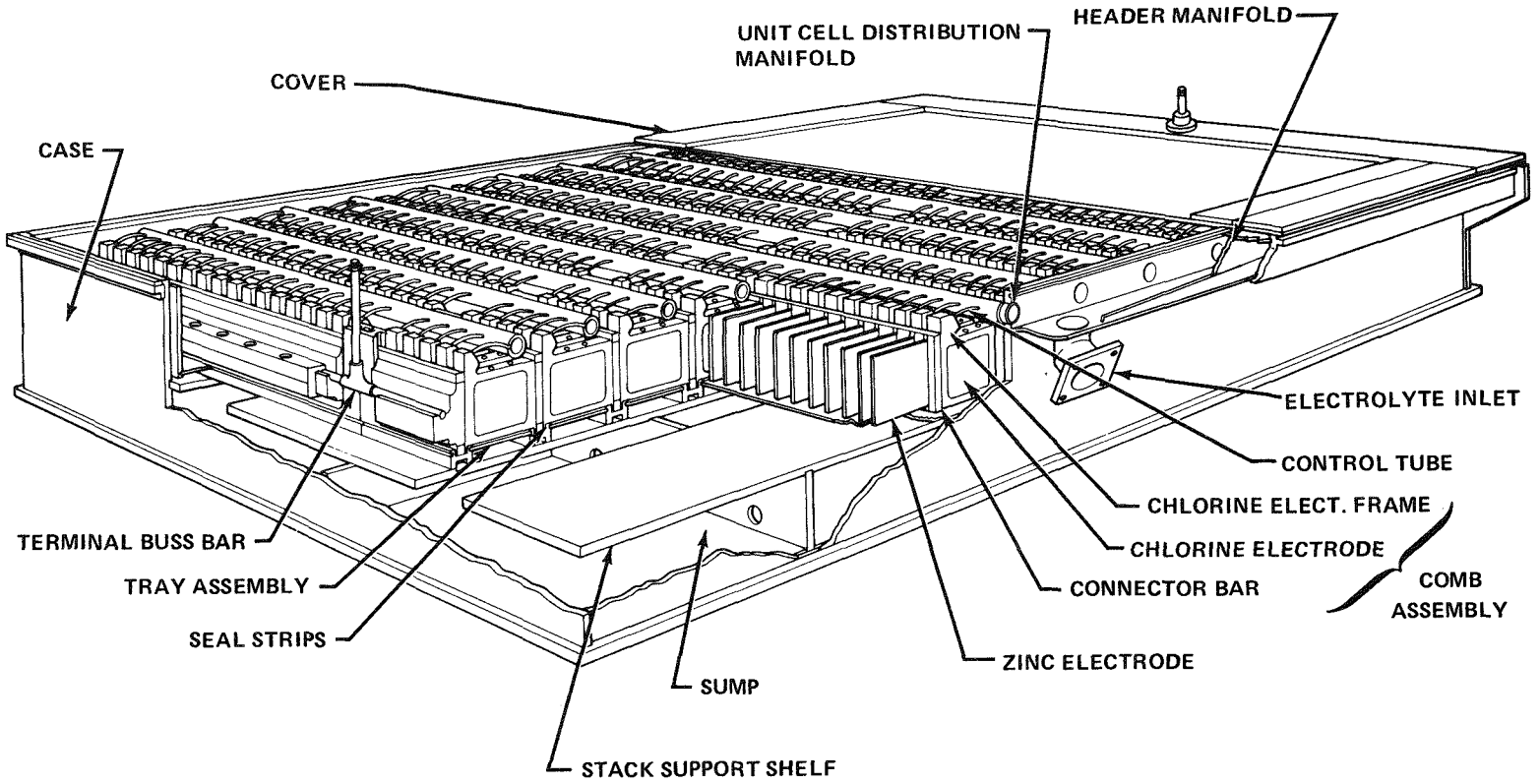

Figure 5-4. Isometric Cut-away View of the 20 kWh Battery Stack Showing the Electrode Arrangement and Manifolding.

Within the case, 20 unit cells are supported on a shelf over the sump in two rows of 10 cells each. Each row is mounted inside a separate tray assembly. The two rows are connected to a common terminal bus at each end thus forming two parallel current paths through the stack. These terminal bus bars are "inverted-T" shaped members. They are fabricated from ½" round copper bar completely clad in titanium metal. The horizontal cross bar is clamped to the end connector of each row of cells. The vertical leg is arranged to extend upward through the cover and to provide an exterior electrical power connection.

The unit cells in each path are series connected by means of collector bars that are common to any two adjoining cells. These collector bars form the backbone for a typical "comb" assembly. They each support a series of chlorine electrode from the opposite face. When intermeshed with an adjacent comb, the individual elemental cells are formed and a unit cell is completed.

The individual combs are located in the stack by inserting their central connector bar into receiving slots formed in the tray assembly. These slots contain compliable seal strips so that each connector bar effectively forms a partition across the tray maintaining a separate electrolyte container for each unit cell.

The electrodes are retained in slots machined in each face of the graphite connector bars by a compression insert pressed in place alongside the edge of each electrode. The zinc electrodes are each a rectangular plate of .080 thick ATJ graphite material. They measure 3.787" x 4.0625". Each chlorine electrode is an assembly of two flat 3.938" square plates of porous PG-60 graphite material 0.080" thick, mounted in a 4-piece frame assembly (see Figure 5-4). The plastic frames accurately space the two electrode plates 0.150" apart so that an electrolyte chamber is formed within. This chamber is vented by two small holes in the top. Further, this chamber is fed a supply of electrolyte through a passage leading down one edge of the frame, from an inlet in the upstanding projection to two nozzles in the side of the frame. This passage serves to control the amount of electrolyte entering each electrode from the manifold. After uniform mixing within the electrode, the liquid passes through the porous faces into the intra-electrode gap between the chlorine and the zinc faces. This gap is accurately set at 0.150" by the frame sealer strip and the zinc mask.

Since each stack of cells is contained within a tray and since the intra-electrode gap is open on top, the pumped electrolyte fills the volume and then overflows out across the top of the electrodes. The plastic cap on each connector bar directs

this electrolyte towards the end where an overflow weir allows the liquid to cascade down each end onto the supporting shelf. From here it runs under the cell to the center where it again cascades over an edge into the sump below. Here in the sump is the first mixing of electrolyte from one unit cell (or one voltage level) with that of any other unit cell (or different voltage level). Central in the sump

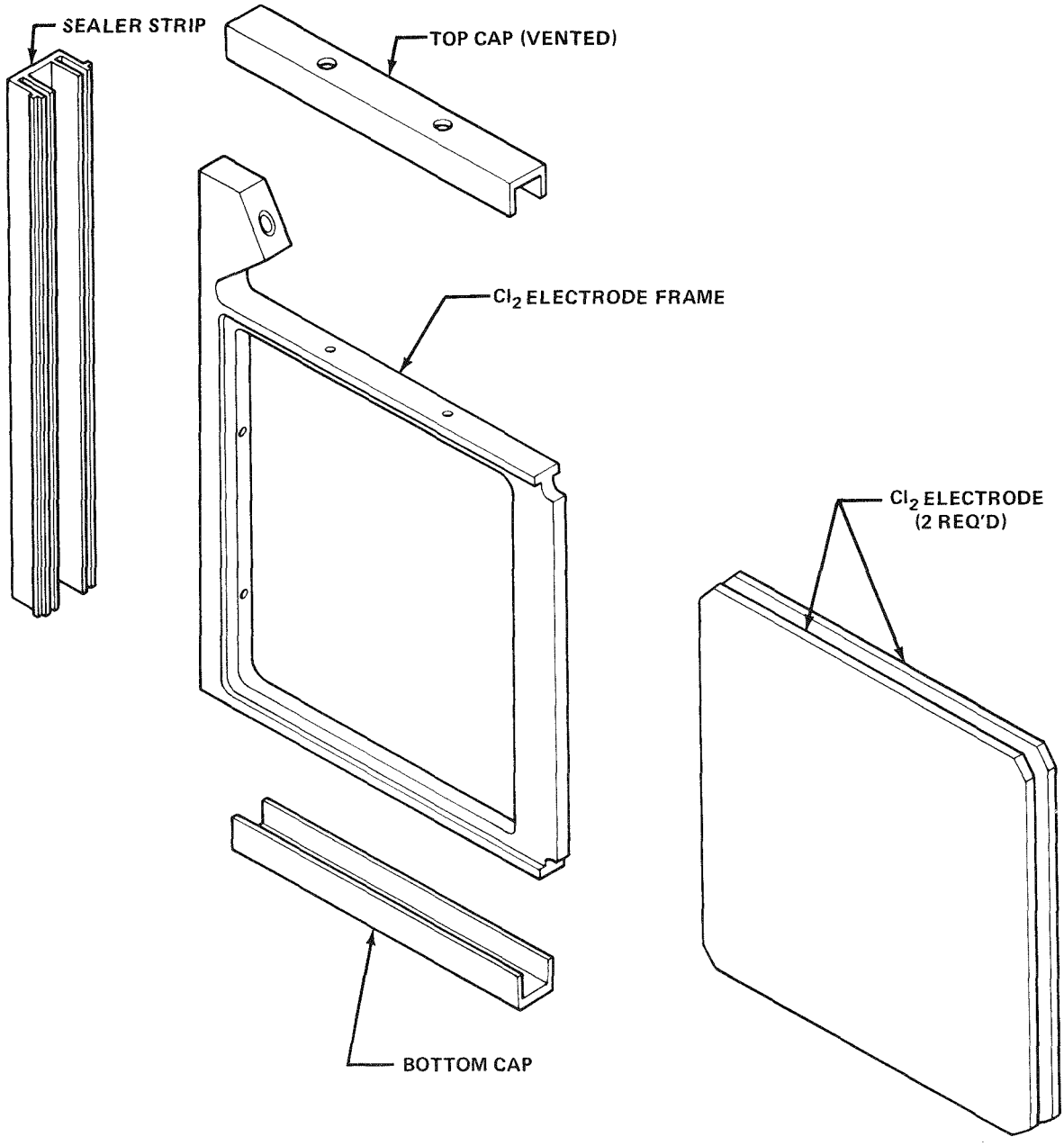

Figure 5-5. Exploded View of the Chlorine Electrode Assembly

bottom is a large opening that allows the electrolyte to drain into the pump intake line which is external to the stack.

Reconditioned electrolyte is pumped back to the stack through an inlet fitting located in the center of the header manifold. This manifold, or distribution duct, runs along the top edge of one side of the battery case. The duct is a box section built as an integral part of the case structure. The inner and outer walls of the box section are not parallel so that the area of the manifold is constantly reducing from the center inlet to the ends.

This maintains a rather constant flow velocity in the header by compensating for the volume lost at each connection to the separate unit cells.

The manifold for each unit cell also has a constantly reducing cross-section for the same reason. This is accomplished by inserting a tapered core into the manifold pipe. These distribution manifolds connect with the header ports by means of a slip fit tubular coupling. Each manifold has 36 outlets to feed electrolyte to the individual chlorine electrodes in that particular pair of unit cells. Both these outlets and the separate chlorine pack frames are built with matching sockets allowing a resilient plastic connecting tube to be slip-fitted between them.

The battery case which surrounds the entire stack is designed to give rigid support to the unit cells, to provide an electrolyte sump, and to form a sealed enclosure for the collecting of chlorine gas. Overall case dimensions are approximately 54" long, 16" high and 37" wide.

This case is constructed as an open box with a removable cover. Halfway down inside is a shelf which separates the box into a sump compartment below and a stack compartment above. The shelf, supported by the case sides and some partitions beneath it, has two openings running lengthwise. One of these is under each stack tray. These openings allow the returning electrolyte to drop into the sump compartment.

Around the upper edge of the box is a sturdy overhanging lip. This provides a seal surface and securing means for the removable cover. This cover is fabricated from a KYNAR sheet reinforced with a stiff edge frame and cross-bracing. A one-piece continous clamp rail is provided for each edge of the cover. Each channel-shaped rail hooks under the lip and carries a row of clamp screws over the edge of

the cover. When these are tightened down, the loose cover is clamped tight to the case upper sealing surface. A TEFLON gasket is used to make a gas-tight joint.

A hole at each end of the cover allows the round terminal bus rod to extend out through the case. A compression type tube fitting mounted in a boss seals this outlet. Similar, but smaller fittings are used elsewhere in the cover and tapped into the case walls to pass various tubes or wires in and out of the case through gas tight connections. As mentioned earlier, at the center of the case bottom is a 3" diameter outlet port to allow electrolyte to pass down into the main circulating pump.

A good many of the detailed features of this design were employed so that the stack would be useful as a laboratory investigative tool. The removable cover clamp details and the slop fit connections for the manifolds, for instance, make possible repeated opening and disassembly of the stack with ease. Supporting the comb assemblies in open slots allows the unit cells to be removed and examined if desired. These slots and the small plastic tubes connecting the electrodes with the manifold allow the thermal expansion and contraction of the assembly without placing stress on the thin graphite electrode plates. The small plastic manifold connecting tubes are also designed for easy replacement with larger or smaller diameter. This would make possible increasing or decreasing the designed pressure drop in the electrolyte control system should this be desired. Pressure drops, velocities, and quantities can be adjusted for a uniform flow throughout the hydraulic system by modifying the tapered plugs inserted in each of the 10 distribution manifolds.

Any projected large scaled system will certainly contain a vast number of individual electrodes. Therefore, the production of these is certainly an important design element. Securing each individual electrode in its connector bar by means of a deforming insert that will adjust to variations helps considerably in this area. Both electrode thickness and slot width can vary with considerable tolerance and still have this juncture perform satisfactorily.

The four-piece frame used to assemble the chlorine electrode is another design element that contributes in this area. A number of required features are contained in these details. The electrode plates are mounted, spaced and sealed along the edges without requiring precise dimensional control of the porous graphite material. The face-to-face spacing of the various electrodes is controlled by the plastic members. The electrolyte feed tube, the inlet nozzles and the gas vent ports are all precisely formed within the frame parts. Lastly, a self-locating snap-together

assembly is envisioned for volume production. All this surely indicates precise injection molded parts. For this 20 kWh battery parts designed to be machined from readily available plastic sheetswere developed to closely simulate such injection molded parts. The assembly sequence is summarized in Figure 5-6.

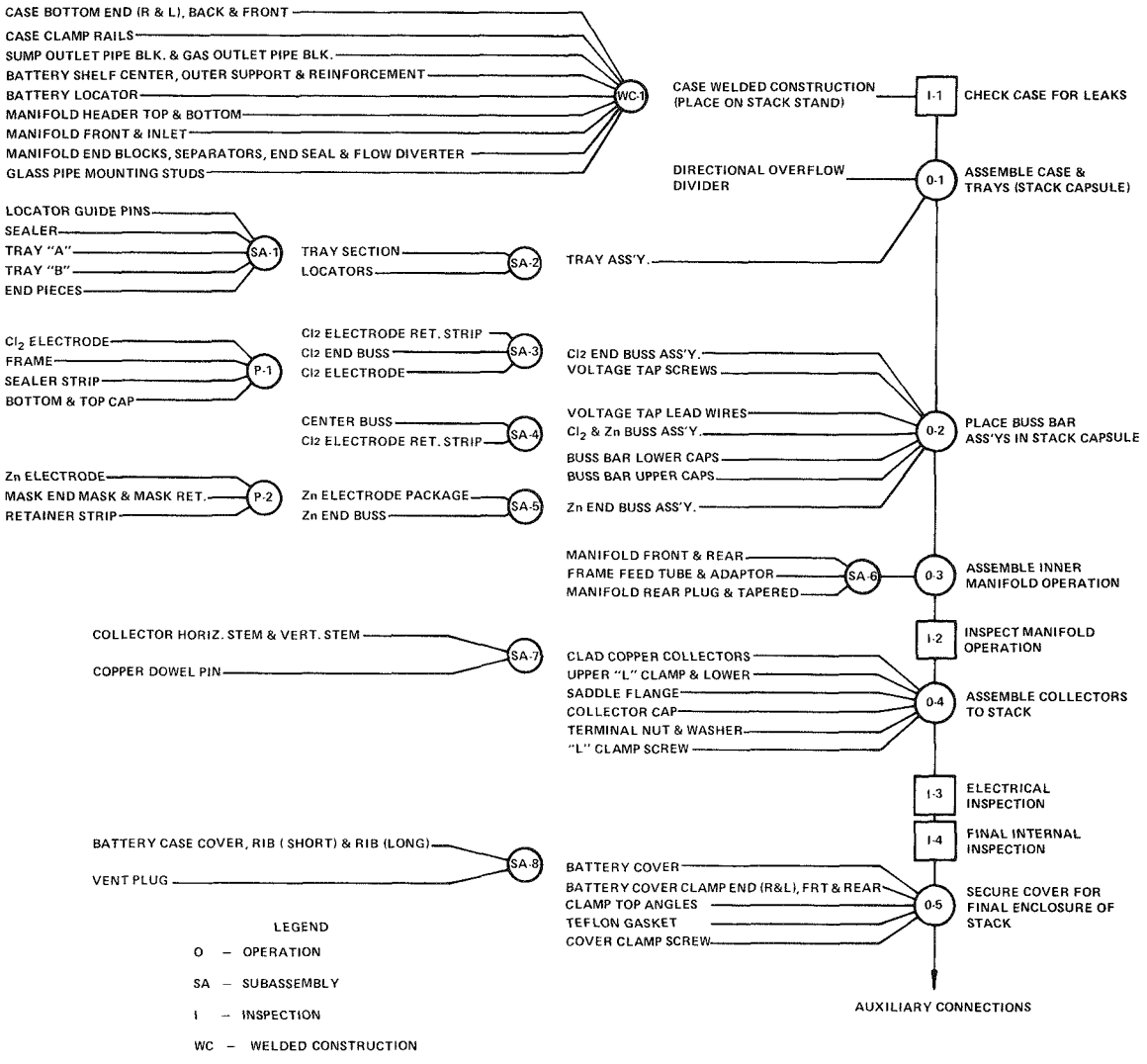

Figure 5-6. Stack Assembly Flow Diagram for 20 kWh Battery.

Store Design

Store design was based on a previous design by N. Fatica at EDA. During charge, chlorine gas is injected into a revolving impeller blade located in a cooled H_2O bath, inside the hydrate forming tub. These conditions bring about a chemical transformation, changing the liquid H_2O and Cl_2 into a yellow precipitate of chlorine hydrate.

The hydrate is then displaced out of the tub into the store body.

To reverse the cycle, the heating coils are activated. This heat decomposes the hydrate. When the chlorine hydrate decomposes, the Cl_2 gas bubbles to the surface where a suction line carries it to the battery, completing the store's function for one cycle.

Structurally, the store consisted of an acrylic store body, acrylic hydrate tub, titanium heating and cooling coils, titanium bearing and drive housings, KYNAR impeller housing, titanium impeller shaft (with ceramic sprayed bushing surfaces) and glass-filled TEFLON bushings.

All of the major "make" details were manufactured by various outside vendors. A few small details were manufactured at EDA. Several purchase items such as standard bearings, seals, ultra-violet lights, pumps, electric motors, KYNAR pipe fittings, gasket material and TEFLON filter cloth were either in stock at EDA, or ordered. As many standard parts as possible were used to minimize cost.

Store Assembly

A store assembly flow chart shown in Figure 5-7 lists the numbers and names of each details, and explains which details went together in the various sub-assemblies.

The assembly of the store took place over a period of about three weeks, requiring one man. Two men were used for another two weeks during which the store underwent testing and modification.

During the assembly, precaution was taken to insure precision. That is, each detail was mocked up with other mating details, torn down, modified if necessary, cleaned and assembled.

The store was assembled in three main sections: (see Store Assembly Flow Chart and the Sub-Assembly Exploded View, Figures 5-7 and 5-8).

- SA-1 Store Sump
- SA-3 Upper Store Assembly
- SA-4 Lower Bushing and Drive Housing

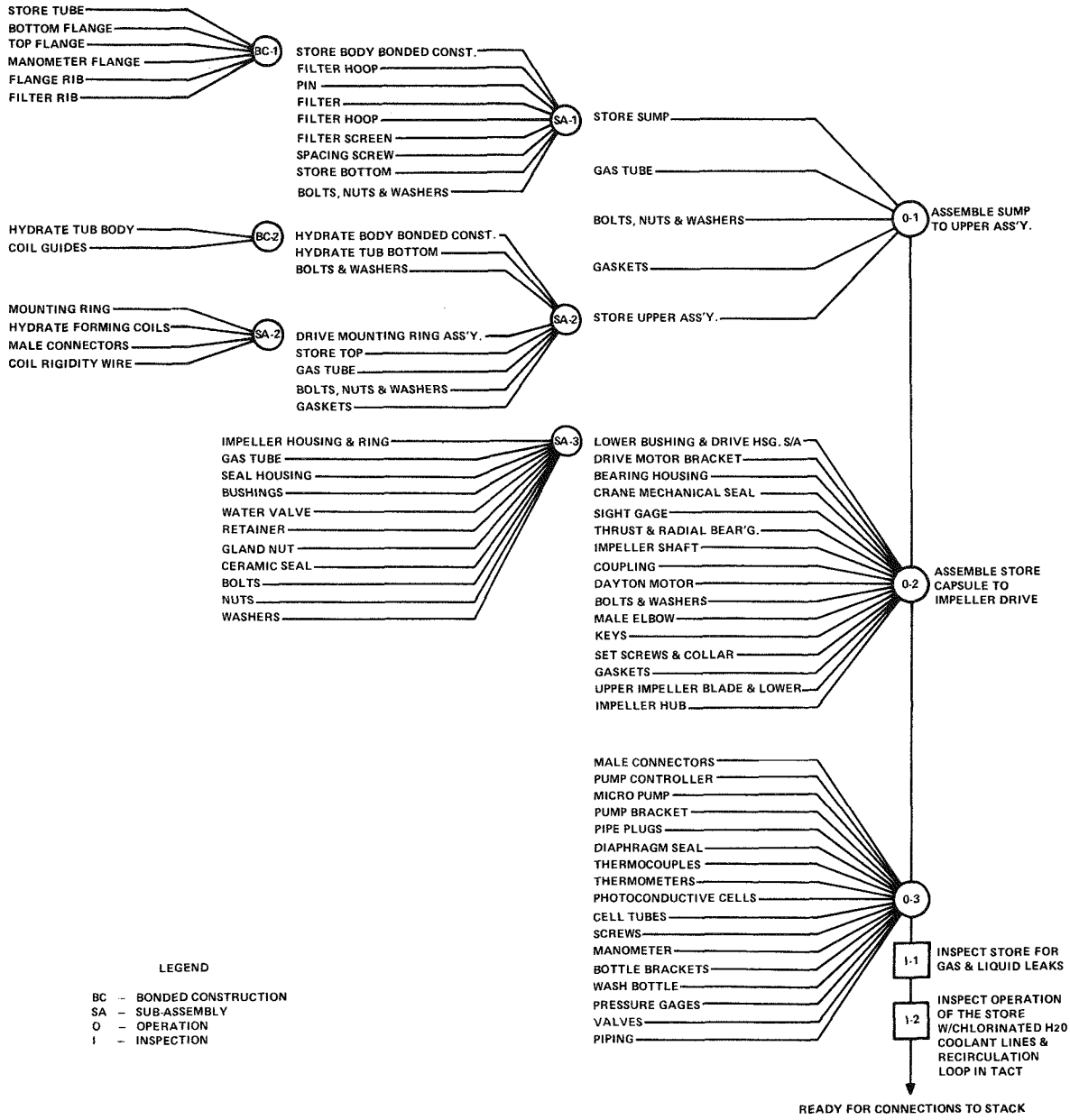

Figure 5-7 Store Assembly Flow Diagram for 20 kWh Battery.

Figure 5-9 is a photograph of the completed store. Figures 5-10 and 5-11 are photographs of the upper store assembly.

After a very successful first test run of the store, a few minor unforeseen problems were identified. They concerned the tear-down and assembly of the lower bushing and drive housing for replacement of bearings and seals. The proper modifications were drawn up and parts reworked to make the mechanical parts more easily accessible for replacement and inspection.

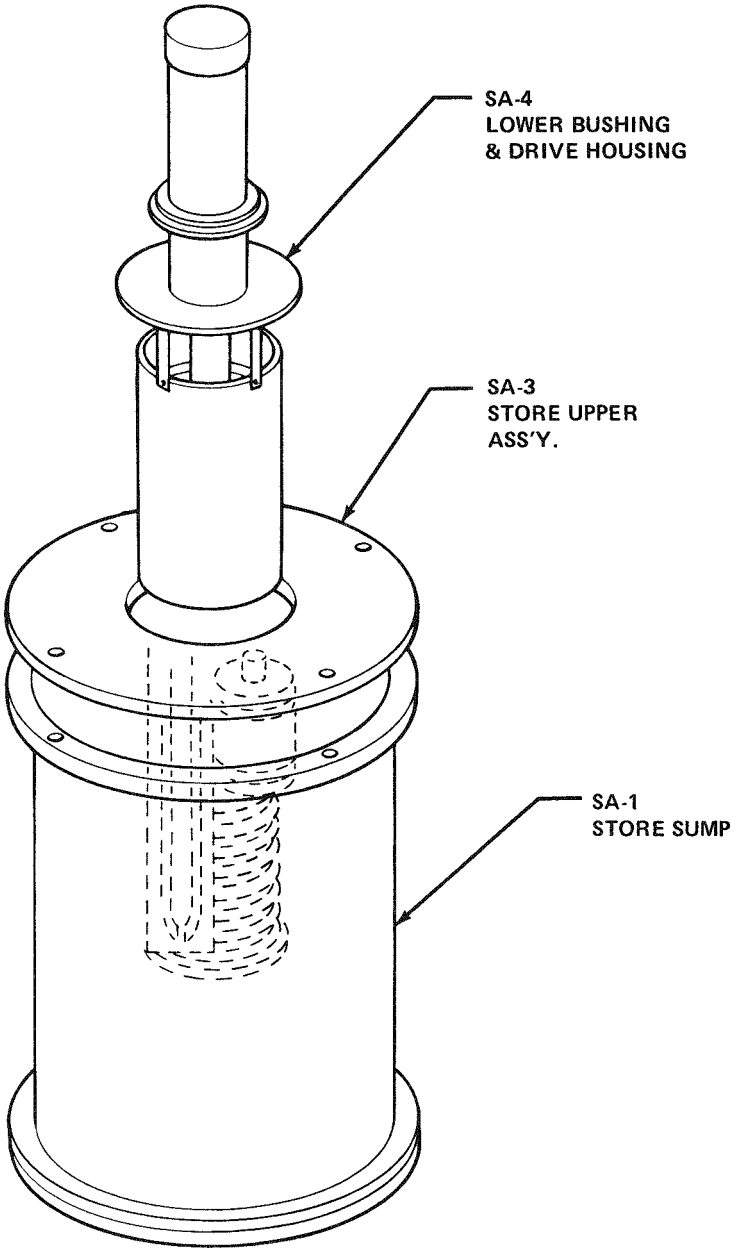

Figure 5-8. Abbreviated Exploded View of Store Identifying the Major Subassemblies.

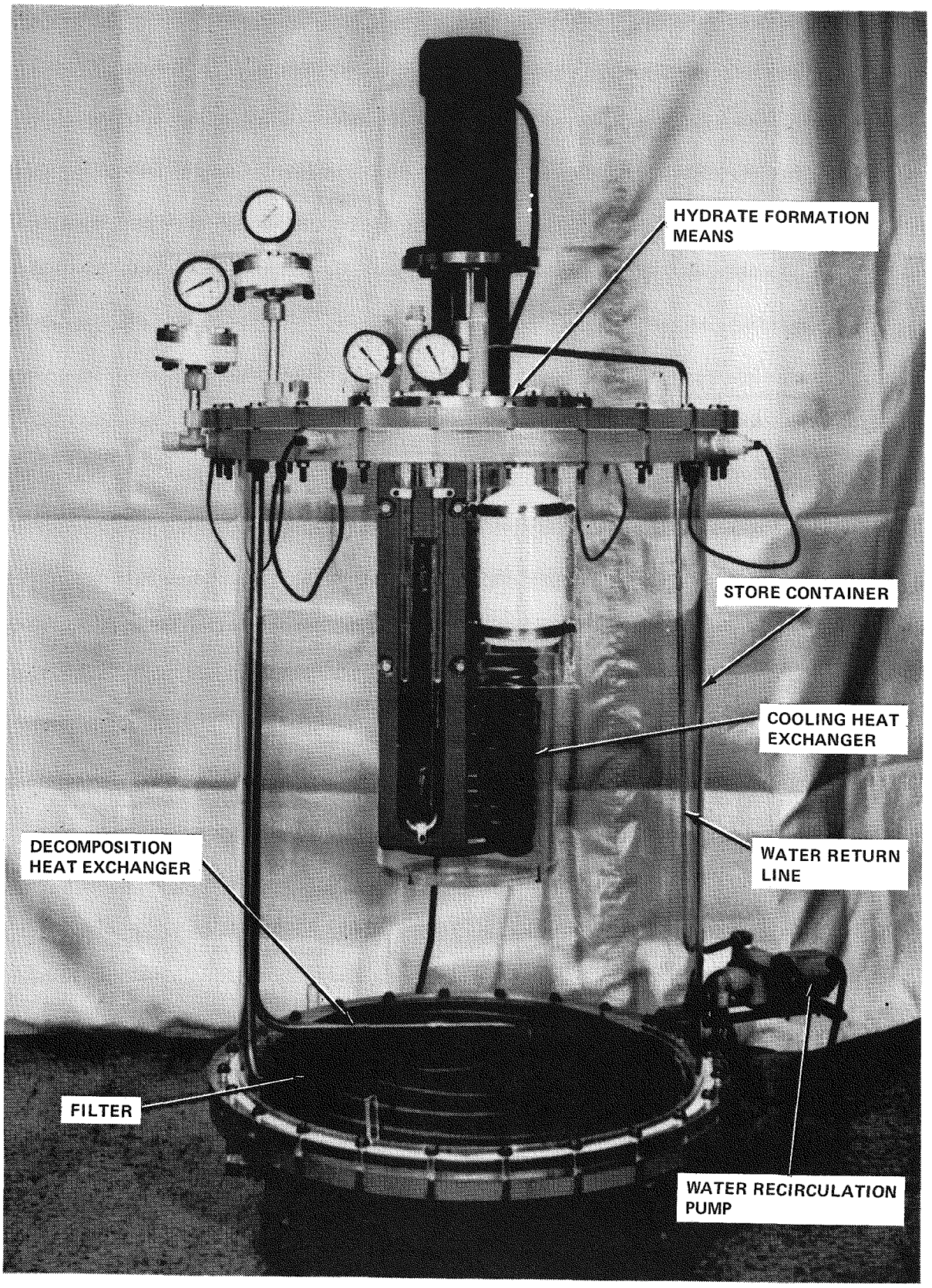

Figure 5-9 Photograph of the Assembled Store Subsystem.

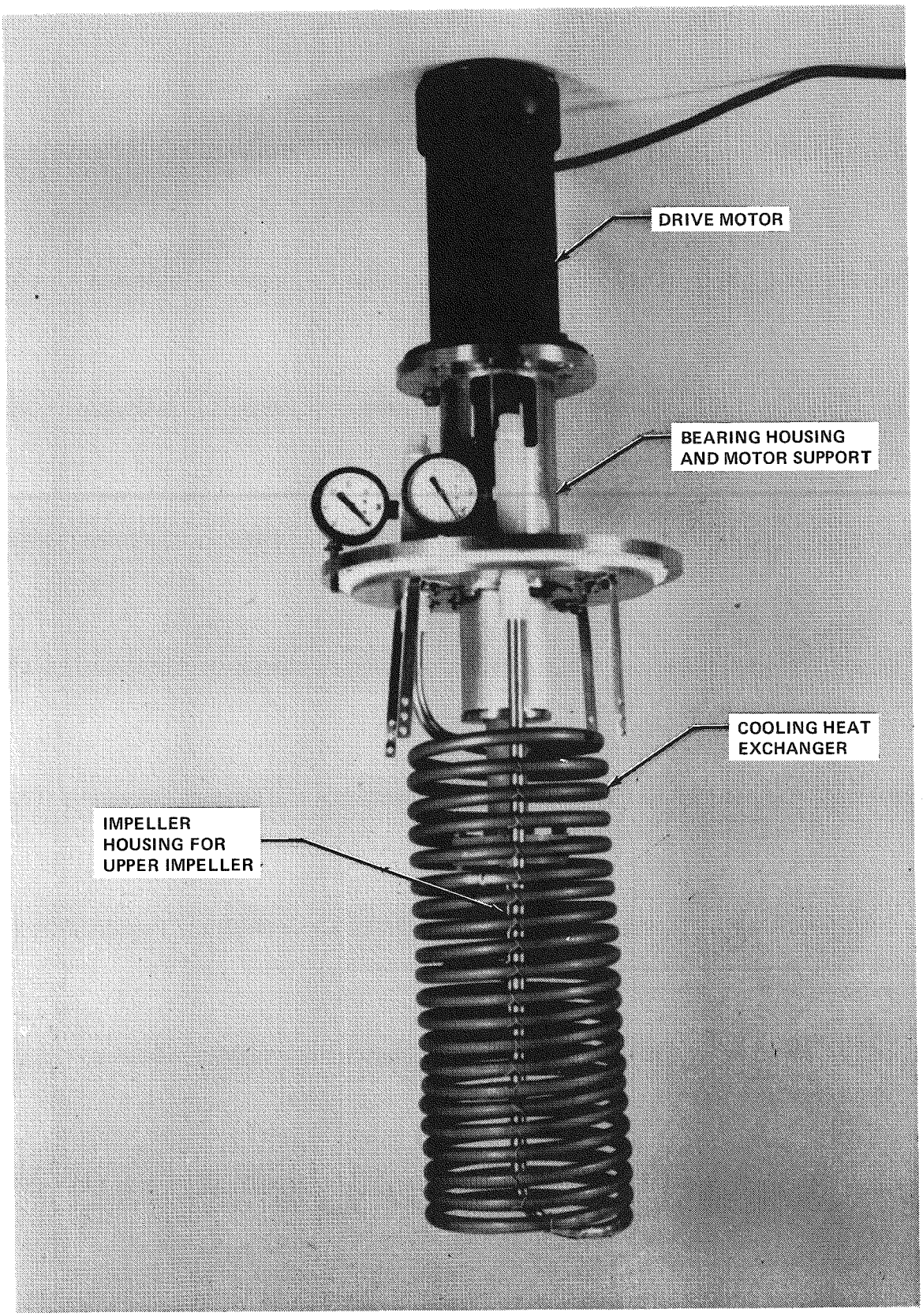

Figure 5-10 Photographs of Hydrate Former Component of Store Subsystem.

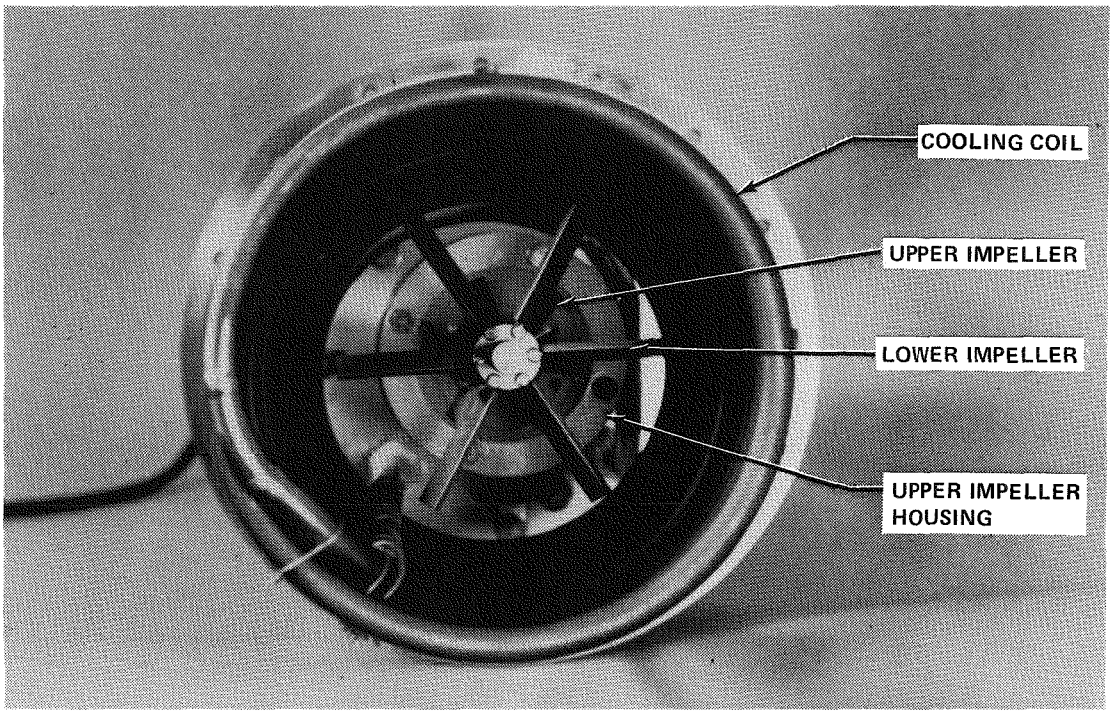

Figure 5-11 End Photographic View of Hydrate Former Component Showing the Impeller.

Battery Assembly

Assembly of the 20 kWh battery (outlined in Figure 5-12) was accomplished in its assigned time frame, but not without a few difficulties which will be dealt with briefly.

A major change was instituted by relocating the main manifold electrolyte ports and reducing the number from two to one. The main manifold was further modified by adding diverter plates set at an angle in order that each secondary manifold would receive an equal amount of electrolyte. A number of modifications were made also to the secondary manifolds to ensure uniform flow to each of the chlorine-electrode parts.

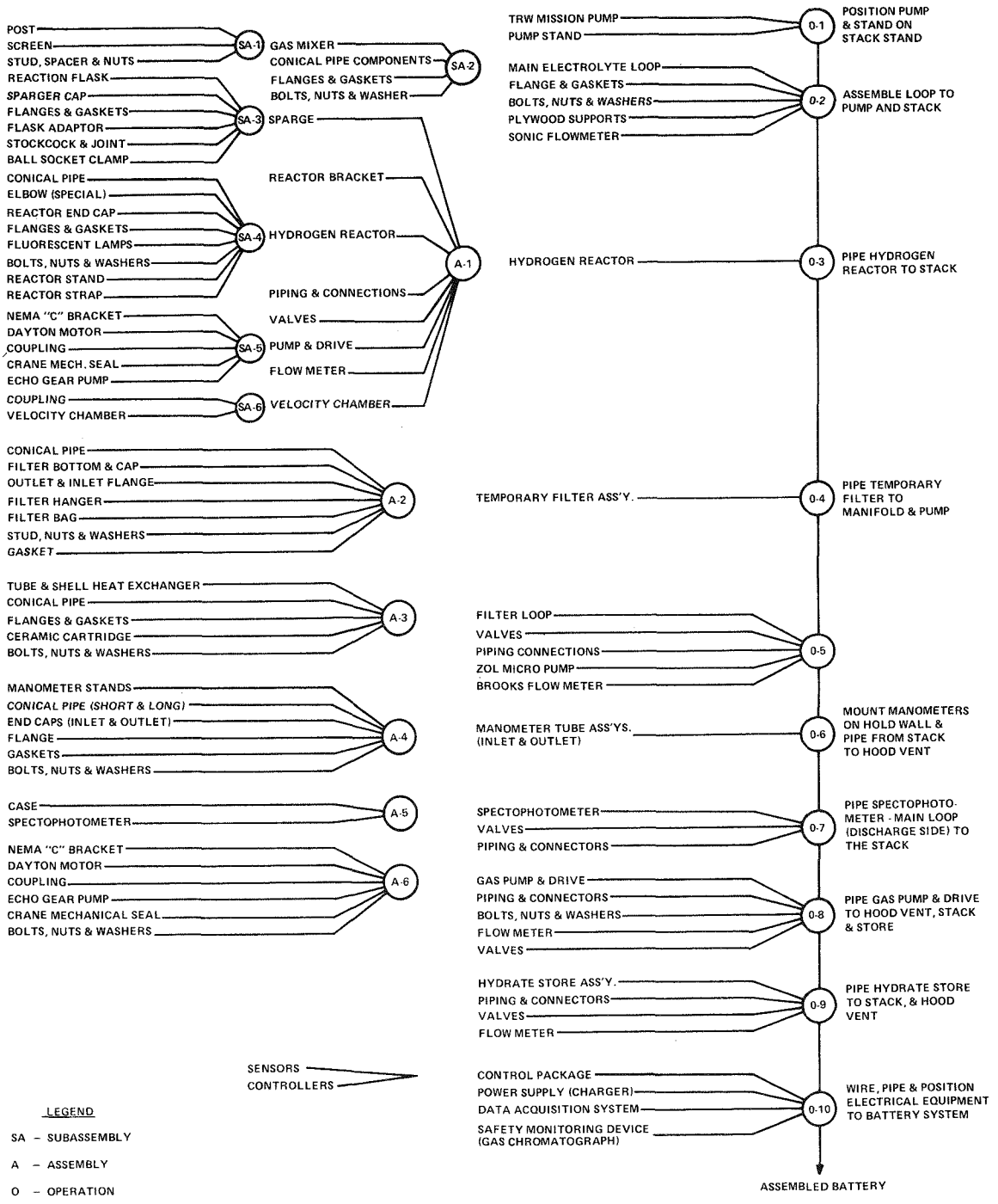

Figure 5-12. System Assembly Flow Diagram for 20 kWh Battery.

A minor problem was encountered in the fabrication of the main battery case when certain welded details tended to distort upon cooling. This problem was solved by going to glued joints and welding only those sections that provided an adequate heat sink.

The battery proper consisted of three sub-assemblies: the case, welded construction, tray assembly and the electrode-bus assembly. Figure 5-6 is a battery assembly flow chart depicting those sub-assemblies. The main case presented no problems other than that above. The tray assembly required a measure of care and creative assembly fixturing to satisfy a specific end-to-end tolerance stack-up.

The chlorine electrode consists of six (6) parts, (see Figure 5-5) and assembly of which required gluing, baking and handling. The handling was minimized and production maximized by a combination fixture shown in Figure 5-13.

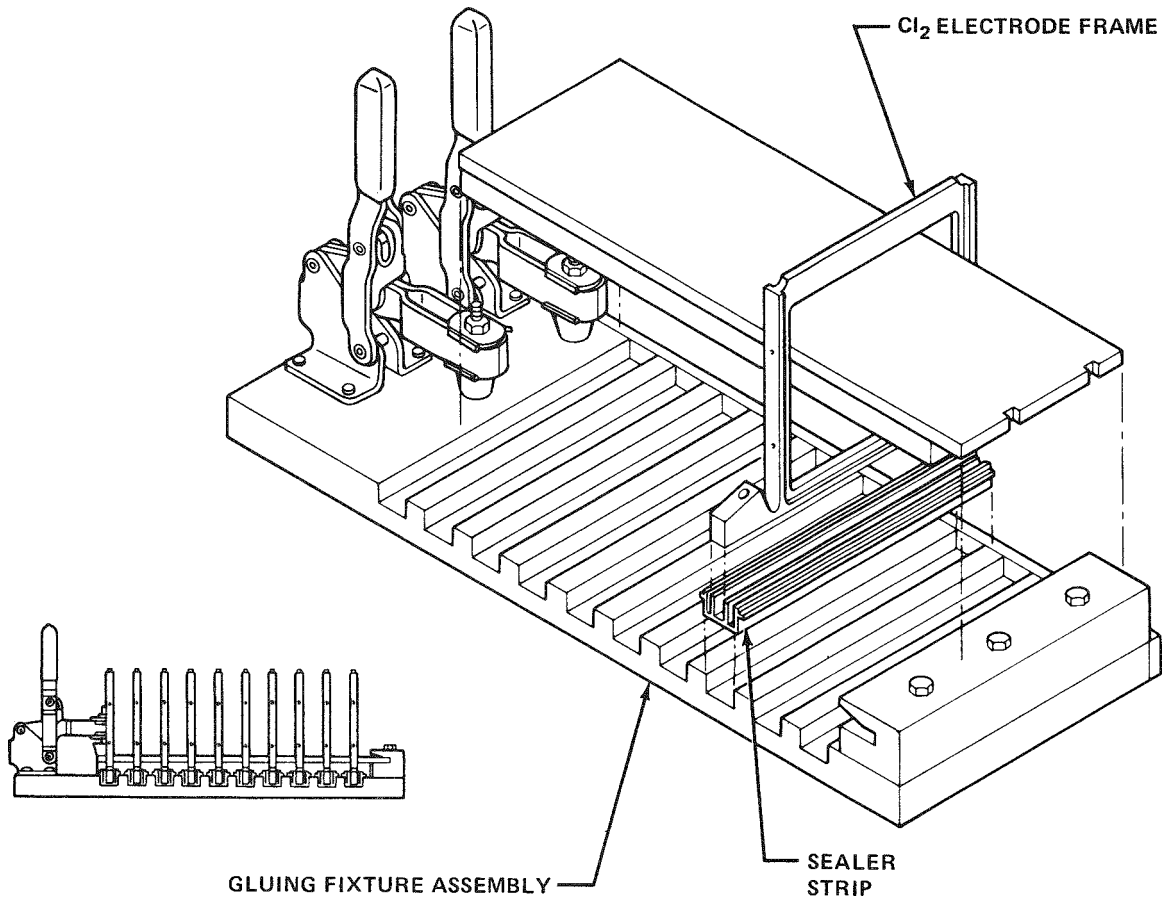

Figure 5-13. Special Fixture to Assemble Chlorine Electrode Frames.

Tooling was also devised to prevent breakage of the zinc electrode as it was being pressed into the bus bar (see Figure 5-14).

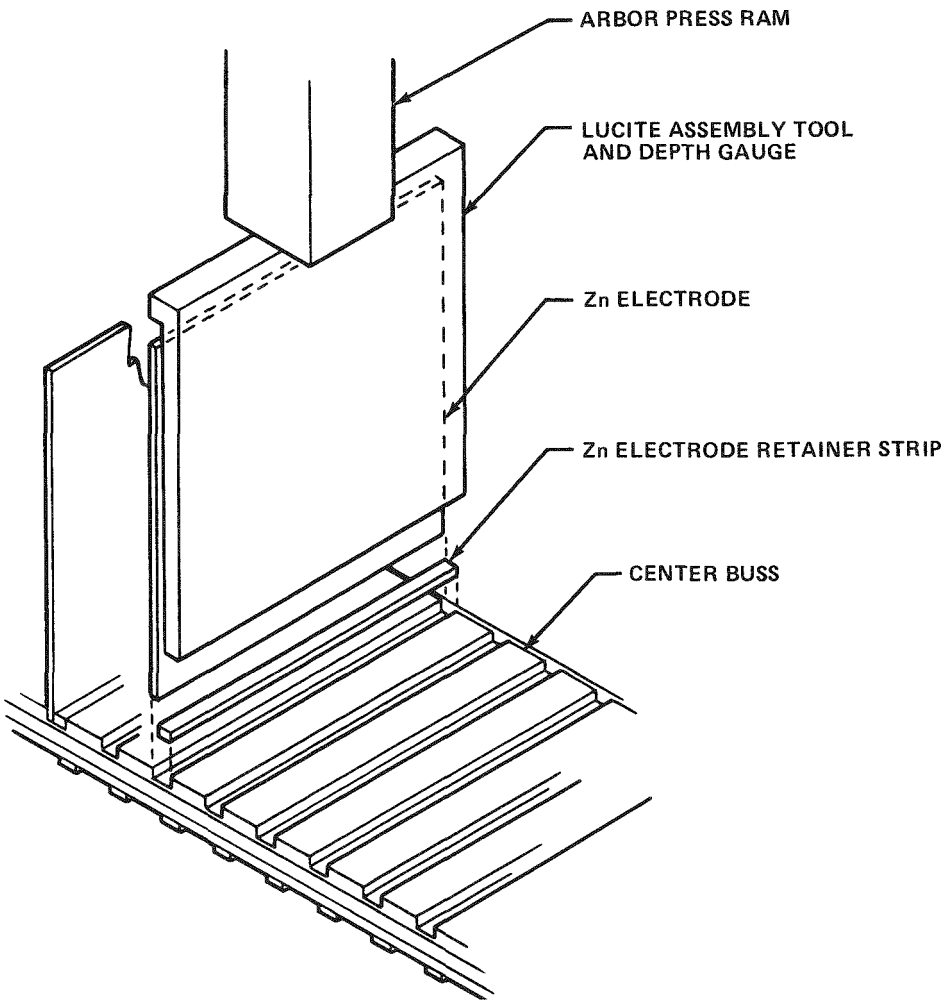

Figure 5-14. Fixturing for Insertion of the Zinc Electrodes into the Bus.

BATTERY OPERATION

A photograph of the completed system ready for testing is presented in Figure 5-15. The light-colored box contains the battery stacks. The cylindrical store is located on the right. The apparatus on the upper left-hand side is the H_2Cl_2 recombination reactor. In the left foreground, is the auxiliary heating and filtration sub-system (Block 3 of Figure 5-1), while in the right foreground the spectrophotometer component of the chlorine-concentration monitoring subsystem

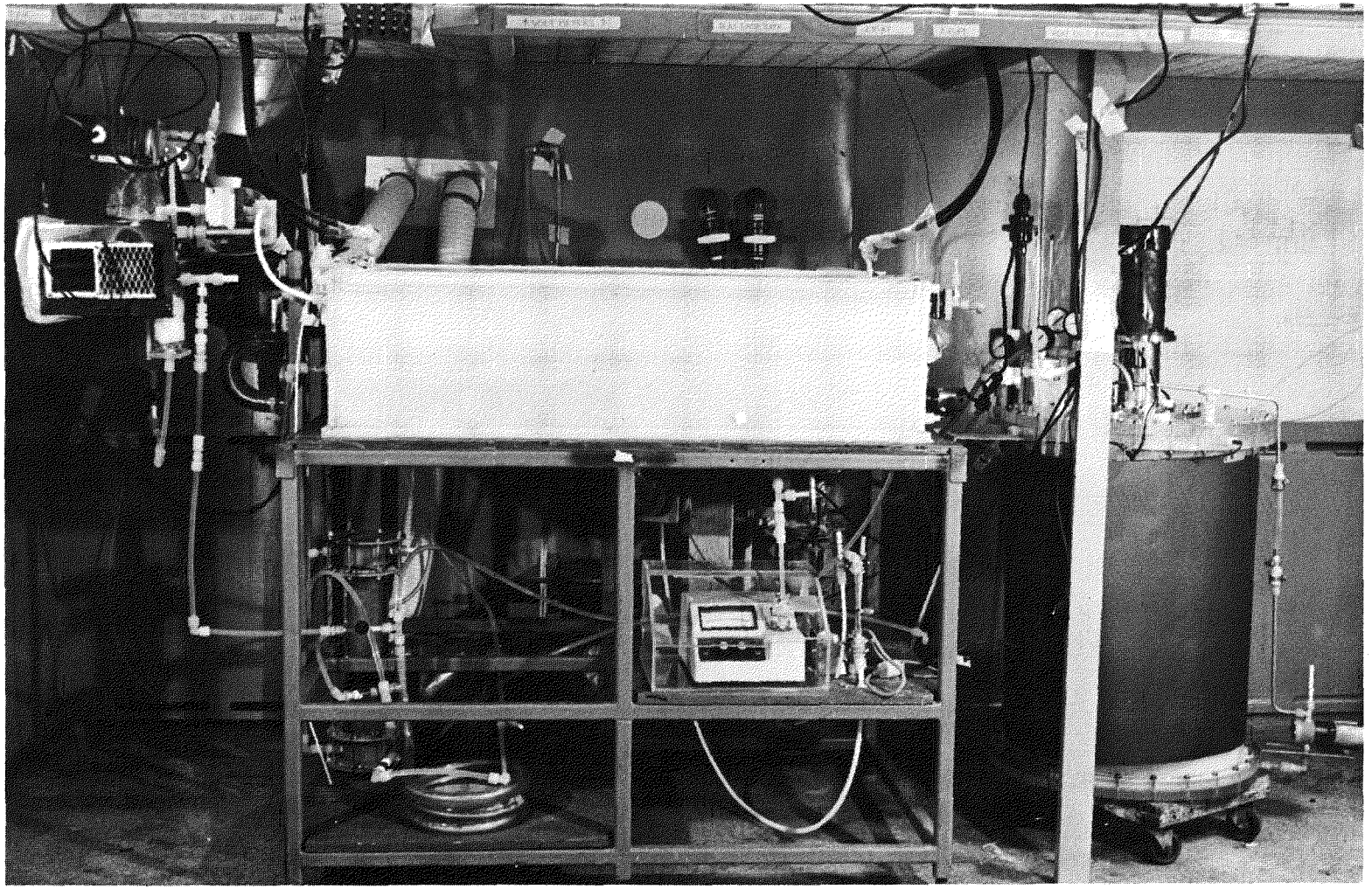

Figure 5-15. Photograph of the assembled 20 kWh battery system ready for testing. The light colored box contains the stack and manifolding. The store is located at the right. The apparatus in the upper left hand side of the photograph is the hydrogen-chlorine reactor system. The pump is located behind the stand and not clearly visible in this photograph.

(Block 4 of Figure 5-1) is readily visible. The main electrolyte pump is located behind the metal rack.

Test Equipment

In Figure 5-16, the power supply for the battery and the electrical monitoring equipment are shown. The power supply was designed and built by the Udylite Corporation. Battery current was measured by placing a digital voltmeter (DVM) across a 300A-50mV shunt. An ampere-minute counter was used to measure ampere-hours of charge and discharge. The accuracy of the shunt is stated to be 0.25%, and the DVM placed across the shunt has an accuracy of 0.5%. The ampere-minute counter, build by EDA, has an accuracy of 0.5%.

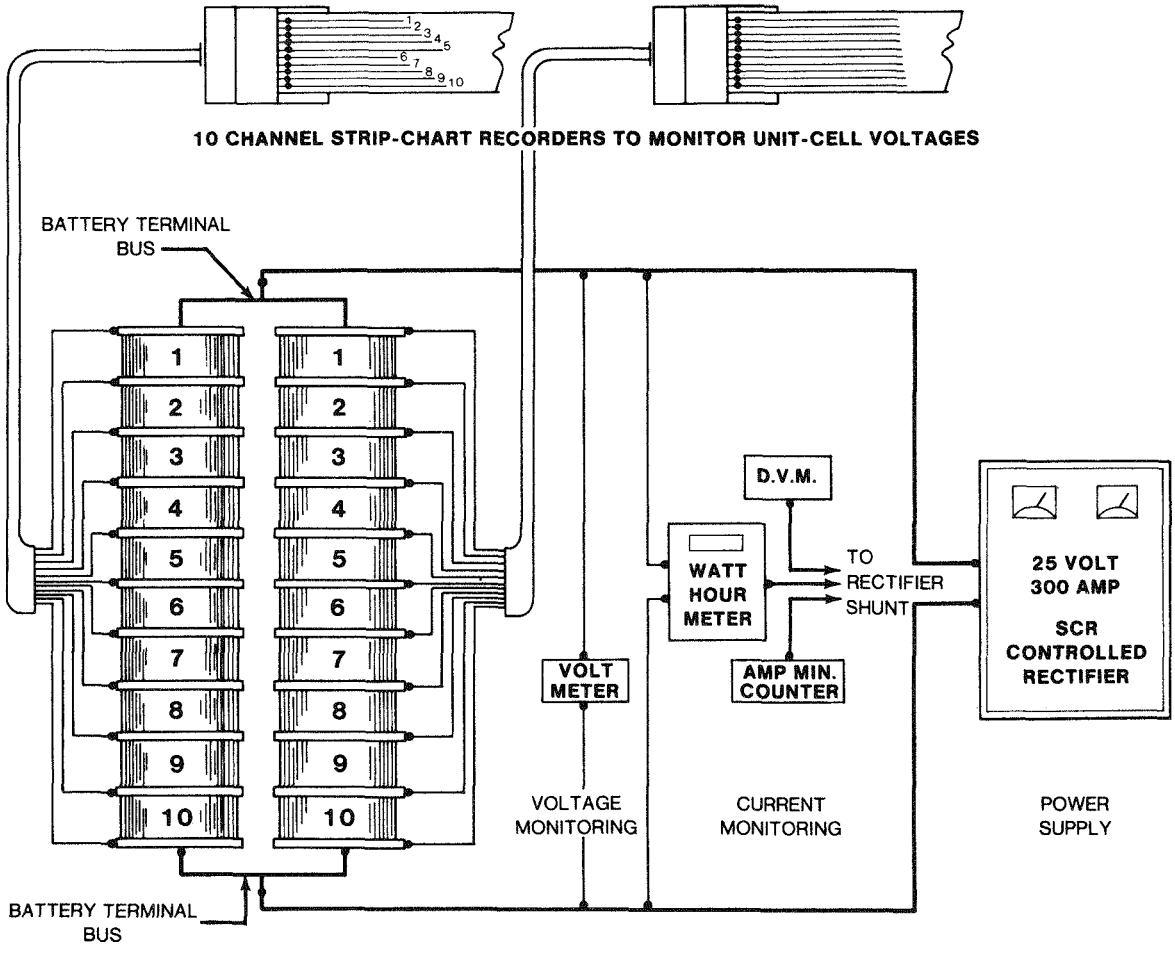

Figure 5-16. Power and electrical monitoring subsystems for the 20 KWh battery system.

The battery voltage was measured by a DVM with an accuracy of 0.5%. The watt-hour meter, designed and built by EDA, was used for energy-efficiency calculations. The voltage-time performance of individual cells in the battery was monitored by two brush 10-Channel strip-chart recorders. In addition, a strip-chart recorder not shown in the figure, was employed to provide a permanent record of battery voltage through charge, turn-around, and discharge.

Scale-up to the 20 kWh level necessitated that the system gas-phase be monitored more closely than had been the practice with previous smaller units. The magnitude of the potential problem due to possible hydrogen build-up was increased substantially. Although highly desirable, continious hydrogen monitoring was determined to be inpracticable at this point in time. The techniques considered either lacked dependability (e.g. the commercial thermal conductivity device employed in the past) or were still in the early developmental stage (use of hydrogen-chlorine recombination reactor temperature as an indication of hydrogen content).

A process control gas chromatograph manufactured specifically for chlor-alkali cell off-gas analysis was therefore purchased from ARCAS, Inc. of Houston, Texas. The installation actually consists of the three units shown in Figure 5-17. Although minor changes have been incorporated to suit EDA's requirements, the analyser is essentially a standard chlorine plant package in that O_2,N_2, CO and CO_2 may be determined in addition to H_2. Dual carriers - nitrogen and helium - are employed in order to obtain maximum sensitivity for all these constituents.

The chromatograph was directly coupled to the battery system as shown in Figure 5-18. The unit was operated initially in a "H_2 only" mode, which permitted determination of the hydrogen level in the gas space above the battery every 60 seconds. This analysis frequency ensured adequate notice of any conceivable hydrogen build-up, thereby allowing sufficient time for the accomplishment of any necessary corrective measures. This proved to be invaluable during start-up. During this period excessive hydrogen levels subsequently determined to be due to incomplete rising of contaminants from the new system were encountered. The on-steam chromatograph routinely gave ample notice of the hydrogen accumulation rate, thereby insuring that system venting or purging with nitrogen was initiated well before dangerous levels could be reached.

In interfacing the chromatograph with the battery, provision was made for monitoring a numberof system points. Significant data was thereby obtained, for example,

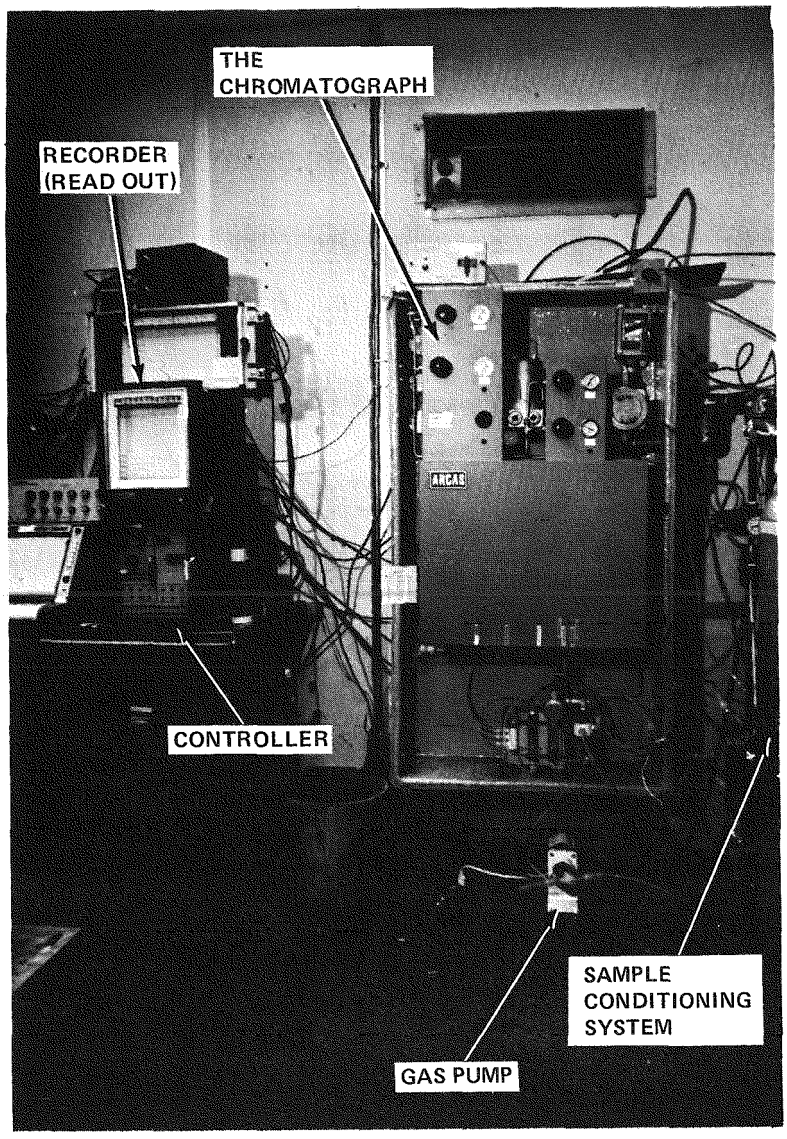

Figure 5-17. Chromatograph Unit for Continuously Monitoring Battery Gas Phase. Shown is the ARCAS Model 905 free-standing chromatograph along with a Model 405-D Control Console. Data presentation is on the Leeds and Northrup Speedmax H Recorder.

on the efficiency of the hydrogen-chlorine recombination reactor. In addition, by monitirong sample points C through G above the battery stack, insight into gas phase circulation was readily available. Although not employed to date, the additional capability of O_2, N_2, CO and CO_2 analyses will prove invaluable in the near future. Insight into battery system life will be provided by CO_2 and CO measurements. The presence of nitrogen and oxygen in a four-to-one ratio serves to alert us to the leakage of air into the system.

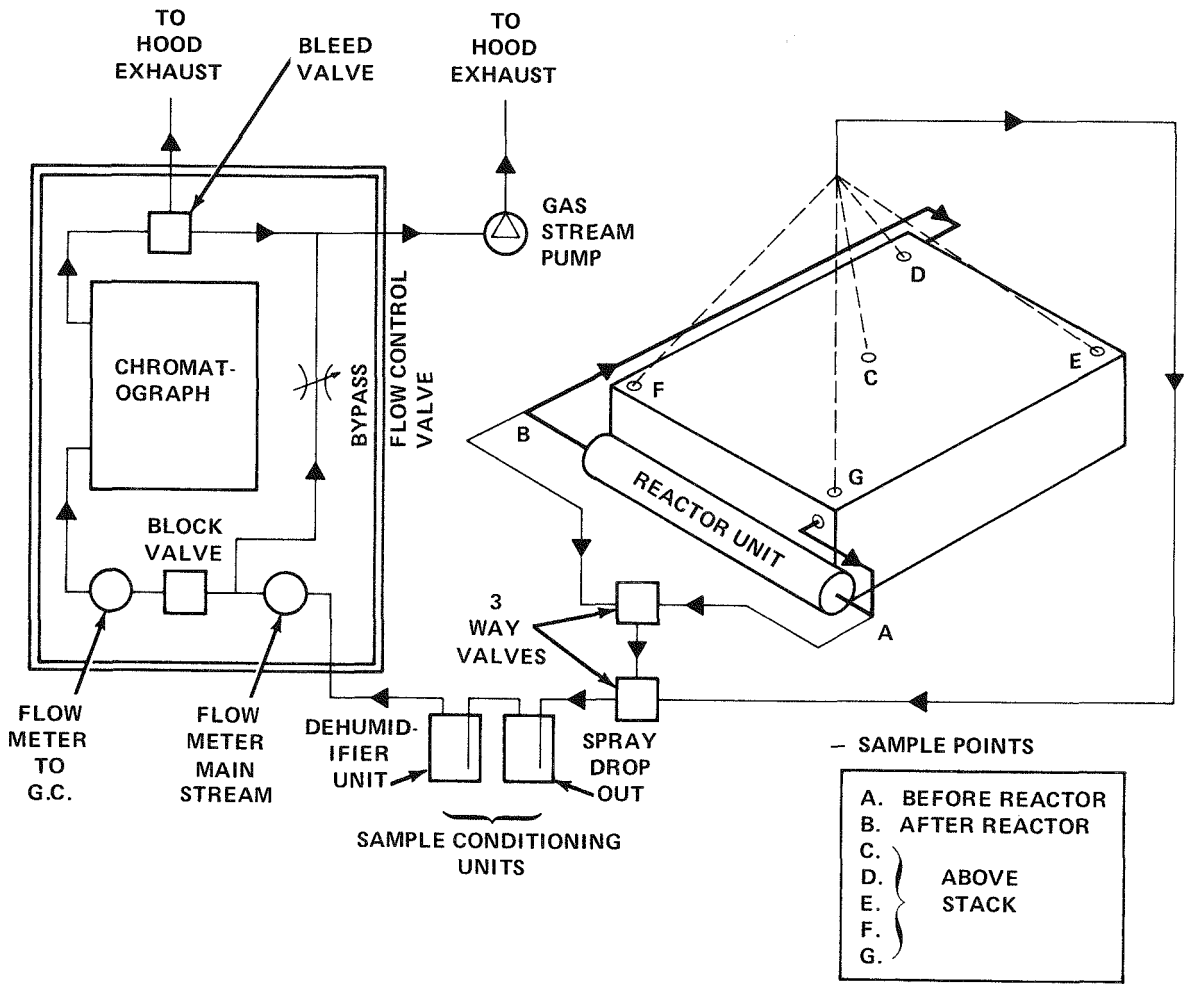

Figure 5-18. Interfacing of Battery System with Chromatograph. Note that sample conditioning to remove liquid water is required before sample stream reaches chromatograph.

Testing Procedure

Prior to beginning the charge phase of the battery testing regime, the specific gravity and pH of the electrolyte were measured and recorded. Also, the speed (in rpm) of this main electrolyte pump (P1) was checked and the Arcas on-line gas chromatograph was recalibrated. The charge phase was begun when the store temperature reached a pre-set level. The charge phase consisted of charging the battery for up to five hours at 45 mA/cm^2 or 260A, as read across the main current shunt. After charging, the glycol feed to the store was turned off. The gas pump (P-G) and the decomposition pump (P3) were turned on (See Figure 5-1)

The discharge current was maintained at 230A (40 mA/cm^2) to a 10V cutoff. When the battery voltage dropped to 10V, the current was decreased continuously to hold 10V. The discharge was terminated when the battery voltage dropped below 10V at 30A (5mA/cm^2). Residual zinc on the electrodes was then removed by shorting the battery across a 0.4 Ω resistor.

Test Results

Final assembly and initial testing of the 20 kWh battery system occurred in mid-December. Early testing consisted of short charge-discharge cycles to evaluate battery performance. The operation of the battery in this phase was greatly simplified by venting the chlorine on charge and using cylinder chlorine to discharge the battery. A 20 mil thick sheet of plastic served as a removable top so that the battery could be easily inspected.

Initial testing showed an unacceptably high outlet pressure on the main electrolyte pump. Also, it was necessary to modify the initial technique used to chlorinate the electrolyte on discharge. These problems were resolved in a few days and the first five-hour charge was put on the battery on December 16, 1976. The electrochemical performance of the battery was quite good. The charge voltage was 22.9 and the discharge voltage averaged about 18.8. The voltage versus time profile on a constant current discharge was also good. The overall coulombic efficiency for the run was 78%. Accurate hydrogen evolution measurements could not be made on the unsealed battery but chromatographic readings and the pH change during the cycle indicated a higher hydrogen evolution rate than was expected. Electrolytes not containing potassium chloride continued to show low levels of hydrogen evolution. Electrolytes containing potassium chloride showed variable amounts of hydrogen.

The store was connected to the battery in mid-February 1977. The lid was sealed and mechanically the battery was ready for cycling. However, electrolytes containing only zinc chloride exhibited poor coulombic and voltaic efficiencies. Electrolyte which contained sodium chloride dendrited early and exhibited very poor voltages on discharge. The lack of energy efficiency and capacity caused further delays in beginnning the battery cycling.

The following week involved more test runs and some modifications in the gas burner loop. The electrochemical performance of the battery remained good. Visual inspections showed the zinc plate to be flat and no problems were encountered in obtaining a five-hour charge capacity at 45 mA/cm^2. Hydrogen evolution remained higher than expected.

During the month of December 1976, the battery was drained, rinsed and replenished with newly prepared electrolyte solution several times in an attempt to reduce the level of hydrogen evolution. In late December, the discharge was interrupted due to a mechanical failure and hydrogen level was observed to increase rapidly while in this partially discharged condition. This phenomenon was verified in a laboratory test cell the following day.

Both the voltaic and the coulombic performance of the battery were in agreement with laboratory results on small cells. The mechanical problems were not of any major concern and corrections involved only minor modifications. Despite EDA's efforts to cleanse the battery and purify the electrolyte, hydrogen evolution continued to be a problem in the operation of the 20 kWh battery.

In the following weeks, extensive laboratory testing indicated that the hydrogen evolution was related to the use of potassium chloride. To verify this, the 20 kWh system was filled with a zinc chloride-sodium chloride electrolyte in late January 1977. Under sealed conditions, the average hydrogen evolution was measured at less than 0.2% throughout the cycle. Electrolyte testing continued throughout the next two months.

In April, 1977, the battery was filled with the standard electrolyte formulation. Short-cycle testing indicated an acceptably low level of hydrogen evolution. Cycle tesing using low current densities on the charge cycle resulted in low coulombic efficiencies. Also, internal shorting occurred before full charge capacity was obtained. Some further testing on electrolyte composition and current density was necessary prior to the start of cycling. Before the actual cycling was started, the battery was inspected and some minor changes concerning the zinc masks were made. Due to internal shorting, the battery capacity was somewhat less than the designed 20 kWh output. The cycling interval was from May 7 through May 13, 1977 and conducted in routine fashion. The cycle data is presented in Table 5-4.

The performance of the battery as an integrated system has been demonstrated. Two unexpected events occurred which caused considerable delays in cycling the system. The hydrogen evolution observed in December 1976, is believed to be caused by an as yet undetermined trace impurity in potassium chloride. Spectroscopic analysis of analytical reagent grade potassium chloride has not shown any deleterious impurities in thel-100 ppm range. The second problem, internal shorting due to dendrite formation was, in part, due to battery design problem and may also be impurity related. An extensive program is continuing by EDA to evaluate trace impurities and their effects on hydrogen evolution and zinc morphology.

Table 5-4

CYCLE DATA FOR 20 KWh BATTERY SYSTEM - MAY 1977

RUN #	DATE	SPECIFIC GRAVITY	pH BEFORE CHG.	$[Cl_2]$ CHG. $g/_l$	MAIN ELECTROLYTE PUMP		KILOWATT HOURS (kWh)		EFFICIENCIES PERCENT			COULOMBIC EFFICIENCY PERCENT		AMPERE HOURS		MAXIMUM PERCENT $[H_2]$		AVG. TEMP.
					CHG. RPM	DISC. RPM	CHG.	DISC.	VOLT	ENERGY	kWh	USABLE	TOTAL	CHG.	DISC.	CHG.	DISC.	
29	5-7-77	1,355	0.6	--	1200	1200 to 1850	25.31	15.36	80.7	61.8	60.7	76.5	79.6	1100	876	.15	.5	49.5
30	5-8-77	1,365	0.5	1.08	1200	1400 to 1600	25.21	14.68	80.4	59.3	58.2	73.7	77.3	1109	858	.1	.5	50.5
31	5-9-77	1,365	0.44	1.27	1200	1500 to 1950	25.24	14.86	80.0	59.8	58.9	74.7	78.0	1100	858	.1	1.0	48.8
32	5-9-77	1,353	0.5	1.18	1190	1500 to 2040	25.23	14.98	82.0	60.4	59.2	73.7	75.4	1100	830	.25	0.9	50.3
33	5-10-77	1,345	0.42	1.14	1450	1820	26.50	15.64	81.2	59.7	59.0	73.5	76.3	1152	879	.15	1.25	49.2
34	5-10-77	1,345	0.5	1.02	1450	1100 to 1200	25.34	15.10	81.2	60.7	59.6	74.7	78.1	1100	860	.15	.9	50.0
35	5-11-77	1,345	0.42	1.18	1440	1600	25.41	15.39	81.0	61.3	60.5	75.7	78.7	1100	866	.1	.55	49.1
36	5-12-77	1,355	0.61	1.18	1450	1600	25.37	15.08	80.6	60.6	59.4	75.2	78.8	1100	867	.05	.6	50.0
37	5-12-77	1,345	0.58	1.1	1600	1600	25.38	15.16	80.8	61.2	59.7	75.7	79.1	1100	868	.2	.9	49.7
38	5-13-77	1,350	0.55	.98	1600	1600	25.34	15.13	81.0	60.9	59.7	75.2	78.8	1100	867	.2	1.15	49.9
39	5-13-77	1,350	0.52	1.2	1900	1600	30.04	17.89	80.7	59.9	57.5	74.3	76.3	1300	993	.3	1.3	49.5

CONCLUSIONS

The preceding discussion describes a resource of experience covering many significant areas of zinc chloride battery technology. It should be clear that the scale-up includes the latest technical innovations. Specifically, this design included a specically designed reactor, novel electrode frame design, a scaled-up former-store combination and a new manifold structure.

In the greater view of this program, it is essential that this developmental effort anticipate the BEST battery construction. In order that this larger system be built, a detailed study of the assembly and processing requirements must be made. In this way, a meaningful planning effort would follow. This 20kWh battery construction effort did provide substantial processing data that allows projections to be made.

PART IV

DESIGN AND COST ANALYSIS OF 100 MWH ZINC-CHLORINE PEAK-SHAVING BATTERY PLANTS

Section 1

INTRODUCTION

In order for a 100 MWh battery plant to be acceptable to the electric utility industry, the following criteria must be met:

- Installed Cost: $30/kWh measured in 1976 dollars
- Overall Efficiency: 70% +
- Footprint: 8 kWh/ft^2
- Maximum Height: 20 ft
- Minimum Siting Restrictions

Reference has been made to the system as a battery plant. Figure 1-1 is a simplified flow diagram of the system. Use of pumps, heat exchangers and refrigeration equipment are characteristics of a plant operation rather than the usual conception of a battery. Briefly, the active material, zinc chloride, is dissolved in water and circulated through the cell stacks. The chlorine gas, involved in the electrochemical reaction, moves between the stack and the store. As shown in Figure 1-1, the store serves to either contain the chlorine gas or deliver the gas in quantities

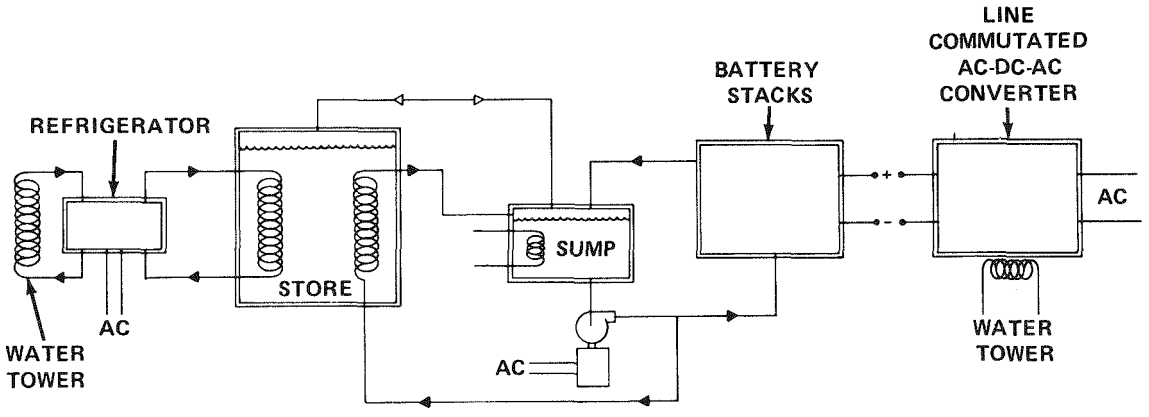

Figure 1-1. System Flow Diagram for a 100 MWh Peak-Shaving Battery Plant.

necessary to meet the power requirements. The chemical, physical, and engineering aspects of the process have been adequately treated in earlier sections. For the purposes here, it must be emphasized that the absorption or delivery of chlorine is determined by the heat removed or added to the store during battery operation. Therefore, the heat exchangers and refrigeration equipment are essential system components.

Another part of the overall battery system is the power conditioning equipment, namely, the rectifier-inverter. This component provides the interface between the electric power transmission system and the battery. For the purposes of this study, the cost of the converter has not been included.

A unique characteristic of the zinc chloride battery is that the active materials are not an integral part of the electrode structure. Each electrode, which is made of graphite, serves only as a current-collection system for the electrode reactions. This current collector is a graphite structure arranged into a comb-type bipolar electrode assembly (Figure 1-2). As shown, both zinc and chlorine electrodes are firmly fixed, mechanically and electrically, to a graphite buss. A collection of these assemblies is known as a stack.

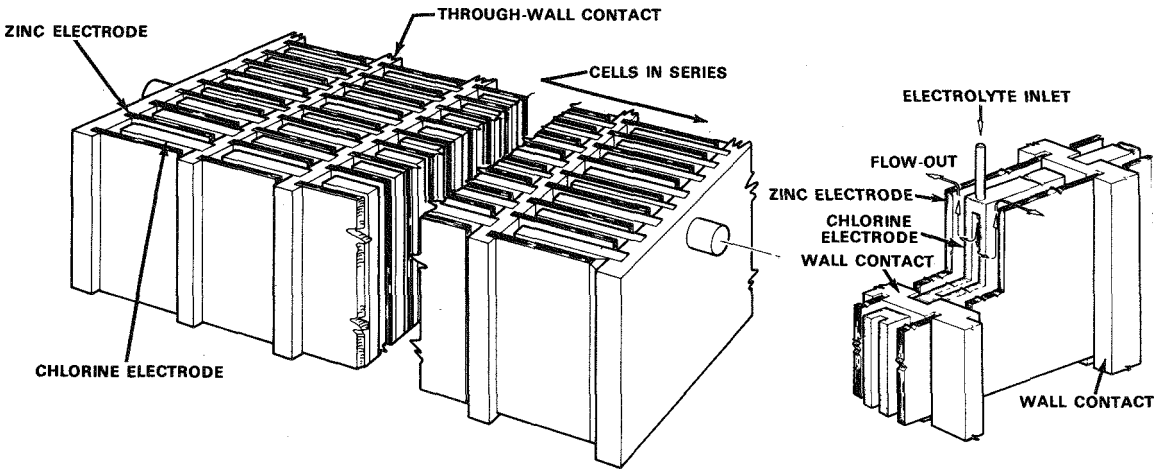

Figure 1-2. Comb-type Bipolar Electrode Assembly

From this perspective, two major battery system designs have been developed for the purpose of analysis and review. These designs served as the basis for receiving needed critical feed-back from the electric utilities, EPRI, and ERDA. In this way, the design evolution was directed to be as responsive as possible to the projected

ultimate system use. The Mark 2 design, described in Section 2, was prepared under EPRI contract number RP226-1 in November, 1975. The Mark 3 revision, conceived in November, 1976, as a part of the EPRI contract number RP226-2, is described in Section 3. In actuality, the Mark 3 design can be considered a variant of the Mark 2 design. The Mark 2 design has received a more detailed examination, as will be evident from the following sections.

A cost analysis of both systems, which is set forth in Section 4, has provided considerable information regarding the approaches necessary to achieve the ultimate cost objectives. Accordingly, programs have been instituted to achieve the major cost reductions projected for a 100 MWh (20 MW) peak-shaving battery plant. A brief comparison of the designs and cost analyses for both systems is provided in Section 5.

Section 2

MARK 2 DESIGN

INTRODUCTION

Concept of the Mark 2 design was the outcome of early design review meetings with EPRI and electric utility representatives. Their comments and observations were crucial for guiding the EDA conception of a peak-shaving battery. Mark 2 design is depicted below so as to effectively describe the design features, yet, be as detailed as possible as to the salient aspects of the design.

Charge current density is 24 mA/cm^2 at an average voltage of 2.235V. Discharge current density and voltage are 30 mA/cm^2 and 2.00V, respectively. For design purposes, electrochemical energy efficiency is assumed to be 80% in the ultimate Mark 2 peak-shaving plant. Voltaic efficiency-the ratio of the average voltages in discharge and charge, (i.e., 2.00V/2.235V)-is 89.5%. Usable coulombic efficiency is, therefore 89%, (i.e., 80%/89.5%). Overall plant efficiency is in excess of 70%. Analysis of the plant's dimensions reveals that the footprint is 9 kWh/ft^2. The maximum height criterion of 20 feet is observed, while the access aisles are 3 feet wide to allow servicing of the module pump motors. The design described below is intended to provide a basis for projecting the physical dimensions, industrial processing, and associated manufacturing cost for a 100 MWh (20 MW) peak-shaving battery.

Beginning with the extrapolation of knowledge gained from EDA's 1 kWh and 2 kWh development batteries and from preliminary cost and performance studies, certain other guidelines were set forth. These design criteria are as follows:

- Graphite electrodes will be flat plates (2.5" x 4" active face size). Close tolerances not required.
- One megawatt hour (1MWh) module will be used as the basic building block.
- Each basic module will employ an electrolyte pump.
- Minimum practical "footprint" will be sought for battery station.
- System to be planned for installation in an open suburban yard with no structure over 20 feet in height.

The following design concept is based upon these parameters, and the technical operating specifications described previously. Conceptually, the battery plant (Figure 2-1) will contain eleven separate rows of battery strings. Each string will be connected through switching equipment to station busses. Ten basic 1 MWh modules connected in series comprise a battery string. Stacking these basic modules, as shown, will minimize the net inductance of the system. Height of this stacked array of 1 MWh modules would be under 10 feet.

Full capacity of the battery station will be reached when ten of these 10 MWh strings are switched into the system. The eleventh may then be disconnected and put on standby. This will offer desirable reserve capacity for the station, will place a string in reserve should a malfunction occur in one of the operating units, and will allow each string to be isolated in turn for routine maintenance procedures. A dimensioned plan view of the battery plant is shown in Figure 2-6.

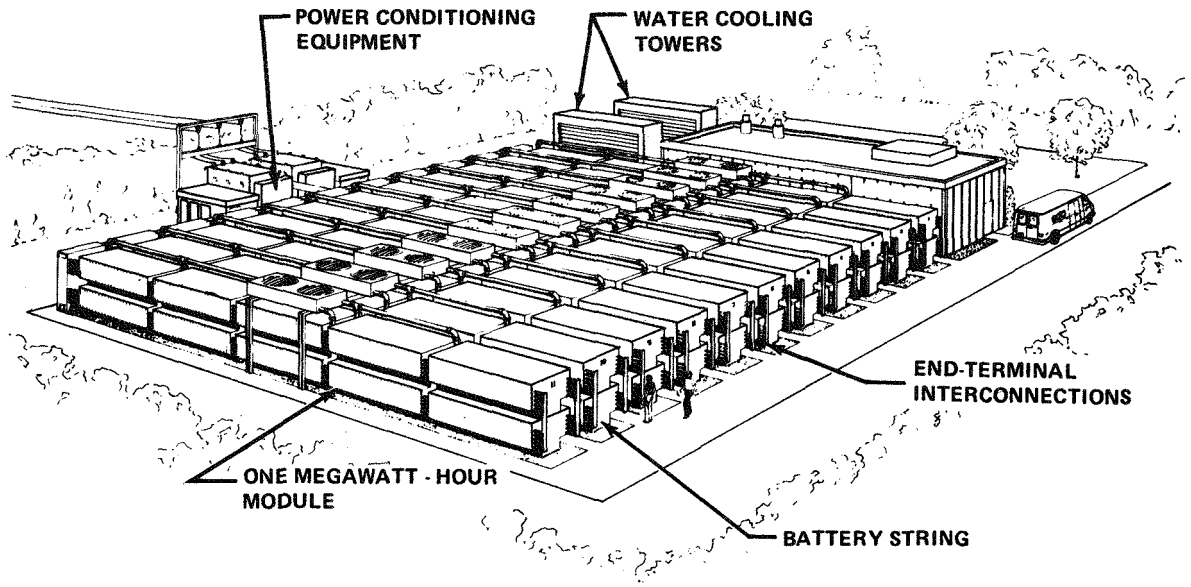

Figure 2-1. Artist's Concept of Mark 2 Design of a 100 MWh (20 MW) Zinc-Chlorine Peak-Shaving Battery Plant Located near a Utility Substation.

Pictured in the left background of Figure 2-1 is the power-conditioning equipment consisting of rectifier-inverter and associated switchgear. The small building at the end of the battery stack will house the hydrate forming refrigeration equipment, the motor starters and controls, and other auxiliaries. Two 20 foot high water cooling towers for the refrigeration system are located at the end of the building. Each 10 MWh string is equipped with an air-to-liquid heat exchanger for accurate

temperature regulation. This unit, pictured with twin fan inlets on top, is supported centrally above each 10 MWh string.

As required, some of the electrolyte is pumped from a reservoir below grade to this heat exchanger and then piped to each module for intermixing with the total electrolyte volume (Figure 2-2). As this liquid flow is continuous for battery operation, temperature will be regulated by control of air flow through low speed fans and shutters. Plastic piping will conduct electrolyte to aluminum finned, titanium tube radiators.

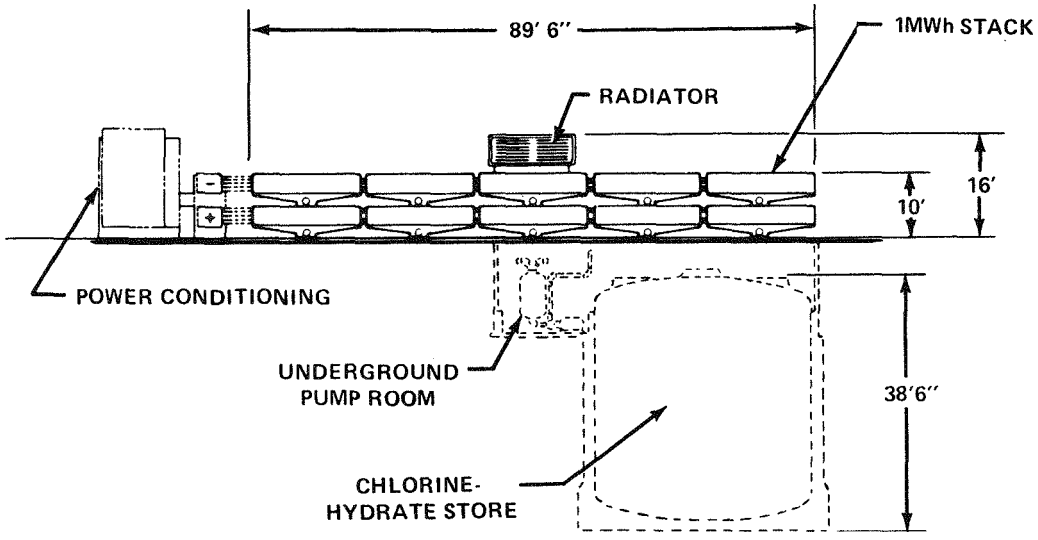

Figure 2-2. Dimensioned End View of Mark 2 100 MWh (20 MW) Peak-Shaving Battery Plant Showing Below-Grade Chlorine-Hydrate Store and Sump in Equipment Corridor.

Ten positive and ten negative terminals are located at opposite end of the basic 1 MWh battery modules. These ten terminals connect each individual module in series with one another. Then, of course, in turn, they connect the battery string to the battery station's positive and negative buss bars. Short interconnection cables are used between module terminals. Since no electrical inner-connection exists between the submodules, each terminal will carry only one-tenth of the total current passing through the string. Note that each sub-string will pass 200 amperes. This low current level allows the use of standard, readily-available, and inexpensive components.

BASIC BATTERY MODULES

Description of the terminal connections, previously presented, implies an important feature in the design of the basic 1 MWh battery modules. Figure 2-3, a simplified cut-away drawing of the module, shows its most salient internal design features.

In the extreme lower front corner of Figure 2-3, one terminal can be seen passing into the core area and bent to lay alongside a battery stack. It is connected to this stack by a group of flexible titanium cables imbedded in the stack collector bar. The opposite terminal is shown in phantom at the other end of the battery stack. All terminals exit from the case through sealed bushings.

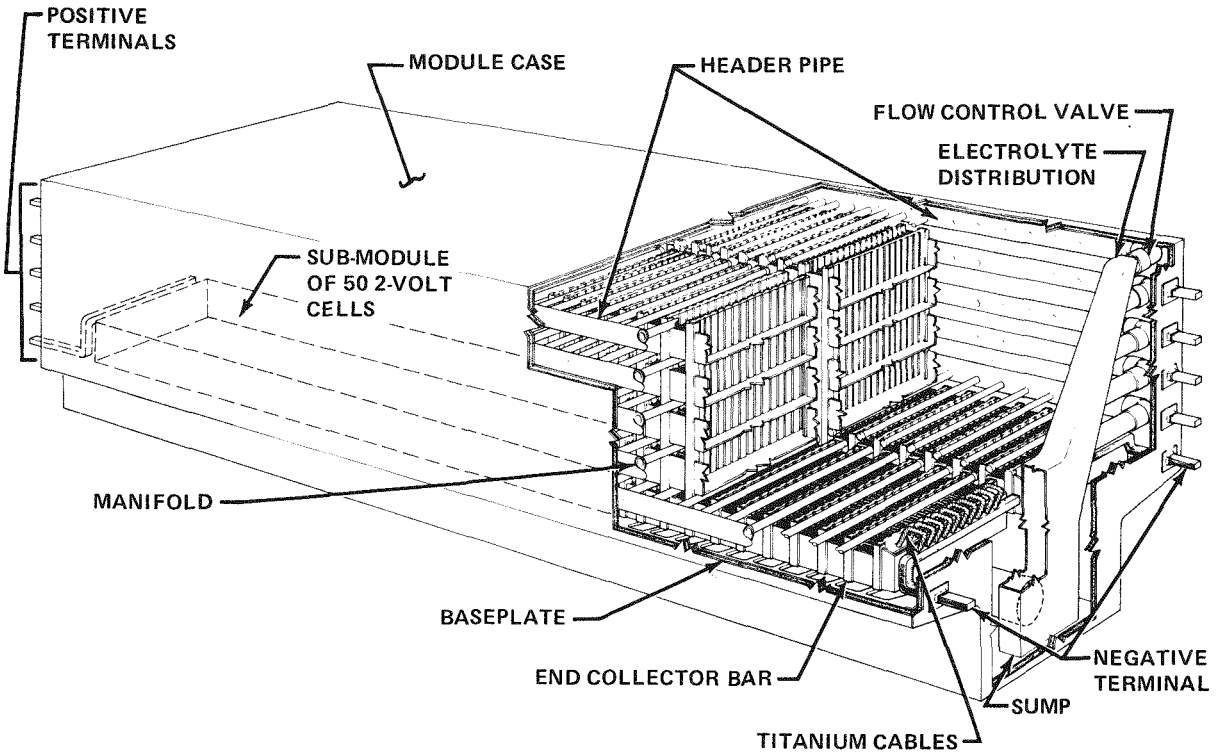

Figure 2-3. Cutaway View of Mark 2 1 MWh Battery Module.

Elemental 2 Volt Cells

To reach the desired 1000 volt plant voltage, each module in the string must operate at 100 volts. Therefore, fifty elemental two volt cells (battery stacks) are series-connected internally (one to the other) between the two terminals. This series of cells represent a "sub-module". Another sub-module is shown on the other side of the case directly behind this stack. It is another lineup of fifty cells with a terminal connection extending outside the case from either end. Shown partially cutaway are eight other sub-modules, four above the first and four above the second. These ten

identical sub-modules, each an electrically separate and independently functioning 100 kWh battery, are packaged in an insulated, gas-tight, plastic case with the associated electrolyte pump and distribution system to form the basic 1 MWh module.

Electrolyte Distribution

Outlet ports, on left and right sides, are connected to header pipes that lead to each end of the module. Here they connect to "Y" shaped distributors that conduct the electrolyte up and out to the sides of the module. Along the outer wall on each side are five header pipes one above the other. Each header serves to distribute electrolyte to all cells in one sub-module. Both ends of these headers are connected at each end of the module through flow-control check valves. This double feed arrangement is designed to insure an even distribution of electrolyte to each manifold. Fifty separate manifolds lead out from each header to supply every chlorine electrode in each 2 kWh battery cell.

An electrolyte collection sump is located within the case below the battery stacks. It collects electrolyte overflowing from the individual cells. The electrolyte flows to a common reservoir near the center of the module. The main electrolyte recirculating pump is mounted directly to this reservoir. A standpipe within the sump drains varying amounts of solution into auxiliary units of the system as other electrolyte is introduced into the module from the heat exchangers. (Refer to Figure 2-4, a schematic flow diagram.)

Recirculating Pumps

Pump costs and pumping energy are important design considerations if the desired results for this system are to be realized. During operation each 1 MWh module will require the continuous circulation of approximately 2,000 gallons per minute of $ZnCl_2$ electrolyte solution saturated with chlorine gas. Very low pressures in the range of 6-7 psi will be required for circulation. Under these volumes and pressure conditions a propeller type pump is indicated. This type of pump is relatively simple in construction and operates at only moderate speeds. These duty factors suggest that it may be possible to develop a pump constructed principally of plastic components having a 6 to 8 inch axial flow. Development of a suitable plastic pump of this type would have a marked influence on a major cost item. An alternate may be a propeller pump made entirely of titanium metal.

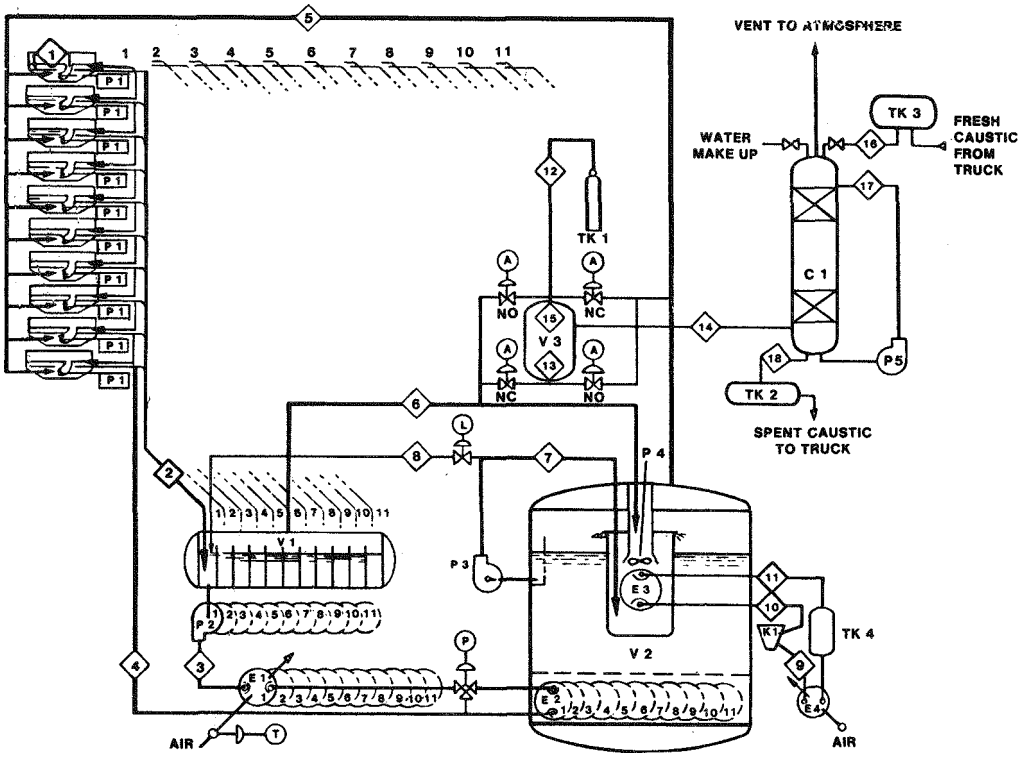

PROCESS STREAMS

1. $ZnCl_2$ FLOW IN 1 MWh MODULE
2. MIXED FLOW DELIVERY:
   A) $ZnCl_2$ FLOW FROM 10 MWh STRING
   B) GAS FLOW
   CHARGE (Cl_2 + 0.1 w/o inerts)
   DISCHARGE — Cl_2
   INERTS AT 33-1/3 w/o
3. $ZnCl_2$ FLOW FROM P-1
4. $ZnCl_2$ FLOW FROM HEAT EXCHANGERS
5. CHLORINE FLOW LINE ON DISCHARGE
6. CHLORINE FLOW LINE ON CHARGE + 0.1 w/o NON-CONDENSIBLES
7. WATER CIRCULATION FLOW IN STORE
8. WATER RETURN LINE FROM STORE TO STACK SUMPS
9. 10 11 SPECIFIED BY REFRIGERATION UNIT USED
12. MAKE-UP CHLORINE FLOW FROM TANKS
13. CONTINUOUS EXHAUST STREAM FROM SYSTEM:
    A) 66-2/3 w/o CHLORINE
    B) 33-1/3 w/o NON-CONDENSIBLES
14. CONTINUOUS EXHAUST STREAM FROM NON-CONDENSIBLE GAS INTENSIFIER
    A) 17 w/o CHLORINE
    B) 83 w/o NON-CONDENSIBLES
15. RETURN FLOW OF CHLORINE FROM NON-CONDENSIBLE INTENSIFIER
16. FLOW OF 50 w/o NaOH
17. RECIRCULATING SCRUBBER FLOW-SPECIFIED BY EQUIPMENT USED
18. RETURN OF SPENT CAUSTIC WITH WATER MAKE-UP SPECIFIED BY EQUIPMENT USED

COMPONENTS

P—1	PROPELLER PUMP (110 UNITS)
P—2	HEAT EXCHANGE LIQUID PUMP (11UNITS)
P—3	WATER RECIRCULATING PUMP
P—4	AGITATOR AND GAS INDUCTOR
P—5	CAUSTIC RECIRCULATING PUMP
V—1	SUMP HAVING 11 NON-INTERMIXING COMPARTMENTS
V—2	HYDRATE FORMER-STORE AND INERT GAS CONCENTRATOR
V—3	NON-CONDENSIBLE GAS INTENSIFIER (ELECTROCHEMICAL DEVICE WHICH WILL BE DESIGNED AND BUILT BY EDA) 10 kW POWER CONSUMPTION
TK—1	RESERVE CHLORINE STORAGE TANK
TK—2	SPENT CAUSTIC STORAGE TANK
TK—3	FRESH CAUSTIC STORAGE TANK
TK—4	REFRIGERATE STORAGE TANK
E—1	HEAT EXCHANGER (11UNITS) FOR SUPPLEMENTAL COOLING HAVING A TEMPERATURE CONTROLLED FAN
E—2	HEAT EXCHANGER (11 UNITS) FOR DE-COMPOSING HYDRATE — ABOUT 1,250 ft TOTAL AREA REQUIRED FOR ALL 11 UNITS
E—3	HEAT EXCHANGER FOR CHILLING WATER FOR PRODUCING THE CHLORINE HYDRATE (ABOUT 3,570 ft AREA REQUIRED)
E—4	AIR COOLED REFRIGERATOR CONDENSER
C—1	SCRUBBER FOR ABSORBING VENTED CHLORINE
K—1	REFRIGERATION COMPRESSOR

Figure 2-4. Schematic Flow Diagram of Mark 2 100 MWh Battery System.

A pump of this design would be incorporated in the basic module. It would be a double elbow style prop pump, with a 7 inch diameter propeller running at 1720 rpm, directly driven with a 10 horsepower synchronous motor at an estimated hydraulic efficiency of 70%. The 8 inch diameter pump inlet would be mounted directly to the side of the sump. This places the pump and motor outside the case under the center of the module for maintainability.

Cell Tray Design

The individual sub-modules, eleven hundred in the 100 MWh load leveling battery, are designed for automatic assembly from mass-produced subassemblies. To facilitate assembly, the sub-modules will be built in two identical parts (each composed of fifty (50) 1 kWh unit cells in series). These cells will be contained in a single-sectioned tray that contains the battery electrolyte and provides location and structure for each cell (Figure 1-2).

Such a tray will be built from injection molded plastic tray sections, sonic welded one to the other with each section being identical to the other. Each is molded with details to self-locate to the adjoining section. As these sections are assembled, a receiver is formed to locate a graphite connector bar across the tray. This divider acts as an electrical connection between cells as well as forming separate compartments within the tray. Into each compartment is inserted an electrode stack.

The electrode stack is assembled from twenty-four (24) chlorine electrode packs interspaced with twenty-five zinc electrode packs (Figure 2-5). Each chlorine pack is produced by securing two, thin, flat rectangular plates of porous material in a plastic frame. The plastic frame, designed as two mating injection molded parts to be sonic welded together at assembly, serves several important functions. First, it holds the two electrodes apart face to face and seals the edges to form a hydraulic chamber into which electrolyte can be pumped. This is accomplished through passages molded in the frame part of the frame assembly. Injection nozzles at the end of each passage control the flow and distribution of electrolyte within the electrode space.

In addition to these hydraulic functions, the frame also isolates the electrodes electrically and provides the required structural support to the pack. Details also are molded in the outer faces of the frame to locate and support the matching zinc electrodes. These thin graphite plates are laid in place between the frame packs as the stack is assembled. The edges of the zinc electrodes are exposed along one side.

This arrangement permits the entire edge of one type electrode to be connected in parallel; then, each group can be series connected to its opposite type in an adjoining cell by means of graphite connector bars. This bipolar arrangement forms a continuous, efficient, and compact array of unit cells for each sub-module.

As mentioned above, each frame assembly has a ring-like chamber at the top. As the frames are stacked together, a plastic short-tube seal is inserted to interconnect these ring-like sections into a continuous manifold. This passage will serve as an electrolyte supply manifold for the stack.

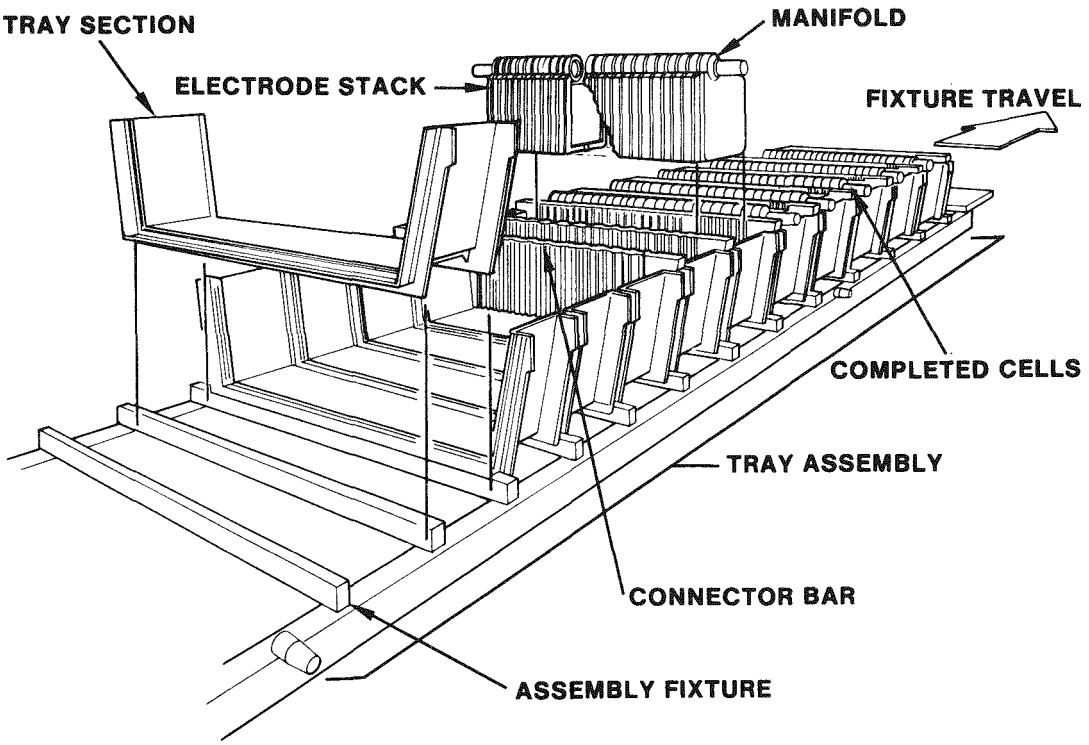

Figure 2-5. Assembly of Sub-Module, Comprising Fifty Single-Sectioned 1 kWh Cell Trays.

HYDRATE STORE

Another important feature of the complete battery system is the chlorine hydrate store. Essentially it is a chilled water, under-ground storage tank as was shown in Figure 2-2. Temperature of the hydrate store will be controlled to close limits.

A single 200,000 gallon tank is planned. This capacity is conservatively estimated based upon hydrate densities in current laboratory battery models. A central location under one side of the array of modules is preferred to minimize plumbling. Such a tank would be built as a 32 foot diameter, reinforced, insulating concrete open foundation 38 feet deep. This would be lined with a thin PVC shell and closed on top with a fabricated plastic cover.

Internally, near the top of the tank, the hydrate forming device is located where incoming gas mixes intimately with near freezing water. Chlorine hydrate, a snow-like solid, settles to the bottom where it is stored. Titanium tube heat exchangers are located near the bottom. Hot battery electrolyte, circulated through the tubes during discharge, warm the hydrate, breaking it down and releasing chlorine gas, as required. A continuous stream of water is recirculated within the tank to operate the forming device and flush the chilling coils. The refrigeration capacity needed is estimated to require three compressors of approximately 350 horsepower each with related pumps, controls, and condensors. As mentioned earlier, this equipment would be housed in the small building beside the associated cooling towers. Some electrolyte must be discharged from each module and collected in a sump where entrapped gases can be separated and transferred to the hydrate store. A gravity overflow system for this transfer is desirable. Therefore, plastic collection tanks would be located below grade in the equipment corridor beneath the center of the stack control radiators described earlier and returned to the electrode stacks in each module. Access to this corridor and to the top of the underground store would be through the building basement.

ASSEMBLING THE BASIC MODULES

Assembly build-up of a basic, unitized, 1 MWh module is visualized as follows:

Each sub-module section will come from automatic assembly machines mounted on a fixture. This construction fixture will place the assembly in proper position on the module base plate. This base plate, a rigid plastic member fitted with locator rails for first tier sub-modules, is integral with a structural stack stand. This stand also supports the sump sections of the case that are sealed to the lower side of base plate and pump.

Four sub-module sections, installed side by side, form the first tier on the base plate. At this point the manifolds for each electrode stack will be coupled together and the connections at each end to the appropriate terminal buss bars completed. These terminal busses previously have been mounted to the inside surface of the

vacuum-formed foamed plastic case end walls. Each buss is made of a 5/8-inch diameter, titanium-clad copper bar to which flexible titanium cable pigtail have been welded. The end of each buss extends through special compression seal fittings to provide external connection to the battery.

Extensive hydraulics and electrical checks can now be made on these two completed (first tier) sub-modules. Likewise, a second tier will then be built, installed and tested using the same assembly fixture; then, four more identical sub-modules constructed to be placed on top of the first tier. The tray sections and the graphite connectors will serve as self-locating load members. When the final tier has been connected and tested, the complete stackup of 5 sub-modules will be tested and qualified against design specifications.

The next assembly step will be to secure the formed plastic case side walls in place. These will be sealed to the base plate and to the previously erected case ends. Five horizontal rows of holes in each wall allow the entry end of each cell manifold to project through. Using an injection-molded, flanged, inlet ferrell and an electric power tool each manifold port will be spin-welded to the case side wall. This design affords a secure anchor to the case, and a gas-tight electrolyte opening for each 2 kWh unit cell within the module.

A vacuum-formed header section fits over each horizontal row of manifold openings. This section of the electrolyte distribution system, described earlier, is sealed to the outer wall surface to form a conductor for the battery solutions from the pump risers to each manifold opening. The shape and size of this header varies along its length to insure an equal flow into each manifold. These long, closed channels also add stiffening to the case walls. The module case is completed by adding the rigidized, formed plastic top panel and sealing it to the side and end walls of the case.

It is planned that each module will be completely factory tested before shipment. Using a suitable test stand, connections can be made in the sump for electrolyte interchange and chlorine gas introduction. A temporary installation of the main pump unit will allow for filling the system with zinc-chloride solution for complete operational check outs. The system will be drained before shipment.

SUMMARY

The design previously described allows the basic 1 MWh modules to be mounted in pairs, one above the other, in a common framework. The structural steel stands, integral with each module, are detailed with columns and locating sockets. Since these "twin-packs" will be somewhat over ten feet in height, this stacking likely will occur during on-site erection. The basic shipping package will probably be an individual completed module. Two such units, each five feet high, 6-1/2 feet wide, and 17-1/2 feet long, will fit comfortably on a standard, 40-foot highway trailer (Figure 2-3). Detailed layouts and part drawings have been prepared for all battery stack components, i.e. the basic module. A proposed general arrangement of the complete battery installed at a utility sub-station is shown in Figure 2-4 and a discussion of some dimensions reflected in these drawings will give an idea of the size and scale of this battery.

Beginning at the elemental cell level, it will be recalled that an active electrode face 2.5 inches by 4.0 inches (10 square inches active area) was selected from experimental experience. The finished cut size for an individual electrode plate is 3.188 by 4.375 inches to accommodate retention frames and intercell connection. Thickness of these plates vary from 0.032 to 0.080 inches depending upon electrode material and type. More than 8 million of these plates are required for the total battery plant. Two thirds of these plates will be porous chlorine type; the other third will be a graphite substrate for zinc types.

Using experimentally selected electrode spacing, plastic retainers, manifolds, and connection details, the basic 1 kWh cell is 12.98 inches long, 3.75 inches wide, and 6.44 inches high. As previously mentioned, each 1 kWh cell contains twenty-four chlorine pairs and twenty-five zinc electrodes. A sub-module section consists of fifty of these cells coupled side-by-side. They are assembled in an electrolyte containing tray with provisions for overflow return, terminal buss connections, and structural support. This sub-module package develops to 16 feet long, 16 inches wide, and 6-3/8 inches high. This is the unit planned for machine assembly on a movable holding fixture. Two thousand two hundred (2200) such units are required for the planned 100 MWh Peak-Shaving Battery Plant. Two of these sub-modular sections, placed side by side and connected electrically and hydraulically, form the 100 kWh sub-module which is the basic link in the station string. A bank of ten sub-modules, two wide and five high, forms the core stack for one 1 MWh module. This stack, including the terminal buss connectors, develops to an assembled size of 16 feet 8 inches long, 5 feet 8-1/2 inches wide, and 33 inches high.

An insulated, gas-tight, plastic case with conduits for distributing the electrolyte supply, and a structural steel supporting frame is constructed around this core. Within the frame and below the core, the reservoir is located with pump unit and external piping for electrolyte and gas circulation. Taken altogether, this dimensional stackup of 1 MWh module components adds up to 17-1/2 foot by 6-1/2 foot by 5 foot high.

Proposed assembly of these modules into a 1 MWh battery for utility sub-station use has already been illustrated. As previously illustrated in Figures 2-1 and 2-2, completely tested units will be placed at a prepared site in eleven rows, or strings. Each row will be assembled with five modules placed end-to-end at grade level, and five additional modules placed on top of these. Allowing space between the ends of adjacent modules (for installing electrical buss connectors and for transfer piping) such a row will be 89 feet 6 inches long and 10 feet high. Spacing the rows closely with a minimum three foot access between each row results in a span of 101 feet 6 inches for the eleven rows. Figure 2-6 shows a planned view of this arrangement.

Also, on the site is a small electrical and mechanical equipment building measuring 21 feet by 59 feet. Two 2421 CFT refrigeration cooling towers complete the grade level facilities. The latter occupies a space approximately 23 feet square. The entire land area for this 100 MWh peak-shaving battery measures 125 feet by 89 feet 6 inches, just 1/4 acre. This area does not, of course, include space for the station busses, transformers, and power conditioning equipment nor for access roadways, planting space etc. that would be desired. All this would possibly double the land required to a half acre site. Nevertheless, the battery proper occupies 11,188 square feet - a "footprint" resulting in a capacity of 8.94 KWh/sq ft.

Layouts and drawings were detailed to a degree sufficient for making a manufacturing cost analysis for the 1 MWh battery modules. Costing information also was developed for graphite, plastics, pumps, motors, and other components. The costing analysis study concluded that at a production rate of one-hundred 100 MWh plants per year, the installed cost in 1976 dollars would be $25/kWh. At a production rate of one 100 MWh plant per year, this cost would rise to $61/kWh, as described later in Section 4.

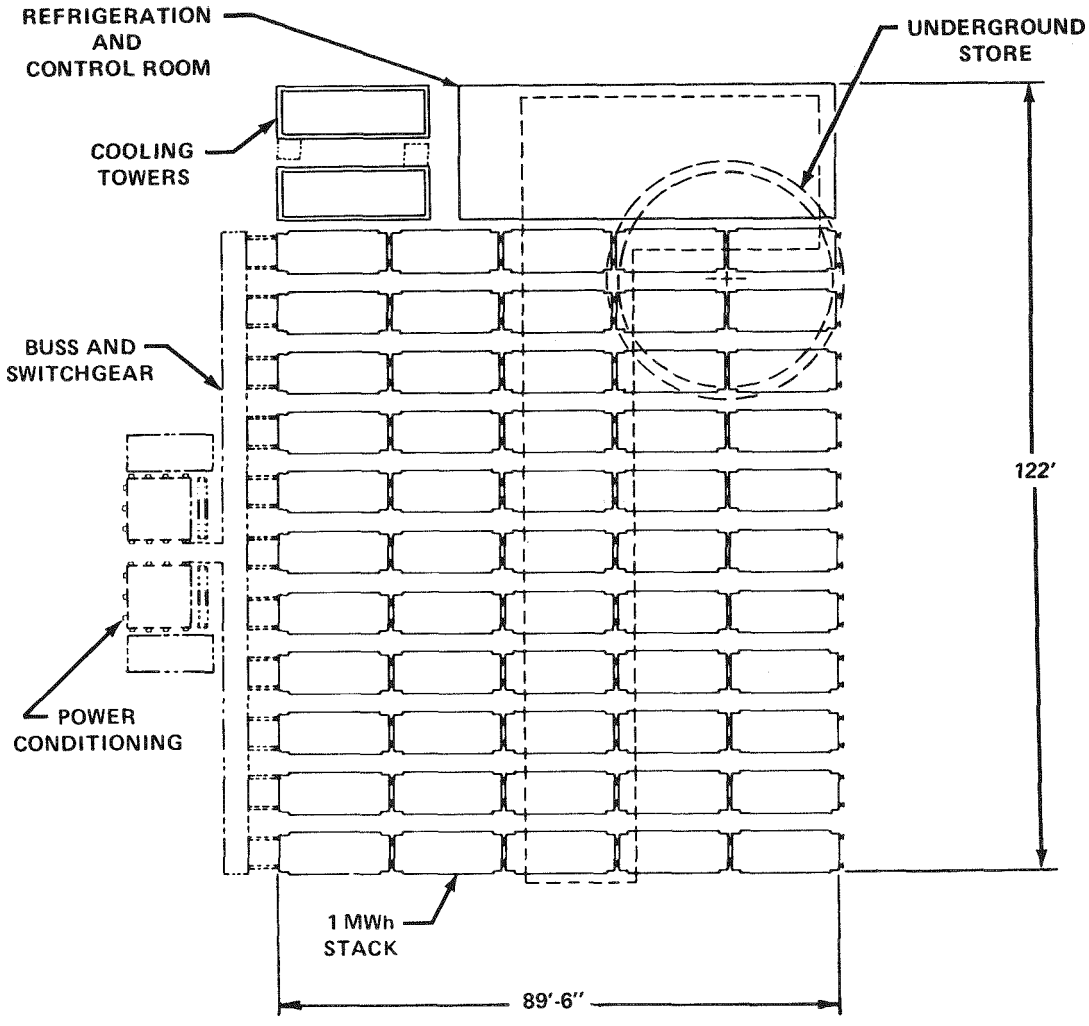

Figure 2-6. Plan View of Mark 2 100 MWh (20MW) Peak-Shaving Battery Plant.

Bechtel Corporation, under EPRI contract RP731-1, estimated the cost for one 220 MWh $ZnCl_2$ battery plant (2-1). Their process plant estimating methodology yielded a cost of $62/kWh for this one-of-a-kind system. It can be shown that this cost is in agreement (to one significant figure) with the costs for chlorine-storage subsystems in EDA's costing efforts.

In all, the following observations constitute a list of negative aspects associated with the Mark 2 design concept:

- The costing presumes a "turn-key" plant which is not considered an accepted approach by the utilities' representatives.
- As the store in this design is underground it is likely that the design will be limited to certain kinds of terrain.
- As warm electrolyte must be circulated from each module to heat exchangers in the store, in order to provide for decomposition of chlorine hydrate during discharge the field-labor charges associated with the piping will be a large cost item.
- Excavation for and construction of the underground store and pump room will be site labor-intensive. It will, therefore, be a significant expense, if utility labor is employed.
- Uniform distribution of electrolyte with a single pump to each and every chlorine-electrode pair in the five tiers of unit cells poses considerable problems from the standpoints of hydraulic-energy conservation and engineering.

REFERENCE

2-1 "Engineering Design and Cost Analyses of Chlorine Storage Concepts for a Zinc-Chlorine Load-Leveling Battery"; prepared by Bechtel Corporation, San Francisco, California; EPRI EM-259, Final Report, November, 1976.

Section 3

MARK 3 DESIGN

INTRODUCTION

Minimization of site labor was the major goal of the Mark 3 design. Thus, all components of this 100 MWh battery plant including the hydrate stores and refrigeration equipment were to be factory assembled so as to be truckable, without special regulation, to the substation location. Each plant component, therefore, had to fit within a volume: 40 feet X 8 feet X 10 feet.

An artist's rendition of the Mark 3 peak-shaving battery plant is shown in Figure 3-1. The plant consists of 3 superstrings, each delivering 36 MWh. Each superstring is comprised of six 6 MWh battery modules, each being transported to the site separatedly. Associated with a superstring are 8 cylindrical hydrate stores and associated hydrate formation equipment. It should be noted that the eight stores are coupled (i.e., have a common gas space) to each other and with the six modules comprising the superstring. In the left background, the buss work may be seen leading to the power-conditioning equipment, shown in the background. Also, in the left

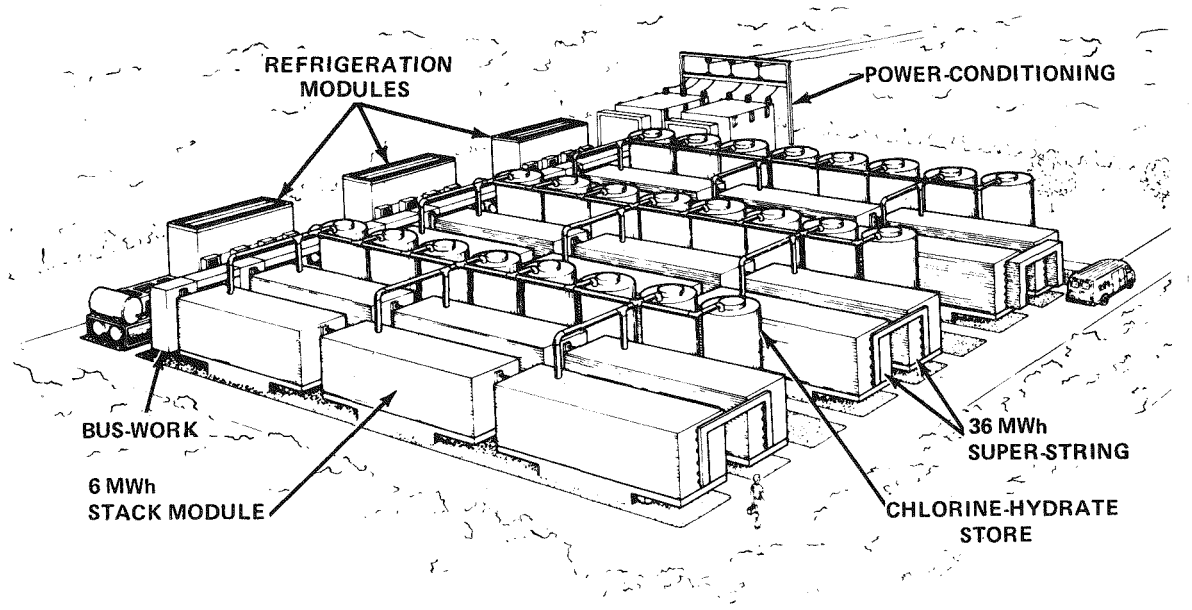

Figure 3-1. Mark 3 102 MWh Zinc-Chlorine Peak-Shaving Battery Plant.

background may be seen three sets of refrigeration equipment on individual skids, each skid having been transported separately to the substation location. Plan and elevation views of this plant are shown in Figure 3-2.

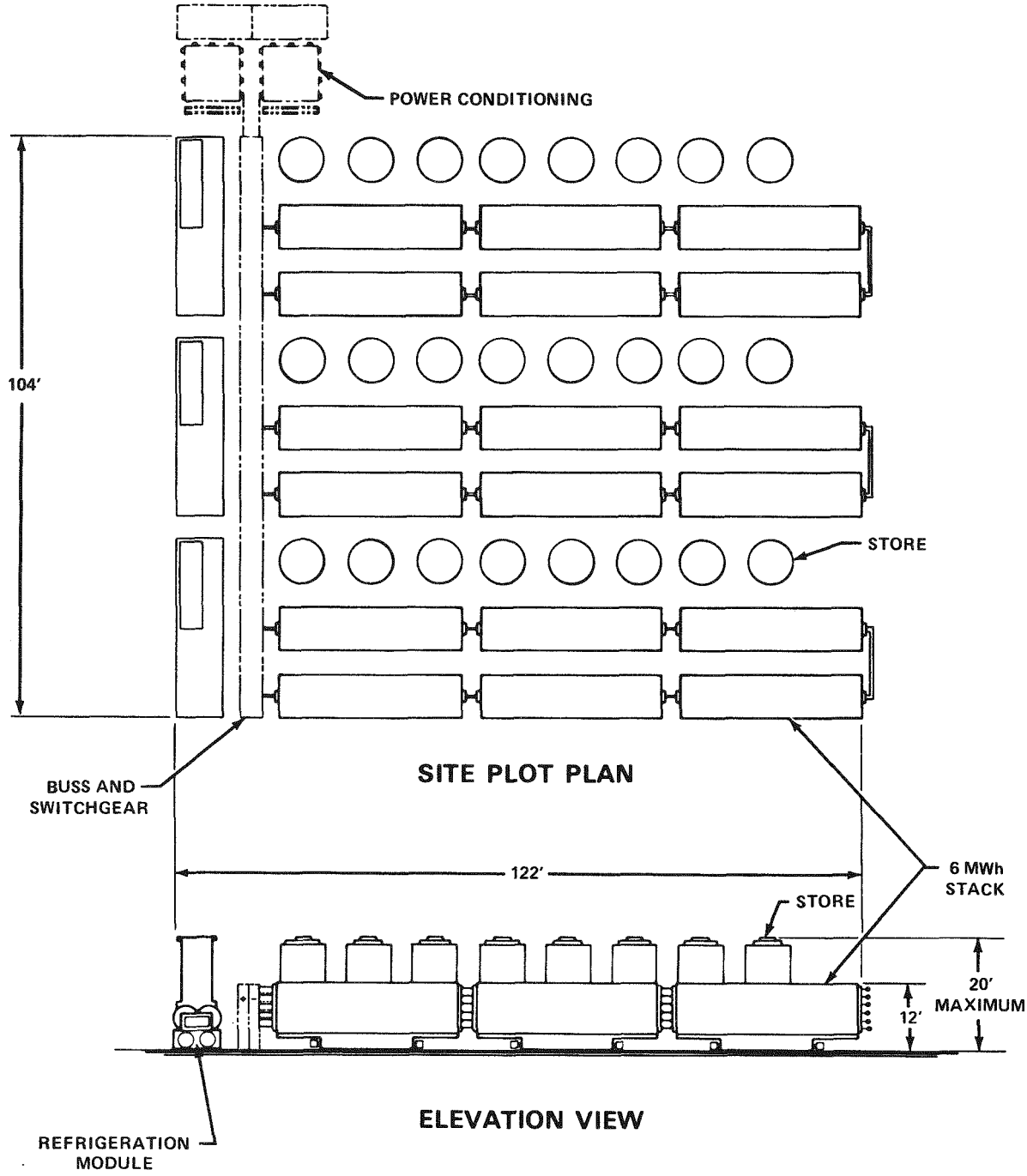

Figure 3-2. Plan and Elevation Views of Mark 3 102 MWh Battery Plant.

The 6 MWh battery module is shown schematically in Figure 3-3. Although the module is a hydraulic unit with a single sump, there are six electrically-separable submodules. Each of the submodules is fed by its own pump located in the sump. The submodule consists of two levels, each with four parallel runs of seventy-two 1.76 kWh cells. One consequence of the electrical isolation of the submodules within each module is that there are six strings within a given superstring, if the submodules on any given level of the six modules comprising the superstring are connected together. In this way, it is possible to have six or less of these strings operating independently within the superstring at any point in time. This is useful

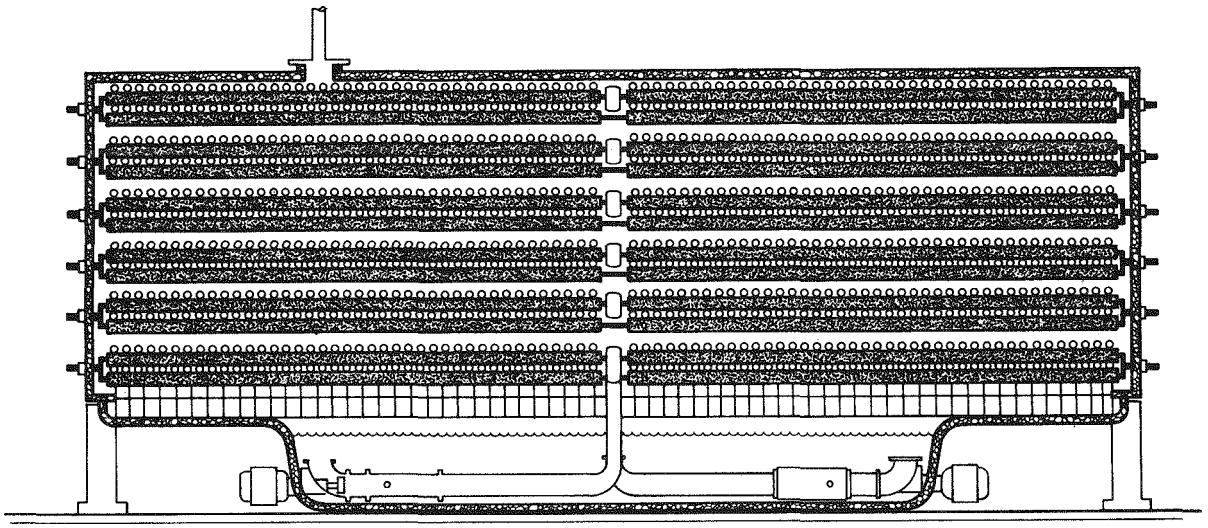

Figure 3-3. Cross-section of a Mark 3 6-MWh module. Note six electrical submodules, each fed by an electrolyte pump mounted in the sump.

from a load-following standpoint. The rated capacity of the battery plant is 102 MWh, i.e., seventeen 6 MWh strings. One extra 6 MWh string is provided because of the need for complete discharge of each string before recharge. A list of definitions is presented in Table 3-1 for clarification purposes. The cell structure is essentially identical with that of the Mark 2 design.

Table 3-1

SELECTED DEFINITIONS FOR THE MARK 3 BATTERY DESIGN

COMPONENT	DELIVERED ENERGY	AVERAGE DISCHARGE VOLTAGE
Superstring	36 MWh	864V
String	6 MWh	864V
Module	6 MWh	144V
Submodule	1 MWh	144V
Unit Cell	1.76 kWh	2V

Charge current density was assumed to be 45 mA/cm^2 at an average voltage of 2.25V. Discharge current density and voltage were assumed to be 40 mA/cm^2 and 2V, respectively, reflecting improvements in cell technology during 1976. The electrochemical energy efficiency was assumed, for design purposes, to be 80% with a voltaic efficiency of 89.9% and a usable coulombic efficiency of 90%. Overall plant efficiency was in excess of 70%. The footprint of the battery plant was 8 kWh/ft^2, while the height criterion of 20 feet was again observed. Access aisles were 4 feet in width, to allow easy servicing of the six pump motors in each module.

Cost estimates for the Mark 3 design indicated that relative to Mark 2 the increased costs due to the replacement for the single underground store by twenty-four above-grade stores are approximately offset by the savings in site-preparation, piping, valving, and installation. A further and significant savings was effected by the increased discharge current density (40 mA/cm^2 in Mark 3 vs. 30 mA/cm^2 for Mark 2) which substantially reduced graphite-electrode costs. This savings was, however, offset by increases in the price of graphite. Nonetheless, a cost of approximately $25/KWh (1976 $) was generated for a production rate of one hundred 100 MWh battery plants per year.

Criticism of the Mark 3 design by electric-utility representatives centered mainly on the safety and environmental aspects of these plants. The presence of 75 tons of chlorine (25 tons per superstring), even as non-explosive, non-flammable, and slowly-decomposing chlorine hydrate, in a fully-charged battery plant led a number of representatives of Florida utilities to declare that the granting of permits for siting the Mark II plants in residential areas was probably an "uphill battle". Representatives of Detroit Edison, which has a good deal of experience with chlorine, both at its generating plants and on its railroad lines, were less intimidated, but pointed out that the burden of proof was on EDA to prove the absence of hazard. A more serious criticism was leveled at the Mark III design as a result of analysis performed at EDA. Briefly, it was concluded that the stack module would be very difficult to manufacture efficiently and cheaply because of its size and the high packing density of its cells. As a result, efforts were directed toward addressing these criticisms with a compatible design philosophy.

Implied in this is that the achievement of these objectives requires that specific developmental steps be taken. Inputs from EPRI and electric utilities representatives together with the design and cost studies generated within EDA, have provided the guidance for identifying significant developmental and system design considerations. Presently, the criticisms raised against the Mark 2 and 3 designs have created the impetus for the next step, Mark 4. Although this new design is in its formative stage, it would appear that the design, cost and performance objectives will be met.

Section 4

COST ANALYSIS OF 100 MWh (20 MW) PEAK-SHAVING BATTERY PLANTS

INTRODUCTION

Design, construction and successful testing of the 1 KWh zinc chloride battery constituted a significant milestone in the overall, R & D load leveling program. The final report, issued in satisfaction of EPRI Contract RP226-1-1, described in detail the basic cell data, the construction and operation of each component, and finally, the experimental results observed after 100 complete charge and discharge cycles (4-1).

Having accomplished this, Contract RP226-1-2 (known as Amendment No. 2) was issued as a cost and design study. Its objective was to estimate the cost of a 100 MWh peak-shaving substation based on the basic zinc chloride battery concept. Another objective of this study was that a comparison be made between the costs of zinc chloride battery systems using graphite and titanium as the substrate material for chlorine electrodes. In so doing, a cost breakdown was to be made with special emphasis given to major cost components. These costs estimates were to be predicated upon an assumption of high production and a mature technology.

Projecting the selling price of a non-existing system raises a host of problems. These problems cannot be approached from a fundamental level; that is, the basic building blocks that constitute the actual cost determining factors cannot be specified at this time.

In lieu of this, two general approaches can be used that "force" an estimated costing. The first is the well-known estimating method used for process plants. This method relies on experiential cost data on plants already in existence. Analytical methods exist for graphically representing the parts of the plant to provide a basic for estimating these cost components in the future. The second method is a well-established technique in the financial analysis of manufacturing processes. This method requires beaking down the cost factors directs itself

toward focusing on the major cost items in order to investigate the reasons underlying the costs and, sometimes, finding more economical alternatives.
A manufacturing cost estimate is a by-product. Many variants of these two methods exists; each suffers from its unique set of uncertainties. In the costing which follows, the second method was selected primarily because it provides a means for identifying areas where significant cost reductions might be achieved. In this manner, a dollar figure of merit is an objective measure of R&D significance. In short, the second method gives direction for further development; whereas, the first method does not.

The approach to the costing is straightforward. The 1 kWh battery was costed in the form that it was in; and then these costs were replicated to provide an estimated cost for 100 MWh of energy storage. Of course, the estimated cost was enormous. However, the purpose was not to determine the cost, but the distribution of costs. Then followed a series of iterations directed at analyzing the major cost contributions. The costing breakdown presented represents a compilation of the estimated component costs at the time. It should be clear that the numbers given are still capable of further reduction upon closer scrutiny. A discussion of these major cost items will be presented later under appropriate headings.

In addition, the costing methodology selected generated a series of design restrictions on the battery system. These restrictions became the basis of a design effort to conceive and detail the battery system, its component parts and its method of assembly. By attempting to generate such a detailed design, the resultant drawings created a basis for specifying the manufacturing process; this, in turn, leads to a substantially improved model for estimating manufacturing costs. These extended studies, however, remain to be done.

A preceding study (RP 226-1-1) addressed itself to the development, construction and test of a 1 KWh zinc chloride peak-shaving battery. By virture of having a complete operating system, projections could now be made of a 100 MWh load leveling battery plant from both a design and cost vantagepoint. A listing of fundamental design specifications is given in Table 4-1. Basic design and performance parameters are presented first; whereas, the projected values at the bottom of the table are considered highly probable goals.

Table 4-1

MARK 2 ZINC-CHLORIDE PEAK-SHAVING BATTERY SPECIFICATIONS

Electrical Requirements

Voltage	1000 volts nominal
Capacity - Rated	100 MWh
Capacity - Reserve	10 MWh
Capacity - Total	110 MWh
Discharge Rate	5 hour
Discharge Power (maximum)	20 MW
Charge Rate	7 hour
Net Energy Efficiency	>70%
Charge Current Density	24 mA/cm^2
Discharge Current Density	30 mA/cm^2
Electrode Area Required for 20 MW	3.33×10^8 cm^2

Projected Efficiency (in %)

Voltaic Efficiency on Charge	94.8%
Voltaic Efficiency on Discharge	94.4%
Coulombic Efficiency on Charge	92.2%
Coulombic Efficiency on Discharge	97.0
Overall Electrochemical Efficiency	80.0%

One possible model for representing mass flows is the system schematic shown in Figure 4-1. Mass flow calculations are shown in legend in this figure. In order to arrive at these numbers, certain assumptions were made. These assumptions are listed for reference in Table 4-2. All other parameters are either well-established constants or are derivable from first principles.

Figure 4-2 represents the energy flow within the system. Energy flow is based on the designed thermodynamic quantities for the reactions and estimated efficiencies of the various system components. Constants used in the calculation are available. These efficiency assumptions are listed in Tables 4-1 and 4-2.

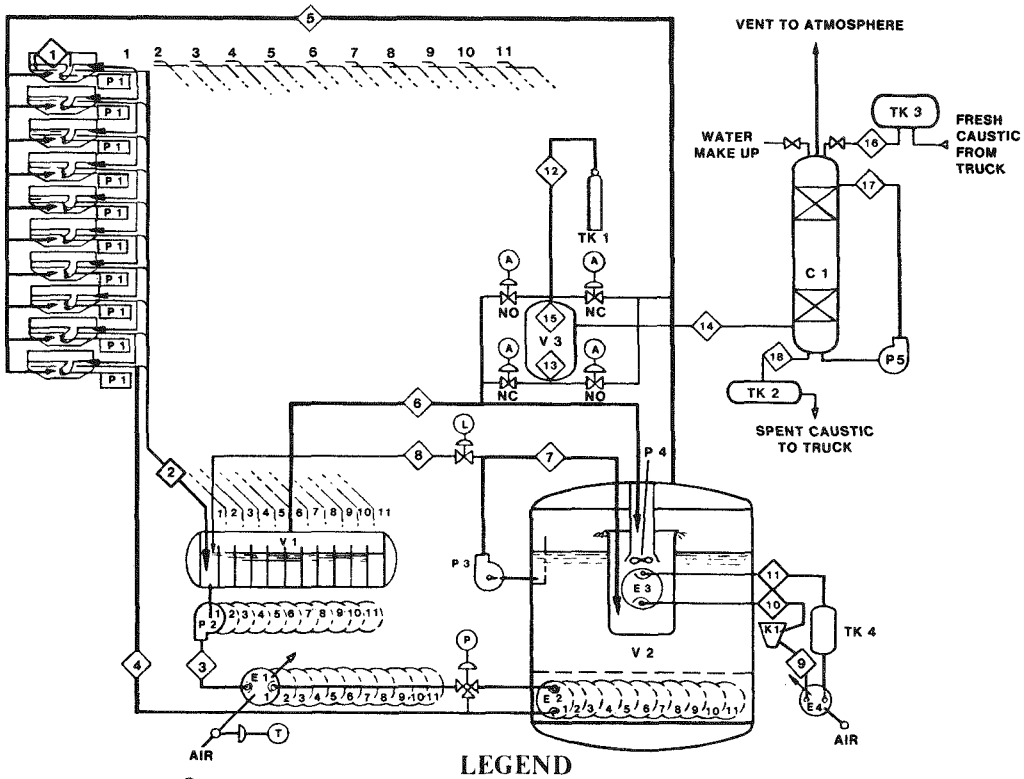

LEGEND

NO.	DESCRIPTION	GM/HR.	CC/MIN.	GM/CC	T (°C)	(N) ATM PRESSURE
1.	$ZnCl_2$ FLOW IN 1 MWh MODULE		3.35×10^4	1.25	50	1.2
2.	MIXED FLOW DELIVERY:					
	A) $ZnCl_2$ FLOW FROM 10 MWh STRING		2.13×10^5	1.25	50	1.0
	B) GAS FLOW			2.7×10^{-3}	50	1.0
	CHARGE (Cl_2 +0.1 w/o inerts)	$9.4 \times 10.^5$				
	DISCHARGE — Cl_2	0.237×10^4				
	INERTS AT 33-1/3 w/o	0.148×10^4				
3.	$ZnCl_2$ FLOW FROM P-1	2.13×10^5	1.25	50		
4.	$ZnCl_2$ FLOW FROM HEAT EXCHANGERS		2.13×10^5	1.25		
5.	CHLORINE FLOW LINE ON DISCHARGE	14.3×10^5			9	1.0
6.	CHLORINE FLOW LINE ON CHARGE +0.1 w/o NON-CONDENSIBLES	9.4×10^5			50	1.0
7.	WATER CIRCULATOR FLOW IN STORE	3.1×10^5		1.0	9	
8.	WATER RETURN LINE FROM STORE TO STACK SUMPS		1.73×10^4	1.0	9	
9.	10, 11 SPECIFIED BY REFRIGERATION UNIT USED					
12.	MAKE-UP CHLORINE FLOW FROM TANKS	2.970		2.3×10^{-3}	25	1.0
13.	CONTINUOUS EXHAUST STREAM FROM SYSTEM:					
	A) 66-2/3 w/o CHLORINE	29.700		3.7×10^{-3}	9	
	B) 33-1/3 w/o NON-CONDENSIBLES	14.800		1.25×10^{-3}	9	1.0
14.	CONTINUOUS EXHAUST SYSTEM STREAM FROM NON-CONDENSIBLE GAS INTENSIFIER					
	A) 17 w/o CHLORINE	2.970				
	B) 83 w/o NON-CONDENSIBLES	14.500				
15.	RETURN FLOW OF CHLORINE FROM NON-CONDENSIBLE INTENSIFIER	25.700				
16.	FLOW OF 50 w/o NaOH		73.3	1.53	25	1.0
17.	RECIRCULATING SCRUBBER FLOW-SPECIFIED BY EQUIPMENT USED					
18.	RETURN OF SPENT CAUSTIC WITH WATER MAKE-UP SPECIFIED BY EQUIPMENT USED					

Figure 4-1. Mass Flows, Temperatures, and Pressures in a Mark 2 100 MWh Zinc-Chlorine Battery Plant.

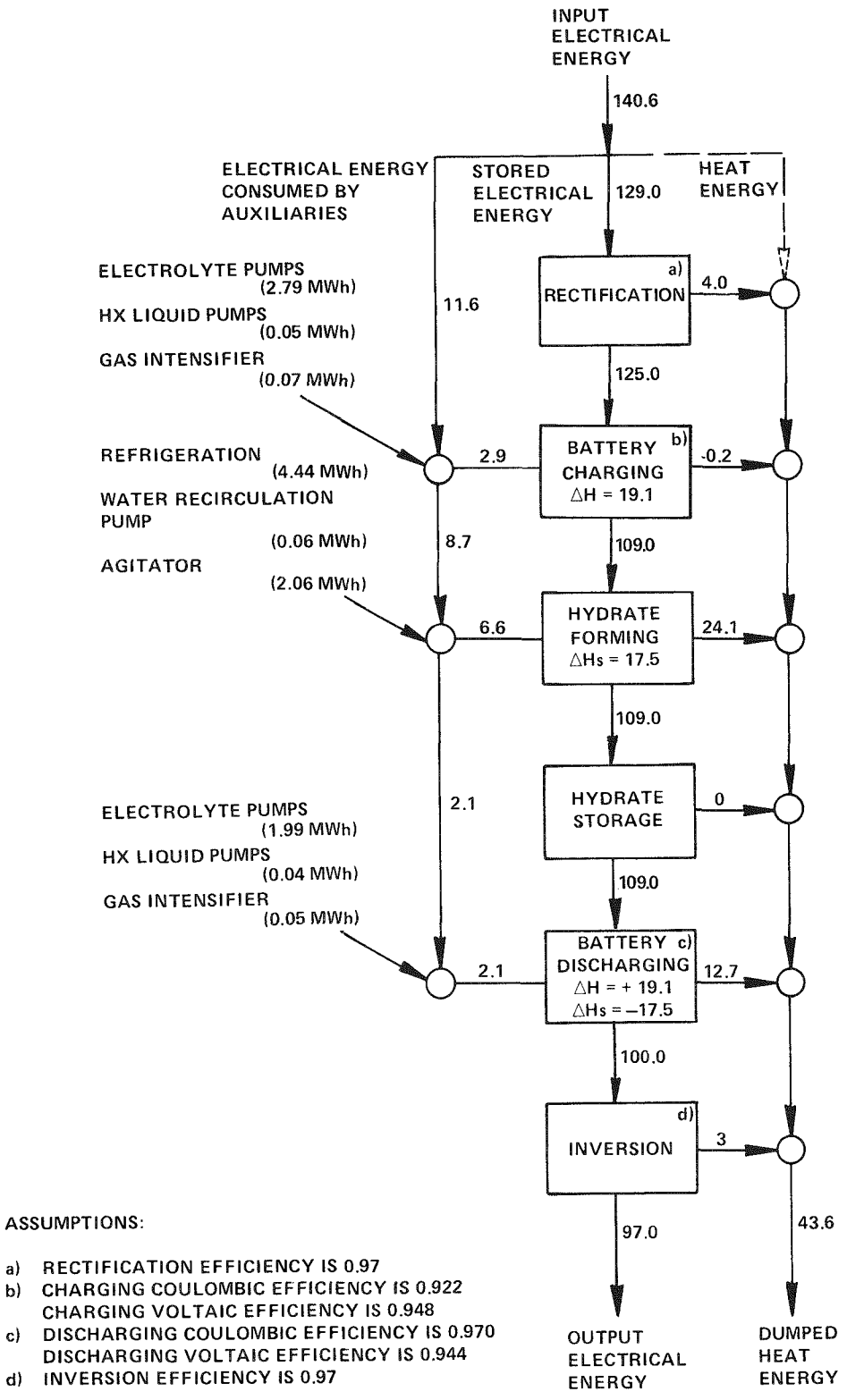

Figure 4-2. Energy Flow Diagram of a 100 MWh (20 MW) Zinc-Chlorine Peak-Shaving Battery.

Table 4-2

MASS FLOW CALCULATION ASSUMPTIONS

Water Recirculation Rate	0.05 grams of chlorine absorbed by 1 cc of water
Condensate Return	Cooled from 50°C to 6°C
Steady-State Composition of Gas (Foreign Gas Concentration Areas)	66-2/3% Chlorine 33-1/3% Foreign Gas
Electrolyte Flow	2.0 $cc/cm^2/min$
Flow to Phase Separating Pump	10% of Total Electrolyte Flow
Electrolyte Temperature in Stack	50° Centigrade
Chlorine Hydrate Temperature in Store During Charge	6° Centigrade

Having reviewed the engineering specifications and assumptions, a topic that has been the basis of some controversy will be addressed.

TITANIUM VERSUS GRAPHITE AS AN ELECTRODE MATERIAL

Introduction

Comparing titanium with graphite as a chlorine electrode material shows that graphite costs about half as much as ruthenized-titanium. However, in examining the factors determining these costs, a multiplicity of dependent factors become evident that, by altering the costing basis, could produce essentially contradictory results. Objectively, it may be concluded that the cost comparison is inconclusive at this time. Below is a full discussion of the cost determining factors based upon the direct material costs of the finished electrodes. In addition, a series of relevant factors are also discussed that can radically alter these costs.

Laboratory experience, as of the time these results were amassed, has shown that graphite can be activated by chemical treatments that show polarization characteristics similar to those of ruthenized titanium. This means that a one-to-one substitution could be made in the battery design for the chlorine electrode. Consequently, the comparison between Ti and graphite can be carried out by comparing only the electrodes themselves. This eliminates the need for introducing the battery costs in order to make the essential comparison.

Because of the large number of electrodes required, the vendor's materials costs are, at best, estimates. The reason is that in all cases, the quantities required exceed their capacity to produce the materials. The estimates, therefore, can vary from current prices for standard items to "blue sky" speculations on possible prices. Further, electrode fabrication costs can vary substantially depending on the methods used and the reliability of activation methods. Scrap and waste estimates can create considerable leverage on the cost of the finished electrodes.

Titanium

The form of the titanium, as we might expect to receive it, is that of a sintered titanium matrix. The porous characteristics would be similar to Gould's 6525 material indicating a 65% porosity and a 25 μ average pore diameter. The material as received is in the form of sheets of convenient area and about 30 mils thick. If it can be assumed that the titanium will be received in the desired dimensions for direct use in the battery without further machining; and further, that the quoted cost per foot for the material includes the waste and scrap associated with preparing the titanium sheets to electrode specification, it is then possible to project the titanium cost for the chlorine electrodes in the cell.

A quotation was received from Gould Inc. for titanium sheet. In view of the large amounts of titanium requested, the quotation is, of necessity, an engineering estimate. In May, 1974, $5.00 per square foot was quoted on a 135,000 square feet per year usage assuming the use of a "cheaper" grade of commercially pure titanium. On a 2 million square foot basis, a price of $5.00 per square foot was also quoted. Additionally, a proposal was made that should be less specialized sintering equipment and a great deal of automation be used, a $2.00 per square foot price is

conceivable. A more recent review of prices indicated that on a two million square foot basic and under the same assumptions used above, the titanium sheet would cost between $2 and $4 per square foot. Although the $2.00 per square foot estimate is attractive, the objection is that non-existing equipment and technology must be used. Consequently, the more realistic number of $5.00 per square foot will be taken as the cost of the titanium sheet.

Next, the sheet must be catalyzed in order to prepare the electrode. This is done via a ruthenization process using ruthenium chloride as a starting material. Without describing the process details, about 0.74 g/ft^2 of ruthenium has been used in a laboratory test battery.

The cost of ruthenium applied for catalyzing the titanium was estimated from data supplied by the D. Goldsmith Co. In 1975, the price of ruthenium ranged from $40-60 per troy-oz ($1.29 - 1.93 per gram). Although the starting material is ruthenium chloride, its cost is essentially that of its ruthenium content. The price figure of ruthenium for this costing will be taken as $2.00 per gram. A concern, in this context, is the amount of ruthenium available in terms of world reserves.

The Bureau of Mines reported that world reserves of ruthenium are 33 million troy-oz. Converting this number to grams, dividing by 0.74 g/ft^2 (ruthenium loading), converting the area to cm^2 and dividing that figure by the area required per battery given in Table 4-2, then the maximum number of 100 MWh (20 MW) batteries producible using ruthenium is 3.9×10^3. Of course, the area given refers only to the active area. All portions used for support are excluded so that only selected portions of the titanium substrate are ruthenized or else, realistically, only about half the number of batteries could be prepared depending upon the electrode design used.

The world's reserve of ruthenium likely would not be available for making batteries. Another perspective is that the 1974 world production of ruthenium was 62,000 troy-oz. Using the same assumptions as to loading and electrode area, a maximum of 7.2 batteries a year could be produced if the yearly productions were made available. It should be evident that the building of large numbers of these batteries would alter the supply and demand conditions and could, thereby, substantially alter the cost of ruthenium.

The above discussion tends to create an unduly pessimistic picture so that some words of explanation are in order. It is believed that the currently used loading

for ruthenium is far too generous. For example, loadings of 0.1 g/ft^2 have been used in single cell testing. The loadings were in fact not optimized and it very well may be that the 0.74 g/ft^2 is an order of magnitude too large. Even in that case, the mature market capacity would be a problem but a respectable yearly production of batteries using ruthenized titanium would be possible. Other mitigating considerations are reviewed in the section on Related Factors.

From the $2 per gram figure, the direct material cost of ruthenized titanium is $6.49 per square foot. This number assumes no waste or scrap. Incidental to this is that the ruthenization process, in its present form, produces an estimated 30% scrap rate. It is anticipated that the process will be refined in the future so as to reduce the scrap to insignificance.

Graphite

The graphite material used as the chlorine electrode must be a high purity, porous material. One such material found to be acceptable is Union Carbide's PG-60. This material is produced in blocks that require subsequent machining in order to produce the final plate structure. The price of a 9 x 14 x 14 block is $287 (8/75). The price quoted was specifically qualified as for any quantity. The reason for this was that the quantity required for a single 100 MWh battery exceeded the suppliers annual production capability. Since graphite production is a capital intensive industry the price quoted is, therefore, assumed to factor in the capital interest charges, risk factors and savings associated with mass production.

The graphite block cost must be considered in the light of the machining requirements for producing plates. Specifically, the block must be sawed into smaller blocks approximating the length and width of specified plate sizes. The blocks must then be milled to the desired tolerance. Next, each of the sized blocks must be sawed into slabs that are, in turn, ground to the desired tolerance. Depending on the specification of plate thickness and tolerance, as little as 18% of the graphite block may turn out as finished plates. The remainder is nothing but waste in the form of graphite powder. Even the most efficient selection of tolerances will utilize the block to less than 50%. For example, PG-60 block could be sawed into size of 2.65 x 4.30 square inches. Use is made of what is believed to be the most efficient cut, i.e. a cut-off wheel pass, and the resulting plate is taken as the final product with not further processing. The plate should have an adequate surface finish and would have a tolerance of about ± 5 mils. In order to do this

the cut-off wheel thickness would be 60 mils. Taking the finished plate thickness as 80 mils and the cutting waste as 60 mils, the number of plates produced from a sized 14" block is 14÷(0.080 + 0.060) = 100. In the case of the original 9 x 14 x 14 block, 1,000 plates would be produced under ideal conditions. The cost per plate is 28.9 cents or \$3.65 per ft^2. This plate would then be processed to produce maximum catalytic activity. A realistic avoidable scrap estimate resulting from the cutting and activation steps would be at most 2%.

Related Factors. At this point, a comparison of \$6.48 per ft^2 for ruthenized titanium does not appear very favorable compared to \$3.65 per ft^2 for PG-60 graphite as a direct material cost for the electrodes. Other factors, however, can have substantial bearing on this matter.

First, the tolerances selected for the graphite plates were selected at ± 5 mils. Should this have been ± 0.5 mils, an entirely different situation would occur. The machining operation would allow another 0.100 inches to each plate cut so that the following grinding operation could achieve the desired tolerance. In that case, the waste is increased and it could be shown that about half as many plates are produced yielding a cost of \$6.22 per sq. ft. Now ruthenized titanium is a practical alternative. Whether to use loose or tight tolerances is directly related to the design specified. As shown in the costing section, the electrode materials are the most expensive single component in the battery system so that electrode tolerance considerations become a significant design restriction. This point will be raised again later in this report.

Second, the estimates given here attempt to assign dollar values at a fixed point in time. Further, one might assume that the dollar inflation rates would affect each electrode material equally. This, however, is not the case. Graphite uses petroleum products directly in its manufacture whereas titanium does not. Both rely on electrical power for their preparation. A review of commodity cost data over a period of years shows that titanium costs are not increasing as fast as that for graphite. Actually, the price of titanium dropped between 1960 and 1962, remained relatively constant between 1962 and 1972 and has just started its present price rise. This suggests that improved productivity in the titanium industry has been a major cost controlling factor.

Third, as a result of discussions held with the various suppliers, indications are that substantial cost reductions in both graphite and titanium porous structures are

possible. It was mentioned that the possibility of porous graphite as low as $2.00 per square foot exists by taking advantage of economies associated with high volume production. Also indicated was the possibility of production economies eventually leading to a price of $1.00 - $1.50 per square foot.

Fourth, the catalyst loading in the titanium structure has not been optimized as yet. A reliably ruthenized surface having a lower leading could substantially reduce the $1.48 per square foot catalyst cost in the present design. It is also possible that other methods of catalyzing the titanium surface could be developed. There is no reason to believe that the activating material must contain a noble metal. However, this latter consideration anticipates further developmental work.

Fifth, although the results are far from complete, the life expectancy of ruthenized titanium should exceed that of porous graphite. This has been the experience of the chlorine industry and the inference may be made here. It may well be that ruthenized titanium at a higher initial cost would be the better value in the long term.

Sixth, it was stated earlier that activated graphite has been found to be as active as catalyzed titanium. As the catalyzing procedures develop and are made more reproducible, the above statement may no longer be true. Should that be the case, the more active electrode will require a proportionately reduced area to achieve the same net power requirements. Since the electrode area is directly proportional to net electrode cost, the balance could be shifted, at least slightly, one way or the other.

Seventh, the relative permanence of the ruthenized titanium electrode together with the fact that it is a high cost component in the battery system provides the possibility of a recycling potential. By being able to reuse these electrodes with, perhaps, some minor processing, the old discarded electrode modules become a ready source of high priced components. This consideration would contribute toward making ruthenized titanium a better value.

Lastly, the problem of ruthenium availability must in some way be factored into the cost of titanium electrodes. Evidently, any large number of batteries would cause an increase in the demand for ruthenium thus forcing a price increase. Further, a mature market could not be supplied by exclusively ruthenized titanium as a chlorine electrode material. Other catalytic materials could, of course, be used to treat the titanium. As a consequence, the cost of catalyzed titanium in large quantities

is an open question dependent upon the amount used and the availability of the catalyst.

The graphite used for cost comparison with titanium was PG-60. There exists another porous graphite on the market which is estimated as having a materials cost less than that of PG-60, specifically, $\$2.41/ft^2$ determined on the same basis. This graphite has some undesirable characteristics. However, there is a strong possibility of altering it to meet the specific requirements of the battery. The adoption of this graphite material would serve to reduce the graphite cost in system.

MARK 2 COSTING

A cost figure of $\$2.41/ft^2$ for graphite was used in the costing study that follows. Table 4-3 contains the cost estimates associated with the production of 1 and 100 of the 100 MWh (20 MW) battery systems. The estimated selling price of the single units determined as 6 million dollars is a realistic figure that is believed to reflect a conservative position. That is, further investigation into the prices is possible, and very probably, other cost reductions will be made. The figures given should be interpreted in that light. Also, an efficient manufacturing business should be able to quote the price given as the selling price of the battery. The large volume costing is an all-stops-pulled estimate wherein the components are near or in some cases slightly below their current materials price. This number should establish what is believed to be the lower price limit of the battery system consistent with the high volume production.

Some further explanation is in order regarding the single unit cost estimate. The costing figures are the result of an iterative process wherein a model was assumed and, thereafter, modifications were made in areas that resulted in substantial cost savings. In so doing, a series of design restrictions were generated that served as a guide for a low cost system concept. This iterative process is, of necessity, an on going process that has been terminated here in order to satisfy the requirements of this contract. Other changes could be made in order to further improve the system cost, however, some of the quotations or other confirmatory data are not on hand at this time. In that context, the number given is believed to be realistic and as stated above, on the conservative side (i.e. favorable to the manufacturer).

The first attempt at costing assumed that the large system was a replication to 100 MWh of the 1 kWh battery originally constructed under this contract. This model

Table 4-3

PRODUCTION COST ESTIMATES
FOR MARK 2

	ONE UNIT PER YEAR				100 UNITS PER YEAR	
	DIRECT		Cost as % of S.P.		DIRECT	
	MATERIALS	LABOR	D.M.	D.L.	MATERIALS	LABOR
Zinc Chloride	73,745		1.213		66,371	
Water (distilled)	8,436		0.139		7,592	
Electrodes (Porous)	1,316,700	3,335	21.660	0.055	546,349	3,335
Electrodes (Solid)	252,736	5,000	4.158	0.082	126,368	5,000
Cell Casing	475,842	20,000	7.828	0.329	142,753	20,000
Electrode Connectors	23,200	20,000	0.382	0.329	11,600	20,000
Direct Costs	2,150,659	45,335			901,033	45,335
O.H. at 150%		68,003		1.119		68,033
Net Labor		113,338				113,338
		2,150,659				901,033
TOTAL STACK		2,263,997				1,014,371
Shell	11,340		0.187		3,780	
Agitator Motor	5,000		0.082		3,750	
Hydrate Cooling Hx	132,000		2.171		44,000	
Hydrate Heating Hx	66,000		1.086		22,000	
Refrigerators	129,750		2.134		64,875	
Hydrate Pumps	23,400		0.385		17,550	
Direct Costs	367,490				155,955	
10% Labor Allowance		36,749		0.605		15,596
		367,490				155,955
TOTAL STORE		404,239				171,551
Intercell Connectors	192,000		3.158		96,000	
Cl_2 Absorption Equipment	28,500		0.469		15,000	
Piping	158,678		2.610		47,603	
Valve and Controls	100,000		1.645		50,000	
Electrolyte Pumps	720,000		11.844		72,000	
Sump Tanks	22,250		0.366		7,416	
Electrolyte Purification	100,000		1.645		25,000	
Direct Costs	1,321,428	1,321,428	63.162		313,019	313,019
Net Cost		3,989,664				1,498,941
5% Assembly Allowance		199,483		3.282		74,947
TOTAL		4,189,147		5.801		1,573,888
G.S.&A. at 29%		1,214,852		19.984		456,428
Interest Charges		162,000		2.666		81,000
Building Preparation		373,000		6.136		373,000
Underground Store Preparation		140,000		2.303		
				31.089		
Estimated Selling Price		6,078,999		100.05		2,484,315

resulted in an estimated selling price of 23 million dollars for the 20 MW - 100 MWh system. As a result of the gross first cut, the high cost components were flagged and were scrutinized closely for the reasons associated with their high cost. This led to some illuminating findings which are discussed more fully in subsequent sections. Essentially, the areas of major concern are:

- the desorber component
- the electrode material
- the electrolyte pumps
- the container materials

The costing given in Table 4-3 assumes that:

1. no desorber is used,
2. low-grade rough cut graphites are used,
3. the best quotes obtained so far for the electrolyte pumps are adequate and
4. the container material is polyvinyl chloride.

The costing attempts to be as complete as possible by including factors that compose the "contribution margin" of manufacturer. That is, a GS and A of 29% and a capital interest charge are included. The labor costs given must be considered as a very rough estimate. Since they are not considered to become a major cost item, the estimate is adequate.

A cursory examination of the individual costs causes certain items to become rather prominent. The major cost items, as mentioned before, will be discussed at length below. Before progressing to that discussion, the specific item of cell casing cost must be raised. This quantity constitutes only part of the casing material cost. The number was revised during the iterations from a rough approximation to a more precise estimate calculated from a detailed set of drawings based on one of the designs studied. It becomes evident that although PVC is not an especially expensive material, the large amounts used in this design turns out to have created a major cost item. Another approach to a viable system design could adopt larger battery sizes housed in the same case. In that way, the need for **most** of the side walls of most of the individual cases would be obviated, and at the same time, their associated cost. On the other hand, a high density stack design can also be conceived which can be packaged in a single container. This design concept was presented earlier in the design section. Although savings are created by minimizing case

materials, increased low-cost graphite usage may have a counterbalancing effect. This remains to be determined.

The result of the costing is an estimated manufacturer's selling price of between 2.5 and 6 million dollars depending on volume. This number implies certain noteworthy assumptions. It assumes that a manufacturing operation exists capable of backing up this quotation and that the manufacturer is experienced in building these batteries. The latter point presumes that no significant risk factor exists. Again, it should be emphasized that the approach to costing is a conservative one implying that further examinations will, very likely, bring further cost reductions.

In fact, the attempt at costing brings attention to the high cost items. As a result, some recent work on operating current densities has indicated the possibility of discharging at 45 mA/cm^2 instead of the original 30 mA/cm^2. This means that the single most expensive item listed in the costing could be reduced to about 30/45 of the amount given. This, in turn, would substantially affect the total system cost. Extensive testing is underway to ascertain the limit of the possible improvement.

Perhaps, the single, most significant advantage of the approach used here for costing is that not only are the areas requiring attention identified, but priority as to their relative importance is revealed. Each area having major impact on cost has been reviewed in order to ascertain the underlying reasons determining that cost and, where possible, to determine if any means exist to reduce that cost. Below are listed areas of major concern together with an analysis of the associated costs:

Graphite

The largest single cost item in the battery system is graphite. At first blush, the cost of graphite would seem to be minor, in that the graphite content is not very large. The problem lies in the fabrication of the electrodes themselves. Raw graphite is produced in the form of blocks. Their production requires substantial electrical energy to operate graphitization furnaces and also, use petroleum coke as raw material. This, in itself, indicates the reason for the recent rapid increase in graphite prices and is suggestive of future price volatility. Next, in the preparation of the electrodes, the blocks must be sawed into smaller blocks having an outside dimension close to that of the finished plate. Large block

dimensions must be carefully selected to minimize waste. An approximate utilization factor for the original block in forming the smaller sized blocks ranges from 95-85%. This is not bad compared to the subsequent operations. The sized blocks are then cut into slabs. The cutting operation is performed by a saw or cut-off wheel of about 0.060" thickness. All of the graphite in the path of the cutting tool becomes waste. Should the graphite slabs thus produced be used as the finished plate, the cell design must thereby accomodate tolerances of ± 5 mils across the electrode surface. If better tolerances are required, a subsequent grinding operations, 0.100 inches is allowed over the final plate thickness to ensure that the plate surfaces can be made parallel within the desired specification. Further, the grinding operation involves a multi-pass sequence to bring the electrodes to specification. The process can, of course, be automated. As an example, an estimate will be made of the utilization of an already sized block. It is to be noted that these sized blocks were produced with a 95%-85% utilization of the raw graphite block. If the assumption is made that the finished plate thickness is 80 mils, utilization of the sized block will be dependent upon the tolerance called out on the plate produced. Specifically, a high tolerance--better that ± 5 mils, the slab thickness will be the sum of the desired plate thickness (80 mils) plus 100 mils for producing parallel faces during the grinding operation. In addition, 60 mils is lost due to the cut-off operation for the slab. The best utilization of the sized block in order to produce high tolerance plates is:

$$\frac{80}{80 + 100 + 60} \times 100 = 33\%$$

If, on the other hand, the slabs produced during the cut-off operation were used directly as the finished electrodes, the utilization of the sized block to produce low tolerance electrodes (± 5 mils) is:

$$\frac{80}{80 + 60} \times 100 = 57\%$$

The above analysis considers only the unavoidable waste. It should be clear that scrap rates for the higher tolerances plates must be greater as a result of the increased number of operations. However, that would be an avoidable waste which could be controlled to a greater or lesser extent depending upon the handling used.

It would seem reasonable to assume that further development work in materials processing could yield better tolerances and, at the same time, improve block utilization. This is being looked into.

In the greater view and with this understanding in mind, a more enlightened dialog is in progress with the graphite manufacturers. Various proposals have been made for improving the yield of graphite plates and maintaining adequate tolerances without having to pay such large penalties. There is a general consensus of opinion that finished electrodes may be produced at $1.00 - 1.50 per square foot. Development continues along these lines.

Another factor to be considered is the quality of the graphite itself. In the case of the porous graphite used for the chlorine electrode, no significant options are available. This graphite material must be prepared with highly controlled physical and chemical properties. No such requirements exist for the negative electrode in the battery system. The original experimental design employed a molded graphite which, although excellent in terms of its machinability, could easily be replaced by a less costly extruded graphite. By specifying an extruded grade together with a low tolerance on the plate, the graphite used for the zinc electrode becomes a minor cost item. It is important to note that it is highly probable that such a graphite will suffice. It must, nevertheless, be qualified for use in the battery by the usual testing methods.

Desorber System

The desorber system in the original zinc-chloride battery system concept served to improve the coulombic efficiency during cycling. In fact, the difference between operating it and not is about 13% in the coulombic efficiency as measured as the test 1 kWh units. This must be balanced against the energy required to run this desorber which would effectively reduce the difference to 9-10% net. The dilemma being faced is whether or not the large cost of the desorber justifies the small benefit it provides. Based on a quote from the Squire-Cogswell Company, the cost of the compressor system adequate for the battery requirements is $1.8 million. It would take an enormous price reduction to bring the cost of the pump to a reasonable level. Further, the construction of this pump suggests that this is unlikely. This pump is a rotary compressor constructed substantially of cast titanium, having a double mechanical seal and cooled by water circulation. It was designed specifically for handling wet chlorine gas. Certain technical

question have been raised regarding whether the pump can function at all in view of the high temperature produced during the compression stroke. This condition is capable of igniting the titanium impeller. Various methods can be used to minimize this, e.g., the use of cascading steps serving to cool the compressed gas. This, however, can only increase costs. There are no obvious materials that could be substituted with a high probability of success. Suggestions have been offered, but they require an extensive development program.

Alternative pump designs, e.g., a liquid-ring pump, can be used but they operate at a relatively low efficiency. This, however, would involve a new design philosophy wherein discrete modules exist with self-contained pumping capability.

The fact that in this design concept the desorber system contributes so little to the battery performance has led to the study of other approaches not requiring the compressor. In principle, the pumping action of the store itself, control of the electrode spacings and modification of the ionic strength of the solution, could produce the same effect. This has been verified in single cell tests and, recently, in a 1 kWh battery.

MARK 3 COSTING

The Mark 3 design concept, as mentioned earlier, is actually a variant on Mark 2. Essentially, the underground store is now 24 above ground stores. Site costs decreased. The most significant reduction comes in the improved discharge current density of 40 ma/cm^2 as compared to 30 ma/cm^2 in the earlier version. In principle, twenty-five percent of the graphite is no longer required.

The Mark 3 design was not subjected to as close a design analysis as the Mark 2. This made the costing less reliable. By virtue of the similarity of the internal designs, a costing by analogy was performed. This costing, however, took into account the areas of significant cost changes. The costing is given in Table 4-4. The estimated selling price of 52 dollars per kWh based on the production rate of one battery system per year is a reduction over Mark 2, both being normalized to 1976 dollars. It should be noted that the cost of the largest cost item-graphite-has risen faster than the economic inflation rate and should be expected to continue to do so.

Table 4-4

1-100 MWh BATTERY COST ESTIMATE
OF THE MARK 3 DESIGN

	ONE UNIT PER YEAR BASIS (000) OMITTED	
Zinc-Chloride Electrolyte	83	
Electrodes (Porous)	987	
Electrodes (Dense)	190	
Cell Casing	476	
Electrode Connectors	23	
Direct Material		1,759
10% Labor Allowance		176
Total Stock		1,935
Hydrate Tanks	50	
Agitator Motors	5	
Hydrate Cooling HX's	132	
Hydrate Heating HX's	66	
Refrigeration Unit	180	
Hydrate Pumps	23	
Direct Material		456
10% Labor Allowance		46
Total Store		502
Intercell Connectors	192	
Cl_2 Absorption Equipment	29	
Piping	160	
Valves and Controls	100	
Electrolyte Pumps	720	
Sump Tanks	22	
Total Auxiliaries	1,223	1,223
Net Cost		3,663
5% Assembly Allowance		183
Total		3,843
GS&A at 29%		1,114
Interest Charges		150
Building Preparation		100
Estimated Selling Price (1976 dollars) (000 omitted)		5,207

REFERENCE

4-1 "Evaluation of a 1 kWh Zinc-Chloride Battery System," EPRI EM-249, Interim Report, September 1976

Section 5

SUMMARY AND DISCUSSION

Each of the battery designs described previously represent different design philosophies - Mark 2 with its single underground store and large 1 MWh stack modules, and Mark 3 with its very large 6 MWh stack modules and multiple stores above ground. Table 5-1 compares the electrochemical design points for the two designs.

Table 5-1

COMPARISON OF ELECTROCHEMICAL DESIGN POINTS
FOR MARK II AND MARK III

PARAMETER	MODE	DESIGN	
		MARK 2	MARK 3
Current Density (mA/cm^2)	Charge	24	45
	Discharge	30	40
Cell Voltages (V)	Charge	2.23	2.25
	Discharge	2.00	2.00
Time (h)	Charge	7	5
	Discharge	5	5
Usable Coulombic Efficiency		90%	90%
Electrochemical Energy Efficiency		80%	80%

The capital costs of the Mark 2 and 3 battery systems have been estimated and are presented in abbreviated form in Table 5-2. The table shows that the battery costs are not very different. Perhaps the most significant observation lies in the battery cost dependence on the discharge current density. This comes about by virtue of the decreased amount of porous graphite required to produce the required number of electrodes.

Table 5-2

PRICE ANALYSIS OF ZINC-CHLORINE PEAK-SHAVING BATTERY PLANT (ONE PER YEAR BASIS)*

Component Group	Cost (000 omitted) Mark 2	Mark 3
Stack	2,264	1,935
Store	404	502
Auxiliaries	1,321	1,223
Other Charges	2,089	1,547
Estimated Selling Price	6,078	5,207
$/kWh	61	52
$/kWh (100 unit/year basis)	25	21

*All numbers are given as 1976 dollars

Presumed in this costing is the qualification of a low cost plastic. As described in an earlier section, a program is proceeding to qualify plastics other than flourocarbons as construction materials. At this moment, PVC, polyethylene and polyester offer great promise.

It is recognized that the costing presented above lacks detailed justification of labor costs. Although the assumptions are adequate for the purposes here, work is, nevertheless, progressing toward detailing the processing required for battery construction and estimating the labor requirements. A more detailed analysis will take place during the next year.

APPENDIX A

FUNDAMENTAL CHEMICAL AND ELECTROCHEMICAL PROCESSES AT ZINC AND CHLORINE ELECTRODES IN ZINC-CHLORINE BATTERIES

Appendix A

FUNDAMENTAL CHEMICAL AND ELECTROCHEMICAL PROCESSES AT ZINC AND CHLORINE ELECTRODES IN ZINC-CHLORINE BATTERIES

INTRODUCTION

This appendix is comprised of two recent papers published in the Journal of the Electrochemical Society and co-authored by Dr. J. T. Kim and Professor J. Jorne of Wayne State University.

The first paper entitled "The Kinetics of Chlorine Graphite Electrode in the Zinc-Chlorine Battery" discusses an experimental investigation of the cathodic and anodic reactions for chlorine at a graphite electrode. Measurements of the fundamental kinetic and transport parameters will be useful in the optimization of a porous-graphite flow-through chlorine electrode.

The second paper is entitled "Mass Transfer of Dissolved Chlorine to a Rotating-Zinc Hemisphere in $ZnCl_2$ Solution". The authors confirmed earlier more approximate observations of EDA that the reaction of dissolved chlorine with zinc in zinc-chlorine solutions is mass transfer-limited. This investigation also indicated that in the pH range of interest for zinc-chlorine battery operation chlorine is present in solution as dissolved chlorine and the trichloride ion, Cl_3^-.

Reprinted from the JOURNAL of the ELECTROCHEMICAL SOCIETY
Volume 124, No. 10 October 1977

The Kinetics of a Chlorine Graphite Electrode in the Zinc-Chlorine Battery

Jung Taek Kim* and Jacob Jorné**

Department of Chemical and Metallurgical Engineering, Wayne State University, Detroit, Michigan 48202

ABSTRACT

The cathodic and anodic reactions for chlorine on a graphite electrode were investigated in concentrated $ZnCl_2$ solution using a rotating-disk electrode. The diffusion coefficient, Tafel kinetic parameters, rate constants, and reaction order were obtained. A likely cathodic reaction mechanism and rate-determining step is postulated.

The Zn-Cl_2 battery has been under intensive investigation and development during recent years for vehicular application and as a load leveling device (1). This secondary battery consists of a Zn electrode, Cl_2 graphite electrode, and $ZnCl_2$ aqueous solution. During charge Zn is deposited on the cathode and Cl_2 evolves at the graphite electrode. During discharge Zn and Cl_2 react to give aqueous $ZnCl_2$.

The Cl_2 graphite electrode represents a major limitation to the Zn-Cl_2 cell performance. In order to reach a stage where the design and performance of a flow-through porous graphite Cl_2 electrode is fully understood, the kinetics and the mass transfer of the Cl_2 electrode should be investigated on a nonporous graphite electrode under well-defined conditions.

In the present investigation, the kinetics of the Cl_2 electrode reaction is studied in a $ZnCl_2$ aqueous solution using a dense graphite rotating-disk electrode (RDE) under various Cl_2 concentrations. Limiting currents were detected at various Cl_2 concentrations and rotational speeds, from which the Cl_2 diffusion coefficient was determined. The kinetic parameters: exchange current density, reaction order, transfer coefficients, Tafel slopes, and apparent rate constants were determined. The mechanism of the Cl_2 electrode reaction is proposed and discussed in light of the present results.

The cathodic over-all reaction for Cl_2/Cl^- on a graphite electrode is $Cl_2 + 2e \rightleftarrows 2Cl^-$ $E^\circ = 1.36V$. The mechanism of this reaction and its kinetics have not been studied in concentrated $ZnCl_2$ aqueous solution. Most of the work in the past covered the anodic reaction in NaCl solution, and little attention was given to the cathodic reduction of Cl_2 (2-5). Frumkin and Tedoradze (2) studied the reduction of Cl_2 using a Pt rotating-disk electrode, and suggested the mechanism

$$Cl_2 + e \rightleftarrows Cl_{ads} + Cl^-$$

and

$$Cl_{ads} + e \rightleftarrows Cl^-$$

however, the mechanism is not fully substantiated. Sureno, Macagno, and Giordano (3) investigated the Cl_2 reaction in nonaqueous solvents using Pt RDE. Hine and Yasuda (6) studied the mechanism of the anodic oxidation of Cl^- on graphite RDE in NaCl solution, and found that the rate-determining step is

$$Cl_{ads} + Cl^- \rightarrow Cl_2 + e$$

Experimental

The graphite rotating-disk electrode consists of a Teflon support rod and a central dense graphite elec-

* Electrochemical Society Student Member.
** Electrochemical Society Active Member.
Key words: chlorine, graphite, zinc chloride, kinetics, zinc-chlorine battery.

trode ATJ Union Carbide. The central graphite electrode was embedded in the Teflon rod. The diameter of the graphite electrode was 0.95 cm, and the diameter of the Teflon rod was 1.9 cm. The rotator was a Pine Instrument ASR rotator with a rotational speed of 0-10,000 rpm. The surface of the electrode was polished with waterproof Al_2O_3 paper and a fine paper using the rotator (ω = 4000 rpm).

A 1000 ml Pyrex vessel fitted with a Teflon cover was used as the cell container. It was equipped with a 2.25 cm^2 platinum counterelectrode compartment connected to the cell by a small glass tube. A saturated calomel electrode (SCE) served as a reference electrode, and was placed in a separate reference electrode compartment connected to the main cell by a capillary extending to the side of the rotating-disk electrode. The tip of the Luggin capillary was located at a distance of 3.5 cm from the center of the disk. The ohmic drops were calculated according to Newman (7).

The potential of the graphite disk electrode was controlled by a Wenking LT 73 potentiostat. A wave form generator TWG 500 was used in conjunction with the potentiostat in order to sweep the potential of the disk electrode. The sweep rate was 10 mV/sec. The potential-current data was recorded on a Houston Instrument 2000X-Y Recorder.

The $ZnCl_2$ solution was obtained from EDA, Incorporated, where it was prepared by direct recombination of Cl_2 gas and pure Zn rods (99.999%, New Jersey). The $ZnCl_2$ concentration was measured by hydrometer. Cl_2-N_2 gas mixtures were fed into the cell by a gas expenser, and the dissolved Cl_2 concentration was maintained by measuring the Cl_2 and N_2 flow rates. The dissolved Cl_2 concentration was measured by standard titration using 1/100 normal $Na_2S_2O_3 \cdot 5H_2O$. Dissolved oxygen was removed by bubbling N_2 prior to the experiments, and the Cl_2-N_2 gas mixture was bubbled throughout the experiments. The pH of the solution was measured with a Beckman pH meter. The temperature was 25° ± 1°C, and the kinematic viscosities were corrected for temperature variations.

Results and Discussion

Cl_2 diffusion coefficient.—Cathodic polarizations of dissolved Cl_2 on a graphite rotating-disk electrode are shown in Fig. 1 and 2. The observed limiting currents depend on the rotational speed and the dissolved chlorine concentration. The cathodic reaction, $Cl_2 + 2e \rightarrow 2Cl^-$, is therefore mass transfer limited, and the diffusion coefficient of dissolved Cl_2 in $ZnCl_2$ solution can be determined from the Levich equation for convective diffusion near the rotating-disk electrode

$$i_l = 0.62nFD^{2/3}\nu^{-1/6}c_b\omega^{1/2} \qquad [1]$$

The kinematic viscosity of 37% $ZnCl_2$ solution at 25°C is 1.53×10^{-2} cm^2/sec (11).

Figure 3 shows the plot of the limiting current *vs.* $\omega^{1/2}$, and the average diffusion coefficient obtained from the slope is $D_{Cl_2} = 0.664 \times 10^{-5}$ cm^2/sec, and is in good agreement with the value of $D_{Cl_2} = 0.633 \times 10^{-5}$ cm^2/sec obtained in our laboratory from weight loss measurements of a rotating Zn hemisphere in chlorinated $ZnCl_2$ solution (8). These values are in general agreement with the diffusion coefficient of Cl_2 in water (9), $D_{Cl_2} = 1.22 \times 10^{-5}$ cm^2/sec, after correction for different viscosities.

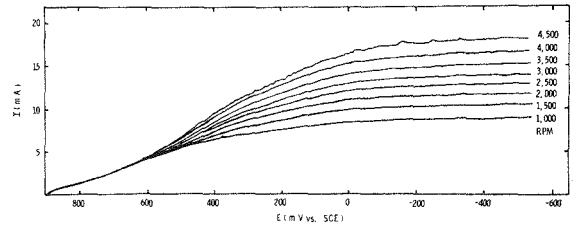

Fig. 1. Cathodic polarization of graphite electrode in 37% weight $ZnCl_2$ solution at different rotational speeds. [Cl_2] = 0.95 g/l; area = 0.713 cm^2; pH = 3.29.

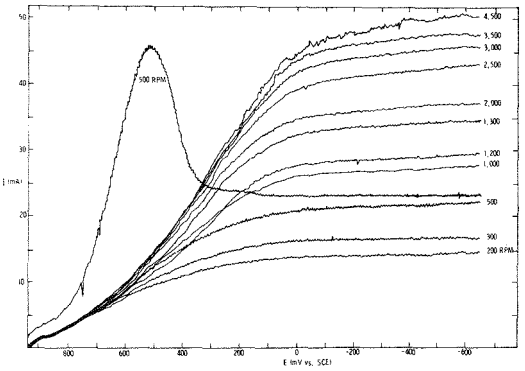

Fig. 2. Cathodic polarization of graphite electrode in 37% weight $ZnCl_2$ solution at different rotational speeds. [Cl_2] = 3.02 g/l; area = 0.713 cm^2; pH = 3.15.

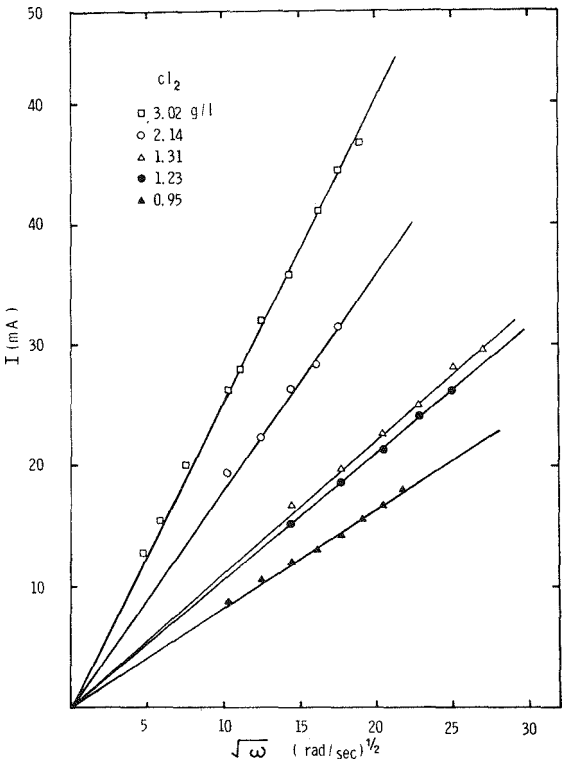

Fig. 3. The cathodic limiting current *vs.* the square root of the rotational speed at different Cl_2 concentrations.

When the potential was scanned cathodically beyond the Cl_2 limiting current, a steep rise in the current was observed at about −1.0V *vs.* SCE, and is attributed to Zn deposition and H_2 evolution. A cathodic peak can be observed in Fig. 2 at 500 rpm during the cathodic scanning of the graphite-chlorine electrode. This current peak is due to unsteady-state effects, and was reproducible after the electrode was pretreated anodically or after leaving the graphite electrode overnight in chlorinated solution. The explanation for this peak is as follows. During anodization, Cl_2 is evolved and accumulated within the graphite porous structure.

Upon cathodic polarization, more Cl_2 is available and the current exceeds the apparent limiting current which is limited by the transport of dissolved Cl_2 to the projected apparent surface of the graphite electrode. After Cl_2 is depleted from the pores the current drops to the steady-state limiting value at the same rotational speed.

Cl_2 reaction order and rate constant.—Figure 4 shows the cathodic current as a function of the square root of the rotational speed for three fixed potentials. At $E = -390$ mV (*vs.* SCE) the potential is well within the limiting current region. The reaction is totally mass transfer limited, and a through-the-origin straight line is obtained according to the Levich convective diffusion equation. When the potential is fixed below the limiting current region ($E = 310$ or 410 mV *vs.* SCE) the reaction is partially controlled by mass transfer and surface reaction, and the I *vs.* $\omega^{1/2}$ plots are not linear (Fig. 4). Using the graphical method of Riddiford (10), the Cl_2 reaction order Z_{Cl_2} can be obtained by plotting arbitrary vertical lines ABC, DEF in Fig. 4, and Z_{Cl_2} is given by

$$Z_{Cl_2} = \frac{\log FE/CB}{\log CA/BA - \log FD/ED} = \frac{\log i_k - \log i}{\log i_l - \log (i_l - i)} \quad [2]$$

The reaction order was found to be $Z_{Cl_2} = 0.6$ in $1.75 \times 10^{-2}M$ Cl_2 in 37.6% $ZnCl_2$ solution. The reaction order was also obtained by the conventional method of varying the Cl_2 bulk concentration, as shown in Fig. 5

$$Z_{Cl_2} = \frac{\partial \log i}{\partial \log [Cl_2]} = 0.74$$

According to the present values, $Z_{Cl_2} = 0.6$ or 0.74, the reaction order can be half-order or first order. The polarization data were tested according to these two possibilities:

(*i*) If the reaction is assumed to be half-order, then the current is given by (10)

$$i^2 = i_k^2 - (i_k^2/B)(i/\omega^{1/2}) \quad [3]$$

where B is a constant ($0.62\ n\mathbf{F}D^{2/3}\nu^{-1/6}C_b$) and $i_k = n\mathbf{F}kC_b^{1/2}$ (surface reaction rate). A plot of i^2 *vs.* $i/\omega^{1/2}$ should give a straight line for a half-order reaction. As shown in Fig. 6, the behavior is not linear and the half-order assumption is incorrect.

(*ii*) If the reaction is assumed to be first order, the current is given by (10)

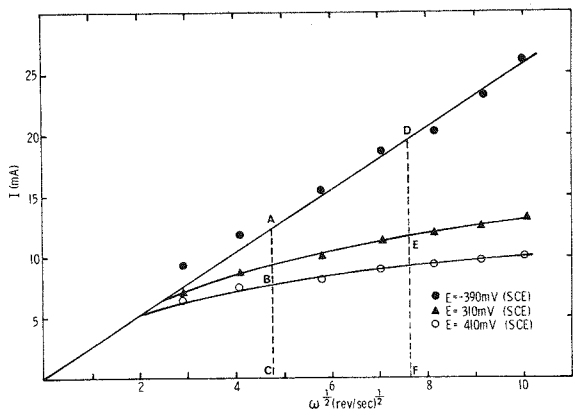

Fig. 4. The cathodic current *vs.* the square root of the rotational speed at three cathodic potentials. $[Cl_2] = 1.23$ g/l; area = 0.713 cm²; pH = 3.29.

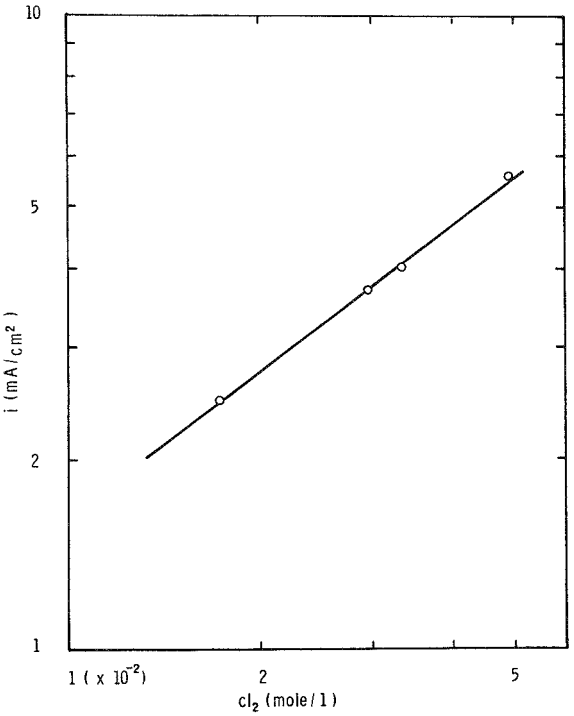

Fig. 5. The Cl_2 reaction order determination: $Z_{Cl_2} = 0.74$

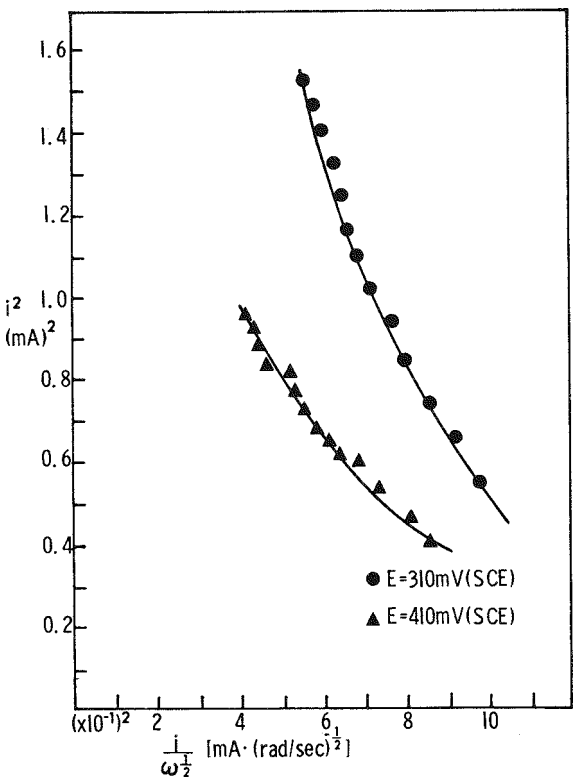

Fig. 6. The test for half-order reaction at different potentials. $[Cl_2] = 1.23$ g/l; area = 0.713 cm²; pH = 3.29.

$$1/i = 1/i_k + 1/i_l \quad [4]$$

where the limiting current is $i_l = 0.62\ n\mathbf{F}D^{2/3}\nu^{-1/6}C_b\omega^{1/2}$ and $i_k = n\mathbf{F}kC_b$. Rewriting Eq. [4] gives

$$1/i = 1/n\mathbf{F}kC_b + (1.61\nu^{1/6}/n\mathbf{F}D^{2/3}C_b)\omega^{-1/2} \quad [5]$$

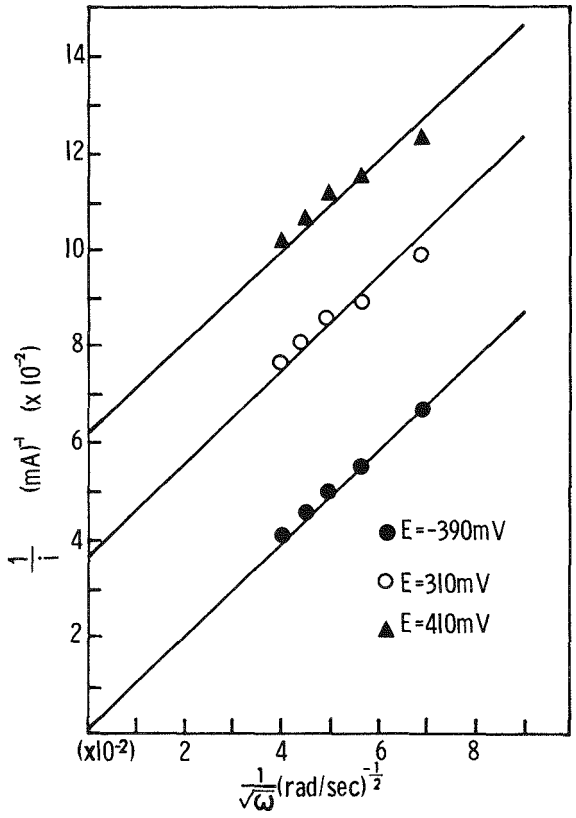

Fig. 7. The test for first-order reaction at different potentials. $[Cl_2]$ = 1.23 g/l; area = 0.713 cm²; pH = 3.29.

Figure 7 shows the plot of $1/i$ *vs.* $\omega^{-1/2}$. The behavior is linear in accordance with Eq. [5], and the reaction is believed to be first order.

Extrapolating to $\omega^{-1/2} \rightarrow 0$ (or $\omega \rightarrow \infty$) permits the determination of the rate constant k. The obtained rate constants are 1.16×10^{-2} and 6.76×10^{-3} cm/sec for E = 310 and 410 mV *vs.* SCE, respectively. The rate constant k is a function of the potential, and increases as the potential becomes more negative (more cathodic). At the far cathodic potential, E = −390 mV *vs.* SCE, the reaction rate is very fast and can be neglected. The reaction is totally mass transfer limited, and a through-the-origin straight line is obtained according to the Levich convective diffusion equation.

Tafel's kinetic parameters.—The Tafel polarization plot for Cl_2/Cl^- on a dense graphite electrode is shown in Fig. 8. The data was corrected for ohmic drop using Newman's method (7). The apparent exchange current density, i_o = 1.11 mA/cm², is obtained from the intercept of the cathodic and anodic polarization branches. The anodic and cathodic Tafel slopes are b_a = 124 and b_c = −120 mV/decade, respectively. The present parameters are in agreement with the results of Hine (6) for NaCl solution (i_o = 1.2 mA/cm², $b_a = -b_c$ = 120 mV/decade). The deviation from linearity at the far cathodic potential range $E < 0.75$V *vs.* SCE in Fig. 8 is due to mass transfer overpotential.

The cathodic Tafel slope at a low cathodic overpotential $E > 0.810$V *vs.* SCE is b_c = −39.7 mV/decade, as can be seen in Fig. 9. In this region it is assumed that the fractional coverage is very small, $\theta_{Cl} \simeq 0$. The fractional coverage changes from $\theta = 0$ at low current density to $\theta = 1$ at high current density below the limiting current. The fractional coverage is assumed to follow the Langmuir isotherm form. The stoichiometric coefficient was obtained from the slope at low overpotential

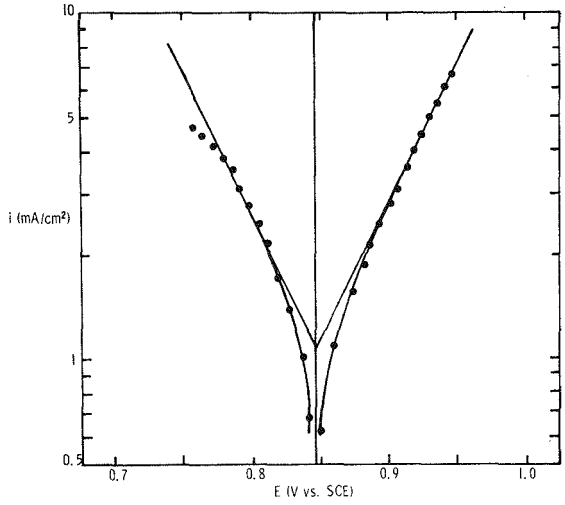

Fig. 8. Anodic and cathodic Tafel polarizations of graphite electrode in 37% weight $ZnCl_2$ solution. $[Cl_2]$ = 1.17 g/l; area = 0.713 cm²; pH = 3.29.

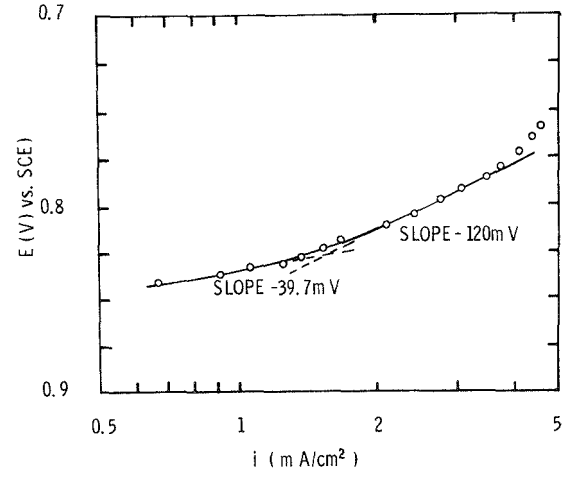

Fig. 9. Cathodic Tafel polarization of graphite electrode in 37% weight $ZnCl_2$ solution. $[Cl_2]$ = 1.17 g/l; area = 0.713 cm²; pH = 3.29; $E > 0.810$V, b_c = −39.7 mV/decade; $E < 0.810$V, b_c = −120 mV/decade.

$$\mu = \frac{2\mathbf{F}}{RT} i_o \left(\frac{\partial E}{\partial i} \right)_{\eta=0} = 1.2$$

The reaction mechansim.—The over-all cathodic Cl_2/Cl^- reaction is given by

$$Cl_2 + 2e \rightleftarrows 2Cl^-$$

The possible hypothetical reaction mechanisms are mechanism A

$$Cl_2 + e \leftrightarrows Cl_{ads} + Cl^- \quad [6]$$

$$Cl_{ads} + e \leftrightarrows Cl^- \quad [7]$$

mechanism B

$$Cl_2 \rightleftarrows 2Cl_{ads} \quad [8]$$

$$Cl_{ads} + e \rightleftarrows Cl^- \quad [9]$$

The theoretical parameters for the two mechanisms are shown in Table I, and were obtained from the Butler-Volmer rate equations including fractional coverage under steady-state assumption. If it is assumed that reaction [6] is the rate-determining step (rds), then the theoretical Tafel slope for reaction [6]

Table I. Parameters for cathodic Cl_2 reaction (theoretical)

Rate determining step	μ	Tafel slope $\theta \to 0$	Tafel slope $\theta \to 1$	Z_{Cl_2} $\theta \to 0$	Z_{Cl_2} $\theta \to 1$
Mechanism A					
(1) $Cl_2 + e \rightleftarrows Cl_{ads} + Cl^-$	1	$-2RT/F$	—	1	—
(2) $Cl_{ads} + e \rightleftarrows Cl^-$	1	$-2RT/3F$	$-2RT/F$	1	0
Mechanism B					
(3) $Cl_2 \rightleftarrows 2Cl_{ads}$	1	$-\infty$	—	1	—
(4) $Cl_{ads} + e \rightleftarrows Cl^-$	2	$-2RT/F$	$-2RT/F$	½	0

is $b_c = -120$ mV/decade under the assumption of $\theta_{Cl} \to 0$ at low current density (Table I). The experimental slope of −39.4 mV/decade in Fig. 9 indicates that reaction [6] is not the rds.

Assuming reaction [7] is the rds, the theoretical Tafel slopes are (Table I) $b_c = -40$ mV/decade for $\theta \to 0$, and $b_c = -120$ mV/decade for $\theta = 1$, in excellent agreement with the experimental values of −39.7 and 120 mV/decade, respectively. Thus, mechanism A appears to be correct, and reaction [7] is the rds. The experimental results are in disagreement with the theoretical parameters for mechanism B, as shown in Table I.

Although the $ZnCl_2$ solutions in the present work are acidic ($pH = 3.2$), and the molecular Cl_2 is the predominant species, the concentrations of hypochlorous acid HOCl and trichloride ion Cl_3^- are not negligible (8). The dissociation constant of hypochlorous acid to hypochlorite is very small $K = 4\ 10^{-8}$ (12), and in the present acidic solution hypochlorite is not present. However the transport and kinetic parameters obtained in the present work represent average values for the predominant molecular Cl_2, and minute concentrations of HOCl and Cl_3^-.

Conclusions

The cathodic reaction for Cl_2/Cl^- on a dense graphite electrode in $ZnCl_2$ solution has been investigated. Cathodic limiting currents were obtained at various rotational speeds and dissolved Cl_2 concentrations, and the Cl_2 diffusion coefficient was obtained. The reaction is first order with respect to the Cl_2 concentration.

The Tafel parameters were obtained for the anodic and cathodic polarizations. The following mechanism was established

$$Cl_2 + e \rightleftarrows Cl_{ads} + Cl^-$$

and

$$Cl_{ads} + e \xrightarrow{rds} Cl^-$$

and the second reaction is the rate-determining step.

The cathodic reaction rate constants were evaluated at several potentials. The cathodic reduction of Cl_2 was found to be partially mass transfer and kinetics limited.

The kinetics and transport parameters obtained in the present work are necessary in the design and optimization of a practical Cl_2 electrode in the Zn-Cl_2 battery. It is clear that a flow-through porous electrode is needed in order to maintain high currents.

Acknowledgments

This work was supported by Energy Development Associates, Madison Heights, Michigan, and Electric Power Research Institute, Palo Alto, California. The stimulating discussions with Drs. Philip Symons and Charles Ward are gratefully acknowledged.

Manuscript submitted April 29, 1977; revised manuscript received June 7, 1977.

Any discussion of this paper will appear in a Discussion Section to be published in the June 1978 JOURNAL. All discussions for the June 1978 Discussion Section should be submitted by Feb. 1, 1978.

Publication costs of this article were assisted by Wayne State University.

LIST OF SYMBOLS

- A electrode area, cm^2
- b_a anodic Tafel slope, V/decade
- b_c cathodic Tafel slope, V/decade
- c_b bulk concentration, $mole/cm^3$
- D diffusion coefficient, cm^2/sec
- E potential, V
- F Faraday's constant, 96,487 C/equiv.
- I current, A
- i current density, A/cm^2
- i_k kinetic current density, A/cm^2
- i_l limiting current density, A/cm^2
- i_o exchange current density, A/cm^2
- k rate constant, cm/sec
- n number of electrons transferred in electrode reaction
- R universal gas constant, 8.3143 J/mole°K
- Z the reaction order
- η overpotential, V
- θ fractional coverage
- μ stoichiometric coefficient
- ν kinematic viscosity, cm^2/sec
- ω rotational speed, rad/sec

REFERENCES

1. P. C. Symons and P. Carr, in Proceedings of the 8th Inter-Society Energy Conversion Engineering Conference, pp. 72-77 (1973).
2. A. N. Frumkin and G. A. Tedoradze, *Dokl. Acad. Nauk, SSSR.*, **118**, 530 (1958).
3. L. Sereno, V. A. Macagno, and M. C. Giordano, *Electrochim. Acta*, **17**, 561 (1972).
4. T. Dickinson, R. Greef, and L. Wynne-Jones, *ibid.*, **17**, 561 (1972).
5. G. Faita, G. Fiori, and J. W. Augustynski, *This Journal*, **116**, 928 (1969).
6. F. Hine and M. Yasuda, *ibid.*, **121**, 1289 (1974).
7. J. Newman, *ibid.*, **113**, 501 (1966).
8. J. T. Kim and J. Jorné, *ibid.*, in press (1977).
9. J. Arnold, *J. Am. Chem. Soc.*, **52**, 3937 (1930).
10. A. C. Riddiford, in "Advances in Electrochemistry and Electrochemical Engineering," Vol. 4, P. Delahay, Editor, Wiley-Interscience, New York (1966).
11. J. Mellor, "Comprehensive Treatise on Inorganic and Theoretical Chemistry," Vol. 2, Longmans, Green and Co., London (1974).
12. M. S. Chao, *This Journal*, **115**, 1172 (1968).

Reprinted from the JOURNAL of the ELECTROCHEMICAL SOCIETY
Volume 125, No. 1 January 1978

Mass Transfer of Dissolved Chlorine to a Rotating-Zinc Hemisphere in $ZnCl_2$ Solution

Jung Taek Kim* and Jacob Jorné**

Department of Chemical Engineering, Wayne State University, Detroit, Michigan 48202

ABSTRACT

The chemical reaction of a rotating-zinc hemisphere with dissolved Cl_2 is mass transfer limited. The diffusion coefficients of dissolved Cl_2 in various $ZnCl_2$ aqueous solutions at 25°C were calculated from the weight loss of the rotating Zn hemisphere at various rotational speeds. The Stokes-Einstein equation was confirmed, $(D\mu/T) = 4.42 \times 10^{-10}$ g cm/sec² °K and can be used to estimate diffusion coefficients of total dissolved Cl_2 in various $ZnCl_2$ solutions. The average Cl_2 Stokes radius in $ZnCl_2$ solution is calculated to be 1.64Å. The dissolution rate follows the Levich equation for convection diffusion. Surface roughness is of major importance, and the dissolution rate of Zn increases rapidly at moderate Reynolds number. Spiral markings can be observed on the corroding Zn hemisphere due to instability of the three-dimensional boundary layer, as a result of the increasing surface roughness.

The zinc-chlorine battery is a secondary battery which incorporates zinc and chlorine electrodes and a flowing aqueous $ZnCl_2$ electrolyte (1). The battery is currently being developed for load-leveling and electric car applications.

The chemical reaction which occurs in the battery is straightforward

$$Zn + Cl_2 \rightleftarrows ZnCl_2 \text{ (aq.)}$$

During charge zinc is deposited at the cathode and chlorine gas is evolved at the anode. The flowing $ZnCl_2$ electrolyte replenishes $ZnCl_2$ and removes the evolving chlorine. On discharge, the flowing electrolyte removes the electrode reaction products, aqueous $ZnCl_2$, and supplies chlorine to the chlorine electrode. The chlorine storage system is cold water, which forms a clathrate compound with chlorine.

One of the main problems facing the use of Zn-Cl_2 battery as a load-leveling device is that of achieving a high coulombic efficiency while maintaining a high voltaic efficiency. The main reason for the coulombic inefficiency in the Zn-Cl_2 battery is the spontaneous reaction between dissolved chlorine and the zinc electrode upon charging. It is expected that the limiting step for this chemical reaction is the mass transfer of dissolved chlorine to the zinc surface. If this is the case, then hydrodynamic conditions and convective effects might be the dominant factors in the design to reduce the coulombic inefficiency during charging.

The effect of hydrodynamic conditions on the mass transfer and consequent reaction of dissolved chlorine with the zinc electrode can be investigated using a rotating-Zn hemisphere is a $ZnCl_2$ solution partially saturated with Cl_2. The rate of the reaction is followed from the weight loss of the rotating Zn hemisphere, and if the rate of weight loss is proportional to the square root of the angular velocity, according to the Levich equations (2), then the process is mass transfer limited and the diffusion coefficient of dissolved chlorine in $ZnCl_2$ solution can be calculated from the slope.

According to Levich (2) the diffusion layer thickness for the laminar flow on a disk electrode is given by

$$\delta = \alpha D^{1/3} \nu^{1/6} \omega^{-1/2} \quad [1]$$

where D is the diffusion coefficient of dissolved Cl_2, ν is the kinematic viscosity, ω is the rotational velocity, and α is a constant which is equal to 1.62 for a disk and 2.109 for a hemisphere (3). Hemispherical electrode is preferred in the present case because the

* Electrochemical Society Student Member.
** Electrochemical Society Active Member.
Key words: zinc, chlorine, battery, rotating hemisphere, diffusion coefficient.

system's geometry remains unchanged. The hemisphere's limiting current, controlled by diffusion, has been corrected by Newman (4)

$$I_l = n\mathbf{F}DC_bA/\delta = 0.451\, n\mathbf{F}C_bD^{2/3}\nu^{-1/6}\omega^{1/2}A \quad [2]$$

$n\mathbf{F}$ is the number of coulombs per mole, C_b is the bulk concentration, and A is the electrode's area.

The dissolution of Zn is controlled by the diffusion of dissolved chlorine, therefore, the limiting current can be expressed by the weight loss

$$I_l = \frac{\Delta W n\mathbf{F}}{Mt} \quad [3]$$

where ΔW is the weight loss of the Zn hemispherical electrode, t is the time of the experiment, and M is the molecular weight of Zn. The mass transfer coefficient, k_c, is given by

$$k_c = \frac{\Delta W}{MAC_bt} = 0.451\nu^{-1/6}D^{2/3}\omega^{1/2} \quad [4]$$

From the plot of $\Delta W/MAC_bt$ *vs.* $\omega^{1/2}$, the diffusion coefficient of dissolved Cl_2 can be calculated.

At very high rotational speed, the flow becomes turbulent, and the Levich equation for convective diffusion does not hold; however, it is expected that earlier transition to turbulence is initiated due to surface roughness and secondary flow patterns.

The dissolution of Cl_2 in chloride aqueous solution is accompanied by the formation of dissolved molecular Cl_2, hypochlorous acid HOCl, and trichloride ion Cl_3^-. The reaction of dissolved Cl_2 with Zn is governed by the mass transfer of these three species and therefore the diffusion coefficients in the present investigation have an average meaning. The concentrations of the various species are estimated in the discussion section, and the Stokes-Einstein products $D\mu/T$ are interpreted as a function of the chloride concentration and the pH.

Experimental

The rotating-zinc hemisphere consists of a Teflon support rod and a replaceable Zn hemispherical head (Fig. 1). The Teflon support was 1.9 cm diam rod. A zinc hemisphere (99.999% New Jersey Zinc) was embedded in the Teflon rod. The diameter of the Zn hemispheres varied from 0.700 to 0.872 cm. At the center of the support there was a 0.396 cm hole in the central stainless steel shaft. The stainless steel shaft contained a 6-32 female thread to accommodate the Zn hemisphere. The other end of the Teflon support rod was attached to a stainless steel collet which was machined to fit a high speed rotator. The rotator was a Pine Instrument ASR rotator with a range of 0-10,000 rpm.

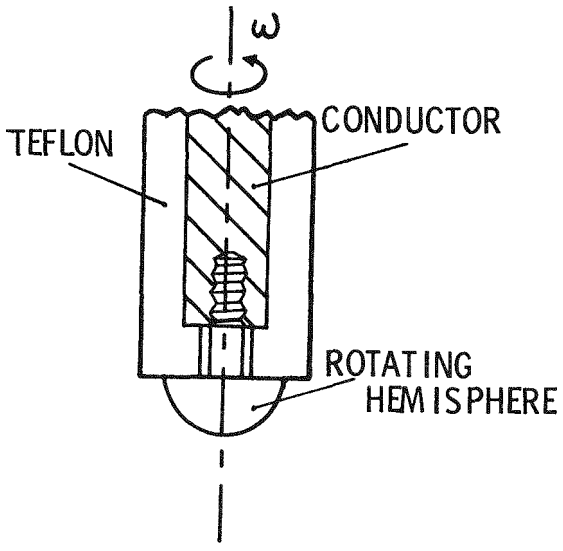

Fig. 1. Rotating Zn hemisphere

A 6-32 Zn screw having a hemispherically shaped head was used as the replaceable hemisphere. The surface of the electrode was polished with waterproof Al_2O_3 paper (grid number 600) and degreased with spectroscopic grade pentane. The Zn hemisphere was weighed on a Mettler Balance and transferred into the cell. After the experiment, the Cl_2-etched Zn hemisphere was rinsed with double distilled water, washed with pentane, and weighed.

A 1000 ml Pyrex vessel fitted with Teflon cover was used as the cell container. It was equipped with Cl_2 gas expenser. The $ZnCl_2$ 37% wt solution was obtained from EDA, Incorporated where the solution was prepared by direct recombination of pure Zn rods with dissolved Cl_2 gas. The $ZnCl_2$ concentrations were measured by hydrometer following the specific gravity data of $ZnCl_2$ (5). Viscosity data was obtained from (6) and the pH of the solution was recorded with Beckman pH meter.

The dissolved Cl_2 concentration was measured by standard titration method using 1/100 normal $Na_2S_2O_3 \cdot 5H_2O$. The solution was deaerated by bubbling nitrogen gas over a 30 min period. Cl_2-N_2 gas mixture was then bubbled for additional 30 min, and continuously bubbled throughout the experiment. Various Cl_2 concentrations were obtained by varying the composition of the Cl_2-N_2 mixture. The flow rates of Cl_2 and N_2 were controlled by needle valves and measured by calibrated rotameters.

Results and Discussion

Chlorinated $ZnCl_2$ solutions.—Table I summarizes the experimental data of the weight losses of Zn hemispheres in chlorinated 37, 22, and 17% wt $ZnCl_2$ solutions and in acidified 26% $ZnCl_2$ solution (pH = 1.0). Figure 2 shows the mass transfer coefficient of chlorine to the Zn hemisphere in chlorinated $ZnCl_2$ solutions *vs.* the square root of the rotational speed. The lines were obtained by a least square method not including the origin. The Levich equation for convective diffusion (2) is satisfied and the diffusion coefficients of dissolved Cl_2 can be determined, using Eq. [4], from the slope of the plot of $\Delta W/MtA(C_b)_{Cl_2}$ *vs.* $\omega^{1/2}$. The obtained diffusion coefficients of dissolved chlorine are shown in Table II. The corrosion of Zn due to H_2 evolution was measured by conducting weight loss measurements without Cl_2 at the same pH range. The weight loss due to H_2 evolution was negligible (<1%).

The value $D_{Cl_2} = 0.633 \times 10^{-5}$ cm²/sec for 37% $ZnCl_2$ solution is in agreement with the value obtained from limiting current measurements of Cl_2 on a rotating nonporous graphite-disk electrode ($D = 0.664 \times 10^{-5}$ cm²/sec) (7).

Table II also shows the calculated Stokes-Einstein product $D\mu/T$ for dissolved Cl_2 in the four $ZnCl_2$ solutions. The Stokes-Einstein product was found to be constant and the average value, $(D\mu/T)_{avg} = 4.42 \times 10^{-10}$ g cm/sec² °K, can be used to estimate the diffusion coefficients of dissolved Cl_2 at various $ZnCl_2$ solutions. This value is in general agreement with the chronopotentiometry data of Chao (16). The calculated Stokes radii for dissolved Cl_2 are shown in Table II and the average value is $(r_{Cl_2})_{avg} = 1.64$Å.

The present diffusion coefficient data are in good agreement with a value $D_{Cl_2} = 1.22 \times 10^{-5}$ cm²/sec in H_2O at 20°C (8). The viscosity of pure water at 20°C is 1.0050×10^{-2} poise, and the Stokes-Einstein product is 4.185×10^{-10} g cm/sec² °K, in agreement with the present data.

The dissolution of Cl_2 in $ZnCl_2$ solution is governed by the formation of molecular Cl_2, HOCl, and Cl_3^-. The corrosion of Zn is therefore the result of the mass transfer and equilibria of the three species and

Table I. Summary of weight loss of Zn hemisphere in chlorinated $ZnCl_2$ solutions

$ZnCl_2$ % wt	Running time (min)	ω (rpm)	Radius HS (cm)	Cl_2 (mole/cm³) (×10⁵)	pH	Re (×10⁻³)	ΔW (mg)
37%	60.0	1,000	0.381	1.90	3.20	0.874	11.94
(3.74M)	60.0	2,000	0.381	1.58	3.27	1.75	12.63
pH = 3.37	60.0	3,500	0.381	1.61	3.27	3.06	20.43
	60.0	4,390	0.406	0.35	3.35	4.37	6.01
	60.0	4,620	0.406	0.45	3.33	4.59	6.49
	30.0	5,000	0.436	2.78	3.05	5.75	26.70
	10.0	6,000	0.406	2.85	3.04	5.96	9.50
	60.0	7,000	0.406	2.05	3.18	6.96	71.09*
	75.0	8,000	0.436	1.27	3.29	9.20	41.69
	31.0	8,000	0.436	1.96	3.20	9.20	50.54*
	120.0	8,000	0.436	1.90	3.20	9.20	247.05*
22%	60.0	1,000	0.356	2.82	2.35	0.977	18.93
(1.95M)	60.0	2,000	0.381	2.40	2.55	2.24	28.44
pH = 3.74	60.0	3,000	0.381	2.36	2.60	3.36	32.14
	60.0	4,000	0.406	2.75	2.47	5.08	49.71
	60.0	5,000	0.406	2.65	2.50	6.35	64.14*
	60.0	6,000	0.406	2.31	2.62	7.62	58.37*
17%	60.0	1,000	0.354	2.26	2.35	1.12	17.00
(1.44M)	60.0	2,000	0.381	2.85	2.26	2.59	39.71
pH = 4.02	60.0	3,000	0.401	2.13	2.36	4.30	36.03
	60.0	4,000	0.386	1.76	2.40	5.32	34.87
	60.0	5,000	0.352	2.17	2.36	5.53	39.74
	60.0	6,000	0.427	1.97	2.37	9.76	72.50*
26%	60.0	1,500	0.395	1.20	1.0	1.76	11.06
(2.38M)	60.0	3,000	0.397	1.21	1.0	3.54	17.09
pH = 1.0	30.0	4,000	0.350	1.34	1.0	3.67	8.19
	30.0	4,500	0.340	1.20	1.0	3.88	7.69
	30.0	6,000	0.397	1.27	1.0	7.07	12.96

* Denotes spiral markings observed on Zn hemisphere.

the measured diffusion coefficients have an average meaning. In the following section the hydrolysis and equilibria of Cl_2 solution are analyzed. The true diffusion coefficient and the Stokes-Einstein product of dissolved molecular Cl_2 are measured in $HClO_4$ + HCl solution and in acidified $ZnSO_4$ solution, and compared to the average values in the $ZnCl_2$ solutions.

The hydrolysis and equilibria of dissolved chlorine.— The dissolved chlorine exists in chloride aqueous solution partly in the form of free molecular chlorine Cl_2, partly in its hydrolized form hypochlorous acid HOCl, and the remainder in the form of the complex trichloride ion Cl_3^-.

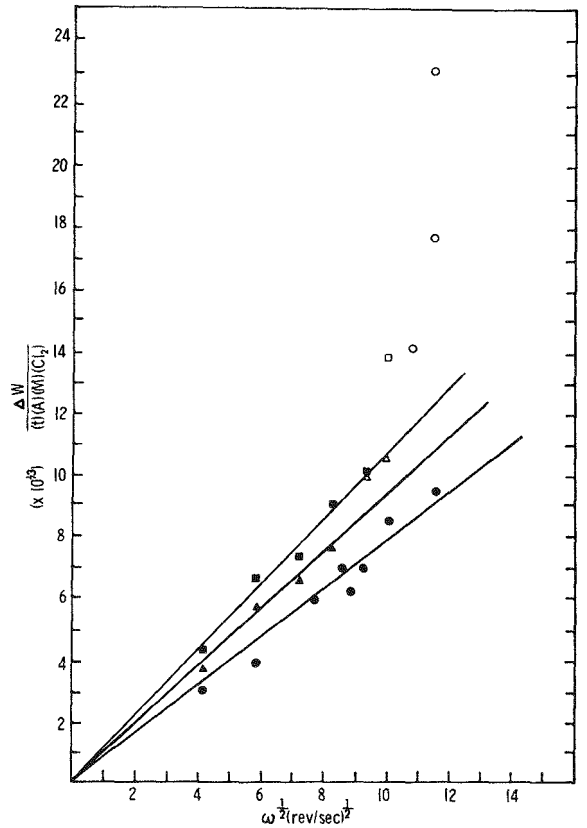

Fig. 2. Zn weight loss *vs.* the square root of the rotational velocity. ● 37%; ▲ 22%; ■ 17%; $ZnCl_2$ solution. Empty points, spiral markings were observed.

Table II. Diffusion coefficients, Stokes-Einstein products and Stokes radii of dissolved Cl_2 in various $ZnCl_2$ solutions

$ZnCl_2$ M	pH	T, °C	D (cm²/sec) ×10⁵	Dμ/T (g cm/sec² °K) ×10¹⁰	$r_{\Sigma Cl_2}$ Å
1.44	2.3	21.3	0.969	4.46	1.64
1.95	2.5	22.0	0.808	4.49	1.63
3.74	3.2	25.0	0.633	4.46	1.64
2.38	1.0	25.0	0.718	4.28	1.70

$(D\mu/T)_{avg} = 4.42 \times 10^{-10}$ g cm/sec² °K
$(r_{Cl_2})_{avg} = 1.64$Å

The hydrolysis of chlorine is governed by the following two equilibria with *K*'s at 25°C (14-16)

$$Cl_2 + H_2O \rightleftarrows HOCl + H^+ + Cl^- \quad K_1 = 3.94 \times 10^{-4} \qquad [5]$$

$$Cl_2 + Cl^- \rightleftarrows Cl_3^- \quad K_2 = 0.191 \qquad [6]$$

The hydrolysis of dissolved Cl_2 depends strongly on the *p*H.

The dissociation constant of hypochlorous acid to hypochlorite (15)

$$HOCl \rightleftarrows H^+ + OCl^- \quad K = 3 \div 4 \times 10^{-8}$$

is very small and in the present acidic solution hypochlorite is not present.

Although the $ZnCl_2$ solutions in the present work are acidic and the dissolved Cl_2 is the predominant species, the concentrations of HOCl and Cl_3^- can be estimated from the equilibrium constants

$$(HOCl)^2 = K_1 \frac{(\Sigma Cl_2) - (HOCl) - (Cl_3^-)}{(Cl^-)\gamma_{HCl}} \qquad [7]$$

$$(Cl_3^-) = K_2[(\Sigma Cl_2) - (HOCl) - (Cl_3^-)](Cl^-) \qquad [8]$$

where ΣCl_2 is the total dissolved Cl_2.

In the following calculations it was assumed that $\gamma_{Cl_2}\gamma_{H_2O}$ cancelled γ_{HOCl} to a good approximation (14), and that $\gamma_{Cl_3^-} \approx \gamma_{Cl^-}$ (15). The initial H^+ concentration can be neglected in comparison to the final H^+ concentration. The activity coefficient of HCl, γ_{HCl}, in $ZnCl_2$ solution was approximated from the available activity coefficient data of HCl in $BaCl_2$ (17).

Table III. Estimated concentration of Cl_2, HOCl, and Cl_3^- in chlorinated $ZnCl_2$, $ZnSO_4$, and $HClO_4$ + HCl solutions

Electrolyte (M)		Initial pH	Final pH	ΣCl_2 10^2 (M)	Cl_2 10^2 (M)	HOCl 10^2 (M)	Cl_3^- 10^2 (M)
$ZnCl_2$	1.44	4.02	2.36	2.0	1.20	0.14	0.66
	1.95	3.74	2.50	2.0	1.09	0.10	0.81
	3.74	3.37	3.20	2.0	0.80	0.06	1.14
	2.38	1.0	1.0	2.0	1.05	0.0004	0.95
$ZnSO_4$	8.74×10^{-3}	1.0	1.0	2.0	1.29	0.71	—
	8.74×10^{-3}	2.5	2.5	2.0	0.25	1.75	—
$HClO_4$+ HCl	0.975M 0.025M	0.02	0.02	2.0	2.0	—	—

Table III presents the calculated concentrations of the various species Cl_2, HOCl, and Cl_3^- in typical 2×10^{-2}M total-dissolved Cl_2 solutions. It appears that for a typical $ZnCl_2$ solution 50 ± 10% of the dissolved chlorine remains as molecular Cl_2, while 50 ± 10% and 5 ± 5% are converted to Cl_3^- and HOCl, respectively. The decrease in the pH upon chlorination is due to the partial hydrolysis of dissolved Cl_2 to HOCl and HCl, according to the first equilibrium (Eq. [5]). The obtained diffusion coefficients of dissolved Cl_2, the calculated Stokes-Einstein product, and the Stokes radius represent an average of the three diffusing species Cl_2, HOCl, and Cl_3^-.

Figure 3 shows the mass transfer coefficient as a function of the square root of the rotational speed in chlorinated acidified 8.74×10^{-3}M $ZnSO_4$ (pH = 1.0), acidified 26% wt $ZnCl_2$ solution (pH = 1.0), and in 0.975M $HClO_4$ + 0.025M HCl chlorinated solution.

In H_2SO_4-acidified $ZnSO_4$ solution (pH = 2.5), most of the dissolved Cl_2, 87.5%, is hydrolyzed to HOCl and therefore, the diffusion coefficient which was calculated from the slope $D = 1.451 \times 10^{-5}$ cm²/sec is the approximate value for HOCl. In the 26% weight $ZnCl_2$ solution (pH = 1.0), HOCl is not present and about 47.5% of the total dissolved Cl_2 is converted to Cl_3^-. The obtained diffusion coefficient $D = 0.718 \times 10^{-5}$ cm²/sec represents an average value for Cl_2 and Cl_3^-.

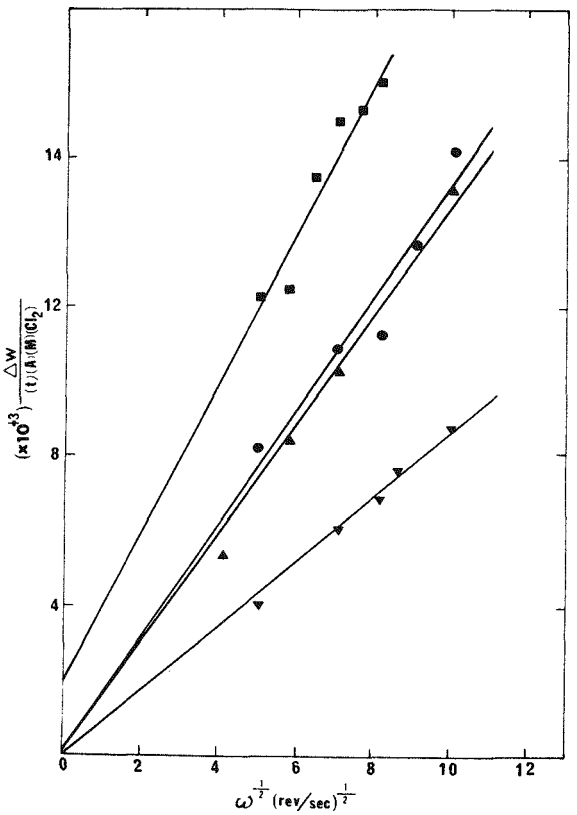

Fig. 3. Zn weight loss *vs.* the square root of the rotational velocity. 8.74×10^{-3}M $ZnSO_4$; ● pH = 1.0; ▲ pH = 2.5; ■ 0.975M $HClO_4$ + 0.025M HCl; ▼ 26% (pH = 1) $ZnCl_2$.

Similar weight-loss experiments were performed in chlorinated 0.975M $HClO_4$ + 0.025M HCl solution. In this solution all the dissolved Cl_2 remains as molecular Cl_2 and therefore the diffusion coefficient $D_{Cl_2} = 2.14 \times 10^{-5}$ cm²/sec is the true value for Cl_2. In this experiment the weight loss due to H_2 evolution was estimated from a weight loss experiment in the absence of Cl_2 and from the intercept at $\omega = 0$ in Fig. 3. The viscosity of the $HClO_4$ + HCl solution was measured at 28° in our laboratory, $\mu = 8.23 \times 10^{-3}$ g/cm sec, using an Ostwald viscometer.

The Stokes-Einstein products and the Stokes radii of dissolved Cl_2 in acidified $ZnSO_4$ solutions and $HClO_4$ + HCl solution are shown in Table IV. The $ZnSO_4$ pH = 2.5 values can be regarded as an approximation for HOCl

$$(D\mu/T)_{HOCl} \cong 4.45 \times 10^{-10} \text{ g cm/sec}^2 \text{ °K}$$

$$r_{HOCl} \cong 1.67\text{Å}$$

The HOCl concentration was quite low in all the experiments, except in the $ZnSO_4$ solutions. The diffusion coefficient of Cl_3^- is expected to be the lowest, followed by HOCl and Cl_2. In $ZnSO_4$ solution at low pH, the diffusion coefficient is higher (Table IV) due to the higher concentration of molecular Cl_2, in agreement with Chao (16).

In the $HClO_4$ + HCl solution, the Stokes-Einstein product is the highest because of the expected high diffusion coefficient of dissolved molecular Cl_2, which is the predominant species. The data from the $HClO_4$ + HCl solution can be regarded as the true values for Cl_2

$$(D\mu/T)_{Cl_2} = 5.85 \times 10^{-10} \text{ g cm/sec}^2 \text{ °K}$$

$$r_{Cl_2} = 1.25\text{Å}$$

A Cl_2 bond length of 1.98Å is given by Pauling (13).

Hydrodynamic effects.—Above a rotational speed of about 100 rps, the Levich equation is not satisfied (see Fig. 2), and the weight loss is much higher than expected for laminar flow. The empty data points in Fig. 2 represent experiments where spiral vortex shape markings were observed on the Zn hemisphere at the end of the experiment. The higher weight losses of the Zn hemisphere under these conditions can be explained by an earlier transition to turbulent flow and the appearance of secondary flow pattern near the surface which enhances the mass transfer of dissolved Cl_2 to the Zn surface.

During the Zn dissolution the Zn surface becomes rough. This surface roughness changes the nature of the flow, and transition to turbulence appears earlier than expected for a smooth surface. Levich (2) discusses convective diffusion to a rough surface and relates the size of the protrusions to the thickness of the hydrodynamic boundary layer. If the size of the protrusion is larger than the hydrodynamic boundary layer, then transition occurs earlier. The thickness of the hydrodynamic boundary layer depends on

Table IV. Diffusion coefficients, Stokes-Einstein products and Stokes radii for dissolved Cl_2 in $ZnSO_4$ solution and $HClO_4$ + HCl solution

Electrolyte (M)		pH	T, °C	D (cm²/sec) $\times 10^5$	$D\mu/T$ (g cm/sec² °K) $\times 10^{10}$	r, Å
$ZnSO_4$	8.74×10^{-3}	1.0	25	1.517	4.57	1.60
$ZnSO_4$	8.74×10^{-3}	2.5	25	1.451	4.38	1.67
$HClO_4$ + HCl	0.975 0.025	0.02	28	2.14	5.85	1.25

$r_{Cl_2} = 1.25$Å $\qquad$ $r_{HOCl} \cong 1.67$Å

the rotational speed through the Reynolds number ($Re = \omega r^2/\nu$). As the rotational speed increases (6000-8000 rpm) the thickness of the boundary layer decreases and reaches the same order of magnitude of the rough surfaces. Secondary flow of small vortexes is initiated, which enhances the mass transfer of dissolved Cl_2 to the surface.

In all the electrodes which exhibited higher weight loss than expected, the corroded surface showed spiral shape patterns of dissolution. Typical spiral markings are shown in Fig. 4 where the rotational speed is high (8000 rpm). The formation of spiral markings on a rotating-disk electrode has been shown (9, 10) to be caused by the formation of wakes behind small protrusions and the formation of secondary flow is due to instability of the three-dimensional boundary layer on the rotating disk or hemisphere. Figure 5 shows the surface of Zn hemisphere after Cl_2 corrosion at lower rotational speed ($Re = 4.37 \times 10^3$). Spiral markings are absent and the grain boundaries can be observed clearly. Ibl (18) explains the formation of the spirals during metal deposition on a rotating-disk electrode by the relative size of the surface protrusions and the mass transfer boundary layer thickness.

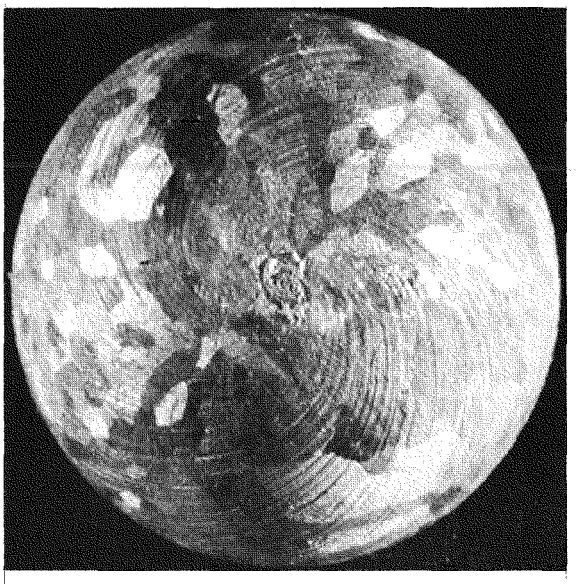

Fig. 4. Zn hemisphere after reaction with dissolved Cl_2. ω = 8000 rpm; radius = 0.436 cm; $[Cl_2] = 1.96 \times 10^{-2}$M; time = 31 min; $Re = 9.2 \times 10^3$; 37% $ZnCl_2$.

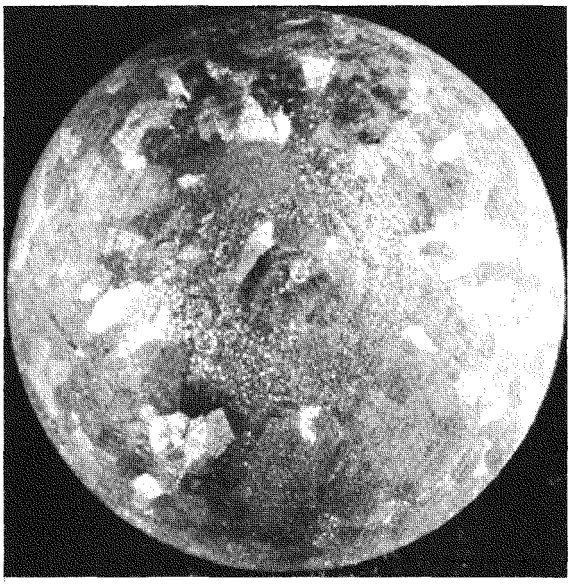

Fig. 5. Zn hemisphere after reaction with dissolved Cl_2. ω = 4390 rpm; radius = 0.406 cm; $[Cl_2] = 0.35 \times 10^{-2}$M; time = 60 min; $Re = 4.37 \times 10^3$; 37% $ZnCl_2$.

The transition flow appears at a Reynolds number of about

$$Re = \frac{\omega r^2}{\nu} = \frac{2\pi(121)(0.4)^2}{1.72 \times 10^{-2}} = 7 \times 10^3$$

which is below the transition Reynolds number of 1.5×10^4 obtained experimentally for a smooth rotating hemisphere (12). The flow near a hemisphere is less stable than near a rotating disk, and the present value for a hemisphere is lower than 10^5, as predicted from linear stability analysis of a flow near a rotating disk (10, 11). The earlier transition in the present case is due to the surface roughness during the corrosion of the zinc surface by the dissolved Cl_2.

In conclusion, it has been shown that the chemical reaction of dissolved chlorine with zinc in $ZnCl_2$ aqueous solution is mass transfer limited. The Zn surface roughness initiates a secondary flow and increases the mass transfer of dissolved Cl_2 to the surface. At low pH the dissolved Cl_2 is in the form of dissolved molecular Cl_2 and trichloride ion, Cl_3^-. At higher pH, the presence of hypochlorous acid, HOCl, is significant.

Acknowledgments

This work was supported by Energy Development Associates, Madison Heights, Michigan, and Electric Power Research Institute, Palo Alto, California. The stimulating discussions with Drs. Philip Symons and Charles Warde are gratefully acknowledged.

Manuscript submitted March 4, 1977; revised manuscript received Aug. 25, 1977.

Any discussion of this paper will appear in a Discussion Section to be published in the December 1978 JOURNAL. All discussions for the December 1978 Discussion Section should be submitted by Aug. 1, 1978.

Publication costs of this article were assisted by Wayne State University.

LIST OF SYMBOLS

A	hemisphere's surface area, cm^2
C_b	bulk concentration, g-mole/cm^3
D	diffusion coefficient, cm^2/sec
F	Faraday's constant, 96,487 C/g-equiv.
I_l	limiting current, A
k_c	mass transfer coefficient, cm/sec
M	molecular weight of Zn
n	number of electrons transferred in the electrode reaction
r	radius of hemispherical electrode, cm
r	Stokes radius, Å
Re	Reynold's number
T	temperature, °K
t	time, sec
W	electrode weight, g
α	rotating electrode constant, dimensionless
δ	diffusion layer thickness, cm
μ	viscosity, g/cm sec
ν	kinematic viscosity, cm^2/sec
ω	angular velocity, rad/sec
ΣCl_2	total dissolved Cl_2

REFERENCES

1. P. C. Symons and P. Carr, in Proceedings of the 8th Inter-Society Energy Conversion Engineering Conference, Paper No. 739010, pp. 72-77 (1973).
2. V. G. Levich, "Physicochemical Hydrodynamics," pp. 60-72, Prentice Hall, Englewood Cliffs, N.J. (1962).
3. D. T. Chin, *This Journal*, **118**, 1434 (1971).
4. J. Newman *ibid.*, **119**, 69 (1972).
5. "Specific Gravity of Aqueous $ZnCl_2$ Solutions," Handbook of Chemistry and Physics, 35th ed., Chemical Rubber Publishing Co. (1953-1955).
6. J. Mellor, "Comprehensive Treatise on Inorganic

and Theoretical Chemistry," Vol. 2, suppl. (1974).
7. J. T. Kim and J. Jorné, *This Journal*, **124**, 1473 (1977).
8. J. H. Arnold, *J. Am. Chem. Soc.*, **52**, 3937 (1930).
9. G. T. Rogers and K. J. Taylor, *Nature (London)*, **200**, 1062 (1963).
10. A. C. Riddiford, in "Advances in Electrochemistry and Electrochemical Engineering," Vol. 4, P. Delahay, Editor, Interscience, New York (1966).
11. F. Opekar and P. Beran, *J. Electroanal. Chem. Interfacial Electrochem.*, **69**, 115 (1976).
12. D. T. Chin, *This Journal*, **118**, 1764 (1971).
13. L. Pauling, "The Nature of the Chemical Bond," 3rd ed., Cornell University Press, Ithaca, N.Y. (1960).
14. R. E. Connick and Y-S. Chia, *J. Am. Chem. Soc.*, **81**, 1280 (1959).
15. M. S. Sherril and E. F. Izard, *ibid.*, **53**, 1667 (1931).
16. M. S. Chao, *This Journal*, **115**, 1172 (1968).
17. H. S. Harned and B. B. Owen, "The Physical Chemistry of Electrolytic Solutions," 3rd ed., pp. 748-751, Reinhold Publishing Co., New York (1958).
18. N. Ibl, Zeitschrift Erzmetall Bd. 22, pp. 87-98, Beiheft Symposium Hydrometallurgie (1969).

APPENDIX B

ANALYSIS OF REFRIGERATION REQUIREMENTS OF A 100 MWH PEAK-SHAVING ZINC-CHLORIDE BATTERY AND ESTIMATION OF COST OF SYSTEM COMPONENTS AND POWER CONSUMPTION

Appendix B

ANALYSIS OF REFRIGERATION REQUIREMENTS OF A 100 MWH PEAK-SHAVING ZINC-CHLORIDE BATTERY AND ESTIMATION OF COST OF SYSTEM COMPONENTS AND POWER CONSUMPTION

W. Leidenfrost, Project Director
J. D. Loveley, Consultant
B. Korenic, Graduate Research Assistant
K. Lee, Graduate Research Assistant

School of Mechanical Engineering
Heat Transfer Laboratory
Purdue University
Lafayette, Indiana

INTRODUCTION AND SUMMARY

The EDA battery system requires a centrifugal chiller system to cool the chlorine/aqueous solution in the process to approximately 5°C - 41°F. The EDA contract with the Purdue University required an investigation of air cooled versus water cooled condensers regarding efficiency and optimum utilization of water because of water limitations in some localities.

An analysis of the refrigeration requirements was undertaken by Liedenfrost and Lee which determined the mass flow rate of the R-12 refrigerant and the compressor work input. The various options of condenser systems were then calculated. This involved the calculations of a two-pass versus a four-pass condensers and the changes in power input for pumping the condenser tower water. By this time, the air-cooled condenser had been determined to be less efficient and more complicated because of its much larger size and about ten times as many fan motors.

Independently, but covering the same components and system, the work of Mr. J. D. Loveley, a consultant working with Purdue University, developed a refrigeration system bill of material using off the shelf items so that reliability could be assured and that no further development of this unit would be required. Using a York Open Turbomaster Centrifugal Compressor Chilling Unit, the cost to the utility buying it from a contractor was developed as of November, 1976. The information supplied is such that the costs could be updated at any time to reflect inflation or other changes in the manufacturers costs.

As pointed out above, the methods of condensing were most carefully analyzed and it became very obvious that an in-depth study should be directed to the Evaporative Condenser. The application of an Evaporative Condenser to this particular refrigeration system used with a chlorine/aqueous system is favorable except that presently Evaporative Condensers are only built up to 150 tons. This does not mean that they can't be built larger. With the arrangement to cool the refrigerant directly by air and water, the power and water usage is lower than in a cooling tower and water cooled condensering system. Lower condensing temperatures are possible with an Evaporative Condenser. Preliminary computer studies by Liedenfrost and Korenic showed that an overall COP of 30 to 65% can be achieved with varying conditions of operation. Obviously these computer studies will require confirmation in an actual test under the same varying conditions.

REFRIGERATION REQUIREMENTS

I. INTRODUCTION

In a load-leveling zinc-chloride battery, the chlorine gas produced during charging period must be stored. One of the available methods is to store the chlorine in form of a hydrate. This is accomplished by bringing the chlorine gas in close contact with water and holding the temperature at 9.6°C or lower. Since the formation of the hydrate is exothermal, heat must be removed in order to maintain the system at the appropriate temperature.

The purpose of this report is to calculate the capacities, specifications and costs of each component to be used in the refrigeration system.

The schematic diagram of the refrigeration system is shown on Fig. 1.

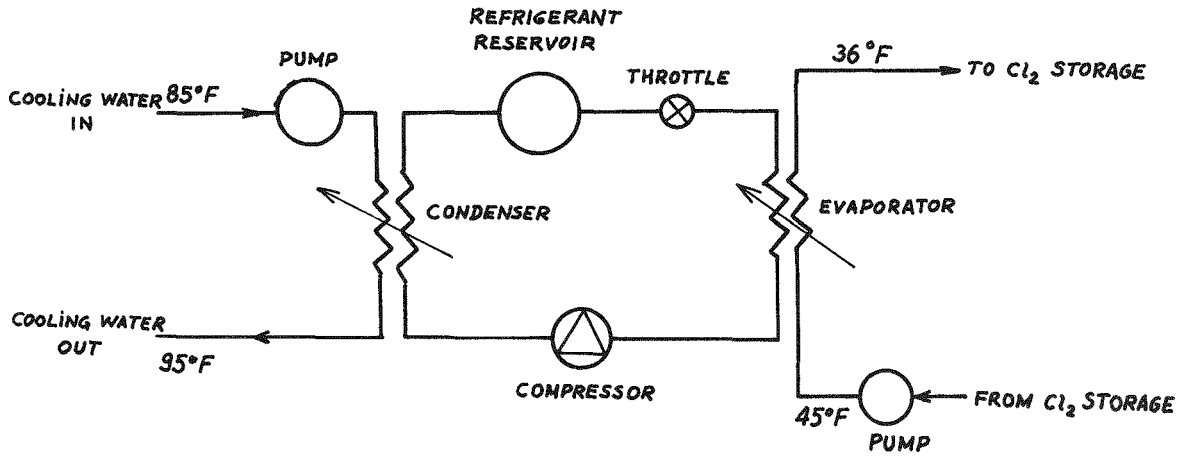

Figure 1. Refrigeration system for chlorine storage.

This report will first determine the mass flow rate of the refrigerant (R-12 is used) and compressor work input by thermodynamics calculations. Then the various options of condenser types are calculated. Afterwards we will determine the evaporator. Finally when the calculation of the system is completed, the costs for each component will be evaluated.

II. THERMODYNAMICS (SUBCOOLED CONDENSATE)

1. Mass Flow Rate of Freon-12

a. General Discussion

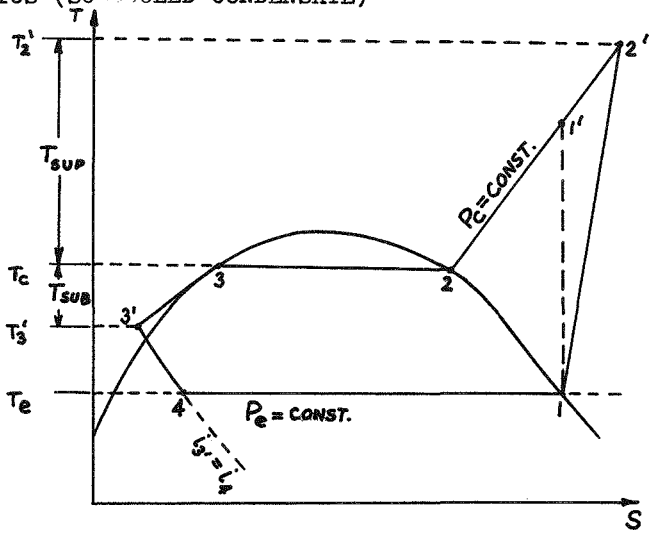

Figure 2. T-S diagram for subcooled condensate

On the T-S (Fig. 2) diagram of the refrigeration cycle, we can see saturated R-12 vapor at state 1 is compressed to state 2' by a centrifugal compressor. At the same time, the temperature of R-12 vapor has been raised from T_e, the evaporation temperature, to T_2', the superheated vapor temperature.

The superheated R-12 vapor is cooled in the condenser. When state 2 is reached, the vapor becomes saturated, and the vapor temperature drops to T_c, the condensation temperature. Condensation begins at state 2 and continues through state 3 where R-12 is in the form of saturated liquid. To minimize the R-12 flow rate $\dot{m}$ and the compressor work input, R-12 at state 3 is cooled to state 3' along the constant-pressure line. The difference between T_c and T_3' is the subcooled temperature.

R-12 is now throttled from state 3' to state 4 along the constant enthalpy line. Meanwhile, the pressure is decreased from p_c, the pressure corresponding to T_c, to p_e, the pressure corresponding to T_e. R-12 at state 4 receives heat in the evaporator and continuously increases its quality. When it leaves the evaporator, state 1 has been reached again. Thus, a cycle is completed.

If the heat load of the evaporator is q_e, then from energy conservation:

$$q_e = \dot{m}(i_1 - i_4)$$
$$= \dot{m}(i_1 - i_3') \qquad (1)$$

where $\dot{m}$ is the mass flow rate of R-12. If q_e, i_1 and i_3' are known, then $\dot{m}$ is

readily determined by:

$$\dot{m} = \frac{q_e}{i_1 - i_3'} \qquad (2)$$

b. Numerical Calculations

In our case, q_e is the heat needed to be removed during charge period of the battery in order to maintain the process of hydrate formation. For the 100 MWH battery considered, the heat to be removed from the storage was specified to be 2.57 MW.

T_c and T_e are chosen to be 103°F(39.44°C) and 29.3°F(-1.5°C), respectively. The criteria for choosing T_c and T_e are:

1. T_c should be high enough and T_e should be low enough to ensure good heat transfer.
2. To minimize compressor work input and $\dot{m}$, T_c should not be too high. To avoid freezing of water inside tubes of evaporator, T_e should not be too low.

After T_e and T_c are known and T_{sub} is given (in our case we let T_{sub} = 5°F = 2.78°C), i_3' and i_1 can be found: *

$i_1 = i_{-1.5°C}(\text{Vapor}) = 186.9$ KJ/Kg

$i_3' = i_{98°F} = i_{36.67°C}(\text{liquid}) = 71.0$ KJ/Kg

$$\therefore \dot{m} = \frac{q_e}{i_1 - i_3'} = \frac{2.57 \text{ MW}}{(186.9 - 71.0)\text{KJ/Kg}}$$

$$= \frac{2.57 \times 10^3 \times 3600 \text{ KJ/H}}{115.9 \text{ KJ/Kg}}$$

$$= 79827.4 \text{ Kg/H}$$

$$= 2933.2 \text{ lb/min}$$

---

* Kenneth Wark: Thermodynamics

2. Compressor Work Input

a. General Discussion

The refrigeration cycle is shown on a p-i diagram (Fig. 3). All states in the cycle are represented by the same symbols as those in the T-S diagram shown before.

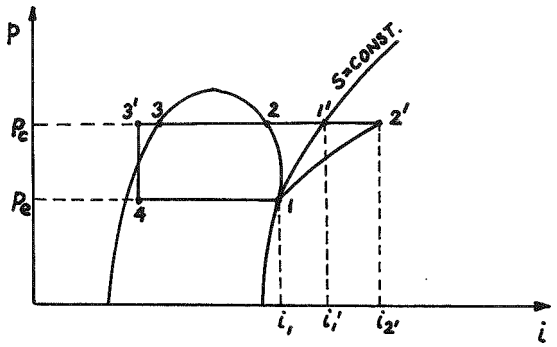

Fig. 3 p-i diagram for subcooled condensate

If the compression is isentropic, then the vapor at state 1 will be compressed to state 1' along the constant entropy line. Then the difference between i_1' and i_1 is the compressor work input needed. Hence,

$$W_{is} = i_1' - i_1$$

Where W_{is} is the compressor work needed per unit mass of R-12 in an isentropic process. However, the actual process is not isentropic. More work than W_{is} will always be needed. The ratio between W_{is} and the actual work, W_{act}, is called the efficiency of the compressor and is denoted by E_f. Therefore, we have:

$$E_f \equiv \frac{W_{is}}{W_{act}} \tag{3}$$

or,

$$W_{act} = \frac{W_{is}}{E_f} \tag{4}$$

Besides,

$$W_{act} = i_2' - i_1 \tag{5}$$

Where i_2' is the enthalpy of the superheated R-12 vapor after compression. Therefore, i_2' can be determined. The intersection of the constant i_2' line and constant p_c line is state 2'. From the constant temperature lines in p - i diagram, T_2' can be determined.

b. Numerical Calculations

p_e = 2.94 bars = 42.7 psia

p_c = 9.60 bars = 139.2 psia

From p-i diagram of R-12, we can read the following values:

$i_1 = 80$ Btu/lb

$i_1' = 89$ Btu/lb

Then,

$W_{is} = 9$ Btu/lb

If we assume that E_f is 80%, then:

$W_{actual} = 11.25$ Btu/lb

Then from the p-i diagram we can also read:

$i_2' = 91.25$ Btu/lb

$T_2' = 125^{\circ}F$

The mass flow rate, $\dot{m}$, has been calculated before. Hence the compressor work input, W_e, is given by:

$W_c = \dot{m} W_{act}$

$= 2933.2$ lb/min x 11.25 Btu/lb

$= 32999$ Btu/min

$= 778$ HP

$= 580.4$ KW

$= 498998$ Kcal/hr

III. THERMODYNAMICS (SATURATED CONDENSATE)

1. Mass Flow Rate of Freon-12

a. General Discussion

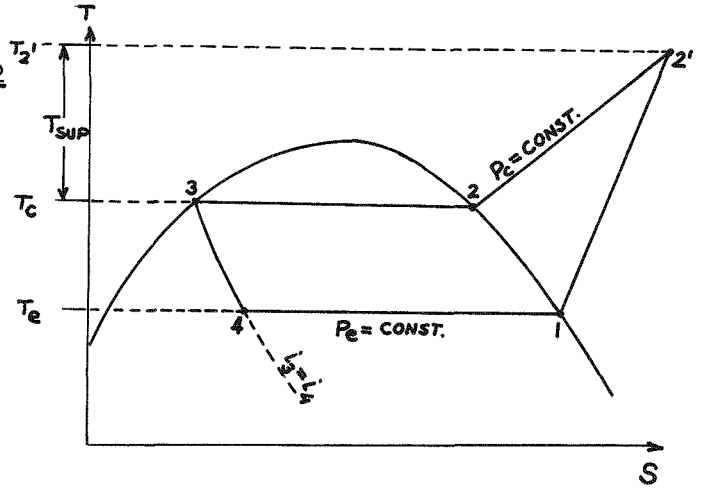

Fig. 4. T-S diagram for saturated condensate

In this case (Fig. 4), when R-12 has been condensed to saturated liquid (State 3), it is throttled to state 4 without being subcooled as in the previous case.

The equation for energy conservation becomes:

$$q_e = \dot{m}(i_1 - i_4)$$
$$= \dot{m}(i_1 - i_3) \qquad (6)$$

where q_e is the heat load of the evaporator, $\dot{m}$ is the mass flow rate of R-12, i_1, i_3, and i_4 are the enthalpies of R-12 at state 1, 3, and 4, respectively.

Then we can obtain $\dot{m}$ by

$$\dot{m} = \frac{q_e}{i_1 - i_3} \qquad (7)$$

b. Numerical Calculations

$q_e = 2.57$ MW

$i_1 = i_{-1.5^\circ C}(\text{Vapor}) = 186.9$ KJ/Kg

$i_3 = i_{103^\circ F} = i_{39.44^\circ C}(\text{liquid}) = 74.0$ KJ/Kg

$$\dot{m} = \frac{2.57 \text{ MW}}{(186.9 - 74.0) \text{ KJ/Kg}}$$

$= 81948.6$ Kg/H

$= 3011.1$ lb/min

2. Compressor Work Input

The only difference in this case (Fig. 5) is that state 3 goes directly to state 4. For this reason, the mass flow rate of R-12 will change, but the compressor work for unit mass will be the same.

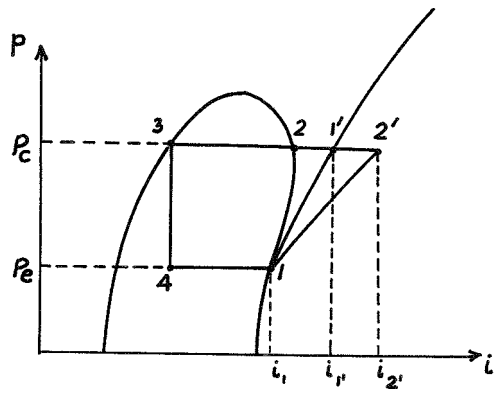

Fig. 5. p-i diagram for saturated condensate

Since $\dot{m}$ and W_{act} have been calculated,

$W_c = \dot{m} W_{act}$

$= 3011.1$ lb/min x 11.25 Btu/lb

= 33875 Btu/min
= 799 HP
= 595.8 KW
= 512244 Kcal/hr

IV. CALCULATION OF SHELL-AND-TUBE CONDENSER (UNFINNED, R-12 IN TUBE, SUBCOOLED)

Since iterative procedure is needed in this calculation, a computer program has been developed. For the convenience of the readers, the same notation as in the computer program will be used in the following discussion.

1. Number of Parallel Rows

NROP, number of parallel rows, is defined as the number of parallel paths needed to carry the mass flow of R-12.

To calculate NROP, we first calculate the mean density of R-12 in the condenser:

$$RHOM = \frac{1.}{SVL + .5(SVG-SVL)} \tag{8}$$

where:

SVL = Specific Volume of liquid R-12 at condensation pressure and temperature

SVG = Specific Volume of vapor R-12 at condensation pressure and temperature.

Then,

$$SVL = \frac{1}{RHOFL} \tag{9}$$

$$SVG = \frac{1}{RHOFG} \tag{10}$$

where:

RHOFL = density of liquid R-12 at condensation pressure and temperature

RHOFG = density of vapor R-12 at condensation pressure and temperature.

Denote the cross section area of one tube by ACWE, then

$$ACWE = \frac{\pi DI^2}{4} \tag{11}$$

where:

DI = inner diameter of one tube.

Then the number of parallel rows is calculated as follows:

$$NROP = \frac{CW}{(RHOM)(VWM)(ACWE)} \tag{12}$$

where:

CW ≡ mass flow rate of R-12, calculated in previous sections and denoted as $\dot{m}$ there.

VWM ≡ mean velocity of R-12 when at .50 of quality, a specified value.

If number of tube passes, XNPAS, is known, the total number of tubes, XNTU, is determined by:

$$XNTU = (NROP)(XNPAS) \tag{13}$$

2. Heat Transfer Coefficients Inside Tubes

The mass flux, SAVE, is calculated by:

$$SAVE = \frac{CW}{(ACWE)(NROP)} \tag{14}$$

a. Condensation Heat Transfer Coefficient

Define equivalent mass flux, GW, by:

$$GW = .5(SAVE)\ [1 + (\frac{RHOFL}{RHOFG})^{\frac{1}{2}}] \tag{15}$$

Then the Reynolds number, REW, is determined by:

$$REW = \frac{(GW)(DI)}{MUW} \tag{16}$$

where:

MUW = the dynamic viscosity of liquid R-12 at condensation pressure and temperature.

Then the Nusselt number, NUW, and condensation heat transfer coefficient are given by:

When REW ≥ 50000.

$$NUW = .0265(REW^{.8})(PRW^{1/3}) \tag{17}$$

When REW < 50000.

$$NUW = 5.03(REW^{1/3})(PRW^{1/3}) \tag{18}$$

$$HW = \frac{(NUW)(RKW)}{DI} \tag{19}$$

where:

PRW = Prandtl number of R-12 liquid at condensation pressure and temperature.

RKW = thermal conductivity of liquid R-12 at condensation pressure and temperature.

b. Subcooling Heat Transfer Coefficient

The Reynolds number in the subcooled section, REWS, is given by:

$$REWS = \frac{(SAVE)(DI)}{MUW} \tag{20}$$

Then the Nusselt number, NUWS, and the heat transfer coefficient, HWS, are given by:

When REWS $\geq$ 2300.

$$NUWS = .023(REWS^{.8})(PRW^{.3}) \tag{21}$$

When REWS < 2300.

$$NUWS = 3.66 \tag{22}$$

$$HWS = \frac{(NUWS)(RKW)}{DI} \tag{23}$$

3. Heat Transfer Outside Tubes

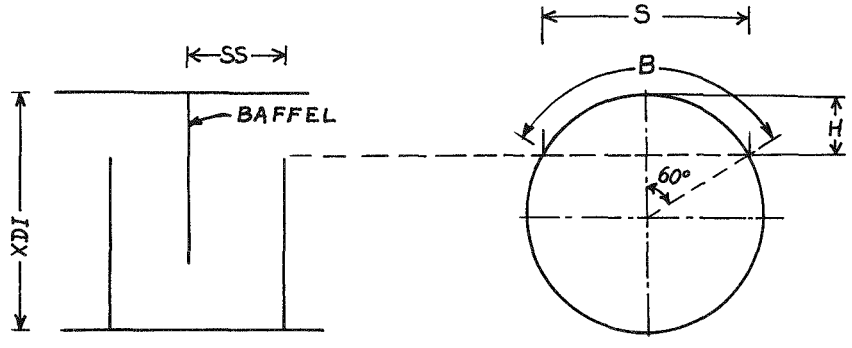

Fig. 6. Geometric arrangement of the shell

From Fig. 6, it can be seen that:

$$B = \frac{\pi(X\,DI)}{3} \tag{24}$$

$$S = \frac{\sqrt{3}}{2}(XDI) \tag{25}$$

$$H = \frac{1}{4}\,(XDI) \tag{26}$$

where XDI is the inner diameter of the shell.

The distance between baffles, SS, is calculated by iterative method.

To calculate the clearance between tube walls, E, we will first count the number of triangles formed by tubes.

From Fig. 7, three tubes are needed to form one triangle, but there are six triangles surrounding each tube. Therefore, we may conclude that for every tube there are two triangles.

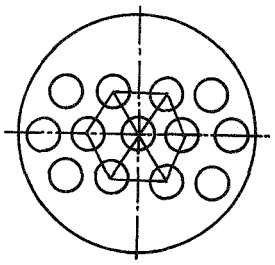

Fig. 7. Tube arrangement in shell

Then the area of each triangle is given by (Fig. 8):

$$XA = \frac{\pi(XDI)^2}{4} \cdot \frac{1}{2(XNPAR)} \tag{27}$$

And E is given by:

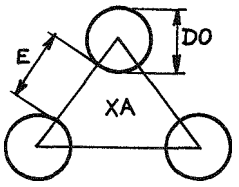

Fig. 8. Triangular arrangement of tubes →

$$E = \left(\frac{4(XA)}{\sqrt{3}}\right)^{\frac{1}{2}} - DO \tag{28}$$

where:

DO is the outer diameter of a tube.

The average number of clearances, X, can be seen by the shell flow is (Fig. 9):

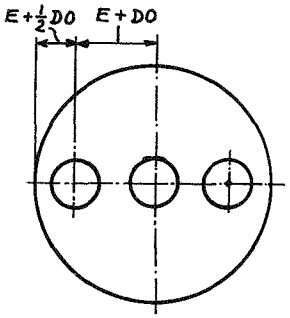

Fig. 9. Maximum number of clearances ←

$$X = \frac{1}{2}\,\frac{XDI-E}{E+DO} \tag{29}$$

Define:

$$AL \equiv A - \frac{\pi(DO)(H)}{4} \tag{30}$$

$$AG \equiv (SS)(X)(E) \tag{31}$$

Then the equivalent area the shell flow can see is:

$$AEQIV = \sqrt{(AL)(AG)} \tag{32}$$

The water mass flow rate in shell, CD, is calculated by:

$$CD = \frac{HEAT}{(RHOD)(AEQIV)} \tag{33}$$

where:

HEAT = HEATE + HEATC + (CW)(CPW)(TSUB)

HEAT ≡ total heat load for the condenser

HEATE ≡ heat load of evaporator, denoted as q_e in previous sections

HEATC ≡ work input by compressor, has been calculated before

CPW ≡ specific heat of liquid R-12 at condensation pressure and temperature

TSUB = degrees of subcooling, equal to $5^{\circ}F$ in our case

RHOD = density of water

Then the velocity of water in shell, VD, is calculated by:

$$VD = \frac{CD}{(RHOD)(AEQIV)} \tag{34}$$

The Reynolds number, RED, Nusselt number, NUD, and heat transfer coefficient, HD, are given then:

$$RED = \frac{(RHOD)(VD)(DO)}{MUWD} \tag{35}$$

$$NUD = .25(RED^{.6})(PRD^{.33}) \tag{36}$$

$$HD = \frac{(NUD)(RKD)}{DO} \tag{37}$$

where:

PRD ≡ Prandtl number of water

RKD ≡ thermal conductivity of water

4. <u>Thermal Resistances and Overall Heat Transfer Coefficients Per Unit Area of Outside Tube Surface</u>

The resistance on shell side, RD, is:

$$RD = \frac{1}{HD} \tag{38}$$

The resistance of the tube wall, RW, is:

$$RT = \frac{(DO)\ln(\frac{DO}{DI})}{RKT} \tag{39}$$

where RKT is the thermal conductivity of tube wall.

The resistances inside tube for condensation and subcooled sections are RW and RWS, respectively:

$$RW = \frac{(\frac{DO}{DI})}{HW} \tag{40}$$

$$RWS = \frac{(\frac{DO}{DI})}{HWS} \tag{41}$$

Then the overall heat transfer coefficients in condensation and subcooled region are denoted by UC and US, respectively, and calculated as follows:

$$UC = \frac{1}{RD + RT + RW} \tag{42}$$

$$US = \frac{1}{RD + RT + RW} \tag{43}$$

5. Heat Transfer Area

The heat transfer area will be calculated by NTU method.* First of all, we will calculate the heat transfer area needed for condensation. Then we will calculate the heat transfer area for subcooling.

a. Heat Transfer Area for Condensation

In this section, R-12 undergoes phase change. Therefore,

$$CMAXC \equiv (CW)(CPW) = \infty \tag{44}$$

$$CMINC \equiv (CD)(CPD) \tag{45}$$

$$EPSC \equiv \frac{TDO-TDI}{TWI-TDI} \tag{46}$$

$$RNTUC \equiv -\ln(1-EPSC) \tag{47}$$

$$AREAC = \frac{(RNTUC)(CMINC)}{UC} \tag{48}$$

*This method has been discussed in detail in report HL 75-52.

where:

TDO = shell outlet temperature for water, 95°F (35°C) in our case.

TDI = shell inlet temperature for water, 85°F (29.44°C) in our case.

TWI = tube inlet temperature for R-12, previously denoted as T_2'. In our case, it is equal to 125°F (51.67°C).

AREAC ≡ heat transfer area needed for condensation.

b. Heat Transfer Area for Subcooling

If (CD)(CPD) > (CW)(CPW):

$$CMINS \equiv (CW)(CPW) \tag{49}$$

$$CMAXS \equiv (CD)(CPD) \tag{50}$$

$$EPSS \equiv \frac{TSUB}{TWO-TDI} \tag{51}$$

If (CD)(CPD) < (CW)(CPW):

$$CMINS \equiv (CD)(CPD) \tag{52}$$

$$CMAXS \equiv (CW)(CPW) \tag{53}$$

$$EPSS \equiv \frac{TDO-TDI}{TWO-TDI} \tag{54}$$

After CMINS, CMAXS, and EPSS are determined, we solve the following non-linear equation for the unknown variable GAMMA. The Bisect-Secant method has been used for this task.

$$EPSS = \frac{2}{\{[1 + (\frac{CMINS}{CMAXS})] + [1 + (\frac{CMINS}{CMAXS})^2]^{\frac{1}{2}} (\frac{1 + e^{-GAMMA}}{1 - e^{-GAMMA}})\}} \tag{55}$$

When we obtain GAMMA, we may calculate the area for subcooling by the following ways:

$$RNTUS \equiv \frac{GAMMA}{[1 + (\frac{CMINS}{CMAXS})^2]^{\frac{1}{2}}} \tag{56}$$

$$AREAS = \frac{(RNTUS)(CMINS)}{US} \tag{57}$$

Where AREAS ≡ heat transfer area needed for subcooling.

Then the total heat transfer area, AREA, is given by:

$$AREA = AREAC + AREAS \tag{58}$$

6. The Computer Program

We need the distance between baffles, SS, to calculate the heat transfer coefficient outside of tubes, HD, and the heat transfer area, AREA. On the other hand, we need to know AREA before shell length and hence SS can be determined.

Therefore an iterative method is necessary. We assume a total heat transfer area AREX. From AREX the value of SS is calculated. Then we calculate HD and AREA. The procedure is continued until a satisfactory agreement between AREX and AREA is reached.

The purposes of the subroutines and functions of the computer program are listed as follows:

SUBROUTINE TUBEC: Calculate NROP, HW, and HWS.
SUBROUTINE SHELL 1: Calculate SS, CD, and VD.
SUBROUTINE SHELL 2: Calculate HD.
SUBROUTINE RESIST: Calculate UC and US.
SUBROUTINE AREO: Calculate AREA.
SUBROUTINE BISECT: Bisect method to calculate GAMMA.
SUBROUTINE SECANT: Secant method to calculate GAMMA.
FUNCTION F: Nonlinear function used to solve for GAMMA.

7. Sample Design

DI	DO	XDI	HW	HWS	HD
.0169	.019	.9144	1137.37	405.56	4783.85

UC	US	E	RED	REW	REWS
828.33	333.82	.001485	2.303×10^4	6.203×10^4	2.15×10^4

SHEL	TUBEL	SS	AREA	AREX	NROP
4.82	9.65	.69	190.66	190.56	330

TDI	TDO	TWI	TWO	TSUB	XNPAS
29.44	35.0	51.67	39.44	2.78	2

Where:

DI ≡ inside diameter of tubes, in m.

DO ≡ outside diameter of tubes, in m.

XDI ≡ inside diameter of the shell, in m.

HW ≡ condensing heat transfer coefficient of R-12 (tube side), in Kcal/m^2h ^oc

HWS ≡ subcooling heat transfer coefficient of R-12 (tube side), in Kcal/m^2h ^oc

HD ≡ heat transfer coefficient of water on shell side, in Kcal/m^2h ^oc

UC ≡ overall heat transfer coefficient for condensing section, in Kcal/m^2h ^oc.

US ≡ overall heat transfer coefficient for subcooling section, in Kcal/m^2h ^oc.

E ≡ wall-to-wall clearance between tubes, in m.

RED ≡ Reynolds number of water

REW ≡ Reynolds number of condensing R-12

REWS ≡ Reynolds number of Subcooling R-12

SHEL ≡ tube length, in m.

TUBEL ≡ length of one parallel row of tube, in m.

SS ≡ distance between baffles, in m.

AREA ≡ calculated heat transfer area, in m^2.

AREX ≡ predicted heat transfer area used to calculate AREA, in m^2.

NROP ≡ number of parallel rows of tubes

TDI ≡ inlet temperature of water, in ^oC

TDO ≡ outlet temperature of water, in ^oC

TWI ≡ inlet temperature of R-12, in ^oC

TWO ≡ condensing temperature of R-12, in ^oC

TSUB ≡ degree of subcooling, in ^oC

XNPAS ≡ number of passes of tubes.

V. CALCULATION OF SHELL-AND-TUBE CONDENSER (FINNED, R-12 OUTSIDE OF TUBE, NO SUBCOOLING)

In this calculation, the following specifications are used:

Tube fluid--treated cooling tower water from 85°F to 95°F.

Shell fluid--R-12

Shell--30"x18', low carbon steel

Tubes---.575"ID, .75"OD, 20 BWG wall, 19 fpi, copper

In-tube velocity--9.3 fps = 2.83 m/sec

Design tube fouling---.0005

Condensation temperature--103°F

1. Number of Parallel Rows of Tubes

$$q_c = \dot{m}\, C_p\, \Delta T \tag{59}$$

Where:

$q_c \equiv$ condenser heat load, equal to the sum of q_e and compressor work input.

$\dot{m} \equiv$ mass flow rate of water.

$C_p \equiv$ specific heat of water.

$\Delta T \equiv$ temperature rise of water in the condenser.

Then:

$$2.57\ \text{MW} + .580\ \text{MW} = \dot{m} \times .997\ \text{Btu/lbm}\ ^\circ\text{F} \times (95^\circ\text{F} - 85^\circ\text{F})$$

$$2986\ \text{Btu/sec} = \dot{m} \times .997\ \text{Btu/lbm}\ ^\circ\text{F} \times 10^\circ\text{F}$$

$$\dot{m} = 299.5\ \text{lbm/sec} = 136.1\ \text{Kg/sec}$$

In addition:

$$\dot{m} = \rho \cdot n \cdot A \cdot V \tag{60}$$

Where:

$\rho \equiv$ density of water

$n \equiv$ number of parallel rows of tubes

$A \equiv$ inner cross section area of one tube

$V \equiv$ velocity of water in tube

From the specifications:

$$299.5\ \text{lbm/sec} = 62.11\ \text{lbm/ft}^3 \times n \times \frac{\pi\left(\frac{.575}{12}\right)^2}{4}\ \text{ft}^2 \times 9.3\ \text{ft/sec}$$

$$n = 288$$

2. Overall Resistance

$$R_{total} = \frac{1}{\eta h_o} + \frac{TT}{\frac{Aw}{A_o} K_w} + \frac{1}{\frac{Ai}{A_o} h_i} + \frac{f}{\frac{Ai}{A_o}} \tag{61}$$

Where:

$\eta \equiv$ fin efficiency

$h_o \equiv$ heat transfer coefficient outside of tube

TT $\equiv$ tube wall thickness

$A_o \equiv$ heat transfer area outside of tube per unit length of tube

Ai $\equiv$ heat transfer area inside of tube per unit length of tube

Aw $\equiv$ (Ao + Ai)/2

Kw $\equiv$ thermal conductivity of tube wall

hi $\equiv$ heat transfer coefficient inside of tube

f $\equiv$ fouling factor

a. Calculation of h_o and Outside Tube Resistance R_o

$$h_o = .728 \left(\frac{g\rho^2 K^3 h_{fg}}{D\mu\Delta T}\right)^{\frac{1}{4}} \qquad (62)^*$$

Where:

$g \equiv$ gravitation

f $\equiv$ density of liquid R-12

K $\equiv$ thermal conductivity of R-12

$h_{fg} \equiv$ latent heat of R-12

D $\equiv$ outside diameter of tube

$\mu \equiv$ dynamic viscosity of R-12

$\Delta T \equiv$ the difference between condensing temperature and tube wall temperature

Then:

$$h_o = .728 \left[\frac{(32.2)(3600)^2(78.48)^2(.04)^3(56.4)}{(\frac{.75}{12})(.59)8}\right]^{\frac{1}{4}}$$

$$= 306.57 \frac{\text{Btu}}{\text{hr-ft}^2\text{-}^o\text{F}}$$

$$R_o \equiv \frac{1}{\eta ho} = \frac{1}{.49 \times 306.57} = 6.64 \times 10^{-3} \frac{\text{hr-ft}^2\text{-}^o\text{F}}{\text{Btu}}$$

b. Calculation of Wall Resistance Rw

$$\frac{Ai}{A_o} = .499$$

$$\frac{A_W}{A_o} = .749$$

* Alan J. Chapman: Heat Transfer

$$Rw \equiv \frac{TT}{\frac{A_w}{A_o} Kw} = \frac{7.2917 \times 10^{-3}}{.749 \times 221} = 4.403 \times 10^{-5} \ \frac{hr\text{-}ft^2\text{-}^oF}{Btu}$$

c. Calculation of hi and Inside Tube Resistance Ri

The Reynolds number is calculated by:

$$R_e = \frac{(\rho)(V)(ID)}{\mu} = 60308$$

where ρ, V, and μ are density, velocity, and dynamic viscosity of water, respectively. ID is the inner diameter of tube.

Hence:

$$Nu = .023\ Re^{0.8}\ Pr^{0.3}$$
$$= .023\ (60308)^{0.8}\ (4.52)^{0.3}$$
$$= 241.31$$

$$hi = \frac{Nu\ k}{ID}$$
$$= 1832\ Btu/hr\text{-}ft^2\text{-}^oF$$

$$Ri \equiv \frac{1}{\frac{Ai}{Ao} hi} = \frac{1}{.499 \times 1832} = 1.094 \times 10^{-3} \ \frac{hr\text{-}ft^2\text{-}^oF}{Btu}$$

d. Calculation of Fouling Resistance R_f

$$R_f \equiv \frac{f}{\frac{Ai}{A_o}} = \frac{.0005}{.499} = 1.003 \times 10^{-3} \ \frac{hr\text{-}ft^2\text{-}^oF}{Btu}$$

e. Overall Resistance R_t

$$R_t = R_o + R_w + R_i + R_f$$
$$= 6.639 \times 10^{-3} + 4.403 \times 10^{-5} + 1.094 \times 10^{-3} + 1.003 \times 10^{-3}$$
$$= 8.78 \times 10^{-3} \ \frac{hr\text{-}ft^2\text{-}^oF}{Btu}$$

In the above calculation, the data of η, Aw/A_o, and Ai/A_o are determined from York's design.

3. Heat Transfer Area

The overall heat transfer coefficient, U, is determined by:

V ≡ velocity of the fluid

ID ≡ inner diameter of tube

Then for one parallel row of tube:

$$\Delta P_\ell = 2 \times \frac{2 \times .008 \times 994.8 \times 4.79 \times 2.83^2}{.0146}$$

$$= 83645 \text{ N/m}^2$$

$$= 12.1 \text{ psia}$$

$$\Delta P_b = 2 \times .008 \times 994.8 \times 2.83^2 \times 50$$

$$= 6374 \text{ N/m}^2$$

$$= .9 \text{ psia}$$

Hence, the total pressure drop is:

$$\Delta P_b = \Delta P_\ell + \Delta P_b$$

$$= 13.0 \text{ psia}$$

$$= 89632 \text{ N/m}^2$$

5. Pumping Power for Water

The pumping power for water, Pu, is calculated by:

$$Pu = \frac{\dot{m}}{\rho} \Delta\rho = \frac{136.1 \text{ Kg/s}}{965 \text{ Kg/m}^3} \cdot 89632 \text{ N/m}^2$$

$$= 12.26 \text{ Kw}$$

$$= 16.44 \text{ HP}$$

VI. CALCULATION OF AIR-COOLED CONDENSER

The results of calculation show that the air condenser has a very large size and needs tremendous amounts of fan power. Therefore, it is considered economically unfeasible to adopt such a system. The following discussion is only for the purpose of completeness.

The calculational procedure of air-cooled condenser is described in detail in Herrick Lab Report No. 6, HL 75-28 under research contract PRF No. 7860. Since the procedure is quite lengthy, it will not be repeated here. The computer program developed in that report has been used with the following modifications:

$$U = \frac{1}{R_t}$$

$$= 113.89 \text{ Btu/hr-ft}^2\text{-}^\circ\text{F}$$

By NTU method:

$$\varepsilon = \frac{Tc_2 - Tc_1}{T_2' - Tc_1} \qquad (63)$$

Where Tc_2 and Tc_1 are the outlet and inlet water temperature, respectively. T_2' is the temperature of the superheated R-12 vapor after compression.

$$\varepsilon = \frac{95^\circ\text{F} - 85^\circ\text{F}}{125^\circ\text{F} - 85^\circ\text{F}} = .25$$

$$NTU = -\ln(1-\varepsilon)$$

$$= .288$$

Then the heat transfer area, A_o, is calculated by:

$$A_o = \frac{(NTU)(\dot{m}C_p)_{H2O}}{U}$$

$$= 2731.6 \text{ ft}^2$$

$$Ai = A_o \cdot \frac{Ai}{A_o} = 2731.6 \times .4985 = 1361.7 \text{ ft}^2$$

If we use two passes for the tube, then the tube length, TL, is given by:

$$TL = \frac{Ai}{2 \cdot n \cdot \pi \cdot ID}$$

$$= 15.7 \text{ ft}$$

$$= 4.79 \text{ m}$$

4. Pressure Drop

$$\Delta P_\ell = \frac{2\bar{f}\rho\ell V^2}{ID} \quad \text{, in straight tube} \qquad (64)$$

$$\Delta P_b = 2\bar{f}\rho V^2 \left(\frac{\ell}{ID}\right)_{equiv} \quad \text{, in the bends} \qquad (65)$$

where:

$\bar{f} \equiv$ Fanning friction factor; its value is found to be .008 from Mollier diagram

$\rho \equiv$ density of the fluid

$\ell \equiv$ tube length

$\left(\frac{\ell}{ID}\right)_{equiv} \equiv$ equivalent tube length for a bend; for a 180° bend, its value is 50

1. The calculations for subcooled condensate is incorporated.
2. Iterative scheme is built in so that as many geometric configurations can be calculated as we wish.
3. The costs of power and heat transfer area are calculated if we know the unit prices of them. This can be used as a criterion for choosing a particular geometric configuration for the condenser.
4. The output of the program has been revised to a more readable form.

In addition, another new program has been developed based on the one we just mentioned. The new computer program is used to calculate the change of heat transfer area versus air-side heat transfer coefficient. This program can be used in the calculation of evaporative air-cooled condensers. For example, if we know the augmented air-side heat transfer coefficient in an evaporative air-cooled condenser, then the needed heat transfer area and power can be looked up from the program output.

1. Sample Design

ST	SL	TF	TT	FPM
2.54×10^{-2}	2.54×10^{-2}	2.54×10^{-4}	8.89×10^{-4}	788
DO	DELT	AFAC	CW	TAI
1.27×10^{-2}	5	18.58	7.983×10^{4}	29.4
VWI	U	AREA	NROP	NR
3614	97.1	1590	191	240
NC	NROPA	TL	WIDE	DEPTH
3	720	3.05	6.10	7.62×10^{-2}
FANP	PUMPP	HA	HW	HWS
4.947×10^{6}	581.5	506.9	3122	1157
TWI	TWO	TSUB		
51.67	39.44	2.78		

Where:

ST ≡ transverse tube spacing, in m

SL ≡ longitudinal tube spacing, in m

TF ≡ fin thickness, in m

TT ≡ tube thickness, in m

FPM ≡ number of fins per meter

DO ≡ outside diameter of tube, in m

DELT ≡ temperature difference between inlet and outlet of air, in ^{o}C

AFAC ≡ face area of the heat exchanger, in m^2

CW ≡ mass flow rate of R-12, in Kg/hr

TAI ≡ inlet temperature of air, in ^{o}C

VWI ≡ velocity of liquid R-12, m/hr

U ≡ overall heat transfer coefficient of condensing section, $Kcal/m^2hr^{o}c$

AREA ≡ heat transfer area, in m^2

NROP ≡ number of parallel rows of tubes

NR ≡ number of rows of tubes

NC ≡ number of columns of tubes

NROPA ≡ number of tubes

TL ≡ tube length, in m

WIDE ≡ width of the heat exchanger, in m

DEPTH ≡ depth of the heat exchanger, in m

FANP ≡ fan power, in W

PUMPP ≡ pump power, in W

HA ≡ heat transfer coefficient of air, in $Kcal/m^2hr^{o}C$

HW ≡ condensing heat transfer coefficient of R-12, in $Kcal/m^2hr^{o}C$

HWS ≡ Subcooling heat transfer coefficient of R-12, in $Kcal/m^2hr^{o}C$

TWI ≡ inlet temperature of R-12, in ^{o}C

TWO ≡ condensing temperature of R-12, in ^{o}C

TSUB ≡ degree of subcooling, in ^{o}C

VII. CALCULATION OF SHELL-AND-TUBE EVAPORATOR (FINNED, R-12 OUTSIDE OF TUBE)

In the condenser calculation, subcooling of the condensate has an effect on the mass flow rate of R-12 and heat load. However, in the evaporator, the subcooling of the condensate will only alter the calculation by the change of mass flow rate of R-12, the heat load will be the same.

The following calculations are based on saturated condensate. If subcooling is desired in the condenser, the whole procedure can be used with proper mass flow rate of R-12.

The following specifications are used:

Tube fluid--liquid water saturated with Cl_2 gas from $45^{o}F$ to $36^{o}F$

Shell fluid--R-12

Shell--48" x 29', low carbon steel

Tubes---.592"ID, .75"OD, .049"wall, 30fpi, Titanium

In tube velocity--5.3 fps = 1.62 m/sec

Design tube fouling---.0005

Evaporation temperature--29.3°F

1. Number of Parallel Rows of Tubes

$$q_e = \dot{m}\, C_p\, \Delta T \tag{66}$$

where:

$q_e \equiv$ evaporator heat load

$\dot{m} \equiv$ mass flow rate of water

$C_p \equiv$ specific heat of water

$\Delta T \equiv$ temperature drop of water in the evaporator

$$2.57\ MW = \dot{m}(1.005 \times 4186.8)\, J/Kg^{\circ}C\ (45^{\circ}F - 36^{\circ}F)$$

$$\dot{m} = 122.156\ kg/sec = 268.743\ lbm/sec$$

In addition:

$$\dot{m} = \rho \cdot n \cdot A \cdot V \tag{67}$$

Where:

$\rho \equiv$ density of water

$n \equiv$ number of parallel rows of tubes

$A \equiv$ inner cross section area of one tube

$V \equiv$ velocity of water in tube

Then:

$$122.156\ Kg/s = 1000\ Kg/m^3 \cdot n \cdot \frac{\pi \cdot (.592/12)^2}{4}\ ft^2 \cdot 5.3\ ft/sec$$

$$n = 426$$

2. Overall Resistance

$$R_{total} = Ro + Rw + Ri + Rf$$

$$= \frac{1}{\eta ho} + \frac{TT}{\frac{Aw}{A_o}\, Kw} + \frac{1}{\frac{Ai}{A_o}\, hi} + \frac{f}{\frac{Ai}{A_o}} \tag{68}$$

where:

$R_o \equiv$ outside tube resistance

$R_w \equiv$ wall resistance

$R_i \equiv$ inside tube resistance

$R_f \equiv$ fouling resistance

$\eta \equiv$ fin efficiency

$h_o \equiv$ heat transfer coefficient outside of tube

$TT \equiv$ tube wall thickness

$A_o \equiv$ heat transfer area outside of tube per unit length of tube

$Ai \equiv$ heat transfer area inside of tube per unit length of tube

$Aw \equiv (A_o + Ai)/2$

$Kw \equiv$ thermal conductivity of tube wall

$hi \equiv$ heat transfer coefficient inside of tube

$f \equiv$ fouling factor

Then:

$$R_o = \frac{1}{\eta h_o}$$

$$= \frac{1}{(.4189)(426.8)}$$

$$= 5.593 \times 10^{-3} \ \frac{\text{hr-ft}^2\text{-}^\circ\text{F}}{\text{Btu}}$$

$$Rw = \frac{TT}{\frac{Aw}{A_o} Kw} = \frac{4.083 \times 10^{-3} \text{ft}}{(.6625)(9.5)\frac{\text{Btu}}{\text{hr-ft}^2\text{-}^\circ\text{F}}}$$

$$= 6.487 \times 10^{-4} \ \frac{\text{hr-ft}^2\text{-}^\circ\text{F}}{\text{Btu}}$$

To calculate Ri, we have to calculate hi first.

$$Re = \frac{(\rho)(V)(ID)}{\mu} = 15631$$

$$Nu = .023 \ Re^{0.8} Pr^{0.3}$$
$$= .023 \ (15631)^{0.8}(11.36)^{0.3}$$
$$= 108.03$$

$$hi = \frac{Nuk}{ID} = 728.78 \ \frac{\text{Btu}}{\text{hr-ft}^2\text{-}^\circ\text{F}}$$

Hence,

$$Ri = \frac{1}{\frac{Ai}{Ao} hi} = \frac{1}{(.325)(728.78)} = 4.2 \times 10^{-3} \ \frac{\text{hr-ft}^2\text{-}^\circ\text{F}}{\text{Btu}}$$

$$R_f = \frac{f}{\frac{Ai}{Ao}} = \frac{.0005}{.325}$$

$$= 1.538 \times 10^{-3} \frac{\text{hr-ft}^2\text{-}^\circ\text{F}}{\text{Btu}}$$

Hence,

$$R_{total} = R_o + R_w + R_i + R_f$$

$$= 5.593 \times 10^{-3} + 6.487 \times 10^{-4} + 4.2 \times 10^{-3} + 1.538 \times 10^{-3}$$

$$= 11.98 \times 10^{-3} \frac{\text{hr-ft}^2\text{-}^\circ\text{F}}{\text{Btu}}$$

In the above calculation, the data of η, h_o, Aw/A_o, and Ai/A_o are determined from York's design.

3. Heat Transfer Area

The overall heat transfer coefficient, U, is then:

$$U = \frac{1}{R_t}$$

$$= 83.474 \frac{\text{Btu}}{\text{hr-ft}^2\text{-}^\circ\text{F}}$$

By NTU method:

$$\varepsilon = \frac{T_{hi} - T_{ho}}{T_{hi} - T_e} \qquad (69)$$

Where T_{hi} and T_{ho} are the inlet and outlet water temperatures, respectively. T_e is the evaporation temperature.

$$\varepsilon = \frac{45^\circ\text{F} - 36^\circ\text{F}}{45^\circ\text{F} - 29.3^\circ\text{F}} = 0.573$$

$$NTU = -\ln (1-\varepsilon) = .852$$

The heat transfer area, A_o, is then determined by:

$$A_o = \frac{(NTU)(\dot{m}Cp)_{water}}{U} = 9944 \text{ ft}^2$$

$$A_i = A_o \cdot \frac{Ai}{A_o} = 9944 \times .325 = 3231.8 \text{ ft}^2$$

If we use two passes for the tube, then the tube length, TL, is given by:

$$TL = \frac{Ai}{2 \cdot n \cdot \pi \cdot ID}$$

$$= 24.5 \text{ ft}$$

$$= 7.47 \text{ m}$$

4. Pressure Drop

In the straight tube:

$$\Delta P_\ell = \frac{2\bar{f}\rho\ell V^2}{ID} \tag{70}$$

In the bends:

$$\Delta P_b = 2\bar{f}\rho V^2 \left(\frac{\ell}{ID}\right)_{equiv} \tag{71}$$

where:

$\bar{f} \equiv$ Fanning friction factor; its value is found to be .008 from Mollier diagram.

$\rho \equiv$ density of the fluid

$\ell \equiv$ tube length

$\left(\frac{\ell}{ID}\right)_{equiv} \equiv$ equivalent tube length for a bend; for a 180° bend its value is 50

$V \equiv$ velocity of the fluid

$ID \equiv$ inner diameter of tube.

Then for one parallel row of tubes:

$$\Delta P_\ell = 2 \times \frac{2 \times .008 \times 1000 \times 7.47 \times 1.62^2}{.015}$$

$$= 41822 \text{ N/m}^2$$

$$= 6.06 \text{ psia}$$

$$\Delta P_b = 2 \times .008 \times 1000 \times 1.62^2 \times 50$$

$$= 2100 \text{ N/m}^2$$

$$= .30 \text{ psia}$$

REFRIGERATION-SYSTEM BILL OF MATERIALS

OPEN TURBOMASTER CENTRIFUGAL COMPRESSOR
LIQUID CHILLING UNITS

COMPRESSOR

The subject compressor is a multi-stage internally geared centrifugal compressor designed to utilize Refrigerant-12 (CCl_2F_2-dichlorodifluoromethane). Model M226A Compressor is designed for 731 tons at 36.2F, leaving chilled water. At these conditions suction and discharge temperature would be approximately 29.3F and 103F respectively. Typical impeller speed will be 7100 rpm with shaft horsepower 791, motor amps 900 and locked rotor current 4000 amps with power factor of 0.89. With normal gear loss of 2% and motor efficiency of 95.5% the chiller only KW/ton is .862 which is 13.92 EER. This open style compressor can be driven by practically any type of drive; open electric motor, gas turbine, steam turbine, gass or diesel engine.

A system with an open style compressor is shown on Page 4 of Form 160.71-NMI.

IMPELLERS

The impellers are aerodynamically designed for maximum efficiency and are accurately cast from durable lightweight aluminum alloy with backward curved blades and cover shrouds. The impeller assembly is mounted directly on the end of the pinion shaft and is dynamically balanced.

COUPLING/DRIVE SHAFT

Light weight, non-lubricated, statically balanced - flexible alloy steel threaded drive shaft - designed to provide access to shaft seal and front journal bearing without disturbing main drive alignment - with high speed coupling guard.

SHAFT SEAL

Rotating cast iron runner - stationary precision carbon ring, spring loaded - small face area, low rubbing speed - pressure lubricated in operation and oil flooded at all times - accessible without removing top half of casing.

Hence, the total pressure drop is:

$$\Delta P_t = \Delta P_\ell + \Delta P_b$$
$$= 6.36 \text{ psia}$$
$$= 43851 \text{ N/m}^2$$

5. Pumping Power for Water

The pumping power for water, P_u, is calculated by:

$$P_u = \frac{\dot{m}}{\rho} \Delta P = \frac{122.156 \text{ kg/sec}}{1000 \text{ kg/m3}} \cdot 43851 \text{ N/m}^2$$

$$= 5.36 \text{ KW}$$
$$= 7.18 \text{ HP}$$

LUBRICATION SYSTEM

Completely factory packaged, assembled and piped (steel tubing) with oil sump (reservoir) as integral part of compressor - bearings and shaft seal oil flooded at all times - main oil pump mounted directly on rotor shaft assures force feed lubrication to all bearings and seals at all times, even under power failure coast-down conditions. External auxiliary oil pump (AOP), motor driven, assures pressure lubrication prior to start-up, during normal shut-down and at any time main oil pump does not maintain required pressure - AOP motor explosion proof (NEMA 7) inherently protected available for 200 thru 600 volts - 3 phase - 60/50 Hertz service; 2 HP for M226, starting contactor furnished separately for field mounting and wiring. Oil filter, external with 15 micron replaceable element and service valves. Oil cooler, external water cooled cleanable shell and copper tube type - for entering water temperatures up to 90°F at .0005 fouling factor. Oil heater(s), 1000 watt, 115 volt - 1 phase - 60/50 Hertz thermostatically controlled immersion type - to maintain 150°F sump oil temperature during shut-down to minimize refrigerant accumulation in oil. Also includes 2" oil level sight glasses (2) in sump, high oil temperature cutout (1) in thrust bearing oil outlet, 5½" scale industrial type bronze case separable socket oil temperature thermometers with brass wells in sump, thrust bearing outlet line and bearing supply line - 3½" gauge indicating thrust bearing oil pressure, oil charging valve and oil drain valves. All electrical components for NEMA 1 application, except AOP motor as noted.

PREROTATION VANES AND OPERATING MECHANISM

Prerotation vanes are used in the inlet of the compressor as a capacity control device, to provide highly efficient part load operation. The PRV's reduce the capacity of a constant speed centrifugal compressor by partially restricting the inlet area ahead of the impeller and introducing pre-swirl to the vapor entering the impeller. The pre-swirl imparted to the suction vapor actually reduces the head producing capabilities of the impeller. The individual vanes are airfoil shaped to produce better efficiency and to keep the required operating force at a minimum. The force required to operate the vanes also is reduced by rotating the vanes about an axis located off the center of the vane.

The PRV's are positioned by a simple steel drive ring, connecting linkage and a specially designed control shaft which requires no shaft seal. Seal is flexible and bonded - no rubbing surfaces or leaks.

SERVICING

The entire compressor was designed with the serviceman's interest in mind. The number of individual components has been held to a minimum for simplicity and compactness. With the open style compressor, with a horizontal split case, all but one of the journal bearings are accessible without disassembling the rotor support section. Prerotation vanes and internal driving mechanism along with the impeller eye seal can be serviced without removal of the rotor scroll.

EVAPORATOR

The Cooler (Evaporator) of York Turbomaster System is of the shell and extruded fin type with tube ends rolled into the tube sheets.

Refrigeration Tons = 731 Refrigerant - R12
Fluid being cooled - 2000 gpm aqueous chlorine solution from 45F to 36F

COOLER: Type - Flooded, York Standard OM design (ASME Code), Marine type water boxes, tubes rolled into tube sheet.

Shell dia. and length - 48" x 29'

Tubes: 871 Titanium finned (Hi Performance #HPT305049) 3/4" O.D., .049" wall, 30 fpi, 24' NTL, 2 pass

In-tube velocity = 5.3 fps; Pressure drop = 6.2 psi
Tubeside design pressure = 150 psi
Design tubeside fouling = .0005; Design ETP = 29.3F

Materials: Refrigerant shell, tube supports and connections will be lo-carbon steel; tubes are titanium; tube sheets and water boxes are steel with titanium cladding (about ¼" thick) on solution side.

CONSTRUCTION AND FUNCTION

The Cooler - horizontal flooded shell and tube type - tubes roller expanded into intermediate tube supports - multiple liquid inlets with integral header - perforated liquid refrigerant and entrained flash gas distributor plate extending

full length and width below tube bundle - gas baffles on sides of shell to force entrained flash gas to flow up thru tube bundle to keep all the tubes wetted, even under varying load conditions - upper portion of shell free of tubes to provide refrigerant liquid/gas separation space - steel suction gas baffle full length of tubes for even distribution of gas flow, and liquid droplet elimination - hot gas bypass inlet baffle assures uniform gas distribution and prevents direct gas impingement on cooler tubes - two 2" sight ports. High capacity relief valve(s) in accordance with ANSI-B9.1 Safety Code in series with a carbon bursting disc(s) for leak tightness (for tield piping). Refrigerant connections: capped bottom liquid inlet header, and liquid transfer, and plugged coupling for thermometer well - flanged top front suction (single suction on shells for 14' thru 20' tube length, and dual suction on shells for 22' thru 30' tube length) - capped rear hot gas inlet - plugged top front unit relief - valved top front gas charging.

OPERATION

The function of the cooler (evaporator) is to transfer the heat of the Cl_2 solution to the refrigerant surrounding the cooler tubes. As this heat is transferred, the liquid refrigerant boils. The rate at which liquid refrigerant is evaporated will vary directly with the amount of heat removed from the Cl_2 water solution.

INTERCOOLER

Single stage, external horizontal type with drop leg, fabricated from steel plate - fusion welded seams - liquid inlet deflector baffle - high pressure float valve - interstage gas mist eliminators - intermediate pressure float valve in liquid drop leg - manual external float valve adjustors - test thermometer wells in high pressure and intermediate pressure chambers - 2" sight ports - for high pressure float chamber (2), eliminator chamber (2), and intermediate pressure float/chamber (2) - float valves and eliminators accessible thru bolted on shell end cover plates - mounting support(s) for spring type isolator(s). Refrigerant connections: capped high pressure liquid inlet, interstage flash gas outlet and low pressure liquid outlet - plugged auxiliary high and intermediate pressure liquid, and drop leg liquid drain.

SERVICE

Service on these coolers consists of replacing leaking tubes, replacing gaskets and cleaning the water sides of the tubes. For general service procedures covering cleaning and tube replacement, refer to Instruction 2J.

CONDENSER

The hot, high pressure discharge gas from the compressor enters the condenser thru the discharge gas inlet. The gas enters the space around the condenser tubes thru a perforated baffle which prevents the hot gas from impinging directly upon the tubes. Diagonal baffles above the tube bundle provides an area of reduced turbulence at the top of the condenser in which any air and non-condensable gas will accumulate.

As the hot gas condenses to a liquid, it falls to the bottom of the condenser shell and flows out to the intercooler thru the liquid outlet.

The Condenser of the York Turbomaster Systems is of the shell and finned tube type with tube ends rolled into the tube sheets. It will be a two (2) pass equipped with water boxes.

Type - York Standard OM design (ASME Code)
Shell diameter and length - 30" x 18'
Tubes: 582 copper finned, 3/4" O.D., 20 BWG wall, 19 fpi, 14' NTL,
2 pass, 2193 gpm coolant 85-95F
In-tube velocity = 9.3fps, pressure drop = 9.1 psi
Tubeside design pressure = 150 psi
Design tubeside fouling = .0005; design condensing temperature = 103F
Materials: Lo-carbon steel except for copper tubes

OPERATION

The function of the condenser is to cool and liquefy the high temperature discharge gas from the compressor. This is accomplished by transferring the latent heat of condensation plus the superheat to the condenser cooling water flowing through the condenser tubes. As this heat is transferred, the refrigerant gas condenses and the heat is carried away by the cooling water.

SERVICE

Service on these condensers consists of replacing leaking tubes, replacing gaskets and cleaning the water sides of the tubes. For general service procedures covering cleaning and tube replacement, refer to Instruction 2J.

MOTOR LINE/BASE ASSEMBLY

MOTOR LINE BASE

Sincle base to mount compressor and motor, and speed increaser - rigid design for controlled alignment - welded structural steel channel construction - steel mounting plates/pads for individual components - mounting brackets for spring type isolators.

MOTOR LINE ASSEMBLY

Components factory assembled and rough aligned on base - mounting holes located, drilled and tapped - components reassembled, aligned and shallow doweled - final alignment and doweling after installation prior to unit start-up. Drive line component (compressor, speed increaser, motor) oil cooler water piping factory assembled to common manifold at the end of the base - galvanized steel pipe and fittings with manual stop valves.

SUMMARY OF COOLING EQUIPMENT

The equipment selection of the Chilled Water System was prepared to meet the requirements of a 100 MWh Load Leveling Zinc Chloride ($ZnCl_2$) Storage Battery System. The above components have been selected as matched to the load as described in the Herrick Laboratories Proposal of June, 1976, after conferences between Herrick Laboratories and York Division, Borg-Warner Corp. personnel and as documented with their correspondence:

1. Chiller:
   - 1.1 Compressor
   - 1.2 Condenser
   - 1.3 Evaporator (Cooler)
2. Cooling Tower (York does not manufacture towers)
   - 2.1 Piping and pumps to tower and from condenser
   - 2.2 Inside tower water storage tank
3. Enclosing Structure and Foundation for Items 1 and 2
   - 3.1 Placement of Equipment on foundation before erecting enclosure
4. Motor Starter and Wiring
   - 4.1 Starter
   - 4.2 Wiring
5. Thermal Insulation of Cooler and Suction Line
6. Test, Check and Start-up

THERMAL DESIGN OF EVAPORATIVE CONDENSER

Preface

Parallel to the optimization of water-cooled condenser a study of wetting the air-cooled type was in progress. Due to the fact that thermal design of the first one has been considered of a prime importance, detailed approach and results of evaporative condenser design and its possible application to the overall system will be described in the next report.

The following is only the brief information about that study.

Characteristics of evaporative condenser

Water is circulated and sprayed on the outside surface of the tube bundle which is either finned or bare, while air is blown from the bottom. The process fluid (freon 12) inside the tube is cooled by utilizing in the first place the latent heat of evaporation. Heat is transferred from the process fluid (freon) to the water spray from which sensible and latent heats are transferred to the passing air stream.

Heat and mass transfer mechanism

Involves heat and mass transfer between three kinds of fluids of a very complex nature. In addition the temperature of the circulating water varies from the top to the bottom of the coil.

The most general case takes into account the presence of both wetted (A_{wet}) and unwetted (A_{dry}) heat transfer surfaces.

The water undergoes heat and mass exchange with air over the phase boundary surface (A_{wa}), and heat exchange with process fluid (freon) over the wetted heat transfer surface (A_{wet}).

The air undergoes heat and mass exchange with the water at the phase boundary surface (A_{wa}) and with refrigerant at the unwetted wall surface (A_{dry}).

Thus, it is apparent that several heat transfer coefficients take place, i.e.,

1. Heat transfer film coefficient between process fluid and tube wall;
2. Heat transfer film coefficient between water and boundary surfaces A_{wa}) and (A_{wet});
3. Heat transfer film coefficient between air and boundary surfaces (A_{dry}) and (A_{wa}); and

overall heat transfer coefficients between process fluid and water (U_{fw}) and between process fluid and air (U_{fa}).

The analysis of such system considered through the heat and mass balance of the control volume cannot determine all unknown parameters, because additional equations are not available.

Thus, step-by-step procedure is required to evaluate heat transfer performance and the change of state of air and water both flowing through the passages of the heat exchanger.

Grapho-analytical method

The system considered for the analysis represents an air channel between two

fins. General consideration specifies three different models:

1. Channel heated both at wetted and unwetted walls;
2. Channel with entirely wetted walls and work with an excess water quantity, while air and water are in counterflow arrangement ($A_{dry} = 0$)
3. Channel with entirely wetted walls and work with complete evaporation, while air and water are in counterflow arrangement.

The above specified models require graphical evaluation by the aid of psychometric charts and "The Partial Value Procedure", as described in technical literature (e.g., see: Technical Thermodynamics, Bosnjakovic, Holt, Rinehart and Winston, 1965).

Evaporative Condenser Design

For the purpose of thermal design and optimization an extended psychrometric chart has been developed for the need of sufficient graphical accuracy. The flow diagrams explaining the design procedure have been also developed for the purpose of optimization.

The brief description of design procedure is as follows:

1. Specify heat exchanger initial geometry (tube diameter, distance between tubes, fin thickness, number of fins per unit length, etc.);
2. Estimate water and air mass flow rates through channel element;
3. Calculate heat transfer film coefficients;
4. Calculate overall heat transfer coefficients U_{fw} and U_{fa};
5. Apply graphical method and the partial value procedure in order to get change of air and water states from the top to the bottom of a coil.
6. Calculate evaporation surface (A_{wa}) according to the number of graphical steps in psychrometric chart ($n_{0.5}$), air mass flow rate (L), heat transfer film coefficient on the air side of the water-air interface (h) according to the following equation:

$$A_{wa} = n_{0.5} \times 0.696 \times \frac{LCp}{h} \ (m^2)$$

   (Note: valid if "The Half-value Procedure" is applied).
7. Calculate the total heat removed from refrigerant per channel with evaporation surface area A_{wa}.
8. Based on total required heat to be removed from refrigerant the number of

element channels becomes known.

9. The total number of channels yields the total heat exchange area and total air and water mass flow rates.
10. Optimization is obtained by changing initial geometry, estimated air or water mass flow rate per channel, desired outlet air state, or lowering the temperature of condensation. That will result in a higher coefficient of performance, i.e., compressor load and its size and power consumption will be reduced.